Annual Research Journal

Electrical Engineering Research Experience for Undergraduates

Vol. V

August 2007

National Science Foundation
Grant No. EEC-0244030

Principal Investigators:
Ruyan Guo and W. K. Jenkins

PENNSTATE

Department of Electrical Engineering
University Park, Pennsylvania

Annual Research Journal, Vol. V
Electrical Engineering Research Experience for Undergraduates

ISBN 0-913260-07-X (http://www.ee.psu.edu/reu/)

EEREU Annual Research Journal

Ruyan Guo (editor)
W. Kenneth Jenkins (co-editor)

Volume **V**
Published in 2007 by
The Department of Electrical Engineering
The Pennsylvania State University
University Park, Pennsylvania, 16802

NSF EE REU Site Program Contact

316 Electrical Engineering East
The Pennsylvania State University
University Park, PA 16802
Telephone (814) 865-0184
Fax (814) 865-7065
E-Mail: eereu@engr.psu.edu
Web Site: http://www.ee.psu.edu/reu/

ISBN 0-913260-07-X
978-0-913260-07-4

Annual Research Journal, Vol. V
Electrical Engineering Research Experience for Undergraduates

ISBN 0-913260-07-X (http://www.ee.psu.edu/reu/)

PREFACE

We are happy to present the **2007 *Annual Research Journal – Electrical Engineering Research Experience for Undergraduates, Vol. V.*** This volume contains highlights of the EEREU program activities in summer 2007 and nineteen technical papers written by EEREU scholars as primary authors.

Summer 2007 marks our fifth year hosting the National Science Foundation sponsored Research Experience for Undergraduates (REU) Site program, by Department of Electrical Engineering, Penn State University. Nineteen outstanding young men and women participated in this year's EEREU program at Penn State's University Park Campus. These EEREU scholars, selected from nation-wide applicants, are primarily college sophomores or juniors with outstanding academic backgrounds and intense interests in exploring research in electrical engineering and related areas.

During the nine-week summer program, EEREU students carried out research projects under the guidance of his or her faculty mentor(s), in laboratories hosted by Department of Electrical Engineering and Materials Research Institute, Penn State. The students also presented their research experience and findings at the 2007 Annual *EEREU Symposium,* held at University Park, in July 2007.

Besides research activities, the EEREU program organized an array of group activities including ***Weekly Scientific Seminar Series*** that introduces a broad range of research topics to the REU students, ***field trip program*** that offers EEREU students opportunities to visit prominent local and regional industrial and research sites, and ***Weekly Workshop on Ethics and Professional Development*** through which students were engaged in debate and analysis of ethical issues in engineering. For more information about Penn State's EEREU program, please visit our website at: http://www.ee.psu.edu/reu/.

We are confident that readers will find that the series of EEREU journals showcases the achievement of our EEREU students and effective mentorship provided by the faculty and graduate student mentoring teams. We are also hopeful that this publication not only document original research that are of value for scientific dissemination and publications, it may stimulate more college students to consider research career and to pursue graduate studies in electrical engineering.

We would like to acknowledge our collaboration with the ***Summer Research Opportunity Program*** (SROP) at Penn State and express our appreciation to **Mr. Jeremiah Turpin** for his assistance in editing this volume.

Ruyan Guo and W. Kenneth Jenkins
Co-Directors of the NSF EE REU Site Program
Dept. EE, The Pennsylvania State University

July 2007
University Park, Pennsylvania

Annual Research Journal, Vol. V
Electrical Engineering Research Experience for Undergraduates

ISBN 0-913260-07-X (http://www.ee.psu.edu/reu/)

Annual Research Journal, Vol. V
Electrical Engineering Research Experience for Undergraduates

ISBN 0-913260-07-X (http://www.ee.psu.edu/reu/)

TABLE OF CONTENTS

Research Articles (* indicates REU student author)

Annual Research Journal, Vol. V
Electrical Engineering Research Experience for Undergraduates

ISBN 0-913260-07-X (http://www.ee.psu.edu/reu/)

Annual Research Journal, Vol. V
Electrical Engineering Research Experience for Undergraduates

ISBN 0-913260-07-X (http://www.ee.psu.edu/reu/)

2007 NSF EEREU FACULTY & STAFF MEMBERS

Faculty Mentors
Prof. Amar Bhalla
Prof. Sven Bilén
Prof. Andres Diaz
Prof. Craig Grimes
Prof. Ruyan Guo, Director
Prof. Heath Hofmann
Prof. Ken Jenkins, Co-Director
Prof. I. C. Khoo
Prof. Mike Lanagan
Prof. Zhiwen Liu
Prof. John Mathews
Prof. Theresa Mayer
Prof. John Mitchell, Seminar Chair
Prof. Robert Nickel
Prof. Victor Pasko
Prof. Joan Redwing
Prof. Jeff Schiano
Prof. Srinivas Tadigadapa
Prof. Kenji Uchino
Prof. Julio Urbina

Prof. Andy Lau, Ethics Workshop Chair
Prof. David Salvia, Activities Chair
Ms. Amy Freeman, Adviser, Engineering Diversity
Prof. Elizabeth Kisenwether, Guest Organizer

Mrs. Linda Becker, Administration
Mr. Donald Natale, III, Assistant Director
Ms. Lana Yezhova, Web editor

Annual Research Journal, Vol. V
Electrical Engineering Research Experience for Undergraduates

ISBN 0-913260-07-X (http://www.ee.psu.edu/reu/)

2007 EEREU Scholars, Research Projects, & Faculty Mentors

2007 REU Scholars	Research Topics	Faculty Mentors
Mr. Jonathan Becker Electrical Engineering Syracuse University	Studies of Electromagnetic Fields in the Atmosphere	Prof. Victor Pasko 121 ELEC ENGR EAST
Mr. Filmon Berhe Computer Engineering Jackson State University	Piezoelectric Cymbal Actuators Implemented in an Laptop Liquid-Cooling System	Prof. Kenji Uchino 134 MATERIALS RES LAB BLDG
Mr. Jarrett Blythe Engineering Norfolk State University	Temperature Dependence of Piezoelectric Property Measured by An Interferometric Method	Prof. Ruyan Guo 108B RUA, MATERIALS RES LAB BLDG
Mr. Martin Bode Applied Physics Linfield College	Design of a Power Regulation Subsystem for NittanySat	Prof. Sven Bilén 213N HAMMOND BLDG
Mr. Christopher Brown Electrical and Computer Engrg University of Rochester	Energy Harvesting From Tires Using Piezoelectric Transducers	Prof. Heath Hofmann 209K ELEC ENGR WEST
Miss Marie Cosgrove-Davies Engineering Swarthmore College	Infrared Detection using Barium Titanate compounds	Prof. Amar Bhalla 187 MATERIALS RES LAB BLDG
Mr. Adam C. Escobar **(SROP and EEREU)** Electrical Engineering Penn State University	Preliminary Design of the NittanySat Langmuir Probe Experiment	Prof. Sven Bilén 213N HAMMOND BLDG
Miss Kathryn Greenberg Physics Mount Holyoke College	Nonlinear Optical Fiber Imaging Array Passive Pulsed Laser Switching and Sensor Protection	Prof. I.C. Khoo 216A ELEC ENGR EAST Dr. Andres Diaz 1 ELEC ENGR EAST
Mr. David Grubbs Physics/Enginnering Lincoln University	Plasma Treatment of Titanium Dioxide Nanotubes	Prof. Craig Grimes 217 MATERIALS RES LAB BLDG

Annual Research Journal, Vol. V
Electrical Engineering Research Experience for Undergraduates

ISBN 0-913260-07-X (http://www.ee.psu.edu/reu/)

2007 EEREU Scholars, Research Projects, and Faculty Mentors (cont.)

Mr. Andrew Hawk Electrical and Computer Engrg The Citadel	Analysis of ACE Satellite and Ground-Based Magnetometer Data Correlating Space Weather Events	Prof. John Mathews 323A ELEC ENGR EAST Prof. Jack Mitchell 330 ELEC ENGR EAST
Miss Anne Itsuno Electrical and Computer Engrg. Franklin W. Olin College Engrg.	Integration of Antimonide-Based Nanowires with Silicon Substrates	Prof. Joan Redwing 108 STEIDLE BLDG Prof. Theresa Maye 230 ELEC ENGR WEST
Mr. Jason Okerman Electrical Engineering Grove City College	Femtosecond Laser Beam Shaping	Prof. Zhiwen Liu 314 ELEC ENGR EAST
Miss Jacqueline Queen Physics West Virginia Wesleyan College	Investigation of the Zeeman Effect for Quadrupole Resonance Imaging	Prof. Jeff Schiano 227D ELEC ENGR WEST
Mr. Christopher Rosser **(EEREU and SROP)** Computer Engineering Jackson State University	Design of a Prototype Communication Interface for NittanySat Subsystems	Prof. Sven Bilén 213N HAMMOND BLDG
Mr. Michael Steiner Electrical Engineering Virginia Polytec Inst & State Univ.	An Exploration of Audio Signal Processing Algorithms for Audio Denoising and Audio Effects	Prof. Ken Jenkins 121 ELEC ENGR EAST Prof. Robert Nickel 111H ELEC ENGR WEST
Mr. Karthik Sridhara Electrical Engineering Pennsylvania State University	Transport Properties of Graphene	Prof. Srinivas Tadigadapa 121 ELEC ENGR EAST
Mr. Juan Tamez **(EEREU and SROP)** Electrical engineering Univ. Texas at San Antonio	Development of a Cognitive Device Driver using mini-itx system	Prof. Jack Mitchell 330 ELEC ENGR EAST Prof. Julio Urbina 315 ELEC ENGR EAST
Mr. Jeremiah Turpin Electrical Engrg with Computer Grove City College	Oxide and Nitride Thin Films for Revolutionary High Power Tunable Devices	Prof. Mike Lanagan 278 MATERIALS RES LAB BLDG
Mr. Michael Wright **(SROP and EEREU)** Electrical and Computer Engrg Florida State University	Implementation of an FPGA-based Adaptive Radar Controller	Prof. Julio Urbina 315 ELEC ENGR EAST

Annual Research Journal, Vol. V
Electrical Engineering Research Experience for Undergraduates

ISBN 0-913260-07-X (http://www.ee.psu.edu/reu/)

NSF EEREU 2007 Summer Program
Weekly Scientific Seminar Series

Room 225 E E West, 9:40 – 10:30 AM, Tuesdays
(*The seminar is open to public*.)

Department of Electrical Engineering
Pennsylvania State University, University Park, PA 16802

Seminar Chairs: **Prof. Jack Mitchell and Prof. Ken Jenkins**

Date	***Topic***	***Speaker***
June 5, 2007	The Joy of Quadrupole Resonance	Jeff Schiano
June 12, 2007	Lightning-related Transient Luminous Events in the Middle Atmosphere	Victor Pasko
June 19, 2007	Software Defined Radio Applications	Sven Bilén
June 26, 2007	Semiconductor Nanowires: Building Blocks for Nanoscale Devices	Joan Redwing
July 3, 2007	Electronics Everywhere	Thomas Jackson
July 10, 2007	What's Next? Graduate School, of Course!	Ken Jenkins
July 17, 2007	Manipulation, Spectroscopy, and Imaging Using White Light Supercontinuum	Zhiwen Liu
July 24, 2007	(reserved for symposium presentation preparation)	
July 26, 2007 (Thursday)	2007 NSF EEREU Symposium	REU Students

Suggestions and inquiries: eereu@engr.psu.edu

The Seminar is followed (at 10:50 -11:50 AM Tuesdays) by
EEREU Weekly Workshop on Ethics and Professional Development

Annual Research Journal, Vol. V
Electrical Engineering Research Experience for Undergraduates

ISBN 0-913260-07-X (http://www.ee.psu.edu/reu/)

NSF EEREU 2007 Summer Program
Weekly Workshop on Ethics and Professional Development

Room 225 EE West, 10:50 am–11:50 am, Tuesdays
Department of Electrical Engineering
Pennsylvania State University, University Park, PA 16802
Chair: **Prof. Andrew Lau** (andylau@psu.edu)

Suggestions and inquiries: eereu@engr.psu.edu

Date	***Workshop Topic Addressed***	***Week***	***Faculty Leader***
May 30	(Welcome/Orientation Activities)	***wk 1***	Prof. Andy Lau (Chair)
June 5	Introduction; Types of Moral Problems; Academic Integrity	***wk 2***	
June 12	Central Professional Responsibilities of Engineers – Codes of Ethics and Their Application; The Responsible Conduct of Research	***wk 3***	
June 19	Global Environmental Issues: Climate Change, Oil Depletion, Sustainability	***wk 4***	
June 26	Technology transfer and commercialization: challenges, pitfalls and ethics	***wk 5***	Prof. Kisenwether
July 3	Happy Valley Values - The Game	***wk 6***	Prof. Andy Lau (Chair)
July 10	Student Presentations of Ethical Issues in Their Research	***wk 7***	
July 17	Student Presentations of Ethical Issues in Their Research	***wk 8***	
July 24	(Reserved: symposium presentation preparation)	***wk 9***	
July 26 (Thursday)	2007 NSF EEREU Symposium	***wk 9***	

Annual Research Journal, Vol. V
Electrical Engineering Research Experience for Undergraduates

ISBN 0-913260-07-X (http://www.ee.psu.edu/reu/)

2007 NSF EE REU Field Trip Program
Academic/Industrial Sponsors and Tour Hosts

Department of Electrical Engineering
Penn State University, University Park, Pennsylvania

Materials Research Institute
Penn State University, University Park, Pennsylvania

Applied Research Laboratory
Penn State University, University Park, Pennsylvania

Breazeale Nuclear Reactor
Penn State University, University Park, Pennsylvania

Nanofabrication National Facility
Penn State University, University Park, Pennsylvania

State of The Art, Inc.
State College, Pennsylvania

Videon Central, Inc.
State College, Pennsylvania

Compunetix, Inc.
Monroeville, Pennsylvania

The Technology Collaborative
Pittsburgh, Pennsylvania

Vocollect Corp.
Pittsburgh, Pennsylvania

Seagate Technology
Pittsburgh, Pennsylvania

Annual Research Journal, Vol. V
Electrical Engineering Research Experience for Undergraduates

ISBN 0-913260-07-X (http://www.ee.psu.edu/reu/)

2007 NSF EE REU SYMPOSIUM

8:30 AM to 4:15 PM, Thursday, July 26, 2007
Room 225 Electrical Engineering West Building
Pennsylvania State University, University Park, PA 16802

Time	Sessions and Topics	Chairs and Speakers
8:30 - 8:55 am	**Symposium Registration (Refreshments Provided)**	**(Linda Becker Donald Natale)**
8:55 – 9:00 am	**Welcome**	**Ken Jenkins**
9:00 – 10:30 am	**Session I** Session Chairs:	**Bilén/Urbina/ Mitchell/Pasko**
9:00 – 9:15	COMPUTER SYSTEM CONTROL BUS: COMMUNICATING WITH NANOSATELLITE SUBSYTEMS	Christopher Rosser
9:15 – 9:30	IMPLEMENTATION OF A FPGA-BASED COGNITIVE RADAR CONTROLLER	Michael Wright
9:30 – 9:45	THE DEVELOPMENT OF A COGNITIVE DEVICE DRIVER (CDD)	Juan Tamez
9:45 – 10:00	DIURNAL AND SEASONAL POWER VARIATIONS OF SCHUMANN RESONANCES	Jonathan Becker
10:00 – 10:15	POWER SUBSYSTEM DESIGN FOR A SMALL SATELLITE	Martin Bode
10:15 - 10:30	PRELIMINARY DESIGN OF THE NITTANYSAT LANGMUIR PROBE EXPERIMENT	Adam C. Escobar
10:30 – 10:45	**Coffee Break** **(Group Photo at 10:30 – All invited. Please plan to be available)**	(Donald Natale)
10:45 – 12:00	**Session II** Session Chairs:	**Hofmann//Mathews /Grimes/Jenkins/ Nickel/ Schiano**
10:45 – 11:00	DISTRIBUTED ENERGY HARVESTING USING PARALLEL CONNECTED PIEZOELECTRIC DEVICES AND RECTIFIERS	Christopher Brown
11:00 – 11:15	ANALYSIS OF ACE SATELLITE AND GROUND-BASED MAGNETOMETER DATA TO TEST CORRELATION OF SPACE WEATHER EVENTS OBSERVED IN SPACE AND ON EARTH	Andrew Hawk
11:15 – 11:30	INVESTIGATION OF THE ZEEMAN EFFECT FOR QUADRUPOLE RESONANCE IMAGING	Jacqueline Queen
11:30 – 11:45	PITCH SHIFTING OF A SPEECH SIGNAL BY SOURCE-FILTER PROCESSING	Michael Steiner
11:45 – 12:00	CARBON DOPED TITANIUM DIOXIDE NANOTUBE ARRAYS	David Grubbs
12:15 – 1:30	**Luncheon (FSC Room, Nittany Lion Inn)**	

Annual Research Journal, Vol. V
Electrical Engineering Research Experience for Undergraduates

ISBN 0-913260-07-X (http://www.ee.psu.edu/reu/)

2007 NSF EE REU SYMPOSIUM (cont.)

8:30 AM to 4:15 PM, Thursday, July 26, 2007
Room 225 Electrical Engineering West Building
Pennsylvania State University, University Park, PA 16802

Time	Sessions and Topics	Chairs and Speakers
1:45 – 2:45 pm	**Session III** Session Chairs:	**Tadigadapa/ Redwing/Liu/ Khoo/Diaz/**
1:45 – 2:00	ELECTRIC FIELD EFFECT IN n-GRAPHENE LAYER (n-GL) FILMS IN DIFFERENT GAS ENVIRONMENTS	Karthik Sridhara
2:00 – 2:15	GROWTH AND CHARACTERIZATION OF GASB CRYSTAL NANOWIRES ON SILICON AND SAPPHIRE SUBSTRATES	Anne Itsuno
2:15 – 2:30	FEMTOSECOND LASER BEAM SHAPING	Jason Okerman
2:30 – 2:45	NONLINEAR OPTICAL FIBER IMAGING ARRAY FOR PASSIVE PULSED LASER SWITCHING AND SENSOR PROTECTION	Kathryn Greenberg
	2:45 – 3:00 pm Coffee Break	
3:00 – 4:00 pm	**Session IV** Session Chairs:	**Lanagan/Bhalla/ Guo/Uchino**
3:00 – 3:15	CHARACTERIZATION TECHNIQUE FOR THIN DIELECTRIC FILMS USING INTERDIGITAL CAPACITORS	Jeremiah Turpin
3:15 – 3:30	LOW TEMPERATURE PYROELECTRIC CHARACTERICS OF BARIUM TITANATE	Marie Cosgrove-Davies
3:30 – 3:45	LONGITUDINAL PIEZO COEFFICIENT OF PMN-PT CRYSTAL AS FUNCTION OF TEMPERANCE & FREQUENCY BY DYNAMIC INTERFEROMETRIC MEASUREMENT	Jarrett Blythe
3:45 – 4:00	PIEZOELECTRIC PUMP WITH A PIEZOELECTRIC CYMBAL ACTUATOR FOR LAPTOP COOLING APPLICATIONS	Filmon Berhe
4:00 – 4:15	**CONGRATULATIONS AND CONCLUDING REMARKS**	**Guo/Jenkins/Natale**

4:15 pm Adjournment

Picnic at Sunset Park, 5:00 pm – sunset, ALL ARE INVITED

Resource:	Donald Natale and Linda Becker
Special Notes:	Laser pointer, desktop PC and LCD PC projector are provided. Speakers please upload presentation files to EEREU group web in Angel by July 25 Wed.. It is strongly recommended that speakers test-run presentation files for audio, video, or special applications prior to Thursday presentation. Each presentation is 15 min, chair introduction, questions and answers included.

Annual Research Journal, Vol. V
Electrical Engineering Research Experience for Undergraduates

ISBN 0-913260-07-X (http://www.ee.psu.edu/reu/)

DIURNAL AND SEASONAL POWER VARIATIONS OF SCHUMANN RESONANCES

Jonathan Becker*, Heng Yang[+], and Victor P. Pasko[#]

Department of Electrical Engineering
The Pennsylvania State University, University Park, PA 16802

*Undergraduate student of
Department of Electrical Engineering
Syracuse University
Syracuse, NY 13210

ABSTRACT

Schumann resonances (SR) are global electromagnetic phenomena sourced by global lightning activity in Earth-ionosphere cavity between the well conducting Earth surface and the ionosphere boundaries. They propagate around the Earth in the extremely low frequency range (ELF) of 3 Hz - 3 kHz with very little attenuation. SR amplitude and frequency variations have been observed because of their ability to model and detect a variety of parameters including the conductivity profile of the ionosphere and the distribution of lightning strikes on the Earth. Hence, SR amplitude and frequency data provide a perfect means to remotely sense the electromagnetic properties of lower ionosphere and the global lightning distribution.

This paper implements an optimization algorithm to reversely derive the distribution of global lightning activity in three main regions (South America, Africa, and Southeast Asia) using the realistic measured Schumann resonance data, specifically the North-South magnetic field component. Furthermore, the diurnal and seasonal variations of the lightning activity in these three regions will be also discussed.

[+]Graduate Mentor
[#]Faculty Mentor

Annual Research Journal, Vol. V
Electrical Engineering Research Experience for Undergraduates

ISBN 0-913260-07-X (http://www.ee.psu.edu/reu/)

1. INTRODUCTION

The region between the Earth's surface and the ionosphere forms a cavity in which electromagnetic waves with wavelengths comparable to the circumference of the Earth may propagate. The cavity is dissipative with an exponential conductivity profile affected primarily to the excitation of free ions and electrons by cosmic rays and solar radiation. Near the ground, the conductivity of the air is approximately 10^{-14} S/m, which makes this region a good insulator. The conductivity of air increases with altitude until at about 100 km its conductivity reaches 10^{-4}-10^{-3} S/m, which is considered a highly conductive layer for ELF waves. The conductivity of the surface of the Earth is also 10^{-4}-10^{-3} S/m

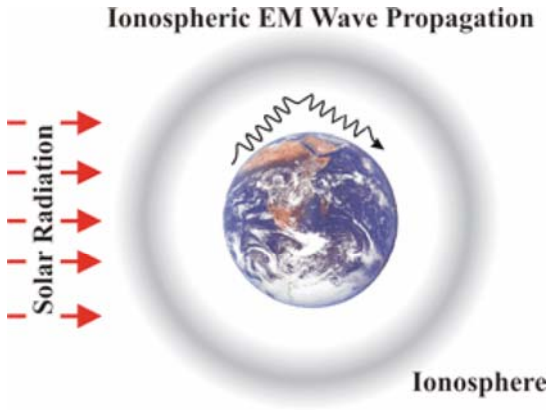

Fig. 1. Diagram of Earth-ionosphere cavity and EM wave propagation and solar radiation exciting the electrons and ions. *Anton Kruger* [2003].

for soil and 4 S/m for sea water. The highly conducting Earth's surface and "conducting but dissipative ionospheric outer boundary separated by a layer of insulating air" forms the Earth-ionosphere cavity [*Sentman*, 1995][1]. Cloud to ground lightning strikes produce a vertical current, creating magnetic and electric fields, and causing wave propagation. Figure 1 illustrates the earth-ionosphere cavity being excited by solar radiation and carrying electromagnetic waves.[2] The high frequencies attenuate rapidly while the electromagnetic waves in the extremely low frequency (ELF) range of 3-3 kHz constructively interfere to form resonances. W.O. Schumann first accurately predicted these resonances in 1952 [*Schumann*, 1952] [3], which led to their being named Schumann resonances (SR). Schumann resonances can be accurately measured from a single receiver anywhere on the Earth and be used to detect global lightning. Electromagnetic signals in the ELF range have come under an increasing amount of attention due to their use in remote sensing applications. Signals in the ELF range can be used to detect oil deposits underneath the Earth's surface through the detection of wave

Annual Research Journal, Vol. V
Electrical Engineering Research Experience for Undergraduates

ISBN 0-913260-07-X (http://www.ee.psu.edu/reu/)

impedance [*Simpson and Taflove*, 2006][4]. In addition, ELF waves are used in monitoring solar proton events (SPE) [5, 6] and x-ray bursts[7] by using the change in the frequency of the SR to notice the change in conductivity of the ionosphere [*Roldugin et al*., 2004]. In particular, the ability to use ELF signals and global lightning trends to detect climate and temperature changes in the atmosphere has become an increasingly researched topic [e.g., *Williams*, 1992][8].

The realistic data collected by *Price and Melnikov* [2004][9] provides a means to observe Schumann resonance characteristics including amplitude, frequency, and Q-factor changes for their diurnal and seasonal changes. This data is used as an aim function for the reverse optimization algorithm to turn relative power data to a global lightning model. SR relative power can be derived using the finite-difference time domain method (FDTD), which is a grid-based differential modeling method [*Yang and Pasko*, 2005] [10]. The FDTD method was first introduced by Kane Yee[11] in 1969 and further developed by Allen Taflove[12] in 1980 with major advances of computer technology. Maxwell's equations in partial differential form are modified to central-difference equations, discretized, and implemented in software. "The FDTD technique represents one of the simplest and most flexible means for find electromagnetic solutions in a medium with arbitrary inhomogeneities" [*Yang and Pasko*, 2005]. *Yang and Pasko* [2005] implemented this method in three dimensions to account for power and frequency variation of Schumann resonances, which is the basis for the algorithm proposed in this paper.

The optimization algorithm is developed and implemented in order to reversely derive diurnal and seasonal global lightning activity from SR relative power data in three primary regions: South America, Central Africa, and Southeast Asia. The results of this global lightning derivation are compared to previously derived from FDTD models in *Yang and Pasko* [2006] to realistic measurements from *Price and Melnikov* [2004].

2. OPTIMIZATION FORMULATION

The global lightning model is treated as three separate Gaussian pulses, for each of the three primary regions, of the Gaussian form

$$\sum_{i=1}^{3} A_i * e^{-((t - tc_i) / w_i)^2} + \text{DC component} \qquad (1)$$

In this case there are 10 variables where i represents the location of lightning activity with i = 1, 2, 3 represents Southeast Asia, Africa, and South America respectively. A_i is the amplitude of the pulse for each region, t is the time in 1.2 hour intervals, tc_i is the central time of each pulse or the time when each region each region reaches its maximum lightning intensity, w_i is the width of each pulse or the time contributes a significant amount of power, and the DC component is the background noise. The earth-ionosphere cavity can be treated as a linear

Annual Research Journal, Vol. V
Electrical Engineering Research Experience for Undergraduates

ISBN 0-913260-07-X (http://www.ee.psu.edu/reu/)

system so each pulse can be determined separately, finding the magnitude of the source varied with respect to time, and then added together to find the total

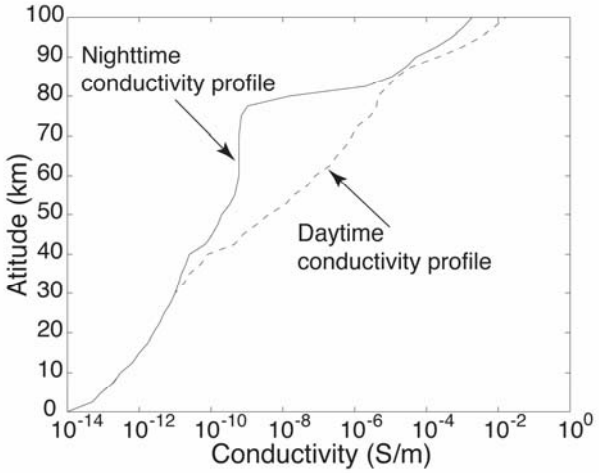

Fig. 2. Conductivity profile of the earth-ionosphere cavity for both daytime (12:00 UT) and nighttime (24:00 UT) [Yang and Pasko, 2005]

relative power on a global scale. An optimization algorithm is employed to reversely derive a global lightning model with respect to three regions during diurnal and seasonal change. The algorithm uses relative power derived from the FDTD model in *Yang and Pasko* [2006], which is north-south magnetic field data from lightning strikes in the hotspot locations of South America, central Africa, and Southeast Asia [*Yang and Pasko*, 2005]. The data was modeled with a receiver in Mitzpe Ramon, Israel and is calculated for each of twenty points separated by 1.2-hour intervals for 0:00 UT to 24:00 UT. For each point in time, three simulations are calculated over an evenly distributed rectangular region, with lengths of 5 km, 1000 km, and 1000 km in the r, θ, and ϕ directions respectively. The three separate simulations are meant to determine the separate contributions of the vertical magnetic field detected by the receivers for each of the three hotspots. The model source is "a vertical lightning current with 5 km length, with linear rise time 500 μs and exponential fall with timescale 5 ms" [*Yang and Pasko*, 2006][13]. The conductivity profile of the earth-ionosphere cavity was derived from International Reference Ionosphere (IRI) model [*Bilitza*, 2001][14]. Figure 2 illustrates the conductivity profiles with respect to altitude for nighttime (24:00 UT) and daytime (12:00 UT) A fast Fourier transform (FFT) is performed on the FDTD data to find the peak amplitude for the first mode frequency only for each set of data. The FDTD peak amplitudes are multiplied by the square root of the lightning pulse for each location. The three pulses are then added together to form a curve, which is to be optimized. The mechanism of

Annual Research Journal, Vol. V
Electrical Engineering Research Experience for Undergraduates

ISBN 0-913260-07-X (http://www.ee.psu.edu/reu/)

optimization is the function *fminsearch*, which is a derivative-free method to allow the user to find the minimum of a function of several variables. An error function finds and returns the mean squared error between the curved derived from the FDTD data and the realistic measurements. Three arrays of data are formed with the first array including the amplitude of each pulse and the DC component, the second including the central time of each pulse, and the third including the width of each pulse. Therefore, *fminsearch* is run three times for each optimization step by taking the initial values of each set of data, and returning new values into the set to make the error between the curves smaller. Thus, all ten parameters are adjusted to optimize the pulses to produce a good model for global lightning. The necessary number of steps necessary in the algorithm was 200 for each season.

3. RESULTS AND DISCUSSION

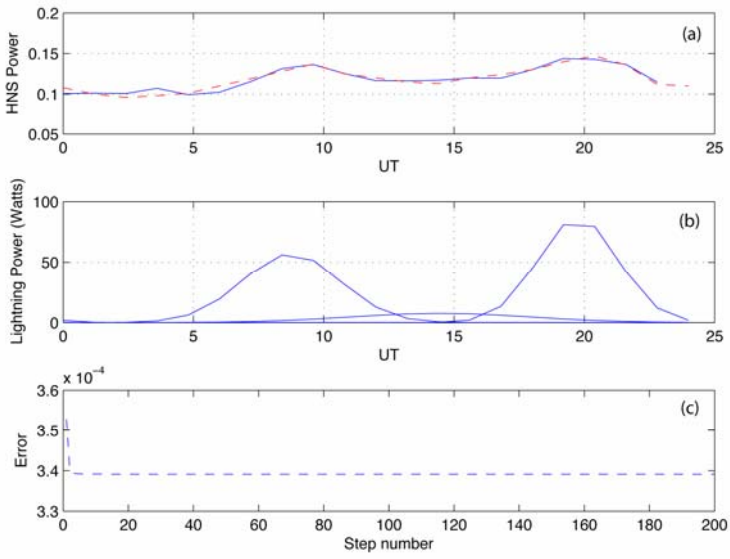

Fig. 3. Diurnal variation for autumn of (a) fitted FDTD data (blue solid line) to realistic data (red dashed line) and (b) lightning intensity for Southeast Asia, Africa, and South America. (c) The change in error between FDTD data and realistic data for each algorithm step.

Figures 3a, 4a, and 5a illustrate the optimization data (dotted line) from the optimization algorithm, fitted to the realistic data measurements (solid line) from *Price and Melnikov* [2004] for autumn, winter and spring respectively. The fitted curves represent the FDTD data after being run through the optimization

Annual Research Journal, Vol. V
Electrical Engineering Research Experience for Undergraduates

ISBN 0-913260-07-X (http://www.ee.psu.edu/reu/)

algorithm for two hundred steps. The error versus the number of steps is shown in figures 1c, 2c, and 3c. The curves show an error that decreases steadily and then levels out at a value, which was 3.39×10^{-4} for autumn, 8.3×10^{-5} for winter, and 5.25×10^{-5} for spring. The global lightning power distributions for Southeast Asia, Africa, and South America are shown for autumn, winter, and spring in figures 3b, 4b, and 5b respectively. The three peaks in each of the global lightning figures are represented by three separate pulses each with their own amplitude, width, and central time. Lightning intensity pulses sourced by Southeast Asia, Africa, and South America are centered around 8:00 UT, 14:00 UT, and 20:00 UT respectively. Each of these central times represent the period of late afternoon for each respective location. The lightning intensity was greatest in Southeast Asia for winter and spring. In autumn, South America had the greatest lightning intensity. In autumn and spring, Africa provides the least intensity.

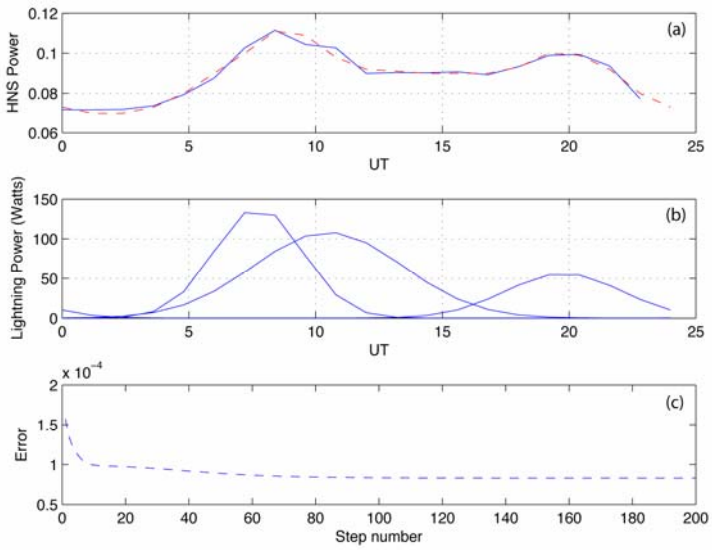

Fig. 4. Diurnal variation for winter of (a) fitted FDTD data (blue solid line) to realistic data (red dashed line) and (b) lightning intensity for Southeast Asia, Africa, and South America. (c) The change in error between FDTD data and realistic data for each algorithm step.

The global lightning figures illustrate the diurnal and seasonal variations of lightning intensity for each hotspot. It is important to reinforce that only the first mode of the north-south magnetic component was analyzed. In addition, the lightning intensity curves are dependent on the optimization algorithm and the effectiveness of the optimization method is highly dependent on initial values for each of the ten values discussed earlier. This explains the relatively larger error in the autumn data. Lightning in South America and Southeast Asia makes up a significantly component of the vertical magnetic for at least the first mode,

Annual Research Journal, Vol. V
Electrical Engineering Research Experience for Undergraduates

ISBN 0-913260-07-X (http://www.ee.psu.edu/reu/)

compared to Africa. Thus, it can be deduced that the lightning from Africa is mainly detected by the east-west magnetic field component and thus is not represented as strongly in the data shown as the other two locations. As such, the vertical magnetic field component is comprised of most lightning from South America and Southeast Asia, which explains their dominance in all three seasons represented. Each location had their peak intensity at their respective late afternoons: around 8:00 UT for Southeast Asia, 14:00 UT for Africa, and 20:00 UT for South America, with slight variation. This diurnal pattern can be explained by weather patterns and storm activity and high solar intensity, which cause the altitude of the highly conducting part of the ionosphere to be lower in altitude than other parts of the day and especially night. This can be observed by referring back to Figure 2, in which the nighttime conductivity increases slower than the daytime conductivity with respect to altitude. The greater contribution of lightning by Southeast Asia in the winter and spring and South America in the autumn is due primarily to climate change and the under representation of African lightning in the first mode vertical magnetic field component.

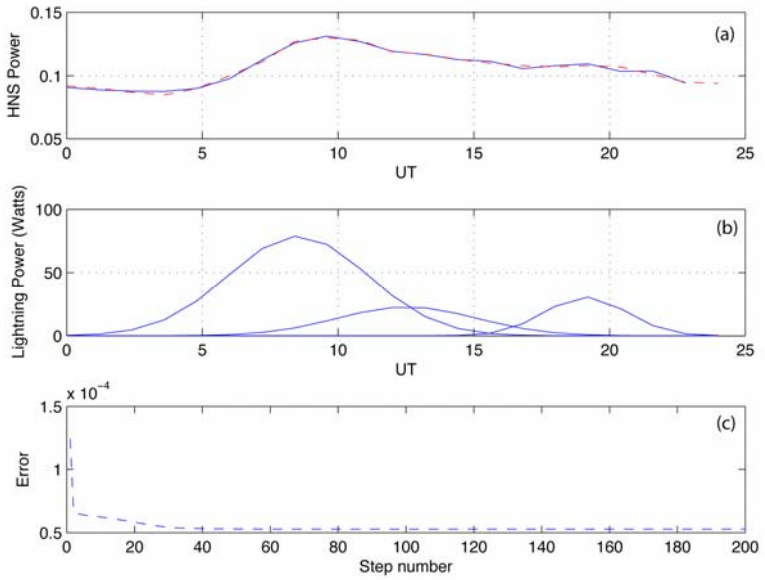

Fig. 5. Diurnal variation for spring of (a) fitted FDTD data (blue solid line) to realistic data (red dashed line) and (b) lightning intensity for Southeast Asia, Africa, and South America. (c) The change in error between FDTD data and realistic data for each algorithm step.

4. CONCLUSION

It is confirmed that Schumann resonance intensity measured from a single receiver can give an accurate depiction of the level of global thunderstorm

Annual Research Journal, Vol. V
Electrical Engineering Research Experience for Undergraduates

ISBN 0-913260-07-X (http://www.ee.psu.edu/reu/)

activity. The algorithm successfully optimized projected data using realistic measurements and produced global lightning intensity pulses to aid in analyzing diurnal and seasonal variation. In each season and location it was observed that the maximum lightning intensity occurred in each respective region's late afternoon, which was approximately 08:00 UT for Southeast Asia, 14:00 UT for Africa, and 20:00 UT for South America, with slight variation. Southeast Asia proved to be the major contributor of first mode north-south magnetic field power for winter and spring while South America was the major contributor for autumn.

5. ACKNOWLEDGEMENTS

The material is based upon work supported by the National Science Foundation under Grant No. EEC-0244030.

6. REFERENCES

[1] Sentman, D.D. (1996), Schumann resonances, in *Handbook of Atmospheric Electrodynamics*, edited by H. Volland, p. 267, CRC Press, Boca Raton, Fla.

[2] Kruger, Anton, (2003) *Construction And Deployment Of An ULF Receiver For The Study Of Schumann Resonance In Iowa* http://www.iihr.uiowa.edu/projects/schumann/images/IonosphereLayers.gif). July 20, 2007

[3] Schumann, W.O. (1952), Uber die strahlungslosen eigenschwingungen einer leitendend Kugel die von einer Luftschicht und einer Ionospharenhulle umgeben ist, *Z. Naturforsch., 7a,* 149.

[4] Simpson, Jamesian J., Taflove, A., 2006, A Novel ELF Radar for Major Oil Deposits., *IEEE Geoscience and Reme Sensing Letters, Vol. 3. No.1*, doi:10.1109/LGRS.2005.856118.

[5] Roldugin, V.C., Y.P. Maltsev, G.A. Petrova, and A.N. Vasiljev (2001), Decrease of the first Schumann resonance frequency during solar proton events, *J. Geophys. Res., 106,* 18,555.

[6] Roldugin, V.C., Y.P. Maltsev, A.N. Vasiljev (2003), A. V. Shvets, and A. P. Nikolaenko (2003), Changes of Schumann Resonance paramets during the solar proton event of 14 July 2000, *J. Geophys. Res., 106,* 18,555.

[7] Roldugin, V.C., Y.P. Maltsev, A.N. Vasiljev, A.Y. Schokotov, and G.G. Belyajev (2004), Schumann resonance frequency increase during solar X-ray burts, *J. Geophys. Res., 108(*A3), 1103, doi:10.1029/2002JA009495.

[8] Williams, E.R., 1992, The Schumann Resonance: A global tropical thermometer. *Science,* 256, 1184–1187.

[9] Price, C., and A. Melnikov, 2004: Diurnal, Seasonal and Inter-annual Variations in the Schumann Resonance Parameters, *Journal of Atmospheric and Solar-Terrestrial Physics*, 66, 1179-1185.

[10] Yang, H., and V.P. Pasko (2005), Three-dimensional finite difference time domain modeling of the Earth-ionosphere cavity resonances, *Geophys. Res. Lett., 32,* L03114, doi:10.1029/2004GL021343.

Annual Research Journal, Vol. V
Electrical Engineering Research Experience for Undergraduates

ISBN 0-913260-07-X (http://www.ee.psu.edu/reu/)

[11]Yee, Kane (1966). "Numerical solution of initial boundary value problems involving Maxwell's equations in isotropic media". *Antennas and Propagation, IEEE Transactions on* **14**: 302–307.
[12] Taflove, A. (1980). "Application of the finite-difference time-domain method to sinusoidal steady state electromagnetic penetration problems". *Electromagnetic Compatibility, IEEE Transactions on* **22**: 191–202.
[13] Yang, H., and V.P. Pasko (2006), Three-dimensional finite difference time domain modeling of the diurnal and seasonal variations in Schumann resonance parameters, *Radio Sci., 41,* RS2S14, doi:1029/2005RS003402 [Printed 42(2), 2007].
[14] Bilitza, D. (2001), International Reference Ionosphere 2000, *Radio Sci., 36(2),* 261.

Annual Research Journal, Vol. V
Electrical Engineering Research Experience for Undergraduates

ISBN 0-913260-07-X (http://www.ee.psu.edu/reu/)

Annual Research Journal, Vol. V
Electrical Engineering Research Experience for Undergraduates

ISBN 0-913260-07-X (http://www.ee.psu.edu/reu/)

PIEZOELECTRIC PUMP WITH A PIEZOELECTRIC CYMBAL ACTUATOR FOR LAPTOP COOLING APPLICATIONS

Filmon Berhe*, Seung Ho Park[+], Aditya Rajapurkar[+], and Kenji Uchino[#]

Intercollege Graduate Degree Program in Materials
Department of Electrical Engineering
Pennsylvania State University, University Park, PA 16802

*Undergraduate Student of:
Department of Computer Engineering
Jackson State University, Jackson, MS39217

ABSTRACT

Piezoelectric materials mechanically vibrate when AC electric field is applied. This motion can be magnified by sandwiching a bimorph piezoelectric disk between two metal (brass) caps that are shaped like cymbals. These cymbal actuators can be used as pumps to circulate coolant (water) in a new laptop cooling system. Using ATILA finite element method (FEM) simulation software, a cardioid like, almost one directional motion can be confirmed by applying forward voltage of 10 V and backward voltage of 1 V in 135^{o} phase difference. This process yielded the maximum forward pressure of 1104.721 dB and a relative backward pressure of -76.62 dB. Cymbal actuators with piezoelectric ceramic thickness of 0.5 mm and 1 mm were fabricated and tested and measured for impedance response, displacement at the center of the actuator, fluid height

---

[+] Graduate Mentors

[#] Faculty Mentor

Annual Research Journal, Vol. V
Electrical Engineering Research Experience for Undergraduates

ISBN 0-913260-07-X (http://www.ee.psu.edu/reu/)

pushed by actuator, and fluid motion. The 1 mm piezoelectric disc yielded 4.419 μm displacement when 1 V and 10 V were applied to top and bottom metal caps at 26.1 kHz frequency with 175^{o} phase difference.

1. INTRODUCTION

The laptop computer technology is getting faster, smaller, and more powerful. Thus, the laptop cooling system becomes a main concern since it is one of the limiting factors of the performance of the central processing unit (CPU). The currently used air fan based cooling system consumes a lot of power and bulky to pump the air around the laptop. Water, with specific heat capacity of 4.2 J/g^{o}C, is a better cooling agent compared with air. However, conventional electromagnetic centrifugal pumps do not have sufficient water pressure to improve CPU performance [1]. These pumps also have problems with miniaturization of the device and radiation of electromagnetic noise [2]. Hence, we proposed in research a water cooling system with small and light weighed piezoelectric pumps based on cymbal actuators.

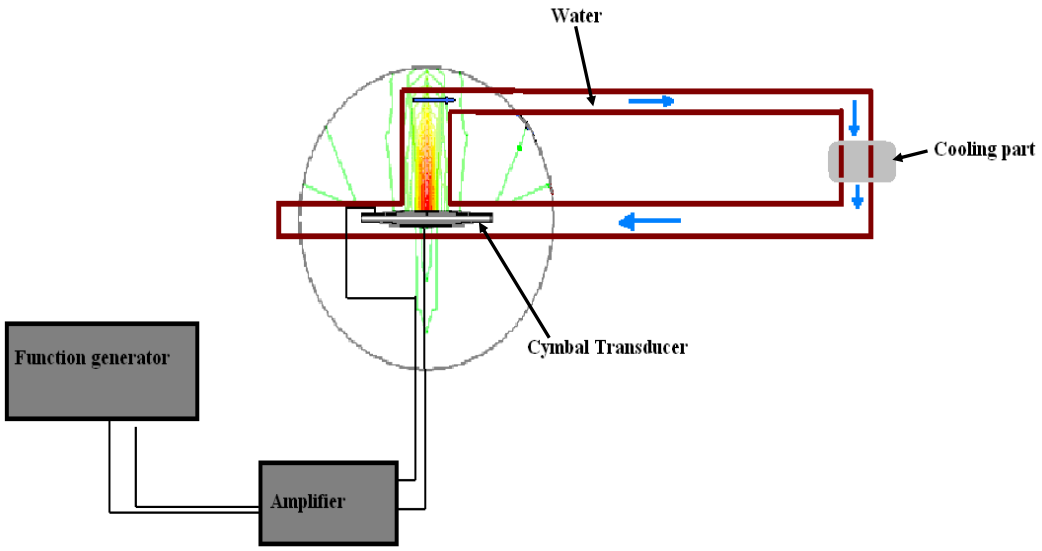

Figure 1. Water circulation with a piezoelectric cymbal pump

Piezoelectric materials are ceramics that generate electricity when exposed to mechanical stress or produce mechanical displacement when electric charge is applied to them. The word piezo means pressure; hence piezoelectric refers to pressure electricity. Piezoelectric materials are widely used in various

Annual Research Journal, Vol. V
Electrical Engineering Research Experience for Undergraduates

ISBN 0-913260-07-X (http://www.ee.psu.edu/reu/)

devices such as transducers, actuators, surface acoustic wave devices, transformers, pressure sensors and ultrasonic motors. [3]

Piezoelectric materials exhibit geometric strain that is proportional to an applied electric field:

$$x = dE \quad (1)$$

where x = magnitude of induced strain, E = external electric field, and d = piezoelectric strain constant [3]. This is called the converse electric effect [3] and enables piezoelectric materials to effectively be used as pumps in fluids, including in a water based laptop cooling system.

NEC Corporation developed a water laptop cooling system in 2003 by integrating a 5 mm piezoelectric pump and a tank with an aluminum radiation plate that contains a water circulation channel. The piezoelectric pump can be driven with 5 V of direct voltage and suppresses the operating noise to 30 dB. This water-cooling module has shown a cooling performance of 80 W, which is two times that of conventional systems [2].

A miniature ring morph ultrasonic pump was introduced in Precision and Intelligence Laboratory in Tokyo, Japan. It contained a 30mm diameter bending disc with a ring shaped bimorph. The vibrator disc was driven at fundamental resonance frequency of 19 kHz. A maximum pressure of 14.8 kPa and maximum flow rate of 10ml/min was achieved [1].

On the other hand, a slimmer piezoelectric pump can be made using cymbal actuators. The cymbal actuator has piezoelectric ceramic discs sandwiched between two metal caps, as shown in Figure 2. It gets the name cymbal from the crescent shape of the metal caps. The cymbal was first produced in the Material Research Lab (MRL), The Pennsylvania State University. It was patented by Newnham and Dogan in 1998 [4]. The cymbal is a very efficient actuator because it magnifies the piezoelectric ceramic displacement, which is measured in microns, by 40 times [4].

Annual Research Journal, Vol. V
Electrical Engineering Research Experience for Undergraduates

ISBN 0-913260-07-X (http://www.ee.psu.edu/reu/)

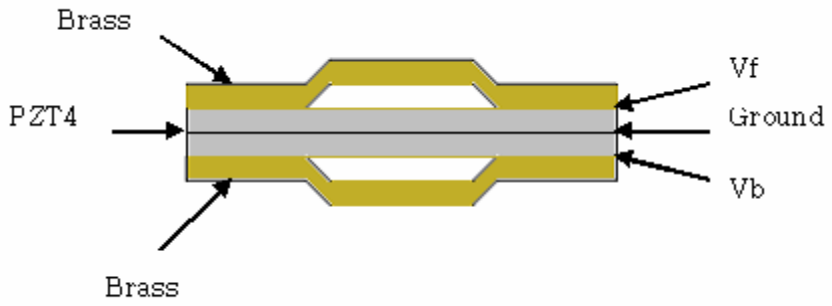

Figure 2. Schematic structure of a cymbal with two PZT discs

A bimorph actuator is a layer of ceramic material bonded together with a flexible metal. It produces a bending motion and has high displacement but low force under water. In contrast, a multilayer actuator has high force but low displacement. A cymbal actuator shows a compromised force and displacement between bimorph and multilayer. The cymbal is advantageous to produce different kinds of motions under water, such as monopole, dipole, and carioid-like motions, depending on how it is driven.

When electric field is applied to the cymbal, the lead zirconate titanate (PZT) ceramic mechanically vibrates across the radial direction forcing the brass caps to stretch and contract across the normal direction to ceramic discs. This process lets the cymbal produce equal pressure in all directions creating a monopole motion. However, by applying two signals with phase difference, a cardioid motion can be achieved with high forward pressure and minimum backward pressure when the actuator is place in fluid. This can create a unidirectional motion that can be useful in circulating water in a laptop cooling application.

2. EXPERIMENTAL PROCEDURE

2.1. Cymbal Fabrication (0.5mm PZT)

Brass metal of 0.25 thickness was first cut into 12.72 mm (0.5 inch) diameter discs. Then it was punched with 3.2 ~ 5.2 metric tons of pressure to bend the brass cap into a cymbal shape with 0.25 mm gap height and 3.22 cap diameter. Hard PZT4 sample was cut into circular discs and grinded with 35μm silicon

Annual Research Journal, Vol. V
Electrical Engineering Research Experience for Undergraduates

ISBN 0-913260-07-X (http://www.ee.psu.edu/reu/)

powder to 0.5 mm thickness. The PZT4 discs were then electroded with DuPont QS 171 silver/platinum conductive pase and fired at 850 ^{o}C furnace for 15 minutes. The discs were then poled in 2.5 kV/mm and 150^{o}C for 30 minutes. Two PZT discs were paired up and connected with islands of conductive epoxy (Tra-Duct BA-2902) on the outside for conductivity and strong insulating epoxy (Stycast 1266) in the middle for adhesiveness. Then the paired discs were connected to two brass caps on top and bottom using strong insulating epoxy and 4 points of conductive epoxy. A conductive wire was side soldered at the intersection of the two PZT discs and connected to the ground. Two wires were also soldered on the top and bottom brass caps and connected to forward voltage (V_f) and backward voltage (V_b).

2.2. Cymbal Fabrication (1mm PZT)

1 mm PZT discs were acquired and were brushed with electrodes. They were then polled in 80 ^{o}C, 350V for 10 minutes. Two PZT discs were paired up and connected by inserting a flat brass disc between two ceramic discs. Soldering on the ground electrode in between two PZT discs from the side without touching the top and bottom brass caps was a main difficulty in fabrication process. To avoid it, a brass disc was inserted between the 1mm PZT discs. Conductive and simple adhesive epoxy were used together to obtain desired adhesion with conductivity. Then the paired discs were connected to two brass caps on top and bottom using epoxy and 4 points of conductive epoxy. A conductive wire was side soldered to the side of the brass disc that was sandwiched between the two PZT discs and connected to the ground. Two conductive wires were also soldered on the top and bottom brass caps and connected to forward voltage (Vf) and backward voltage (Vb). The soldered parts were brushed with Scotch Super Glue Gel to prevent detaching during experiments.

Prepared actuators were investigated by impedance response analysis, displacement measurement and underwater pressure test.

3. RESULTS AND DISCUSSION

3.1. Finite Element Method Simulation Results

ATILA Finite Element Method (FEM) simulation was used to draw a two dimensional picture of the cymbal and investigate behavior of the actuator under water. When 1V of forward and backward voltage was applied in the same phase

Annual Research Journal, Vol. V
Electrical Engineering Research Experience for Undergraduates

ISBN 0-913260-07-X (http://www.ee.psu.edu/reu/)

at 22 kHz frequency, the cymbal produced equal amount of pressure in all direction creating a monopole motion, as shown in Figure 3.

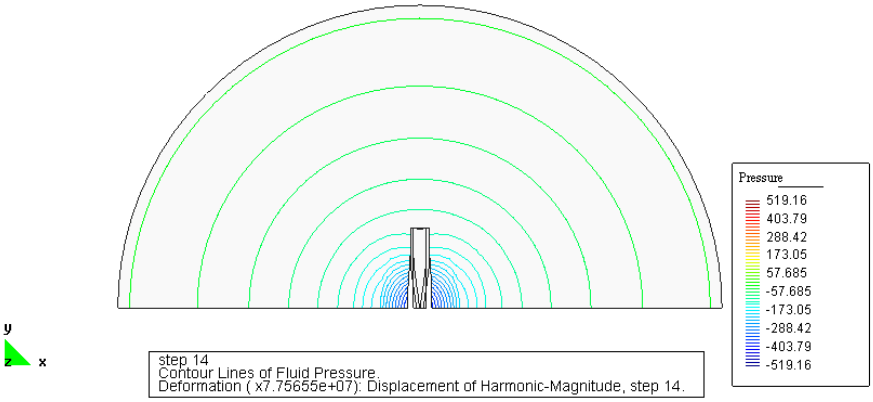

Figure 3: Monopole fluid motion of the cymbal actuator in water.

When 1V of forward and backward voltage was applied in 180^{o} phase difference at 22 kHz frequency, the cymbal produced equal but opposite of pressure in front and back sides of the cymbal which is called dipole motion as shown in Figure 4. In this case pressure at the sides of the cymbal was reduced compare to monopole simulation results.

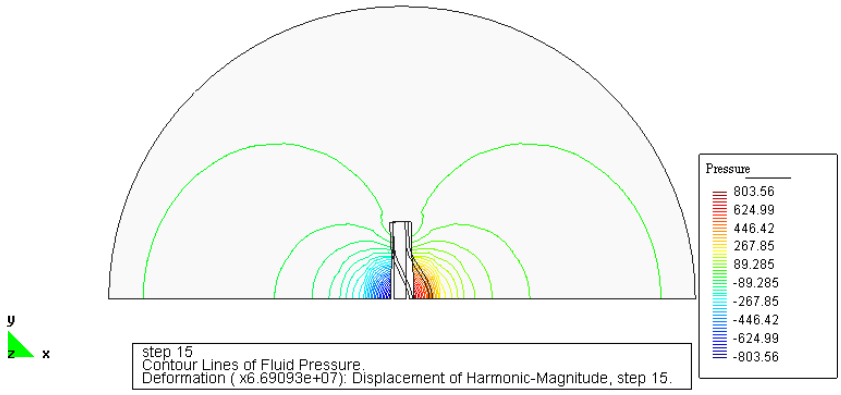

Figure 4: Dipole fluid motion of the cymbal actuator in water.

When 10V of forward voltage and 1V of backward voltage was applied in

Annual Research Journal, Vol. V
Electrical Engineering Research Experience for Undergraduates

ISBN 0-913260-07-X (http://www.ee.psu.edu/reu/)

135^{o} phase difference at 22 kHz frequency, the forward pressure was maximized and the backward pressure was minimized creating a cardioid like motion as shown in Figure 5. This process produced a maximum forward pressure of 1104.721 dB and a relative backward pressure of -76.62dB. Details of the simulated data are summarized in Table 1.

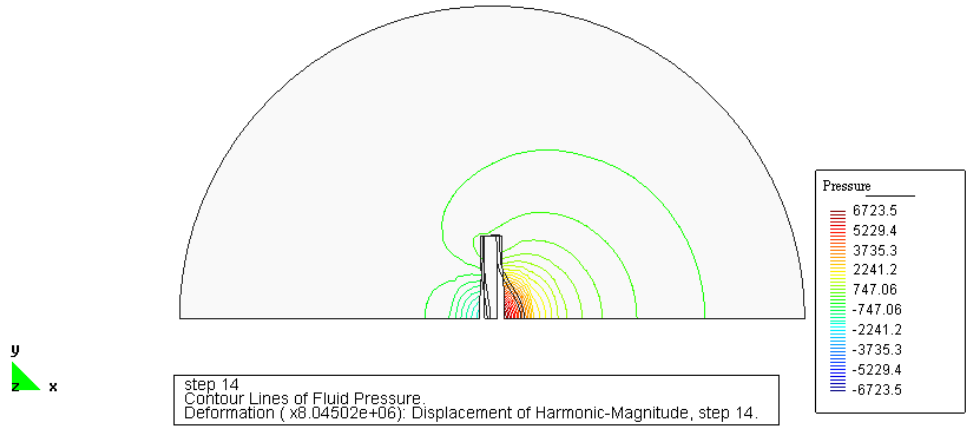

Figure 5: Cardioid like motion of the cymbal actuator in water.

Figure 6 shows forward and backward pressure difference when the Cymbal actuator is driven at 22 kHz with 135^{o} phase difference. When harmonic magnitude is 13, backward pressure is 0 and forward pressure is the maximum. This simulation results are corresponding to cardioid like water motion.

Annual Research Journal, Vol. V
Electrical Engineering Research Experience for Undergraduates

ISBN 0-913260-07-X (http://www.ee.psu.edu/reu/)

Table 1. Forward and backward pressure difference of a cardioid like motion

	Frequency= 22kHz		
#	Point (5.99606, 0.933275, 0) analysis		
#	Point (-6.08087, 0.934814, 0) analysis		
Harmonic-Magnitude	Forward P.	Backward P	Pressure Difference
1	-945.6857	-124.2263	-821.4594
2	-1109.047	-60.98821	-1048.05879
3	-1163.847	8.219831	-1172.066831
4	-1104.721	76.62325	-1181.34425
5	-937.4579	137.5263	-1074.9842
6	-678.4299	184.9672	-863.3971
7	-352.9923	214.3024	-567.2947
8	6.99864	222.66	-215.66136
9	366.3047	209.2222	157.0825
10	689.7541	175.3043	514.4498
11	945.6857	124.2263	821.4594
12	1109.047	60.98822	1048.05878
13	1163.847	-8.219851	1172.066851
14	1104.721	-76.62331	1181.34431
15	937.4583	-137.5262	1074.9845
16	678.43	-184.9672	863.3972
17	352.9922	-214.3024	567.2946
18	-6.99844	-222.6601	215.66166
19	-366.3045	-209.2222	-157.0823
20	-689.7542	-175.3042	-514.45

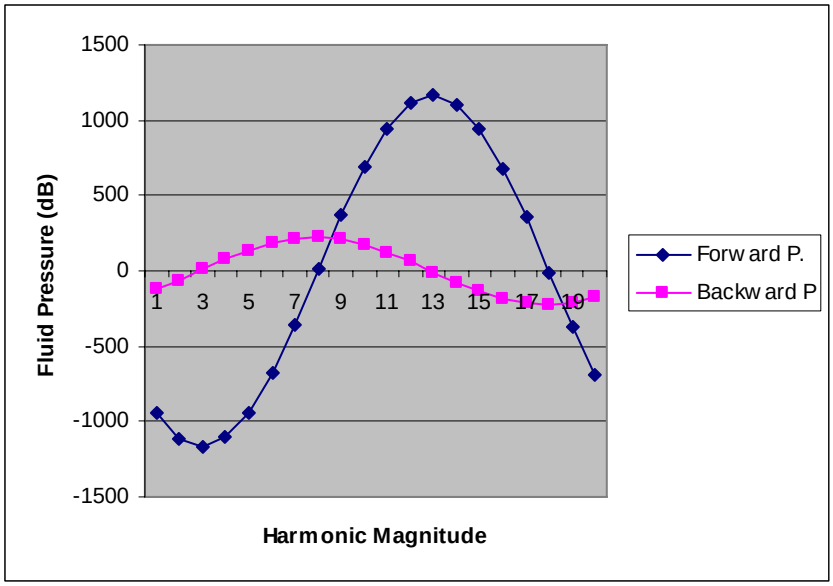

Figure 6: Fluid pressure vs. harmonic magnitude of a cardioid like motion.

Annual Research Journal, Vol. V
Electrical Engineering Research Experience for Undergraduates

ISBN 0-913260-07-X (http://www.ee.psu.edu/reu/)

3.2. Impedance Measurement

Cymbal actuators with 0.5 mm and 1 mm PZT cymbals were measured for impedance response. The 0.5 mm PZT cymbal showed a resonance frequency of 192.84 kHz and antiresonance frequency of 198.84 kHz. And the cymbal with 1 mm PZT presented a resonance frequency at 160 kHz.

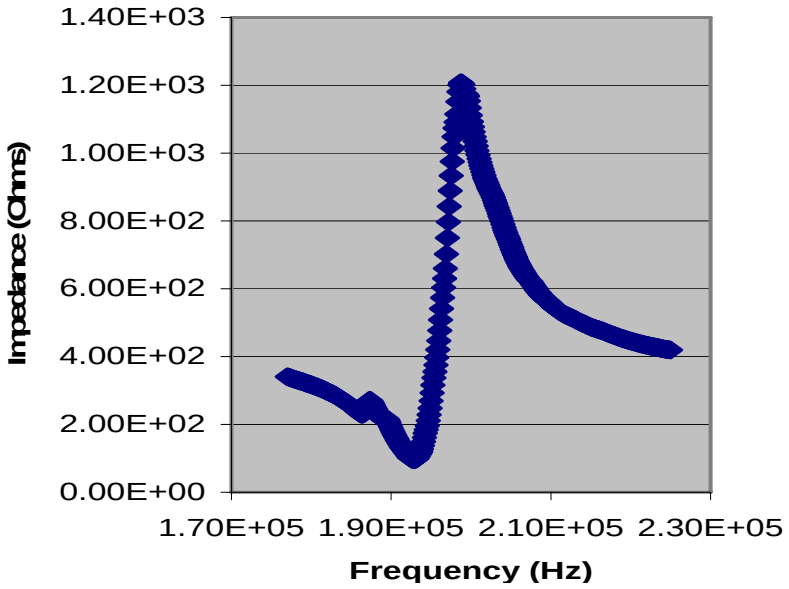

Figure 7a: 0.5mm PZT cymbal impedance vs. frequency.

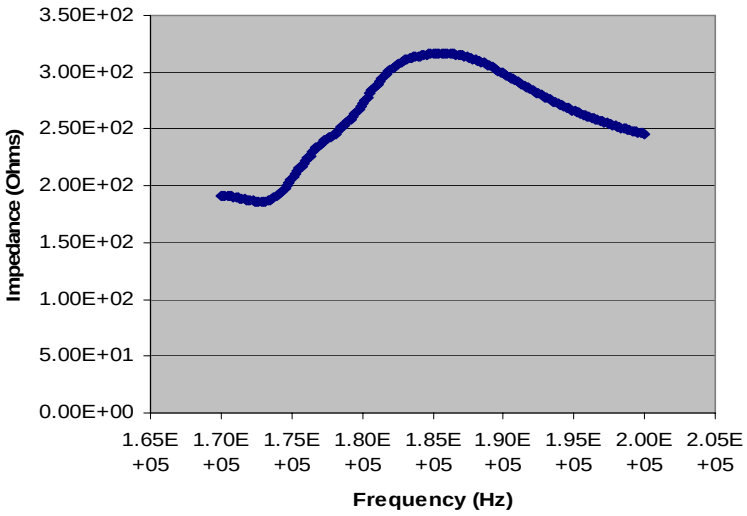

Figure 7b: 1mm PZT cymbal impedance vs. frequency.

Annual Research Journal, Vol. V
Electrical Engineering Research Experience for Undergraduates

ISBN 0-913260-07-X (http://www.ee.psu.edu/reu/)

3.3. Displacement Measurement

The cymbal is inserted into a delta shaped styrofoam with sides of 3.99mm, 4.12mm and 4.7mm thickness to support the actuator without damping. The styrofoam containing the cymbal is made to stand vertically between two lasers that are equal distance away from the cymbal.

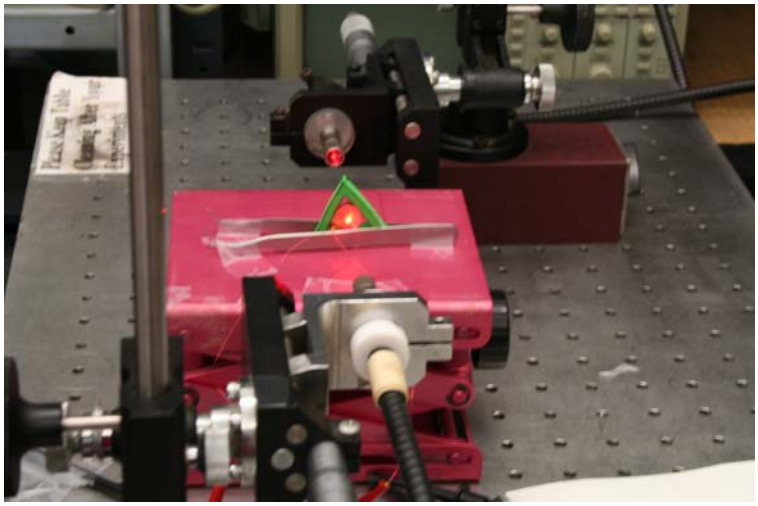

Figure 8: Vibration displacement measurement

The 1 mm PZT thickness cymbal was tested for displacement measurement. A resonance frequency was found at 26.1 kHz and a second harmonic frequency at 84.7 kHz by measuring displacement variation. It was not found in the impedance analysis. 1 V and 10 V were applied at 26.1kHz frequency to the front and back sides of the cymbal with 100kHz velocity filter, 125 mm/s/v velocity range, and 20 um/V displacement range using laser interferometers. The intensity of the cymbal was tested in various phases and velocity (V_{RMS}) was calculated as shown in Table 2. The forward and backward displacement was then calculated from the equation:

$$A = V_{RMS}/\sqrt{2}\,\pi f \qquad (2)$$

where A = amplitude and f = frequency.

Annual Research Journal, Vol. V
Electrical Engineering Research Experience for Undergraduates

ISBN 0-913260-07-X (http://www.ee.psu.edu/reu/)

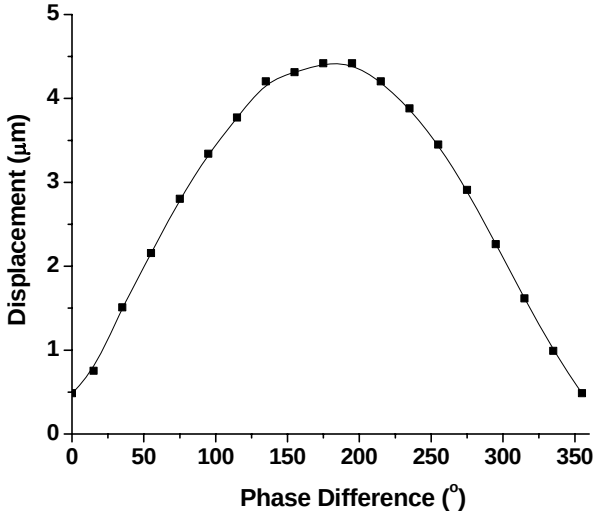

Figure 9a: Forward Displacement

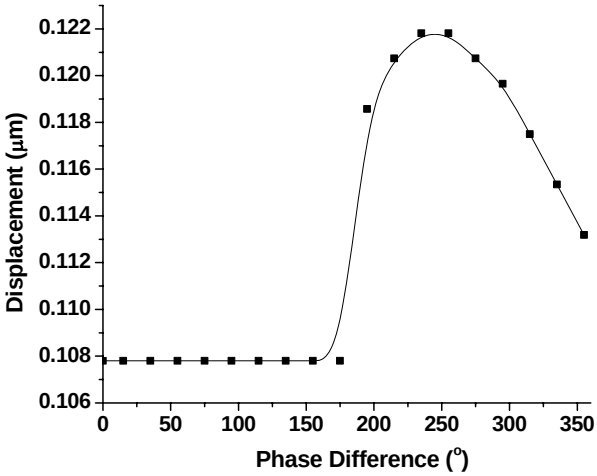

Figure 9b: Backward Displacement

3.4. Pressure Test

The cymbal was coated with conformal coating for waterproof. The coating was cured at 120 °C oven for 15 minutes and then 65 °C for 1 hour again. Then it was inserted into a delta shaped styrofoam to be supported in the water without severe damping. The styrofoam was inserted in a transparent glass

Annual Research Journal, Vol. V
Electrical Engineering Research Experience for Undergraduates

ISBN 0-913260-07-X (http://www.ee.psu.edu/reu/)

container supported with three standing clips. Water was poured in the container until the styrofoam was completely submerged under the water. A transparent pipe was suspended above the styrofoam to check the height resulted from the vibration of the cymbal actuator. Even though pressure was not sufficient to push the water in the pipe upward, slight increase of surface height was observed. To investigate this motion, colored water was put in by drops. Turbulence in the water was observed with this method when the Cymbal actuator is driven.

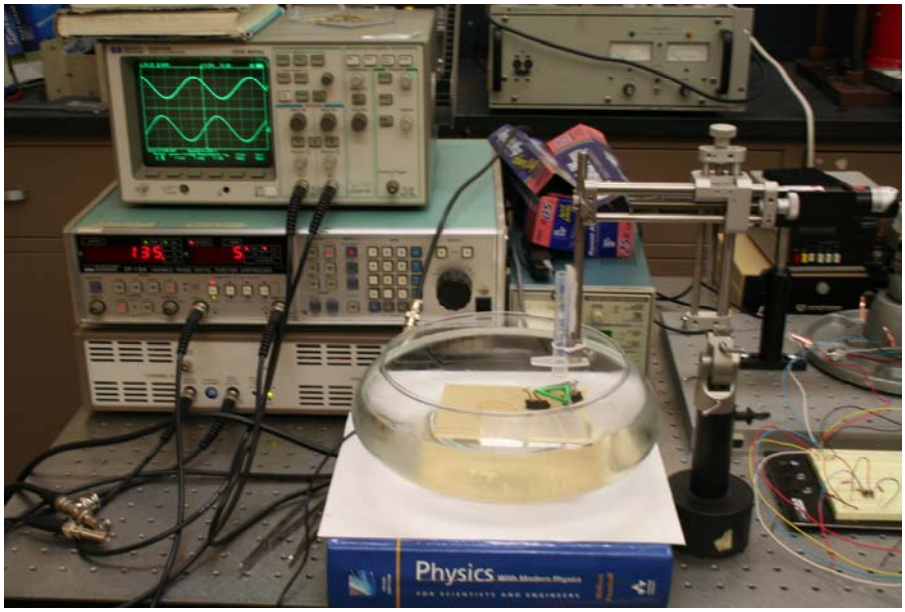

Figure 10: Cymbal with an underwater test

4. CONCLUSIONS

When 1V and 10V were applied to the 1 mm PZT cymbal at 175^{o} phase difference and it produced a maximum displacement of 4.419 μm. This cymbal also caused water vibration when submerged under water. However it was not sufficient to produce a significant height change in water pipe. The colored water drops in the pressure test showed some fluidic motion but it was not clear to show cardioid motion which was simulated with ATILA FEM simulation.

Even though performance of the Cymbal actuator was not sufficient, from the performed and simulation and experiments, the Cymbal actuator showed a possibility as a piezoelectric pump, especially in a water based laptop cooling application.

Annual Research Journal, Vol. V
Electrical Engineering Research Experience for Undergraduates

ISBN 0-913260-07-X (http://www.ee.psu.edu/reu/)

FUTURE WORK

Future research will test cymbals with different diameters at higher amplitudes. A laptop cooling system will be produced and integrated in to a laptop.

ACKNOWLEDGMENT

I would like to thank my advisor Dr. Kenji Uchino for having me as an REU scholar. I would also like to highly thank my graduate mentors Dr. Seung Ho Park and Aditya Rajapurkar for their unmatched support and exquisite mentorship. I extend my gratitude to the members of team ICAT and EE REU program affiliates.

This material is based upon work supported by the National Science Foundation under Grant No. EEC-0244030.

REFERENCES

[1] T. Hasegawa, K. Nakamura, S. Ueha, "A Miniature Ultrasonic Pump Using a Bending Disk Transducer and a Gap", ScienceDirect, 2002.

[2] "NEC Develops Water Cooling Notebook Module", http://www.mobilemag.com/content/100/334/C1811/, 2003.

[3] K. Uchino, *Ferroelectric Devices*, New York: Marcel Dekker, Inc.,2000.

[4] R.J. Meyer, W.J. Hughes, T.C. Montgomery, D.C Markley, and R. E. Newnham, "Design of and Fabrication Improvements to the Cymbal Transducer Aided by Finite Element Analysis," *Journal of Electroceramics*, **8**, 163- 174 (2002).

Annual Research Journal, Vol. V
Electrical Engineering Research Experience for Undergraduates

ISBN 0-913260-07-X (http://www.ee.psu.edu/reu/)

Annual Research Journal, Vol. V
Electrical Engineering Research Experience for Undergraduates

ISBN 0-913260-07-X (http://www.ee.psu.edu/reu/)

POWER SUBSYSTEM DESIGN FOR A SMALL SATELLITE

Marty Bode[*], Sven G. Bilén[#], and Perry Edwards[+]

Department of Electrical Engineering
The Pennsylvania State University, University Park, PA 16802

[*]Undergraduate Student of
Department of Applied Physics
Linfield College
McMinnville, OR 97128

ABSTRACT

This paper describes the preliminary design of the power subsystem for NittanySat, a small satellite being designed and built by the Student Space Programs Laboratory at The Pennsylvania State University. The goal of NittanySat is to measure the effect of ionization processes on radio waves in the *D*-region of the ionosphere. Correct design of the power subsystem is important because all subsystems will require power to operate.

INTRODUCTION

The Pennsylvania State University is one of the universities competing in the Nanosatellite-5 competition. The object of this contest, sponsored by the Air Force and the American Institute of Aeronautics and Astronautics, is to design a working nanosatellite that meets all of the competition requirements. The winning university will have their satellite launched into orbit. Penn State's effort is called NittanySat and it is being designed and constructed by the Student Space Programs Laboratory. The primary goal of the science mission for NittanySat is to study the effects of ionization processes on radio waves in the *D*-region of the ionosphere using a radio absorption experiment.

[#]Faculty Mentor
[+]Graduate Mentor

Annual Research Journal, Vol. V
Electrical Engineering Research Experience for Undergraduates

ISBN 0-913260-07-X (http://www.ee.psu.edu/reu/)

POWER SYSTEM OVERVIEW

With the correct design of the power subsystem, NittanySat will be able to function properly. Shown below is a top-level diagram of the power subsystem layout, which shows the connections between the different components of the subsystem and power and data flows.

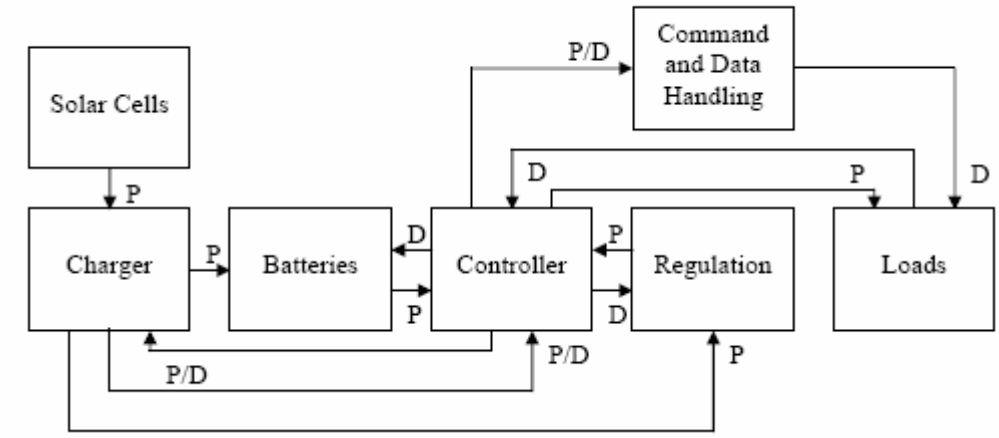

Figure 1: Top-level systems diagram of the power subsystem

The controller decides whether the power supplied to the satellite comes from the solar cells or from the batteries. When the satellite can't see the sun, the controller switches to the batteries, and when the satellite can see the sun, the controller switches to the solar cells. Whatever power is left over on the solar cells after the power needs of the rest of the satellite are met goes to the charger to charge the batteries. The command and data handling subsystem is responsible for controlling the power distribution to the loads.

DESCRIPTION OF SUBSYSTEMS

Solar Cells and Charger:

The solar cells that are currently being considered for use on NittanySat are the Emcore Advanced Triple Junction cells. These cells are rated at a minimum of 27.5% efficiency and they are space qualified. If the batteries have an almost full charge, the charger will only provide a trickle charge from the solar cells and if the batteries are mostly empty, the charger will provide a higher charge rate from the solar cells. Also, command and data handling will monitor the depth of the discharge and the temperature of the batteries and adjust the charge rate accordingly.

Annual Research Journal, Vol. V
Electrical Engineering Research Experience for Undergraduates

ISBN 0-913260-07-X (http://www.ee.psu.edu/reu/)

Batteries:

The batteries that are currently being considered for use on NittanySat are Sanyo's N-4000DRL 1.2-V 4000-mAh Ni-Cd D-cells. The main reason for this is that they are proven to be safe and effective by their long flight history. Another reason is that they contain almost no electrolytes, which is preferable for extended use in space. Some of the other types of batteries that are being researched are Lithium–Ion and Nickel–Metal Hydride. Both of these options are more expensive, but they offer a greater energy density, which would reduce mass.

Power Regulation:

There are many different types of voltage regulators. One type is called three terminal or linear regulators. The advantage to these is that they are simple. They also come with a predetermined output, which may or may not be an advantage. There are also adjustable three-terminal regulators, which are the same as three terminal regulators, except that the output is adjustable from 1.25 volts to 25 volts. Another type of voltage regulator is the dual tracking regulators. These output a positive and a negative voltage of the same value. Also, there are step-down regulators, which produce an output voltage that is lower than the input voltage. Step-down regulators are more efficient than other types of regulators, but they also produce more noise in their output. Step-up regulators are the same as step-down regulators, except that their output voltage is higher than the input voltage. The last common type of voltage regulator is the buck/boost or flyback regulator. This regulator produces a higher or lower voltage of an opposite polarity of the input voltage.

CONCLUSION

Many factors come into play when designing the power subsystem for a small satellite. Cost is a major thing to consider. With any small satellite project, especially one run by a university group like NittanySat, funding is always limited and has to be carefully watched to make sure that the project can be completed. Weight is also important to consider. It is one of the many constraints that the satellite has to fit into if it hopes to win the competition. Also, all of the components of the satellite have to be protected so that the solar radiation does not damage them. Everything has to be designed correctly or none of the subsystems of the satellite will work. This design will go through much thought and revision by the NittanySat team before it is ready to actually be implemented on the satellite.

ACKNOWLEDGEMENT

I would like to thank the Penn State EEREU program for giving me the opportunity to experience what it is like to do real research. I would also like to thank Prof. Sven Bilén for all of his help and guidance throughout this program.

Annual Research Journal, Vol. V
Electrical Engineering Research Experience for Undergraduates

ISBN 0-913260-07-X (http://www.ee.psu.edu/reu/)

Finally, I would like to thank Perry Edwards for graciously providing me assistance whenever I had questions or needed more information.

This material is based upon work supported by the National Science Foundation under Grant No. EEC-0244030.

REFERENCES

[1] A.K. Hyder, R.L. Wiley, G. Halpert, D.J. Flood, and S. Sabripour, "Power Management and Distribution," 353-411, *Spacecraft Power Technologies,* Space Technology-Volume **1**, edited by N. Hanson, Imperial College Press, London (2000).

[2] P. Horowitz, W. Hill, "Voltage Regulators and Power," 307-384, *The Art of Electronics*, Second Edition, Cambridge University Press, New York (1989).

[3] R. Fleeter, "Batteries Not Included," 173-185, *Micro Space Craft*, Reston, Edge City Press (1995).

Annual Research Journal, Vol. V
Electrical Engineering Research Experience for Undergraduates

ISBN 0-913260-07-X (http://www.ee.psu.edu/reu/)

DISTRIBUTED ENERGY HARVESTING USING PARALLEL CONNECTED PIEZOELECTRIC DEVICES AND RECTIFIERS

Christopher G. Brown*, Donald J. Natale III[+], Guanghui Wang[+], and Heath F. Hofmann[#]

Department of Electrical Engineering
The Pennsylvania State University, University Park, PA 16802

*Undergraduate student of
Electrical and Computer Engineering
Cornell University (formerly University of Rochester)
Ithaca, NY 14850 (Rochester, NY 14627)

ABSTRACT

We investigated a concept for a method of harvesting energy using a physically flexible distributed energy harvesting system. In this system only one piezoelectric device is assumed to be excited at one time. Mathematical models showed that if the piezoelectric devices were directly connected in parallel, maximum power would not be transferred due to the small current generated and large internal capacitance of the piezoelectric devices. Maximum power transferred is maintained if each piezoelectric device is connected to an AC-DC rectifier as a pair. Each pair is then connected in parallel with other piezoelectric device and AC-DC rectifier pairs. This idea of parallel piezoelectric device and AC-DC rectifier pairs could be the basis of further research on creating a mesh, fabric, or film piezoelectric system with rectifiers and electrodes built in. By using polyvinylidene fluoride (PVDF) film and printing electrodes or attaching electrical ribbons to the film, the entire transducing portion of the system would be physically flexible. Multiple tiny integrated circuit (IC) chips could be used for the AC-DC rectifiers so that the entire system could remain physically flexible.

[+] Graduate Mentor
[#] Faculty Mentor

Annual Research Journal, Vol. V
Electrical Engineering Research Experience for Undergraduates

ISBN 0-913260-07-X (http://www.ee.psu.edu/reu/)

Proof of concept was demonstrated by creating a simplified version of this system using standard electrical components. Experimental tests were performed by placing the piezoelectric transducer disc up to a speaker cone and using the speaker for mechanical stimulation. A sinusoidal signal with a 10 volt peak to peak amplitude was applied so that the mathematical models more accurately represented conditions in the experiment. In the first test the piezoelectric transducer discs were connected directly in parallel and in the second test piezoelectric disc and AC-DC rectifier pairs were connected in parallel. The results supported the previously mentioned mathematical models for both situations.

INTRODUCTION

For many years, piezoelectric devices have been restricted to being made of stiff ceramics. Recently, though, researchers have been experimenting with flexible ferroelectric polymers such as polyvinylidene Difluoride (PVDF) [4]. The use of flexible materials in energy harvesting opens up a world of imaginative possibilities that traditional piezoelectric devices do not allow. In most research on energy harvesting with piezoelectric devices, only one ceramic or polymer strip has been considered [1,2]. In order to allow for new and creative methods of energy harvesting, such as from clothing, we must be able to maximize the energy harvested in a distributed system. This research takes the first, simple step of considering a situation where many piezoelectric devices are attached together in one energy harvesting system, but only one device is being excited at a time. We consider two situations in this research. The first situation, Situation 1, is when all the piezoelectric devices are connected in parallel and then are connected to single AC-DC rectifier. The second situation, Situation 2, is when each piezoelectric device is connected to its own AC-DC rectifier. These piezoelectric device and AC-DC rectifier pairs are then para-linked together. Mathematical models and experimental results are used to compare the two situations and determine which one maximizes the energy harvested from the system.

MATHEMATICAL MODEL: SITUATION ONE

Using circuit analysis and the work of Geffrey K. Ottman [3], the power output from a piezoelectric energy harvesting system with one piezoelectric transducer being excited at a time can be modeled for *n* number of piezoelectric devices connected in parallel to a single rectifier (Figure 1). Each piezoelectric element is modeled as a parallel capacitor and current source pair.

Note:

For all equations and diagrams C_1-C_n are specific piezo capacitances, C_p is any piezo capacitance, V_{out} is the output voltage across a load, i_1-i_n are specific piezo currents, and I_p is any piezo current.

Annual Research Journal, Vol. V
Electrical Engineering Research Experience for Undergraduates

ISBN 0-913260-07-X (http://www.ee.psu.edu/reu/)

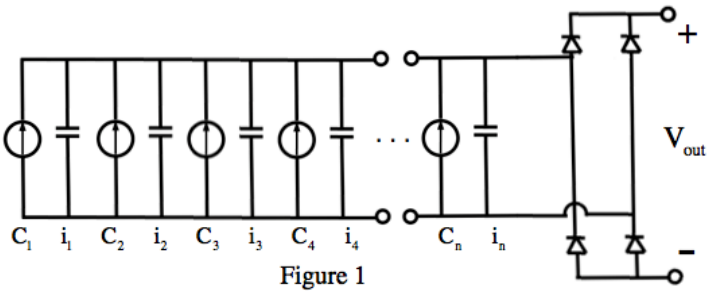

Figure 1

Since only one piezoelectric device will be stimulated at a time, all the capacitance values of each device can be summed and all the current sources go to zero except the one being stimulated. The stimulated piezoelectric device uses a sinusoidal wave to model its input excitation signal (Figure 2).

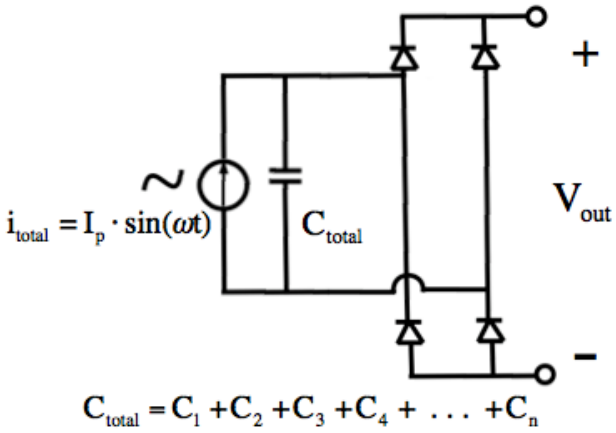

Figure 2

Using Ottman's previous work, we can assume that for this situation $C_1 = C_2 = C_3 = C_4 = \ldots = C_p$.

Power output for one piezoelectric can be calculated as

$$< P(t) > = \frac{2V_{out}}{\pi}\left(I_p - V_{out}\omega C_p\right) \quad (1)$$

$$V_{out} = \frac{I_p}{2\omega C_p} \quad (2)$$

$$< P > = \frac{I_p^2}{\pi\omega C_p} \quad (3)$$

For *n* number of piezoelectrics, a substitution can be made and the derivation for power output is as follows.

Annual Research Journal, Vol. V
Electrical Engineering Research Experience for Undergraduates

ISBN 0-913260-07-X (http://www.ee.psu.edu/reu/)

$$< P(t) > \;=\; \frac{2V_{out}}{\pi}\left(I_p - V_{out}\omega n C_p\right) \tag{4}$$

$$V_{out} \;=\; \frac{I_p}{2\omega n C_p} \tag{5}$$

$$< P(t) > \;=\; \frac{I_p^2}{\pi\omega n C_p} - \frac{2V_{out}^2\omega n C_p}{\pi} \tag{6}$$

$$< P(t) > \;=\; \frac{2I_p}{\pi 2\omega C_p n}\cdot\left(I_p - \frac{I_p\omega C_p n}{2\omega C_p n}\right) \tag{7}$$

$$< P(t) > \;=\; \frac{2I_p}{\pi 2\omega C_p n}\cdot\left(I_p - \frac{I_p}{2}\right) = \frac{2I_p}{2\pi\omega C_p n}\cdot\left(\frac{I_p}{2}\right) \tag{8}$$

$$< P(t) > \;=\; \frac{I_p^2}{\pi\omega C_p n} \tag{9}$$

By comparing the output power of one piezoelectric device to *n* number of piezoelectric devices it is shown that there is an inverse proportional relationship between the number of piezoelectric devices and power output.

$$< P > \;\propto\; \frac{1}{n} \tag{10}$$

MATHEMATICAL MODEL: SITUATION TWO

For situation two, each piezoelectric device is connected to its own AC-DC rectifier. These piezoelectric device and AC-DC rectifier pairs are then para-linked together (Figure 3). The power output for this system can be calculated to be the same as having only one piezoelectric device connected to the circuit. The diodes in the AC-DC rectifiers of the other attached piezoelectric devices do not conduct due to the polarity and magnitude of the voltage across them. As a result, there are no parasitic energy loses.

Power output for this situation can be calculated as

$$< P(t) > \;=\; \frac{2V_{out}}{\pi}\left(I_p - V_{out}\omega C_p\right) \tag{11}$$

$$V_{out} \;=\; \frac{I_p}{2\omega C_p} \tag{12}$$

$$< P > \;=\; \frac{I_p^2}{\pi\omega C_p} \tag{13}$$

Annual Research Journal, Vol. V
Electrical Engineering Research Experience for Undergraduates

ISBN 0-913260-07-X (http://www.ee.psu.edu/reu/)

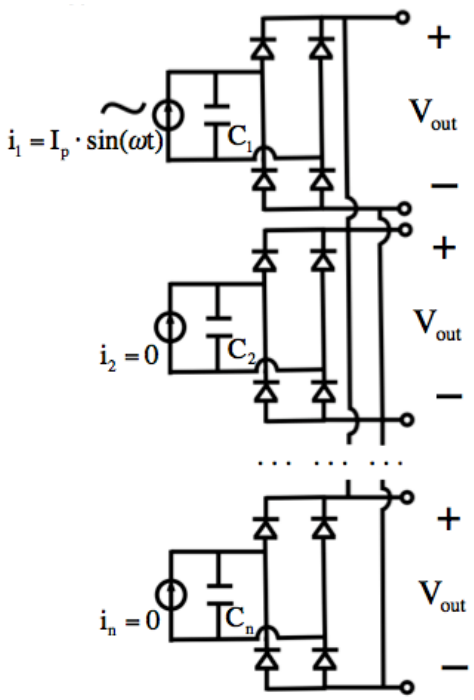

Figure 3

EXPERIMENTAL EQUIPMENT

The piezoelectric devices used in all experimental tests were 3/4" diameter Murata 7BB-18R2-11 Mini Piezo Discs. They were mechanically excited using two Dual XS10 10" subwoofers and input signals supplied by an Agilent 33220A 20 MHz Function/Arbitrary Waveform Generator and a Hewlett Packard 33120A 15 MHz Function/Arbitrary Waveform Generator. A Wish Board no. 204 was used for the rectifier circuitry and a Tektronix TDS 3012B Oscilloscope was used to view voltage waveforms and to take voltage measurements. Each piezoelectric disc was mechanically stimulated by placing it up against a subwoofer speaker cone (Figure 4). The entire setup can be seen in Figure 5, below.

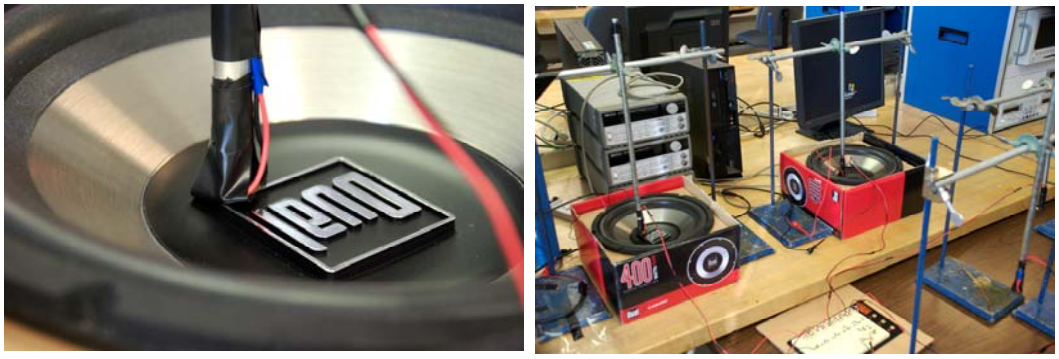

Figure 5.

Annual Research Journal, Vol. V
Electrical Engineering Research Experience for Undergraduates

ISBN 0-913260-07-X (http://www.ee.psu.edu/reu/)

EXPERIMENTAL SETUP

For situation one and two, the experimental conditions all remained the same except for the AC-DC rectifier arrangement. A single piezoelectric disc was stimulated by a vibrating subwoofer speaker at the frequencies of 40 Hz, 80, Hz, and 120 Hz. The input signal to the subwoofer had the same frequencies and a peak to peak voltage of 10 volts. For each frequency additional piezoelectric discs were added one at a time to see how they effected the average power. The output voltage waveform was captured across the load of the 10 MΩ internal impedance of the oscilloscope. The average voltage was also measured by the oscilloscope and was used to calculate the average power.

RESULTS

All experimental results and output voltage waveforms were collected and summarized in the following pages.

DISCUSSION

All the results show that average power output from the arrangement of piezoelectric disc and AC-DC rectifier pair is greater, and not subject to parasitic loses, than the average power output from parallel piezoelectric devices attached to one AC-DC rectifier. Even though the experimental results show that the average power reduction from the single AC-DC rectifier setup does not accurately follow the mathematical model previously used, they still support the hypothesis that power will be lost as more piezoelectric devices are attached. In the experimental results this decrease was greater than predicted by the mathematical model because the model assumed all the piezoelectric discs were exactly the same. In reality, each piezoelectric disc has very different impedance properties that probably lead to the discrepancy between the predicted *1/n* power reduction rate and the actual power reduction rate. There were no power output changes for the piezoelectric disc and AC-DC rectifier pair arrangement as additional piezoelectric devices were added. The diodes in the AC-DC rectifiers prevented parasitic power loss. This further supports the original hypothesis.

CONCLUSION

We are a long way from being able to create a highly efficient flexible energy harvesting material. A lot more work needs to be done to maximize the output power from such a device. This research project took the first, simple step of showing how attaching an AC-DC rectifier to each piezoelectric element can maximize output power when only one piezoelectric element is excited at one time. To take this work to a more practical level further research must be done to optimize output power from multiple piezoelectric elements being excited at one time.

Annual Research Journal, Vol. V
Electrical Engineering Research Experience for Undergraduates

ISBN 0-913260-07-X (http://www.ee.psu.edu/reu/)

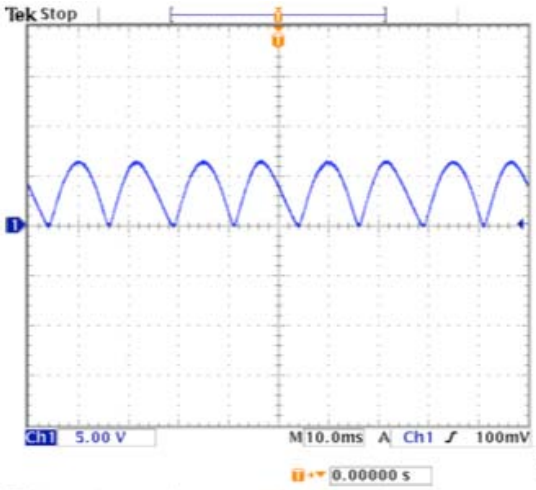

Average Power: 13.54μW
Excited Piezo Discs: 1
Unexcited Piezo Discs: 0
Frequency: 40 Hz
Arrangement: Single Rectifier

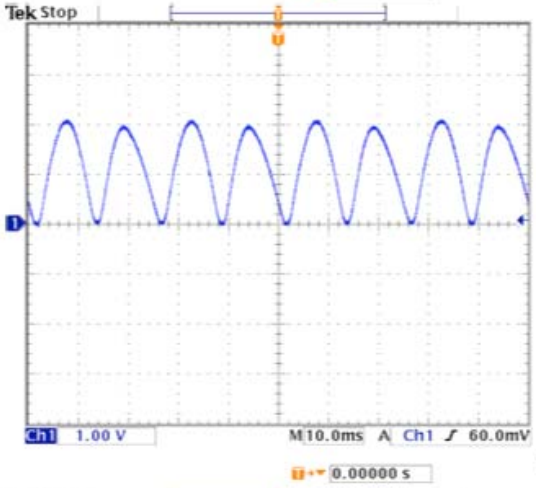

Average Power: 1.254μW
Excited Piezo Discs: 1
Unexcited Piezo Discs: 2
Frequency: 40 Hz
Arrangement: Single Rectifier

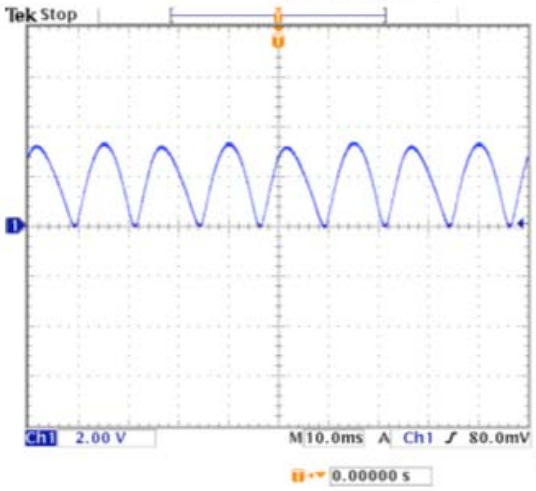

Average Power: 3.460μW
Excited Piezo Discs: 1
Unexcited Piezo Discs: 1
Frequency: 40 Hz
Arrangement: Single Rectifier

Annual Research Journal, Vol. V
Electrical Engineering Research Experience for Undergraduates

ISBN 0-913260-07-X (http://www.ee.psu.edu/reu/)

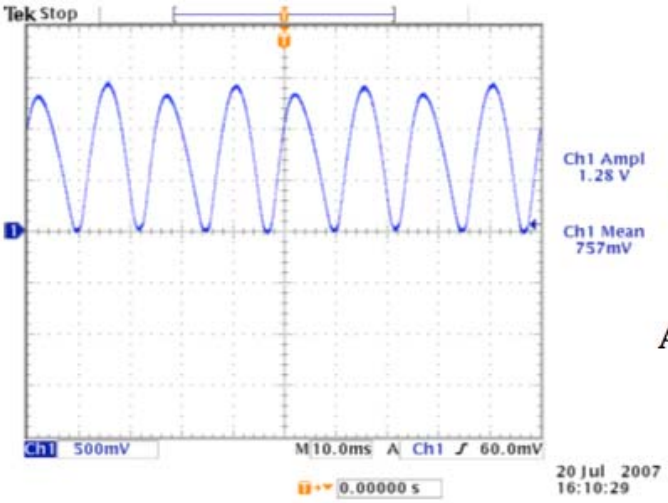

Average Power: 0.5731μW
Excited Piezo Discs: 1
Unexcited Piezo Discs: 3
Frequency: 40 Hz
Arrangement: Single Rectifier

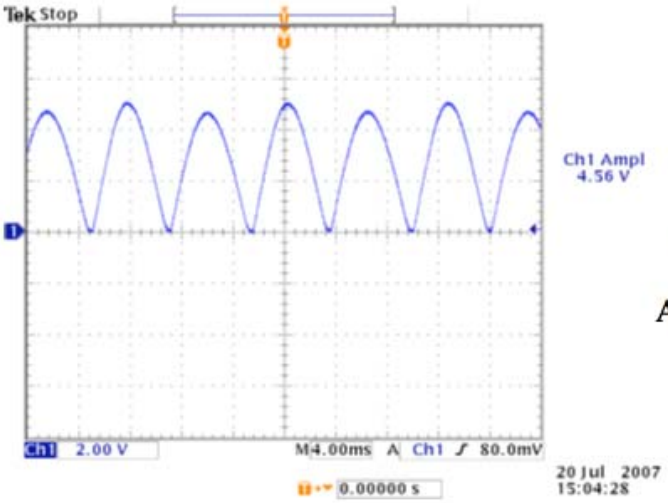

Average Power: 8.123μW
Excited Piezo Discs: 1
Unexcited Piezo Discs: 0
Frequency: 80 Hz
Arrangement: Single Rectifier

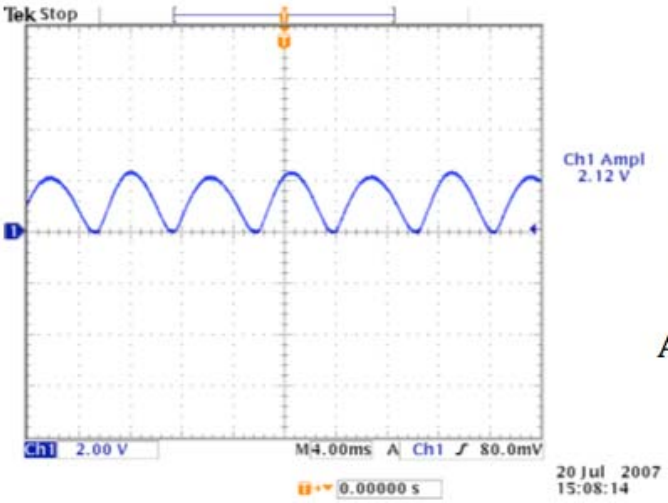

Average Power: 2.132μW
Excited Piezo Discs: 1
Unexcited Piezo Discs: 1
Frequency: 80 Hz
Arrangement: Single Rectifier

Annual Research Journal, Vol. V
Electrical Engineering Research Experience for Undergraduates

ISBN 0-913260-07-X (http://www.ee.psu.edu/reu/)

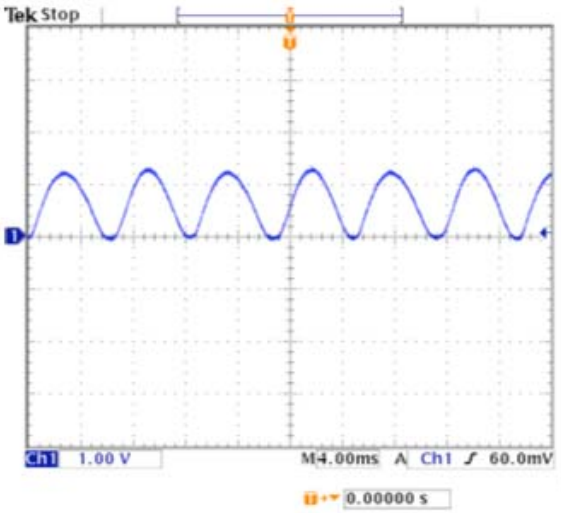

Average Power: 0.659μW
Excited Piezo Discs: 1
Unexcited Piezo Discs: 2
Frequency: 80 Hz
Arrangement: Single Rectifier

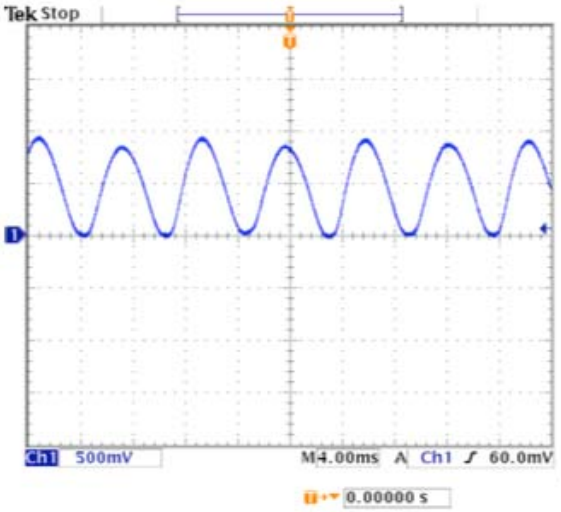

Average Power: 0.279μW
Excited Piezo Discs: 1
Unexcited Piezo Discs: 3
Frequency: 80 Hz
Arrangement: Single Rectifier

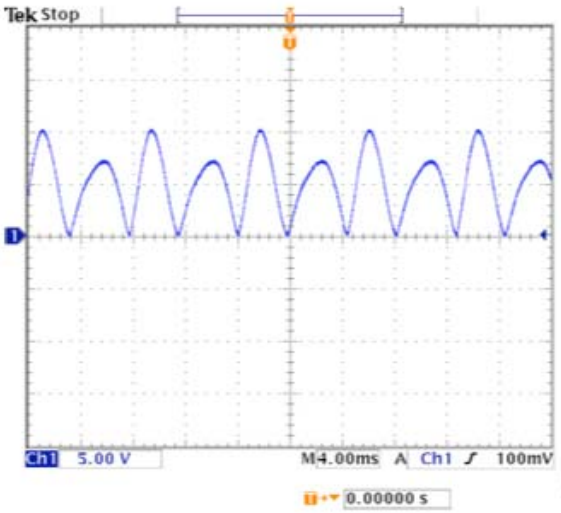

Average Power: 25.81μW
Excited Piezo Discs: 1
Unexcited Piezo Discs: 0
Frequency: 120 Hz
Arrangement: Single Rectifier

Annual Research Journal, Vol. V
Electrical Engineering Research Experience for Undergraduates

ISBN 0-913260-07-X (http://www.ee.psu.edu/reu/)

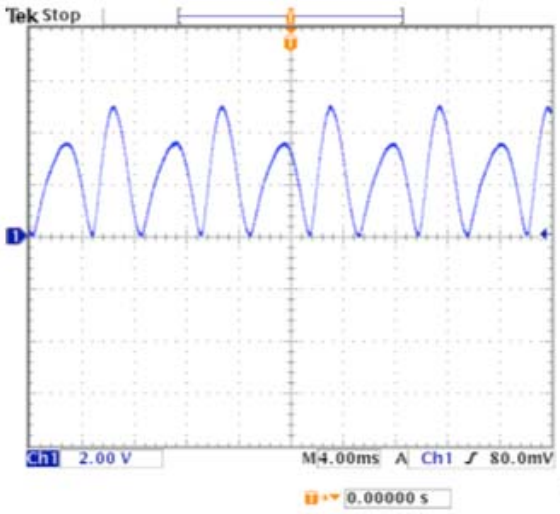

Average Power: 5.570μW
Excited Piezo Discs: 1
Unexcited Piezo Discs: 1
Frequency: 120 Hz
Arrangement: Single Rectifier

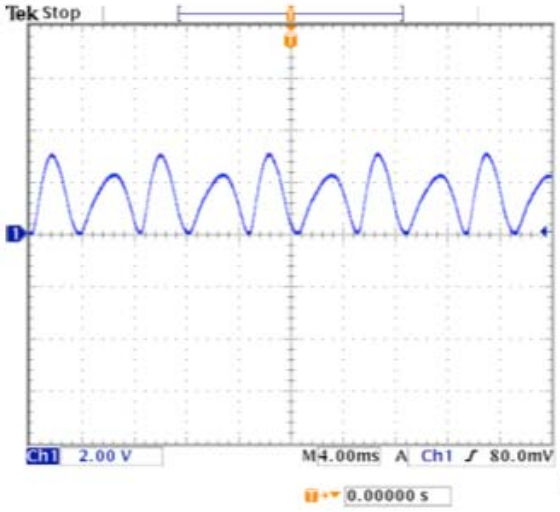

Average Power: 2.074μW
Excited Piezo Discs: 1
Unexcited Piezo Discs: 2
Frequency: 120 Hz
Arrangement: Single Rectifier

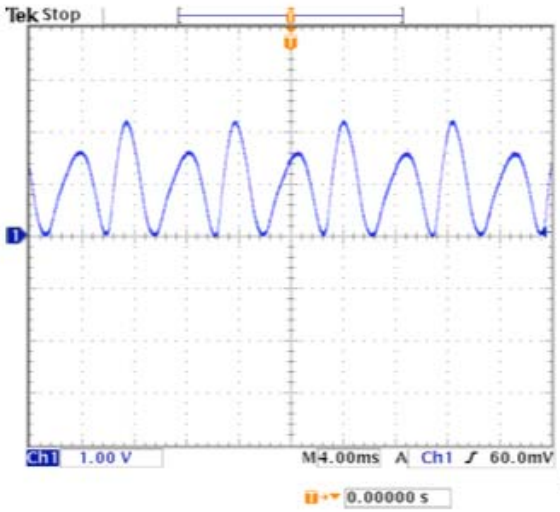

Average Power: 0.9044μW
Excited Piezo Discs: 1
Unexcited Piezo Discs: 3
Frequency: 120 Hz
Arrangement: Single Rectifier

Annual Research Journal, Vol. V
Electrical Engineering Research Experience for Undergraduates

ISBN 0-913260-07-X (http://www.ee.psu.edu/reu/)

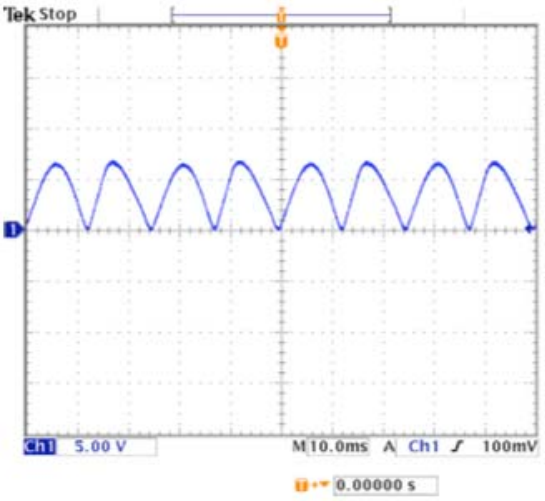

Average Power: 14.44μW
Excited Piezo Discs: 1
Unexcited Piezo Discs: 1-3
Frequency: 40 Hz
Arrangement: Multiple Rectifiers

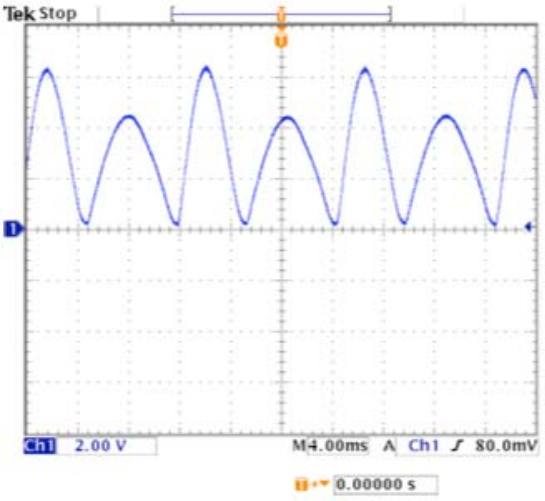

Average Power: 10.05μW
Excited Piezo Discs: 1
Unexcited Piezo Discs: 1-3
Frequency: 80 Hz
Arrangement: Multiple Rectifiers

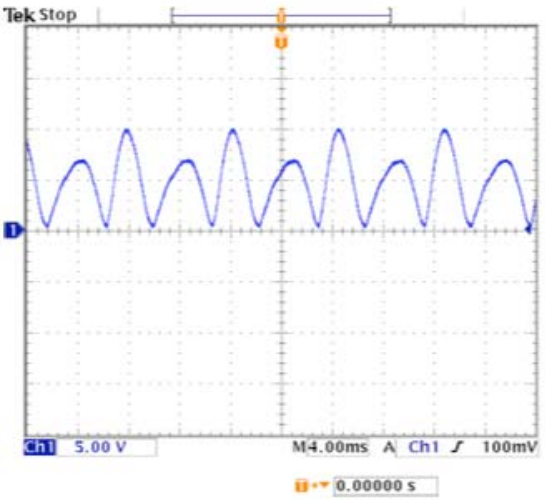

Average Power: 22.09μW
Excited Piezo Discs: 1
Unexcited Piezo Discs: 1-3
Frequency: 120 Hz
Arrangement: Multiple Rectifiers

Annual Research Journal, Vol. V
Electrical Engineering Research Experience for Undergraduates

ISBN 0-913260-07-X (http://www.ee.psu.edu/reu/)

ACKNOWLEDGMENTS

This material is based upon work supported by the National Science Foundation under Grant No. EEC-0244030.

REFERENCES

[1] G. K. Ottman, H. F. Hofmann, A. C. Bhatt, and G. A. Lesieutre, "Adaptive Piezoelectric Energy Harvesting Circuit for Wireless Remote Power Supply," *IEEE Transactions On Power Electronics*, Vol. 17, No. 5, pp. 669-676, September 2002.

[2] G. K. Ottman, H. F. Hofmann, and G. A. Lesieutre, "Optimized Piezoelectric Energy Harvesting Circuit Using Step-Down Converter in Discontinuous Conduction Mode," *IEEE Transactions On Power Electronics*, Vol. 18, No. 2, pp. 696-703, March 2003.

[3] G. K. Ottman, Piezoelectric Power Flow, pp. 7-10, *A Piezoelectric Energy Harvesting Circuit For Wireless, Remote Power Supply*, 2002.

[4] Y. Liu, K. L. Ren, H. F. Hofmann, and Q. Zhang, "Investigation of Electrostrictive Polymers for Energy Harvesting," *IEEE Transactions On Ultrasonics, Ferroelectrics, and Frequency Control*, Vol. 52, No. 12, pp. 2411-2417, December 2005.

Annual Research Journal, Vol. V
Electrical Engineering Research Experience for Undergraduates

ISBN 0-913260-07-X (http://www.ee.psu.edu/reu/)

LOW TEMPERATURE PYROELECTRIC CHARACTERISTICS OF BARIUM TITANATE

Marie Cosgrove-Davies*, Tanmoy Maiti[+], and Amar S. Bhalla[#]

Department of Electrical Engineering and Materials Research Institute
The Pennsylvania State University, University Park, PA, 16802

*Undergraduate student of
Engineering Department
Swarthmore College
Swarthmore, PA, 19081

ABSTRACT

The pyroelectric response of various barium titanate ($BaTiO_3$) samples was examined over a temperature range of 25K to 300K. The samples included crystals, composites, and chromium-doped materials. Characterization curves for the various samples were collected and compared. The chromium-doped sample was found to have the most advantageous characteristics for aerospace applications.

INTRODUCTION

Pyroelectric materials produce electric potential when they are subjected to a change in temperature. When the heating or cooling occurs, positive charges move to one end of the material and negative charges to the other, causing the changes in polarization and creating the electric potential. The pyroelectric coefficient, p, in typical pyroelectric materials under constant electric field and stress is defined as $p = -\frac{\partial P}{\partial T}$, where P is the polarization of the material and ∂T is the change in temperature of the sample. Pyroelectrics' sensitivity to even very small changes in temperature ($\sim 10^{-3}$-10^{-1} degrees K) makes them ideal for passive heat or IR sensing. They are used extensively in infrared detection, since infrared waves are heat waves and therefore change the temperature of any surface they -

[+] Graduate Mentor
[#] Faculty Mentor

Annual Research Journal, Vol. V
Electrical Engineering Research Experience for Undergraduates

ISBN 0-913260-07-X (http://www.ee.psu.edu/reu/)

strike. Pyroelectric materials are used in spectrometers, burglar alarms, fire detection, night-vision, and other thermal imaging applications.

Low-temperature characteristics of pyroelectric materials are of interest because, when cooled, the dielectric constant and dielectric loss both decrease, which has the potential of increasing efficiency (Zhong et al)[1]. Cooled sensors can be used in normal applications if the cooled properties are advantageous enough to justify the cooling, and can also be extremely useful in aerospace applications, where no cooling is necessary because ambient temperature is quite low (around 80K).

Barium titanate has been well-characterized and is known for its ferroelectric properties. It goes through two structural phase transitions below room temperature, at around 280K and 190K (Zhong et al). These phase transition regions are of interest because at phase transitions the most pronounced change in properties over the shortest period is found. This makes sensing more efficient, since a smaller change will produce a larger result. In this report, the pyroelectric characteristics of barium titanate samples at temperatures ranging from 25 to 300 degrees Kelvin were examined. Measurements were taken only during the heating cycles, so no hysteresis effects were observed. Zhong et al. had previously examined the pyroelectric characteristics of barium titanate between 150 and 300K, and other researchers have worked with pyroelectric characteristics above room temperature (Chynoweth, Cook, C.A. Miller, R. Miller, Perls)[2,3,4,5,6] and characterization of thin films and composites by Cwikiel and Nogas-Cwikiel [7], Muralidhar and Pillai [8], and Murphy [9]. Here, undoped barium titanate samples and a chromium-doped sample were examined, and their relative pyroelectric characteristics compared.

EXPERIMENTAL

The pyroelectric measurements are taken using the Byre-Roundy[10] technique in which the charge or current is measured as a function of temperature on a sample of known dimensions. For a crystal of area *A*, the collected current density *I* can be related to the pyroelectric coefficient using the equation:

$$p = \frac{dP}{dT} = \frac{q}{AdT} = \frac{idt}{AdT} = \frac{i}{A\frac{dT}{dt}}$$

In order to use a material for sensing purposes, one has to establish the material's figure of merit, which depends on the targeted applications of the sensor. Several "material figure of merit" factors have been established for pyroelectric materials, including:

Annual Research Journal, Vol. V
Electrical Engineering Research Experience for Undergraduates

ISBN 0-913260-07-X (http://www.ee.psu.edu/reu/)

$$F_D = \frac{p}{C_p \rho \sqrt{\varepsilon_0 \kappa \tan\delta}}$$

$$F_i = \frac{p}{C_p \rho}$$

$$F_V = \frac{p}{C_p \rho \varepsilon_0 \kappa}$$

$$F_{Vid} = \frac{p\gamma}{C_p \rho \varepsilon_0 \kappa}$$

where C_p is the specific heat, ρ is the density, ε_0 is the vacuum permittivity (8.85×10^{-12} F/m), κ is the dielectric constant, γ is the reciprocal thermal diffusivity, $tan\delta$ is the dielectric loss tangent, and p is the pyroelectric coefficient of the material. F_D is the pyroelectric point detector, F_i is the fast pulse detector, F_V is the large area detector, and F_{Vid} is the vidicon (Bhalla and Guo)[11].

For the selection of suitable pyroelectric sensing material, the typical guiding property of $\frac{p}{\kappa}$ or $\frac{p}{\sqrt{\kappa}}$ is evaluated. Hence, the current measurements are focused on studying the pyroelectric and dielectric behaviors of barium titanate samples.

The dimensions of each sample (area and thickness) were measured and recorded. Samples were then prepared by attaching one-inch-long silver leads with a diameter of 0.005" to both flat sides using SPI flash-dry silver paint. The paint was allowed to dry overnight under a bright light to ensure that it dried completely.

The sample was placed on nonconductive glass slide inside an airtight chamber. The silver leads were soldered to two terminals (across which all signals were applied), and the chamber was vacuum sealed. A vacuum was applied to the chamber using an Alcatel Drytel 31 system, and a voltage of 10 kV/cm was slowly applied to the sample.

Prior to the measurement, the sample was electrically poled by applying an external electric field to the sample. Once the field was applied, the sample was cooled using an APD Cryogenics HC-2 unit controlled by a LakeShore 330 Autotuning Temperature Controller. The electric field was maintained across the sample while cooling, and for half an hour after the sample reached the lowest temperature point (around 25K), to ensure that the sample poled properly. The sample was shorted and grounded to remove any excess surface charge built up during poling, then hooked up to a pyroelectric measurement box that amplified input signal (and which was attached to a multimeter). A computer program was run which controlled the heating/cooling setup and data was collected by interfacing between the computer and the assisted measurement setup (Fig. 1).

Annual Research Journal, Vol. V
Electrical Engineering Research Experience for Undergraduates

ISBN 0-913260-07-X (http://www.ee.psu.edu/reu/)

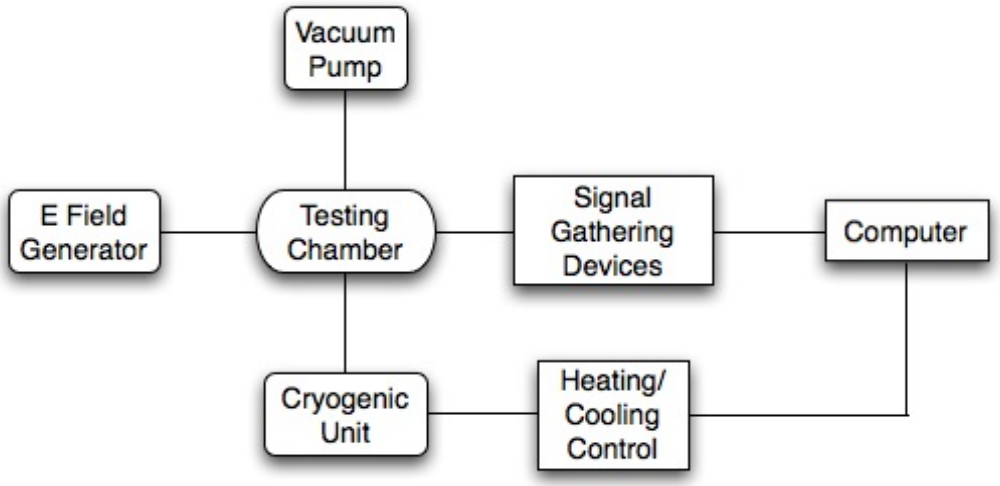

Figure 1: Block Diagram of Experimental Set-Up

The sample was heated by approximately two degrees Kelvin per minute, and two thousand measurements were taken over the course of the data collection, which ranged from the low temperature (around 25K) to 300K. The data were computed and plotted as p vs. T and P vs. T. This was repeated for all samples.

RESULTS AND DISCUSSION

Three single-crystal barium titanate samples developed by the float zone technique and one chromium-doped barium titanate sample developed by the flux zone technique were examined. Barium titanate samples #1 and #2 were found to have pyroelectric peaks at approximately 200K (Figs 2, 3). The peak of sample #1 was broad and bell-shaped, beginning around 160K and ending around 240K, while the peak of sample #2 was a sharp increase and decrease at 200K with a width of less than 5K on either side of the maximum. The temperatures at which the polarization dropped and the shapes of the drops corresponded with the pyroelectric peaks' temperatures and sizes. Sample #1's drop was gradual and broad, while sample #2's drop was abrupt and sharp. Sample #3 showed a broad peak around 30K, with a correspondingly gradual drop in polarization (Fig. 4). The chromium-doped barium titanate sample showed two peaks, one at around 195K and the other around 290K, corresponding to the two phase transitions (Fig. 5). The additional peak is attributable to the addition of chromium. Both peaks were very sharp, with almost no width, and the drop in polarization was also found to be extremely sharp, with transitions that are vertical. From this it can be concluded that the chromium-doped sample is an extremely high-quality sample and would be useful in sensing around the temperatures of 195K and 290K (if the samples can be maintained around the temperatures at which the peaks occur),

Annual Research Journal, Vol. V
Electrical Engineering Research Experience for Undergraduates

ISBN 0-913260-07-X (http://www.ee.psu.edu/reu/)

although the peak at 290K might lead to cracking of the sample due to stresses around room temperature.

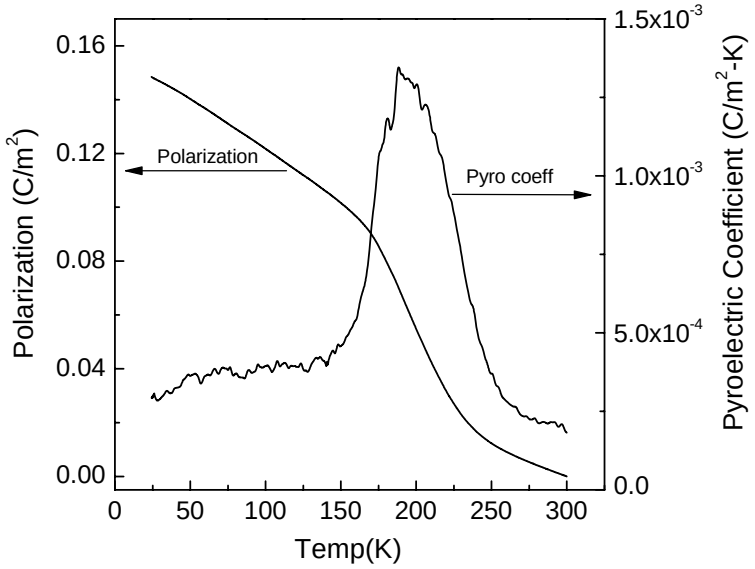

Figure 2: Temperature dependence of Polarization and Pyroelectric Coefficient of Barium Titanate Single Crystal Sample 1 from 25 to 300 K.

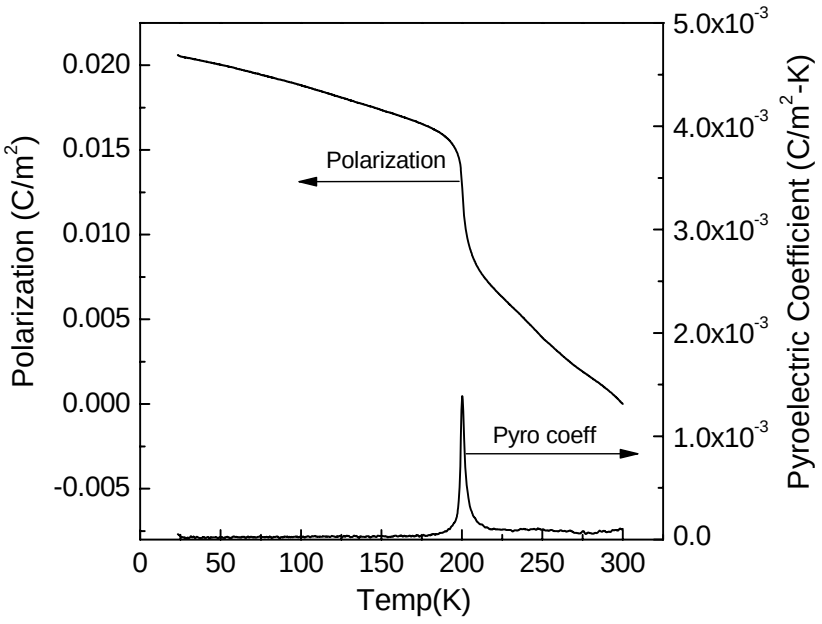

Figure 3: Temperature dependence of Polarization and Pyroelectric Coefficient of Barium Titanate Single Crystal Sample 2 from 25 to 300 K.

Annual Research Journal, Vol. V
Electrical Engineering Research Experience for Undergraduates

ISBN 0-913260-07-X (http://www.ee.psu.edu/reu/)

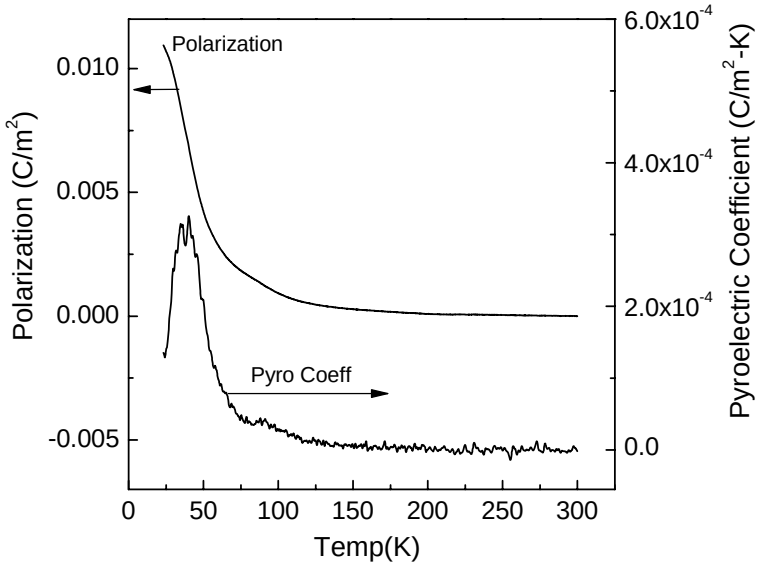

Figure 4: Polarization and Pyroelectric Coefficient of Barium Titanate Single Crystal Sample 3 as a function of temperature from 25 to 300 K.

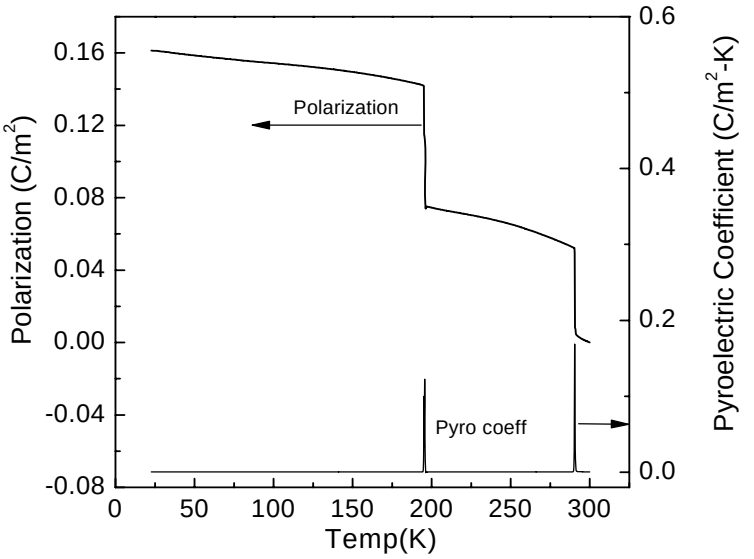

Figure 5: Polarization and Pyroelectric Coefficient of Chromium-doped Barium Titanate Single Crystal in the temperature range from 25 to 300 K.

The dielectric constants for the samples proved to have characteristic curves similar to the pyroelectric curves at low frequencies. The temperature dependence of dielectric constant (ε') and loss tangent ($\tan\delta$) at various frequencies for Barium Titanate single crystal Sample #3 and Chromium-doped Barium Titanate single

Annual Research Journal, Vol. V
Electrical Engineering Research Experience for Undergraduates

ISBN 0-913260-07-X (http://www.ee.psu.edu/reu/)

crystal is shown in figure 6 and 7 respectively. There is a shift in peak location from the pyroelectric characteristic curve (Fig. 4 & 5), but because the pyroelectric curve was obtained during heating and the dielectric curve during cooling, this is likely due to a hysteresis effect. The presence of similar shapes in similar locations in the pyroelectric and dielectric constants of the sample indicate that the peaks are genuine and not artifacts of the particular test.

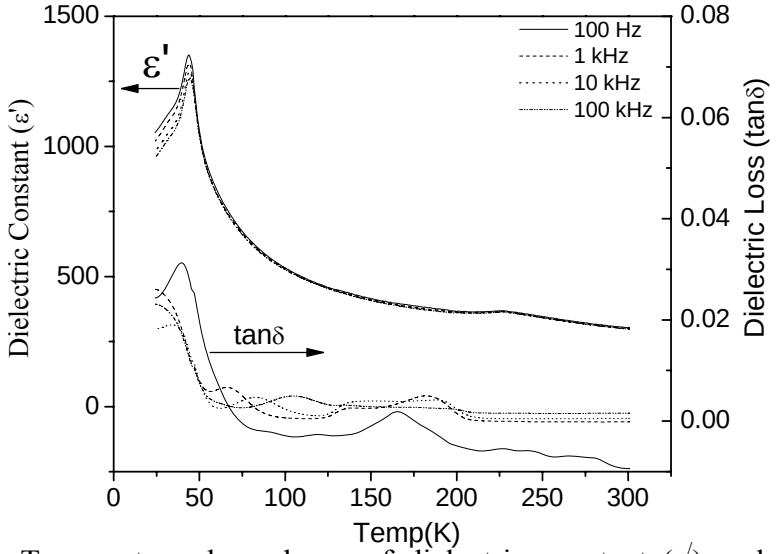

Figure 6: Temperature dependence of dielectric constant (ε') and loss tangent (tanδ) at various frequencies for Barium Titanate single crystal Sample #3

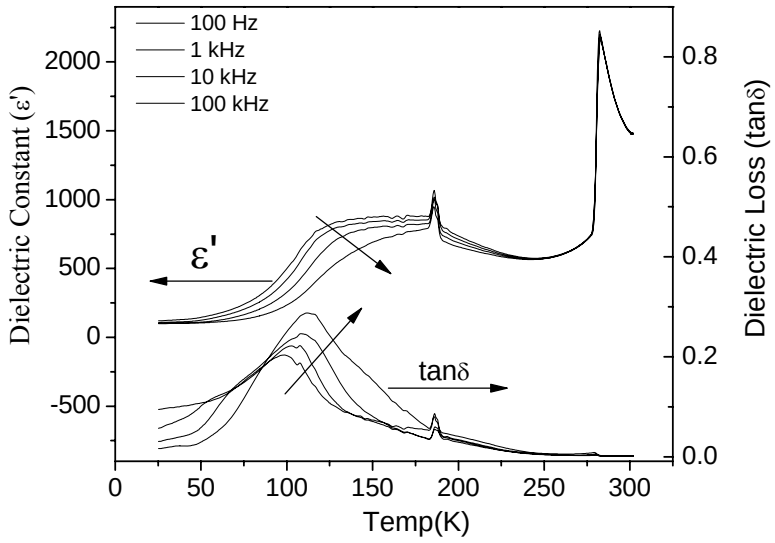

Figure 7: Temperature dependence of dielectric constant (ε') and loss tangent (tanδ) at various frequencies for Chromium-doped Barium Titanate single crystal (Arrows indicate the direction of increasing frequency).

Annual Research Journal, Vol. V
Electrical Engineering Research Experience for Undergraduates

ISBN 0-913260-07-X (http://www.ee.psu.edu/reu/)

CONCLUSION

The maximum polarization and pyroelectric coefficients for all materials in 50K ranges are shown in Table 1.

Table 1
Maximum Polarization and Pyroelectric Coefficients for Barium Titanate Samples In 50K Ranges from 25K to 300K.

		Maximum in Range					
		25-50K	50-100K	100-150K	150-200K	200-250K	250-300K
BT #1	Polarization	0.149	0.140	0.122	0.102	0.055	0.012
	Pyro Coeff	3.54E-04	3.87E-04	4.72E-04	1.37E-03	1.41E-03	4.07E-04
BT #2	Polarization	0.021	0.020	0.019	0.017	0.013	0.004
	Pyro Coeff	1.00E-04	1.00E-04	1.00E-04	1.50E-03	1.70E-03	1.00E-04
BT #3	Polarization	1.09E-02	4.20E-03	9.00E-04	3.00E-04	1.00E-04	0
	Pyro Coeff	3.00E-04	2.00E-04	1.00E-04	0	0	0
BT Cr	Polarization	0.162	0.158	0.154	0.149	0.075	0.065
	Pyro Coeff	1.00E-04	1.00E-04	1.00E-04	1.23E-01	3.00E-04	1.69E-01

(Note that Polarization Units are C/m^2 and Pyroelectric Coefficient Units are C/m^2-K)

From Table 1 and the above figures it can be seen that samples #1 and #2 have good profiles for non-temperature-controlled space sensing (their polarization remains relatively constant within the temperature range of 25K to 80K) but non-ideal profiles for orbital and sub-orbital applications (the temperature gradient becomes steeper after it passes 200K). The chromium-doped sample, in contrast, remains relatively flat in both ranges, with sudden, sharp drops between them. The chromium-doped sample is therefore the best suited to aerospace applications, with a flat profile and abrupt jumps. If very precise sensing is required, the sample's temperature can be maintained at 190K or 290K, yielding a very large change when the temperature changes. For more general non-temperature-controlled sensing purposes, the chromium-doped material will operate relatively linearly within the areas of interest.

ACKNOWLEDGEMENTS

This material is based upon work supported by the National Science Foundation under Grant No. EEC-0244030.

Annual Research Journal, Vol. V
Electrical Engineering Research Experience for Undergraduates

ISBN 0-913260-07-X (http://www.ee.psu.edu/reu/)

REFERENCES

1. Zhong, W.L., Zhang, P.L., and Zhao, H.S. "Low Temperature Pyroelectric Behaviour of Barium Titanate." *Ferroelectrics*, v. **118** (1-4), p. 1-6 (1991).
2. Chynoweth, A.G. "Dynamic Method for Measuring the Pyroelectric Effect with Special Reference to Barium Titanate." *Journal of Applied Physics*, v **27** (1), p. 78-84 (1956).
3. Cook, W.R. "Thermal Expansion and Pyroelectricity in Lead Titanate Zirconate and Barium Titanate." *Journal of Applied Physics*, v **34** (5), p. 1392-1398 (1963).
4. Miller, C.A. "Hysteresis Loss and Dielectric Constant in Barium Titanate." *British Journal of Applied Physics*, v **18**, p. 1689-1697 (1967).
5. Miller, R. and Savage, A. "Asymmetric Hysteresis Loops and the Pyroelectric Effect in Barium Titanate." *Journal of Applied Physics*, v **30** (6), p. 808-811 (1959).
6. Perls, T.A. "Primary Pyroelectricity in Barium Titanate Ceramics." *Journal of Applied Physics*, v **29** (9), p. 1297-1302 (1958).
7. Cwikiel, K and Nogas-Cwikiel, E. "Dielectric and pyroelectric properties of the Ba0.3Na0.7Ti0.3Nb0.7O3 ceramics obtained by sol-gel method." *Phase Transitions*, v **80** (1-2) (2007).
8. Muralidhar, C. and Pillai, P. K. C. "Pyroelectric Behavior in Barium Titante/Polyvintlidene Fluoride Composites." *IEEE Transactions on Electrical Insulation*, v **21** (3) (1986).
9. Murphy, C.E. "Pyroelectric properties of fine barium titanate/70:30 mol% poly(vinylidene fluoride:trifluoroethylene) thin-film composites." *Ferroelectrics*, v **152** (1-4) (1994).
10. Byer, R. L. and Roundy C. B. "Pyroelectric coefficient direct measurement technique and application to a nsec response time detector," *IEEE Trans.* SU-**19**, 333 (1972).
11. Bhalla, A.S. and Guo, R. "Pyroelectricity," p. 465-469, *Wiley Encyclopedia of Electrical and Electronics Engineering*, Vol. **17**, Ed. John G. Webster. John Wiley & Sons: New York (1999).

Annual Research Journal, Vol. V
Electrical Engineering Research Experience for Undergraduates

ISBN 0-913260-07-X (http://www.ee.psu.edu/reu/)

Annual Research Journal, Vol. V
Electrical Engineering Research Experience for Undergraduates

ISBN 0-913260-07-X (http://www.ee.psu.edu/reu/)

PRELIMINARY DESIGN OF THE NITTANYSAT LANGMUIR PROBE EXPERIMENT

Adam Escobar* and Sven G. Bilén[#]

Department of Electrical Engineering
The Pennsylvania State University
University Park, PA, 16802

*Summer Student Intern of the
Department of Electrical Engineering
The Pennsylvania State University
University Park, PA, 16802

ABSTRACT

The purpose of NittanySat is to investigate the high latitude D-region of the ionosphere and its effects on radio frequency communications. This is accomplished by monitoring three science phenomena: radiowave absorption, the local plasma environment, and the energetic particle flux. The Langmuir probe experiment measures the local plasma environment and determines the following characteristics: plasma potential, electron density, electron temperature, and mean ion density.

Orbital motion limited theory is applied, where the probe radius is much smaller than the Debye length of the local plasma. The probe geometry is similar to that of the Dynamic Explorer-2 and Pioneer Venus Orbiter satellites, except for some minor improvements. The composition is brass with gold plating, which allows for a low work function. To clean the surface of the probe due to any contamination, high voltage will be utilized.

1.0. INTRODUCTION

NittanySat is a student nano-satellite project that is part of the University Nano-Satellite-5 Program sponsored by the Air Force Research Laboratory and Space Vehicles Directorate (AFRL). In this program, NittanySat is the Pennsylvania State University project. Penn State is one of eleven universities competing for an orbital launch. Each university has to develop a functional nano-satellite by use of system engineering principles.

[#] Faculty supervisor

Annual Research Journal, Vol. V
Electrical Engineering Research Experience for Undergraduates

ISBN 0-913260-07-X (http://www.ee.psu.edu/reu/)

The purpose of NittanySat is to investigate the high latitude D-region of the ionosphere and its effects on radio frequency communications. The payload is designed to be in a polar low earth orbit (90° inclination) at an altitude of optimally 800 km. The mission is accomplished by monitoring three science phenomena: radiowave absorption, the local plasma environment, and the energetic particle flux. The RF Absorption experiment determines the radiowave absorption. The Langmuir probe experiment finds the local plasma environment characteristics, and Energetic Particle Detectors measures the energetic particle flux.

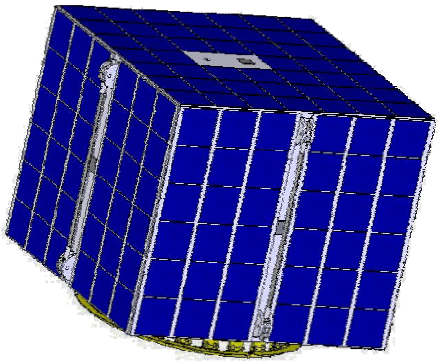

Fig. 1 – Model of NittanySat.

The earth's ionosphere is composed of free electrons and positive ions. This is caused by solar radiation. The Langmuir probe experiment measures the plasma potential, electron density, electron temperature, and mean ion density. The fundamental concept is to bias a voltage on a conductor with respect to the spacecraft. Depending on the voltage bias, the conductor will collect electrons or positive ions (*See Fig. 2*). Knowing the conductor geometry and the current associated with the charged particle collection, the plasma characteristics can be found.

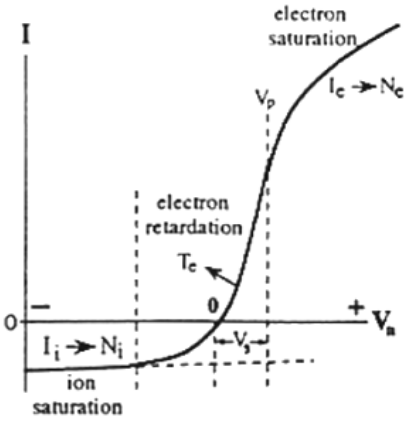

Fig. 2 – Langmuir Probe I-V relationship [3].

Annual Research Journal, Vol. V
Electrical Engineering Research Experience for Undergraduates

ISBN 0-913260-07-X (http://www.ee.psu.edu/reu/)

2.0. PROBE DESIGN

The probe design is based on orbital motion limited (OML) theory. This theory drives the probe geometry, where the probe radius is much smaller than the Debye length, λ_d, of the local plasma.

2.1. Probe Radius

To find the Debye length equation 1 is used with typical plasma values. Since the minimum desired orbit of NittanySat is 600 km and the expected launch is during the solar cycle maximum, typical values from this altitude and solar cycle were used: electron density, N_e, of 5 x 10^{11} m^{-3} and electron temperature, T_e, of 2900 K [2].

$$\lambda_d = \sqrt{\frac{\varepsilon_0 k T_e}{N_e e^2}} \qquad (1)$$

where

ε_o = permittivity of free space
k = Boltzmann constant
T_e = electron temperature
N_e = electron density
e = elementary charge

Solving this equation gives a Debye length of 5.3 mm. To find a suitable probe radius, a series of values of probe radii were calculated in table 1. The probe diameter chosen was between the 1/3 λ_d and 1/4 λ_d values at a diameter of 3.175 mm (0.125 in.). This value is chosen because it is a stock value sold by many distributors. This diameter gives a radius that is approximately 3/10 λ_d.

Table 1 – Used in selection of probe diameter
Probe Diameter vs. Debye Length

Relation to λ_d	Radius [m]	Diameter [m]	Diameter [in.]
1/2 λ_d	0.00265	0.00530	0.2087
1/3 λ_d	0.00177	0.00353	0.1391
1/4 λ_d	0.00133	0.00265	0.1043
1/5 λ_d	0.00106	0.00212	0.0835

2.2. Probe Geometry

The probe geometry used is a cylindrical design (*See Fig. 3*). Using this geometry, the probe radius can remain small enough to be orbital motion limited and long enough to collect a measurable current [3]. This allows for use in high and low densities.

Annual Research Journal, Vol. V
Electrical Engineering Research Experience for Undergraduates

ISBN 0-913260-07-X (http://www.ee.psu.edu/reu/)

To determine the length of the cylinder needed, the length used in Dynamic Explorer 2 (DE-2) was taken as a testing point, since the range of densities in both missions is similar. The length of the collector for DE-2 was 5 cm (approx. 2 in.) [3]. Using orbital motion limited theory in the electron saturation region, electron current, I_e, is related to electron density, N_e, in equation 2. This equation can be solved further.

$$I_e = \frac{2N_e Ae}{\sqrt{\pi}} \sqrt{\frac{kT_e}{2\pi m_e}} \sqrt{1 + \frac{e\left(V_{\text{probe}} - V_{\text{plasma}}\right)}{kT_e}}, \tag{2}$$

where

A = surface area of probe
m_e = electron mass
V_{probe} = probe potential respect to spacecraft
V_{plasma} = plasma potential respect to spacecraft

Since a cylindrical probe was used, the electron temperature, T_e, measurements are not necessary to obtain electron density measurements [3]. The reason for this is due to the fact that

$$\frac{e\left(V_{\text{probe}} - V_{\text{plasma}}\right)}{kT_e} >> 1. \tag{3}$$

For these measurement conditions, the kT_e terms cancel out, and the resulting equation for the electron current is

$$I_e = \frac{AN_e e}{\pi} \sqrt{\frac{2e\left(V_{probe} - V_{plasma}\right)}{m_e}}. \tag{4}$$

The ranges of currents can be found using equation 4 with the typical values: minimum electron density of 1 x 10^{10} m^{-3}, maximum electron density 5 x 10^{11} m^{-3}, minimum probe voltage with respect to the plasma of 0.5 V, and maximum probe voltage with respect to the plasma of 4.5 V. Using the probe length of 5 cm (approx. 2 in.), the probe area was found to be 5.067 x 10^{-4} m^2 (0.7854 $in.^2$); therefore, the current range is from 0.108 μA to 16.256 μA. A 50% margin is needed to ensure measurability. This gives the electron current range:

0.05 μA to 25 μA

Which gives the electron density range of

4.6 x 10^9 m^{-3} to 7.7 x 10^{11} m^{-3}

Annual Research Journal, Vol. V
Electrical Engineering Research Experience for Undergraduates

ISBN 0-913260-07-X (http://www.ee.psu.edu/reu/)

These ranges agree with the electrometer range during the ESPRIT mission. Therefore, similar electronics will be used for the NittanySat mission. The ESPRIT electrometer's range was 0.01 μA to 50 μA, which encompasses this calculated necessary range [1]. With this confirmation, the NittanySat probe geometry is set as a cylinder with a diameter of 3.175 mm (0.125 in.) and a length of 5 cm (2 in.).

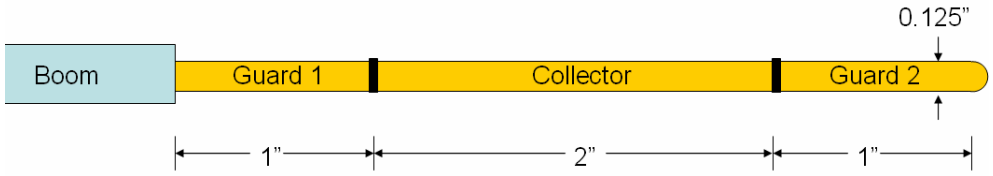

Fig. 3 – Proposed NittanySat Langmuir probe design.

One major concern with probe geometry is "end-effects" of the probe. The electric field of the probe is perpendicular to the surface of the conductor. If only a cylindrical probe was used, then there may be error in the calculations due to an uneven collection of electrons or positive ions. To receive uniform collection, guards are placed on both sides of the cylindrical collector (*See Fig. 3*). With the guards placed at both ends of the collector, the electric field will remain perpendicular to the surface. The guard should be at least 2.5 cm (approx. 1.0 in.) [3].

2.3. Probe Composition

The composition of the probe is an important factor in the design of the experiment, because of its interaction with the surrounding environment. There are several factors that should be taken into consideration when determining the composition: work function, conductivity, oxidation, and price.

Three materials of high work functions were compared: gold, nickel, and platinum (*See Table 2*). DE-2 utilized Rhenium probes; however, this material is not naturally found in nature and costs are very expensive to manufacture [3]. Rhenium is not a top candidate in this trade study due to its excessive cost.

Gold is selected as the best element to use. This element has the second best work function, highest conductivity, non-oxidizing, and is the second cheapest. Platinum is another ideal material; however, the cost is too much when weighed against its performance. Nickel will degrade due to exposure to atomic oxygen in the ionosphere. Gold has been used on the ESPRIT mission, and the preliminary data analysis has shown similar results to the ground based measurements [1].

Annual Research Journal, Vol. V
Electrical Engineering Research Experience for Undergraduates

ISBN 0-913260-07-X (http://www.ee.psu.edu/reu/)

Table 2 – Comparing gold (Au), nickel (Ni), and platinum (Pt) element characteristics.

Probe Composition Trade Study

Material	Work Function [eV]	Conductivity [Ω^{-1} cm^{-1}]	Oxidation	Price*
Gold	5.1	0.45	no	2
Nickel	5.01	0.14	yes	1
Platinum	6.35	0.1	no	3

*Price is ranked from lowest (1) to highest (3) in cost per unit weight – exact prices vary

The only problem is gold will be too expensive and stock of the necessary diameter is hard to find. Therefore, plating gold over a cheaper and more available material is the best solution. ESPRIT used brass as the material for the primary structure of the probe [1]. Brass provides good mechanical support and conductivity. There are two issues found with gold plating any copper alloy: degrades hardness and non-oxidizing properties [4]. The main issue is the non-oxidizing property. If the probe oxidizes, this allows for particles to leave the surface and an oxidation layer will be form on the surface of the probe. This creates errors in the measurement. To preserve the properties of gold, the brass is plated with electroless nickel then gold [4]. The nickel layer does not allow the gold to interact chemically with the brass. A current investigation is determining if stainless steel can be used instead of brass.

3.0. ELECTRICAL INSTRUMENT DESIGN

The electrical design of the instrument is similar to the electrical design on ESPRIT. The instrument block diagram can be seen in *Fig. 4*. The primary components are: the probe, the electrometer, voltage bias circuitry, and data processing.

3.1. Electrometer

The purpose of an electrometer is to convert a current into a voltage. The electrometer will utilize a logarithmic amplifier and instrumentation amplifier. The logarithmic amplifier is used due to the large range of currents experienced from the probe (*See Section 2.2. Probe Geometry*). This logarithmic amplifier needs to have input bias currents much smaller than the measurements, and the measurements need resolution as small as the nano-amp, nA. The logarithmic amplifier used on ESPRIT had input bias currents on the order of femto-amps, fA. The instrumentation amplifier is used to measure the small scale changes from the logarithmic amplifier and provide a gain to allow for a measurable voltage.

Annual Research Journal, Vol. V
Electrical Engineering Research Experience for Undergraduates

ISBN 0-913260-07-X (http://www.ee.psu.edu/reu/)

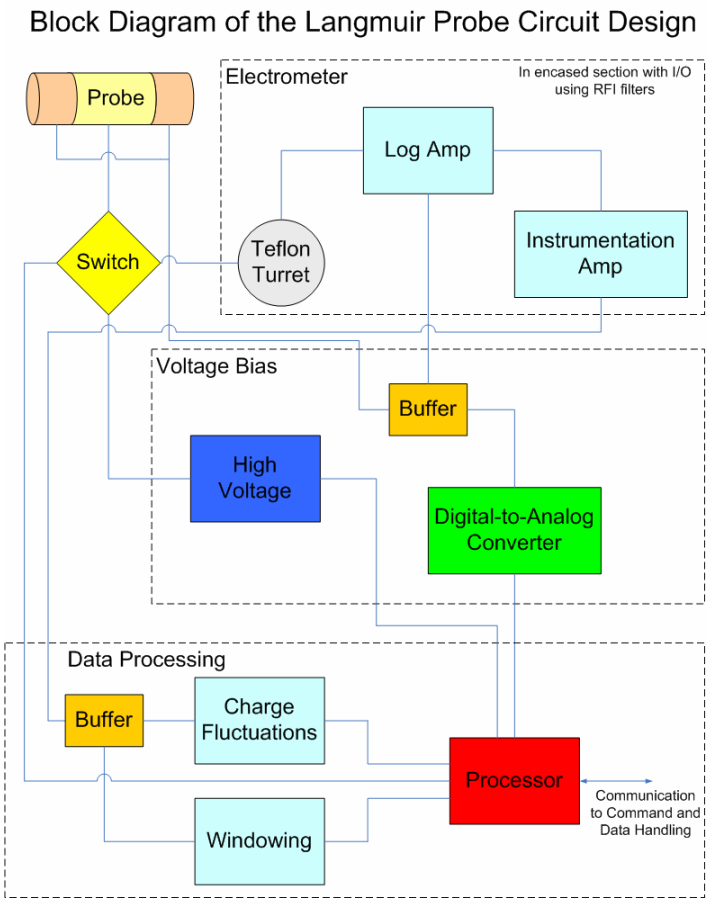

Fig. 4 – Block diagram of the Langmuir probe design.

The Teflon turret seen in *Fig. 4* allows for impedance matching between the probe and the electrometer. To account for radio frequency interference (RFI), RFI filters are panel mounted on the aluminum tray. All inputs and outputs to the electrometer have these filters. RFI is a major issue when measuring at these small values.

3.2. Voltage Bias

The voltage bias can be programmed to any sort of function. The bias can sweep between the ion saturation and electron saturation regions of the I-V curve, or a constant voltage can be applied to have a high spatial resolution. This operation is accomplished by the digital-to-analog converter (DAC).

High voltage (HV) is needed to clean the probe surface of any contamination [3]. Contamination can occur even after the probe is cleaned and placed on the launch vehicle. Outgassing or other particulate matter can be deposited on the probe surface during launch or after. The solution is to heat the probe, and this can be done by using a heating element. This method uses plenty of power, and an alternate method is to use high voltage. Depending on the

Annual Research Journal, Vol. V
Electrical Engineering Research Experience for Undergraduates

ISBN 0-913260-07-X (http://www.ee.psu.edu/reu/)

voltage bias, the high voltage allows electrons or positive ions to bombard the probe and clean the surface. A 150 V bias over one orbit was used on the DE-2 spacecraft to clean the probe surface [3].

3.4. Data Processing

The data processing circuitry includes monitoring for charge fluctuations, windowing, and processing. The charge fluctuations are determined by use of a high pass filter. Filtering out the DC component allows for any small scale fluctuations to be found. Gain in this stage is adjusted by a digital potentiometer. Gain can swing from unity to a higher value.

The windowing circuitry includes a gain stage similar to the charge fluctuation stage. Digital potentiometers will adjust the gain of the windowing stages. The purpose of this stage is to allow for better resolution of the electrometer output.

Prior to converting the analog signals to a digital value, anti-aliasing filters will be designed to prevent aliasing due to sampling. Then the analog signal will go to an analog-to-digital converter (ADC). The processor controls all processes in the instrument and provides external communication.

REFERENCES

1. Escobar, Adam C., Bilén, Sven G., and Philbrick, C. Russell. "Preliminary Langmuir Probe Analysis from ESPRIT". 18th ESA Symposium. 2007.
2. Jursa, Adolph S., *Handbook of Geophysics and the Space Environment,* Chapters 9 and 10, Air Force Geophysics Laboratory, 1985.
3. Brace, Larry H., "Langmuir Probe Measurements in the Ionosphere," in *Measurement Techniques in Space Plasmas: Particles*, American Geophysical Union: Monograph 102, 1998.
4. Mil-G-45204C. "Electro-plating Gold".

Annual Research Journal, Vol. V
Electrical Engineering Research Experience for Undergraduates

ISBN 0-913260-07-X (http://www.ee.psu.edu/reu/)

NONLINEAR OPTICAL FIBER IMAGING ARRAY FOR PASSIVE PULSED LASER SWITCHING AND SENSOR PROTECTION

Kathryn Greenberg*, Michael Stinger[+], Andres Diaz[#], and Iam Choon Khoo[#]

Department of Electrical Engineering
The Pennsylvania State University
University Park, PA 16802

*Undergraduate student of
Department of Physics
Mount Holyoke College
South Hadley, MA 01075

ABSTRACT

A passive imaging system for pulsed laser sensor protection was designed, tested, and characterized. Both bulk cells and fiber arrays with different limiting media were tested throughout the study. These provide a nonlinear optical response which is enhanced by focusing the beam through an input lens. Furthermore, in the case of a fiber array, the interaction length is increased to several millimeters by beam confinement. Strong laser pulses with incident energies in the range of μJ-mJ are limited to a threshold that is safe to the eye. This paper addresses a device that can protect against a variety of different lasers (sub picosecond to continuous wave) in the visible and the infrared. Finally, the imaging and limiting capabilities of this device are discussed.

INTRODUCTION

Lasers are used in a variety of different settings from military to communication applications. It is important that any sensors used (or the eye) be protected from accidental or intentional exposure to prevent temporary or permanent damage. Sensors, or the eyes, can be greatly affected by both

[+] Graduate Mentor
[#] Faculty Mentor

Annual Research Journal, Vol. V
Electrical Engineering Research Experience for Undergraduates

ISBN 0-913260-07-X (http://www.ee.psu.edu/reu/)

continuous-wave and pulsed beams produced by various types of lasers. Even lasers with only moderate power can be of great concern because the eye takes the light and focuses it down to a small spot size on the retina[1]. The usual damage threshold of sensors is about one joule per square centimeter. If the entrance area to the sensor (or eye) is 1 cm^2 with a gain of 10^6, the maximum exposure ($\approx$1 μJ) is a fraction of the energy that a pulsed laser emits [2]. This can cause anywhere from temporary loss of vision to permanent damage of the retina. Infrared and ultraviolet lasers are even more dangerous because the eye does not realize that they are present and therefore cannot react. For lasers where the wavelength is known, filters can be used to protect the sensor. However, these filters are of little use when it comes to lasers that can span a large range of wavelengths. Filters have been designed that can be tuned depending on the wavelength, but they only offer protection from continuous waveform lasers at a certain wavelength. Q-switched lasers can have very strong pulses that last for as little as a few picoseconds. Therefore it is important that protection can be provided for these pulses at a variety of different wavelengths.

An optical limiting material that is able to protect the sensor should be transparent for low inputs of light and become less transparent as the intensity of the light is increased. This decrease in transparency allows for protection of the sensor against a dangerous laser beam [2]. Much research has been done to find materials and design devices that are able to accomplish this optical limiting performance [3-4]. In particular, liquid crystals [5] and other organic liquids that exhibit nonlinear behavior have been used. These posses reverse saturable absorption (RSA), two-photon absorption (TPA), and excited-state absorption (ESA) properties that have been shown to be effective [6-8]. Our purpose in this paper is to design an imaging limiting device which uses optically nonlinear liquids. In addition, we also optimized the response of the device by using a fibber array instead of the nonlinear liquid bulk.

Nonlinear Optical Mechanisms and Laser-Pulse Beam Propagation Through a Fiber Array

Fiber arrays consist of an array of fiber cores surrounded by a common cladding. In our case, these arrays are formed by filling capillary arrays with a nonlinear liquid. If a laser is fired at the system, the input optics will focus the laser into one (or more) of the fiber arrays. The fiber uses total internal reflection, determined by the difference in the refractive indices of the core (nonlinear liquid) and cladding, to guide the light to the opposite end of the fiber. Hence, within each fiber, the interaction length between the light and the nonlinear liquid is increased to the length of the fiber array (several millimeters), as compared to an interaction length on the order of tens of microns if only a cell with liquid bulk is used. The length of the fiber arrays used is typically 2-5 mm, with cores of 25 micron diameter.

There are several limiting mechanisms that take place inside of the fiber array as shown in Figure 1. At very high intensities, bubbles begin to form and

Annual Research Journal, Vol. V
Electrical Engineering Research Experience for Undergraduates

ISBN 0-913260-07-X (http://www.ee.psu.edu/reu/)

nonlinear scattering and self defocusing take place, aiding the overall limiting effect.

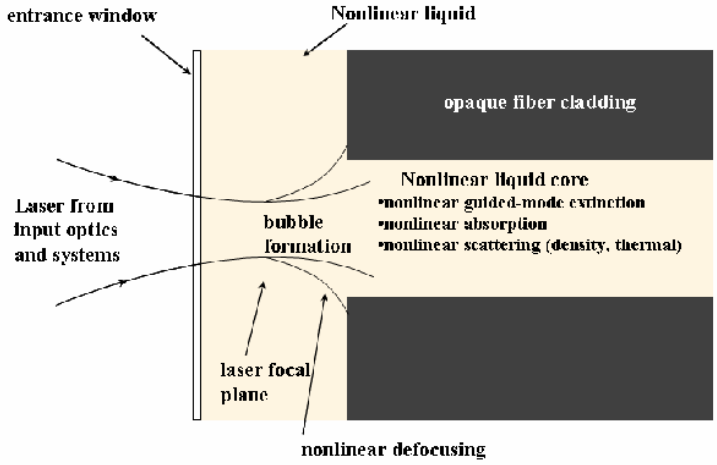

Figure 1: Nonlinear optical limiting mechanisms in fiber array

Two-photon absorbers are particularly effective as limiters since they are transparent at low intensities and become more opaque as the intensity increases. We used nonlinear organic L34 [9] developed at Pennsylvania State University's Chemistry Department. The L34 structure and absorption spectrum are shown in Figure 2.

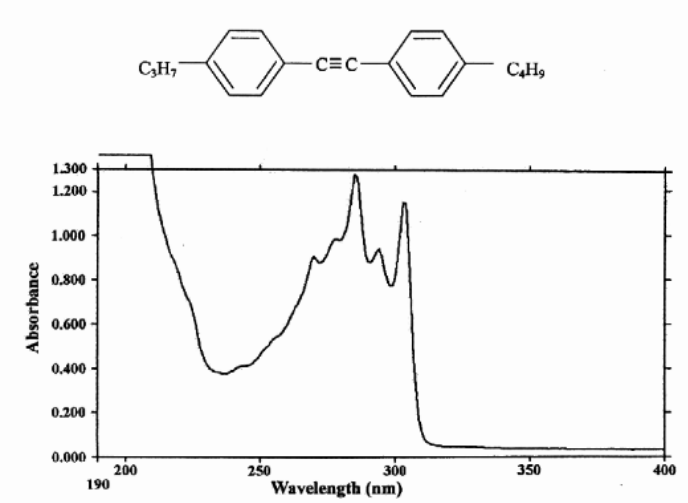

Figure 2: Structure and absorption spectrum for L34

L34 is a transparent organic material that is known to exhibit nonlinear properties. This liquid exhibits both TPA and higher ESA processes. The most significant of these nonlinear properties is two photon absorption as shown in

Annual Research Journal, Vol. V
Electrical Engineering Research Experience for Undergraduates

ISBN 0-913260-07-X (http://www.ee.psu.edu/reu/)

Figure 3. Two photon absorption is a process where a molecule absorbs two photons at the same time and can therefore attain an excited state that would have been impossible to reach by single photon absorption from the ground state (N_1). The excited molecule will then decay to energy level N_5 with decay rate $\tau_2 \approx 1$ ns. The limiting process continues as a photon can be absorbed taking the molecule from energy level N_5 to N_3. The molecule can decay from the high-lying electronic state N_3 back to N_5 with decay rate $\tau_3 \approx 1$ps. Due to τ_3 being so small, there will be plenty of molecules in N_5 to continue the limiting process [10]. As a result of the strong nonlinear effect in L34, the amount of light that gets absorbed increases as the number of photons entering the system increases while the output stays below a certain threshold.

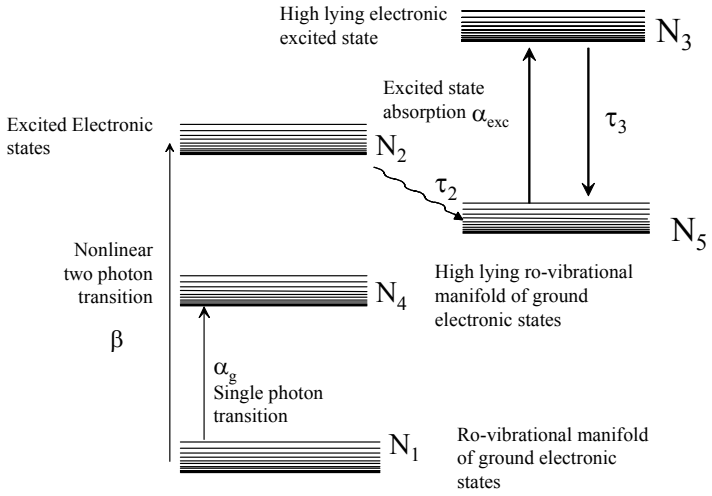

Figure 3: L34 two photon absorption energy level diagram

EXPERIMENTAL SETUP

Imaging

A portable imaging system has been designed in several steps to characterize the imaging and limiting capabilities of the organic material L34. The first part of the research dealt with the imaging capabilities of the designed device described below. For all of the imaging devices a rail system was used to align the different components of the device. The first setup designed for this imaging is shown in Figure 4. It consists of two 16mm lens arrays that have adjustable aperture size and focus. A HeNe laser was used to align the two lens arrays and ensure that a clear image would be obtained. By looking at the change in the spot size of the laser beam after passing through the setup the correct z-position of the lens arrays could be obtained. The resulting output beam was collimated.

Annual Research Journal, Vol. V
Electrical Engineering Research Experience for Undergraduates

ISBN 0-913260-07-X (http://www.ee.psu.edu/reu/)

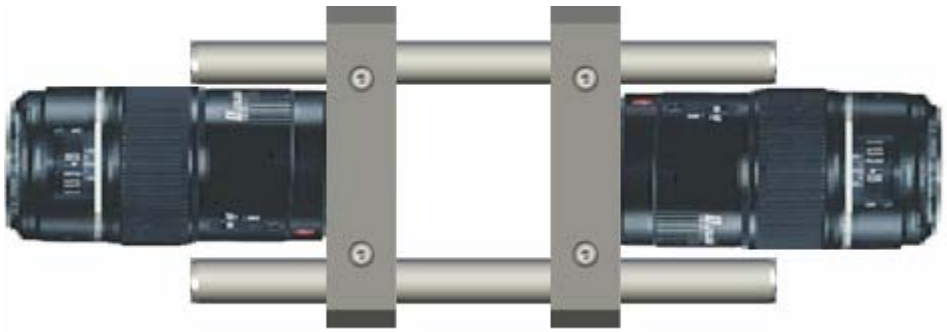

Figure 4: Experimental setup without sample using 16mm focus lens arrays

The second imaging setup consisted of the same two 16mm lens arrays as well as a piece to hold bulk nonlinear material (CE10). This setup is shown in Figure 5. A glass slide was attached to a 2 mm thick piece of plastic that had a 10 mm diameter hole cut in the center of it. The plastic piece was filled with CE10 and another glass slide was attached to hold the nonlinear material in. The organic material was then placed in between the two lens arrays and imaging was done through the system.

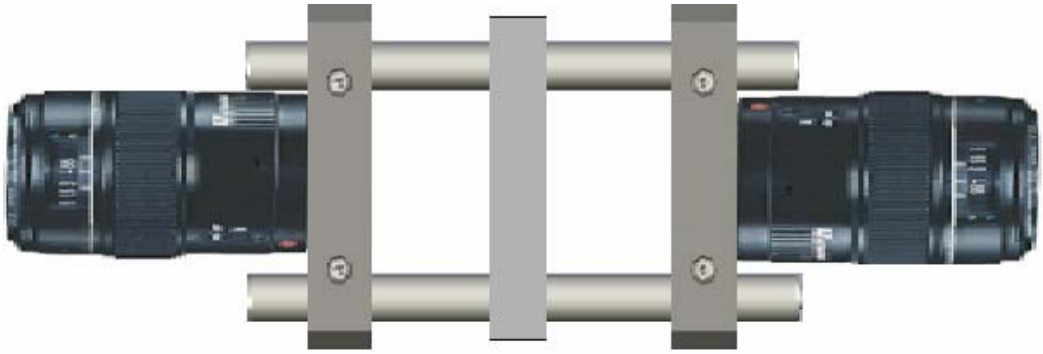

Figure 5: Experimental setup with two 16mm lens arrays and CE10 nonlinear sample

An imaging system using fiber arrays was also developed. The sample used a 2 mm thick plastic piece with a 10 mm hole cut in the center along with two glass slides as shown in Figure 5. Instead of filling the piece only with L34, a fiber array was placed in it and then L34 was added.

Limiting

The limiting experiments were done using a tunable pulsed Alexandrite laser at a wavelength of 750nm. The setup is shown in Figure 6. A HeNe laser was initially used to ensure that all the components were aligned correctly. Light traveling from the Alexandrite laser passed through two polarizers which were used to adjust the amount of light that would reach the sample. The first polarizer was adjusted during the experiments to change the amount of incident light. A

Annual Research Journal, Vol. V
Electrical Engineering Research Experience for Undergraduates

ISBN 0-913260-07-X (http://www.ee.psu.edu/reu/)

glass slide was used to reflect part of the beam to a photodetector so that the initial energy of the beam could be measured. The glass slide reflects part of the pulsed laser beam and the other part gets transmitted through to a lens that collects the light and focuses the image inside the sample. The light then travels through the sample and into a detector which measures the output energy. This setup allows measurements to be made about how well different materials limit the amount of light that passes through them.

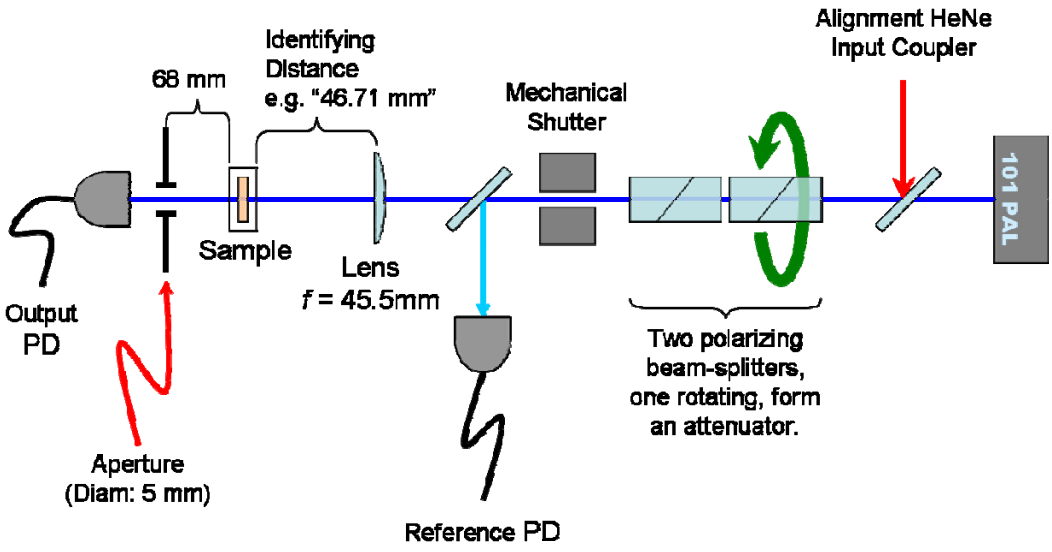

Figure 6: Experimental setup for limiting experiments using pulsed Alexandrite laser and 45.5mm focus length lens (PD refers to photodiode and 101 PAL indicates the input laser)

RESULTS AND DISCUSSION

Figure 7 shows an image through two 16mm lens arrays with no sample between them. The picture is very clear and small details can be seen through the device. The original image was upside-down due to the geometric optics of the two lens array system but in Figure 7 the photo has been flipped.

Another picture was taken with the nonlinear material CE10 placed in between the two lens arrays. Figure 8 is the image through the device with the CE10 sample in place. The image was again upside down due to the geometric optics and was flipped in Figure 8. This image is very clear and small details can be made out in the picture. From the absorption characteristics of CE10, the image acquires a very faint yellowish tint, but otherwise did not seem to have a noticeable effect on the color or sharpness of the image, or on the overall transmittance of the device.

Annual Research Journal, Vol. V
Electrical Engineering Research Experience for Undergraduates

ISBN 0-913260-07-X (http://www.ee.psu.edu/reu/)

Figure 7: Flipped image obtained through two lens arrays

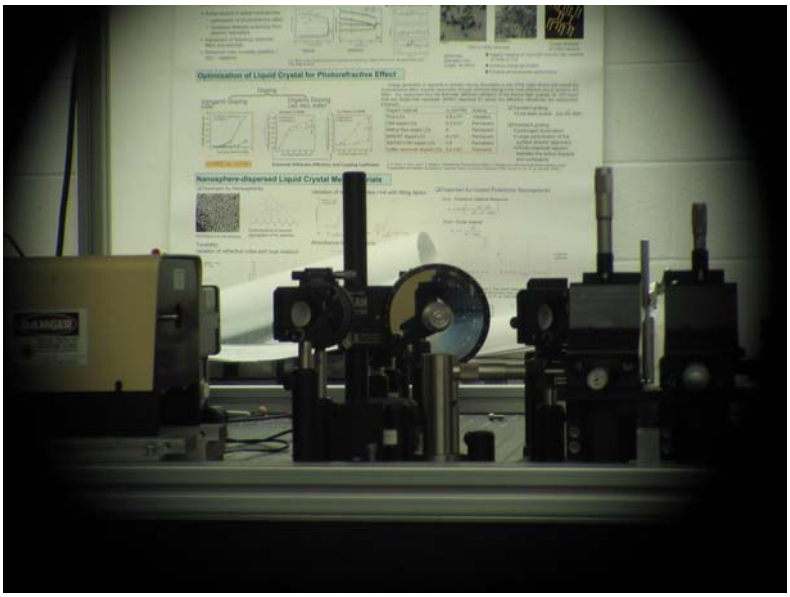

Figure 8: Flipped image obtained through two lens array system containing CE10 sample

An image through a fiber array, with input and output optics similar to that used in the previous two images, is shown in Figure 9. The image taken through the fiber array is darker than the area that does not pass through the fiber array. While the image is darker it does not completely block out an object on the other side.

Annual Research Journal, Vol. V
Electrical Engineering Research Experience for Undergraduates

ISBN 0-913260-07-X (http://www.ee.psu.edu/reu/)

Figure 9: Image through a fiber array filled with a nonlinear material

The limiting experiments were carried out for several different nonlinear liquids in bulk inside a 2mm thick cuvette using a pulsed Alexandrite laser operating at 750nm. The pulses during the experiment were monitored using an oscilloscope and had a duration of approximately 350 ns, as shown in Figure 10. To measure the intensity of the incident beam, part of the beam was reflected off a slide and its energy measured by a detector, and the ratio of the reflected to transmitted energy was measured as shown in Figure 11. Data was collected when the samples were placed at two positions close to the focus of the 45.5 mm lens.

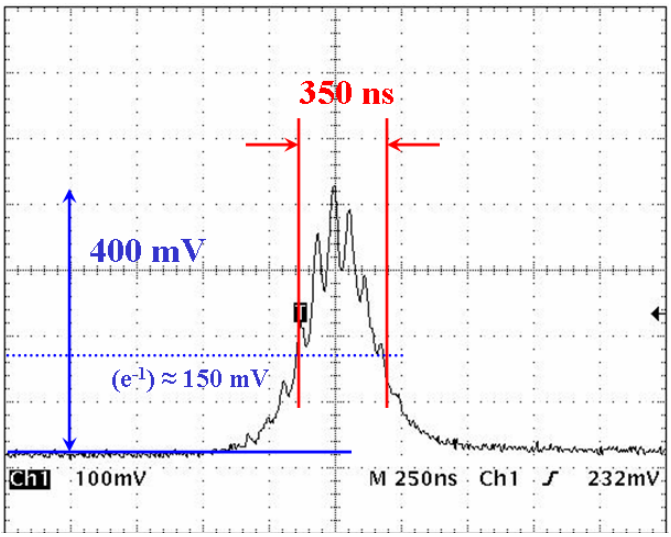

Figure 10: Pulse length from q-switched Alexandrite laser

Annual Research Journal, Vol. V
Electrical Engineering Research Experience for Undergraduates

ISBN 0-913260-07-X (http://www.ee.psu.edu/reu/)

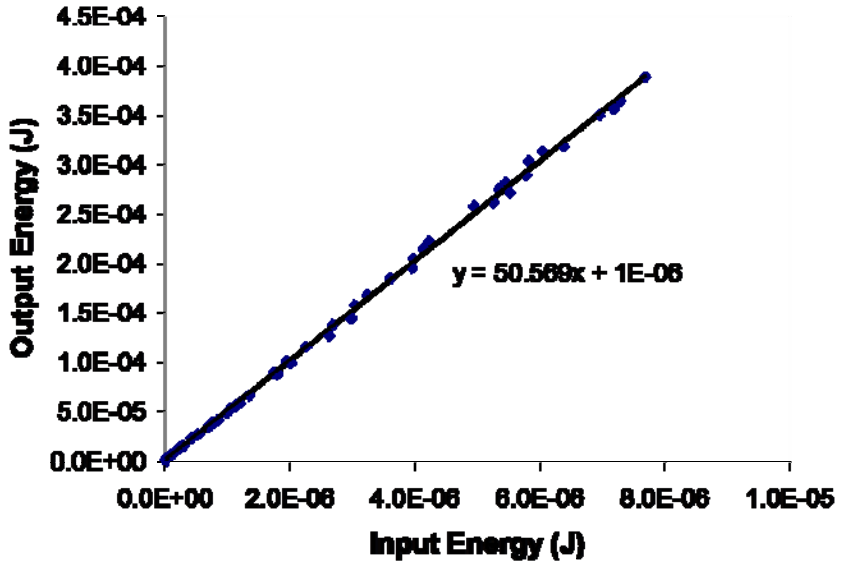

Figure 11: Linear relationship between the reflected (input) versus the transmitted (output) energy on a slide, used to determine the energy incident on the sample

Limiting experiments were done for the bulk organic material L34. Figure 12 shows the input energy versus output energy for the sample at two different positions.

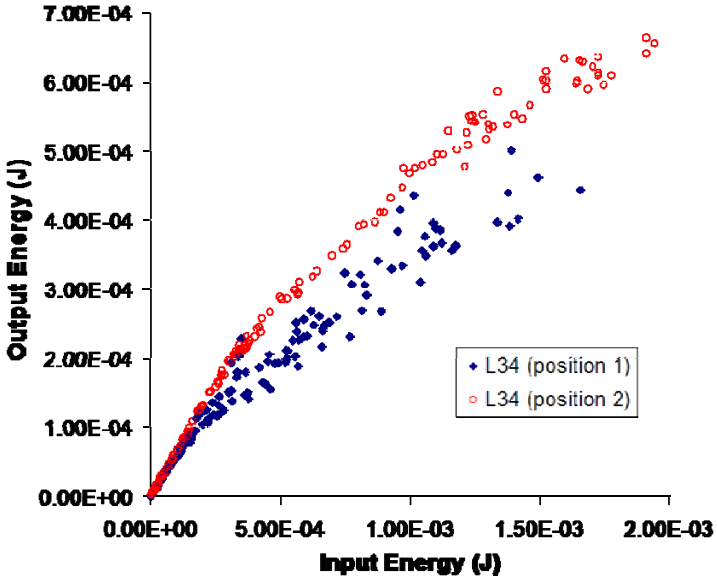

Figure 12: Input energy versus output energy with L34 bulk material in two different positions

Annual Research Journal, Vol. V
Electrical Engineering Research Experience for Undergraduates

ISBN 0-913260-07-X (http://www.ee.psu.edu/reu/)

When the sample was at position 1 the L34 bulk material limited slightly better than when the sample was placed at position 2. This was due to several factors including the intensity of the beam, where exactly in the cuvette the beam was focusing, and the nonlinear processes that took place in the material (RSA, TPA, ESA). The two curves in Figure 12 are very similar to each other and both limit at energies much higher then what is safe for a sensor.

Figure 13 shows the limiting experiment done with a sample of L34 doped with 2.5 nm gold nano particles. Doping the organic material allows for the beam to be scattered more when it travels through the sample and therefore reduces the amount of energy that passes through the sample. In Figure 13 the sample that was placed at position 2 limited better than the sample that was placed at position 1. This was again due to several factors that depended on where the focusing was taking place in the sample, nonlinear effects, and the linear and nonlinear absorption coefficients among other things.

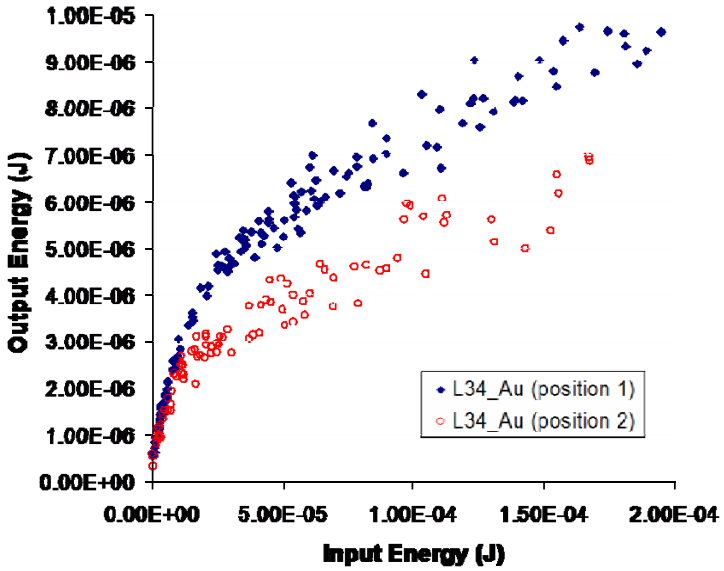

Figure 13: Input energy versus output energy with L34 doped with 2.5 nm gold nano particles at two different positions

There were several features in all of the various graphs that were very similar regardless of what type of sample was present. The first similarity was that for low input energies, the transmission is linear as shown in Figure 14. When the input energy is high enough (reaches a threshold), the transmission decreases and the output energy levels off.

Annual Research Journal, Vol. V
Electrical Engineering Research Experience for Undergraduates

ISBN 0-913260-07-X (http://www.ee.psu.edu/reu/)

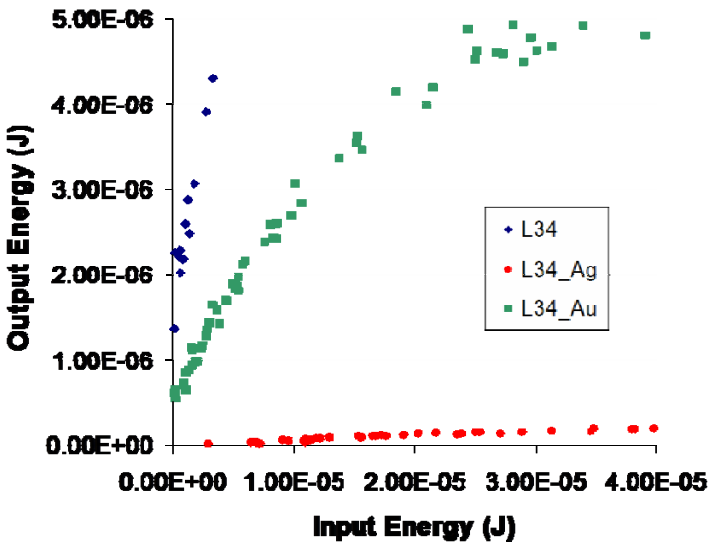

Figure 14: Low input energies for L34, L34 doped with silver nano particles, and L34 doped with gold nano particles

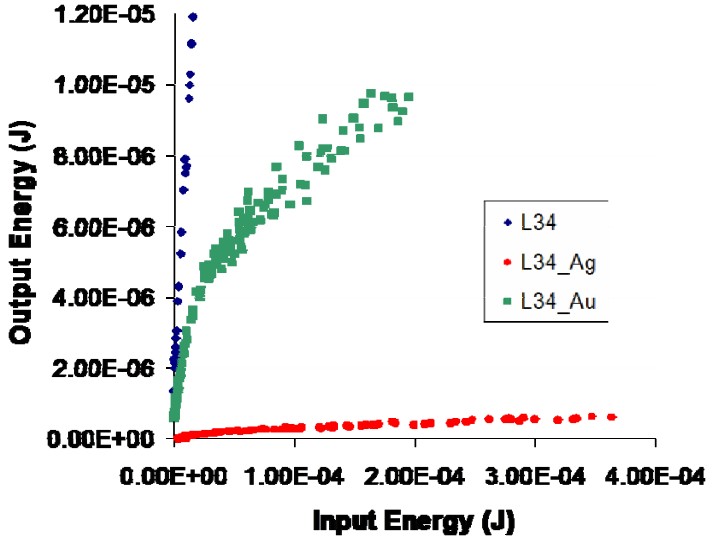

Figure 15: Output energy versus input energy for L34, L34 doped with silver nano particles, and L34 doped with gold nano particles

Figure 15 compares the amount of limiting that took place in the L34 bulk material, the L34 doped with silver nano particles sample, and the L34 doped with gold nano particles. The L34 doped with silver nano particles limited better (showed a lower threshold) than both the bulk L34 and the L34 doped with gold nano particles. The L34 doped with silver nano particles limited to a threshold

Annual Research Journal, Vol. V
Electrical Engineering Research Experience for Undergraduates

ISBN 0-913260-07-X (http://www.ee.psu.edu/reu/)

($\approx 1.00 \times 10^{-6}$ J) that would be safe for a sensor such as eyes. The L34 doped with gold also limited the high intensity laser pulse, although not to a threshold that would be safe for a sensor.

CONCLUSION

Overall, it was shown through both the imaging and limiting experiments that an effective device to limit powerful laser pulses is possible. The imaging experiment provided a device that was small and portable as well as able to provide a sharp picture when imaged through. The image taken with the nonlinear CE10 sample in the device illustrated that there was no noticeable effect with the material present. The limiting experiments showed that the organic material L34 doped with 4.5 nm silver particles limited better than the L34 doped with gold and the L34 bulk material. It limited to a threshold that used in a device could prevent the damage done by a pulsed laser. Nonetheless, this greater limiting comes at the expense of a much lower linear transmission. Hence, gold-doped L34 may prove to be a better candidate for a limiting device, since the limiting threshold may be lowered when the interaction length is increased to several millimeters when used in a fiber array configuration. These results will be shown in a future article.

ACKNOWLEDGEMENT

Thank you to Dr. Ruyan Guo, Dr. Kenneth Jenkins, and Mrs. Linda Becker for organizing the 2007 Research Experience for Undergraduate program at Penn State University. I would also like to thank Dr. Khoo for giving me the opportunity to work in his lab for nine weeks. Lastly, thank you to Mike Stinger, Andres Diaz, Justin Liou, and Junbin Huang for all of their help and guidance this summer.

This material is based upon work supported by the National Science Foundation under Grant No. EEC-0244030.

REFERENCES

[1] American National Standards Institute, Inc., *ANSI Standard Z136.1* for the Safe Use of Lasers, Z136.1, New York (2000).

[2] I.C. Khoo, A. Diaz, J. Ding, "Nonlinear-Absorbing Fiber Array for Large-Dynamic-Range Optical Limiting Application Against Intense Short Laser Pulses," *J. Opt. Soc. Am.* B **21**, 1234-1240 (2004).

[3] C.W. Spangler, Recent Development in the Design of Organic Materials for Optical Power Limiting," *J. Mater. Chem.* **9**, 2013-2020 (1999).

[4] R.L.Sutherland, M.C. Brant, D. M. Brandelik, P.A. Fleitz, D. G. McLean, T. Pottenger, "Nonlinear Absorption Study of a C_{60}-Touene Solution," *Opt. Lett.* **18**, 858-860 (1993).

[5] I.C. Khoo. *Liquid Crystals: Physical Properties and Nonlinear Optical Phenomena.* John Wiley & Sons, Inc. New York, NY (1995).

Annual Research Journal, Vol. V
Electrical Engineering Research Experience for Undergraduates

ISBN 0-913260-07-X (http://www.ee.psu.edu/reu/)

[6] M. Brunel, F. Chaput, S. A. Vinogradov, B. Campagne, M. Canva, J.P. Boilot, A. Brun, "Reverse Saturable Absorption in Palladium and Zinc Tetraphenyltetrabenzoporphyrin Doped Xerogels," *Chem. Phys*. **218**, 301-307 (1997).

[7] G. S. He, G. C. Xu, P. N. Prasad, B. A. Reinhardt, J. C. Bhatt, and A. G. Dillard, "Two-photon Absorption and Optical-limiting Properties of Novel Organic Compounds," *Opt. Lett*. **20**, 435-437 (1995).

[8] T. Xia, D. J. Hagan, A. Dogariu, A. A. Said, and E.W. Van Stryland, "Optimization of Optical Limiting Devices Based on Excited-state Absorption," *Appl. Opt*. **36**, 4110-4122 (1997).

[9] I. C. Khoo, A. Diaz, M. V. Wood, and P. H. Chen, "Passive Optical Limiting of Picosecond-nanosecond Laser Pulses Using Highly Nonlinear Organic Liquid Cored Fiber Array," *IEEE J. Sel. Top. Quantum Electron*. **7**, 760-768 (2001).

[10] A. Diaz. Theory and Applications of Molecular and Collective Nonlinear Optical Behavior of Nematic Liquid Crystals, *PhD Thesis, Penn. State University*, Electrical Engineering Department (2004).

[11] A. Yariv, "The Propagation Rays and Beams"; pp. 55-56 in *Optical Electronics in Modern Communications*, 5th ed. Edited by M.E. Van Valkenburg, New York (1997).

Annual Research Journal, Vol. V
Electrical Engineering Research Experience for Undergraduates

ISBN 0-913260-07-X (http://www.ee.psu.edu/reu/)

Annual Research Journal, Vol. V
Electrical Engineering Research Experience for Undergraduates

ISBN 0-913260-07-X (http://www.ee.psu.edu/reu/)

CARBON DOPED TITANIUM DIOXIDE NANOTUBE ARRAYS

David Grubbs[*], Thomas LaTempa[+], and Craig Grimes[#]

Department of Electrical Engineering
The Pennsylvania State University
University Park, PA 16802

[*]Undergraduate Student of
Department of Physics/Engineering
Lincoln University, PA 19352

ABSTRACT

This project reports the properties of plasma treated titania nanotube arrays. They were modified through RF plasma treatment, in which the plasma is being used for carbon doping into the titanium dioxide. After treating the titanium dioxide nanotube arrays, these samples were tested through ultraviolet visual spectroscopy (UV-Vis), photocurrent measurements, and incident photon conversion efficiency (IPCE) measurements, in order to determine the results of plasma treatment. The plasma conditions were varied with power and exposure time. Acetylene gas was used to strike the plasma and to introduce carbon dopants. Results obtained from measurements were used to analyze the nature of dopant incorporation into the TiO_2 nanotube arrays.

INTRODUCTION

Titanium Dioxide (TiO_2) has been widely investigated for its water photolysis properties. This material can be used as a renewable source of energy in the splitting of water molecules, which generates hydrogen and oxygen. Although the process is stable, efficiencies in solar applications are limited because TiO_2 is a wide band gap material (3.2 eV). This limits its response to the UV spectrum of light. Previous attempts at efficient water splitting focused on the material architecture. Grimes and coworkers developed an approach for

[+] Graduate Mentor
[#] Faculty Mentor

Annual Research Journal, Vol. V
Electrical Engineering Research Experience for Undergraduates

ISBN 0-913260-07-X (http://www.ee.psu.edu/reu/)

making TiO_2 nanotubes which demonstrated enhanced efficiencies[1]. This unique architecture improved conversion efficiencies relative to thermally grown oxide layers, and nanoparticle materials.

Alternatively, several approaches have been made in doping TiO_2 to increase the visible light response of the material. Several approaches, including that of anions, have been investigated. These anions include C, N, F, P, and S for substitutional doping of oxygen to increase the visible light activity of the titanium dioxide material. The most effective anion used for doping has been determined as nitrogen[2]. However, most attempts in raising visible light response with nitrogen were made with limited success. Khan and coworkers have doped TiO_2 using carbon to substitute oxygen atoms instead of nitrogen. In this method controlled combustion of Ti metal was carried out using a natural gas flame[3]. This method of flame annealing proved to be effective for measuring better photocurrent densities.

Carbon doping of titanium dioxide nanotubes has also been studied in an effort to improve visible light activities. Nanotubes have been carbon doped through flame annealing[4] as well as annealing in carbon monoxide[5]. In the present study we use an alternative approach to introduce carbon. Plasma is used to introduce carbon from a source gas (C_2H_2). TiO_2 nanotubes are exposed to plasma under different operating conditions to correlate results. In this study we investigate the effect of doping on the photoelectrochemical properties of titanium dioxide (TiO_2) nanotubes. Plasma conditions are varied with power and exposure time. In plasma irradiation the source gas, C_2H_2 becomes ionized, and the material is bombarded with ions, electrons, and neutral atomic species from the gas. As the nanotubes are bombarded, TiO_2 bonds are expected to break and can be substituted with dopants from the plasma. Plasma treated samples are evaluated using UV-Vis spectroscopy and photocurrent measurements. IPCE measurements are conducted to verify contribution from different wavelengths of light to the overall current.

EXPERIMENTAL DETAILS

Titanium dioxide nanotubes are created through an anodization process in fluorine containing solution. Platinum foil is used as cathode, while titanium is used as an anode in an electrochemical cell. The dimensions of the nanotubes can be controlled including the tube thickness, pore diameter, and overall length. In this case, nanotubes are grown to 6 um in length using a KF based electrolyte previously reported on[6]. Nanotubes form through a balance of anodic oxidation and fluorine etching assisted by an applied bias. According to Mor and coworkers the mechanistic model for nanotube formation is related by the following equations for oxidation:

Annual Research Journal, Vol. V
Electrical Engineering Research Experience for Undergraduates

ISBN 0-913260-07-X (http://www.ee.psu.edu/reu/)

$$2H_2O \rightarrow O_2 + 4e + 4H^+$$

$$Ti + O_2 \rightarrow TiO_2 \quad (1)$$

and,

$$TiO_2 + 6F^- + 4H^+ \rightarrow TiF_6^{2-} + 2H_2O \quad (2)$$

for the simultaneous etching of the oxide layer. Through precise control of the parameters nanotubes can form through this process. The samples were anodized for 17 hours to reach a length of 6 μm. After the anodization process the titanium dioxide nanotubes are amorphous. To improve their water photolysis properties, titanium nanotubes are annealed in oxygen at 580º C to become poly-crystalline. To introduce dopants samples are treated with C_2H_2 plasma. This results in $TiO_{2-x}C_x$ nanotubes. Doped samples are then measured using UV-Vis spectroscopy, which characterizes the absorbance at different wavelengths of light. The response to sunlight is also simulated using photocurrent measurements obtained through a 500W Xenon lamp with filters to obtain comparable intensities of sunlight. To check for doping IPCE (Incident Photon Conversion Efficiency) measurements were taken using a 300W Xenon lamp with a monochromator to measure the current as function of wavelength. Photocurrent measurements and IPCE were measured in 1 M KOH solution.

RESULTS

Figure 1 shows an FE-SEM image of nanotube arrays from the top surface. This is after the process of anodization. After the annealing in oxygen, samples were plasma treated to introduce carbon dopants. UV-visible spectroscopy was used to measure the absorbance of the doped samples as a function of wavelength.

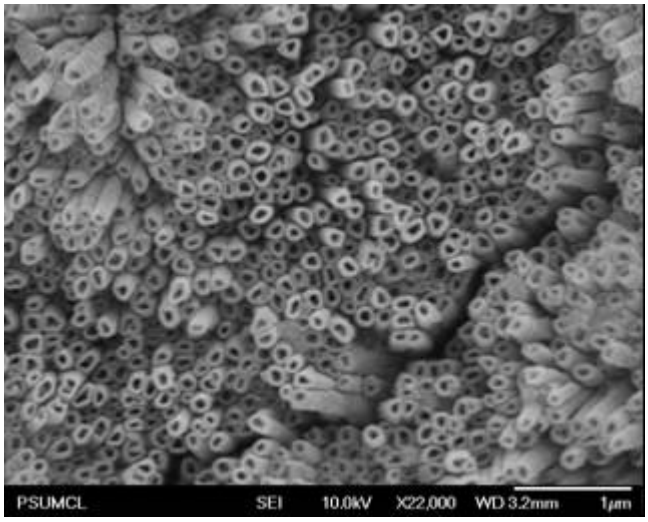

Figure 1: FE-SEM image of TiO_2 nanotube array from the top surface

Annual Research Journal, Vol. V
Electrical Engineering Research Experience for Undergraduates

ISBN 0-913260-07-X (http://www.ee.psu.edu/reu/)

These nanotube arrays are at least 6 μm long, from the titanium surface. After the anodization process, the nanotube samples were plasma treated with carbon and in some cases, reannealed in oxygen for more efficient set of data. These arrays were used to make measurements of the absorbance as a function of wavelength from the UV-visible spectroscopy.

For the UV-visible spectroscopy, the data is as follows:

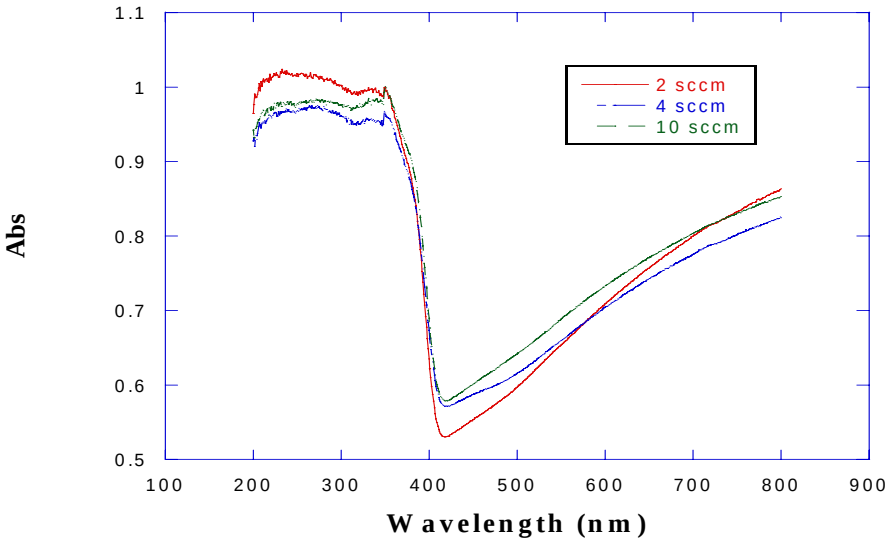

Figure 2: Annealed Samples at Low Concentration

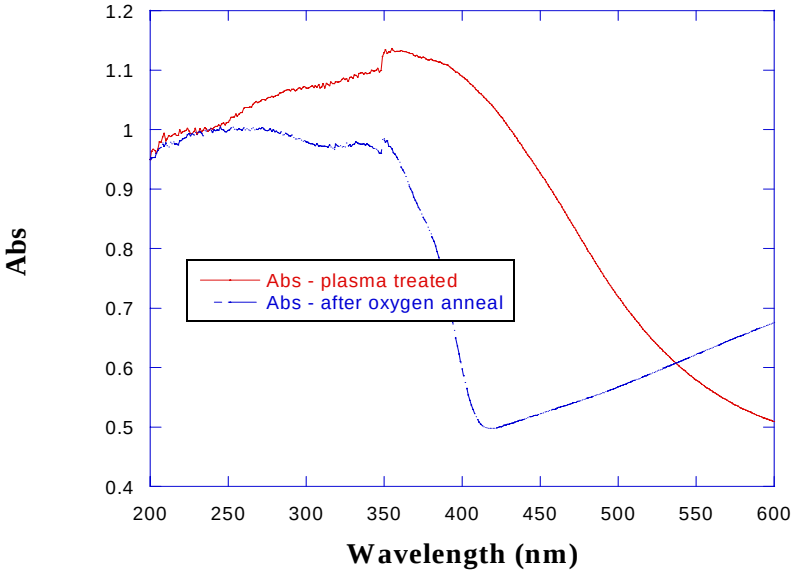

Figure 3: Plasma Treated and Oxygen Annealed Titania Nanotube Array at High Concentration

Annual Research Journal, Vol. V
Electrical Engineering Research Experience for Undergraduates

ISBN 0-913260-07-X (http://www.ee.psu.edu/reu/)

Figure 2 illustrates the profile of the annealed samples when plasma was struck at low concentration. Acetylene was used to strike a plasma in order to break up TiO_2 bonds and dope the nanotubes with carbon. Plasma was struck for about 2- 5 minutes at a low concentration level. The outcome for the absorbance was just about the same for each level of concentration.

For Figure 3, the absorbance for the titanium dioxide nanotube samples was measured at high concentration for about 10-15 minutes at room temperature with an increased power of 60 W. It illustrates one sample which was plasma treated under these conditions, which developed a carbon surface. Because it was on the surface and not bonded to the TiO_2 structure, this won't change the bandgap of the material. Knowing this, the sample was reannealed with oxygen. The purpose is to remove the carbon from the surface and to try to get it to bond to TiO_2 through an additional annealing step. The UV-visible measurement from this step indicates that it burnt off the sample and did not bond to the nanotubes. This is assumed because there was no shift in the spectrum afterwards. Doped samples usually have a second band edge and/or shift into the visible region. To verify these assumptions additional tests were conducted to measure properties of the material while the samples were submerged in a water solution.

The photoelectrochemical properties of the plasma treated nanotubes were characterized by photocurrent measurements, which is an indication of how efficient the material is for water splitting. The diagram of photocurrent measurements is as follows:

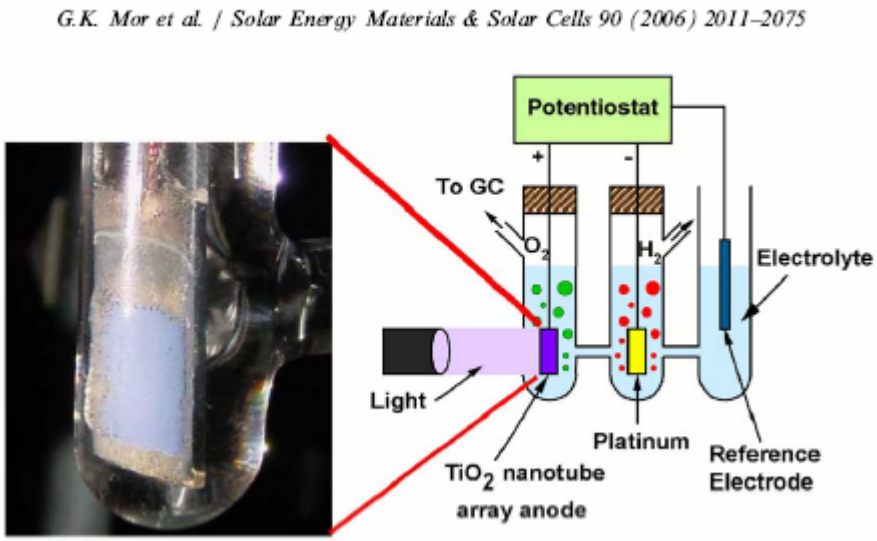

Figure 4: Illustration of Water Photolysis apparatus[7]

Figure 4 shows an illustration of the titanium nanotube samples going through photocurrent measurements[7]. These measurements are used to calculate

Annual Research Journal, Vol. V
Electrical Engineering Research Experience for Undergraduates

ISBN 0-913260-07-X (http://www.ee.psu.edu/reu/)

the titania nanotube sample's efficiency in splitting water molecules. Oxygen forms on the TiO_2, while hydrogen forms on the platinum electrode. The equations for the effect of water photolysis are as follows:

$$\begin{aligned} &2hv(light) \rightarrow 2e^- + 2holes \\ &2holes + H_2O \rightarrow 2H^+ + \frac{1}{2}O_2 \\ &2H^+ + 2e^- \rightarrow H_2 gas \end{aligned} \qquad (3)$$

Overall this leads to,

$$2hv + H_2O \rightarrow \frac{1}{2}O_2(gas) + H_2(gas)\,. \qquad (4)$$

Current is being measured as a function of the potential. In this case, the total current is measured as the difference between the current of the sample with the light source and the dark current, without the light source. The light source is calibrated to 1 sun using a silicon-based, calibrated solar cell, which is certified by the NREL. This creates a light source of equivalent sufficiency to the outdoor sun. Figure 5 shows this for three of the doped titania nanotube array samples.

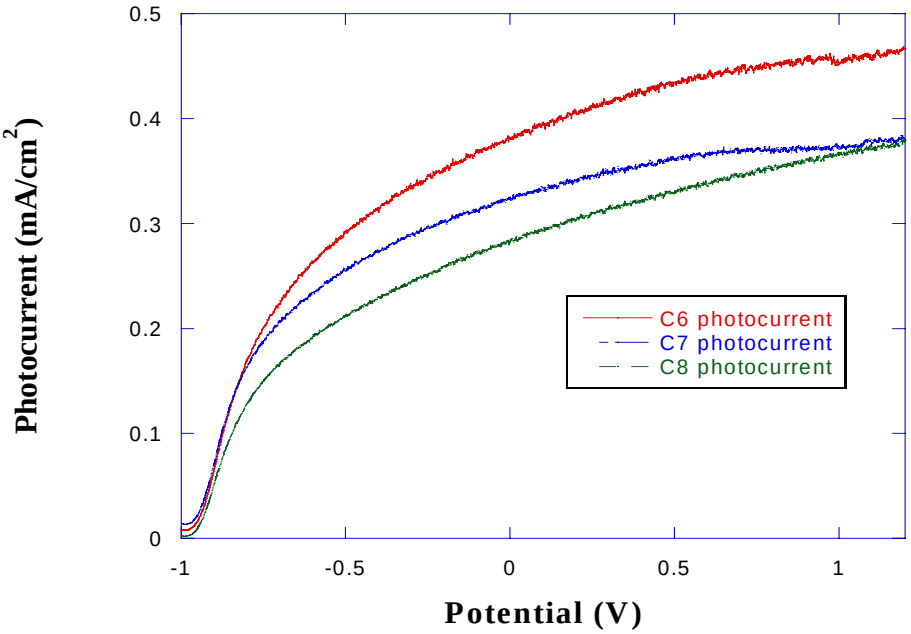

Figure 5: Titania Nanotube Arrays with Measured Photocurrents as Functions to Potential Energy

Annual Research Journal, Vol. V
Electrical Engineering Research Experience for Undergraduates

ISBN 0-913260-07-X (http://www.ee.psu.edu/reu/)

This reaction occurs because of the properties of water photolysis, as explained in the equations above. During photocurrent measurements electron hole pairs are created while illuminated with light, which is of greater energy then the materials bandgap. This leads to charge carriers being generated and contributes to current measurements. The higher the current portrays, the better the sample is for water photolysis.

Incident Photon Conversion Efficiency (IPCE) was also used in this analysis to measure light induced current while submerged in water. Current is measured as a function of wavelength at a constant voltage and to check for increase at visible wavelengths. The equation for this particular measurement is given:

$$IPCE = \frac{(1240 \times I_\lambda)}{(\lambda \times P_\lambda)} \times 100\% \qquad (5)$$

where λ is the incident wavelength and I_λ and P_λ are the corresponding current and power at each wavelength. Figure 6 shows the IPCE measurements of a sample plasma treated at low concentration:

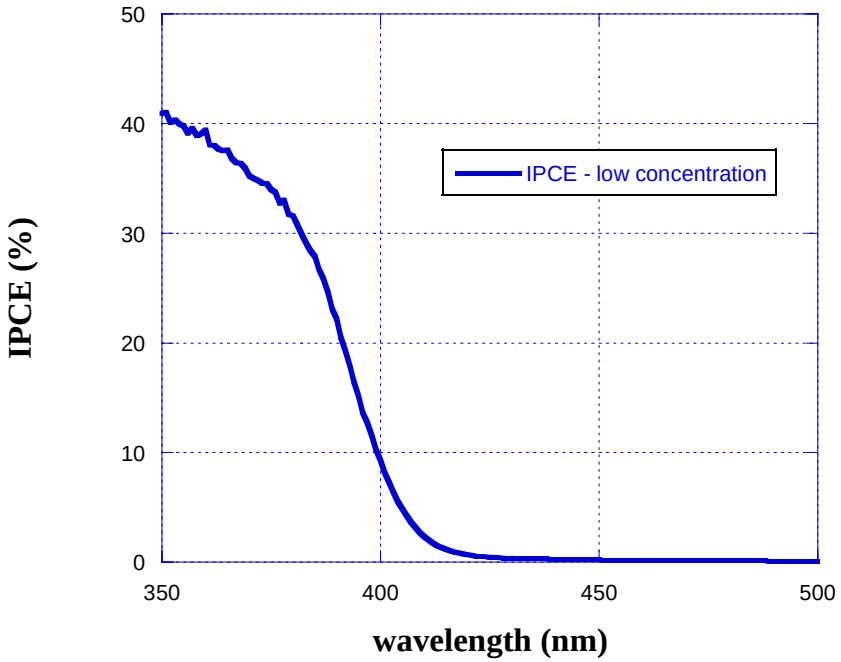

Figure 6: IPCE for a sample plasma treated at low acetylene concentration

As shown in Figure 6, there was no drastic change in IPCE at larger wavelengths. There was a significant decrease in current after 400 nm and remained constant at

Annual Research Journal, Vol. V
Electrical Engineering Research Experience for Undergraduates

ISBN 0-913260-07-X (http://www.ee.psu.edu/reu/)

higher levels of visible wavelengths. Both photocurrent measurements and IPCE were lower then comparable samples not plasma treated. There are several reasons which explain this.

DISCUSSION

Carbon doping can be achieved in 3 ways for TiO_2. It can be achieved by

1. substitutional Ti-C bonding
2. substitutional C-O bonding
3. interstitial carbon bonding

according to the theory of carbon doping by Valentin and co-workers[8]. For substitutional Ti-C and C-O bonds, TiO_2 bonds are broken. In this case atoms are replaced by carbon through substitution. One O atom is replaced by one C atom, or O will bond to C rather then Ti. For both bonds, if carbon is substituted, it can change the band structure of the nanotube materials. For an interstitial C bonding, carbon rests between the TiO_2 crystal lattice, in which it does not break up TiO_2 bonds. This can also affect the bandgap of the material according to theoretical considerations. However, in our case the carbon appeared to be deposited on the surface, not in the crystal lattice. This will not change the band structure because it acts as a coating instead of disrupting chemical bonds.

Additional studies are need to optimize the operating conditions of the plasma. This doping technique may be useful in increasing the visible light response of the nanotubes if carbon can be doped, satisfying the criteria listed above. Carbon may be present in this study of doping, but it needs to be incorporated in larger quantities in order to modify the band structure of TiO_2. Carbon is present on the titanium surface, but a greater amount of would be needed to make significant changes in the visible light response. Depending on how it bonds, it will cause different effects on the band structure of TiO_2. The process of doping modifies the band structure through a mixture of band gap narrowing and midgap states. This will decrease the energy needed to create electron hole pairs, thus expanding the spectrum of light that can be harvested.

A possible consequence of doping is that it can form oxygen vacancies (Ti^{3+} states) and act as recombination centers for electron hole pairs. Theoretical considerations indicate oxygen vacancies become more prevalent when dopants are added to the TiO_2. This can negate the effects of carbon doping and could lead to reduced efficiencies.

CONCLUSION

TiO_2 nanotubes have been formed through an anodization process and annealed in oxygen at 580º C to become crystallized. TiO_2 had two forms: anatase and rutile. The nanotubes were predominantly anatase, which is observed at lower annealing temperature. The nanotubes were plasma treated, in which dopants are added to

Annual Research Journal, Vol. V
Electrical Engineering Research Experience for Undergraduates

ISBN 0-913260-07-X (http://www.ee.psu.edu/reu/)

the material with the idea being to enhance the visible light response of the material. Samples were examined through UV-visible spectroscopy, in which they were used to check for increase at visible wavelengths. Light reflectance was measured to calculate the absorbance of the material at different wavelengths. At low concentrations no shift was observed in the UV-visible measurements. Meanwhile, at higher concentrations, the UV-visible profile shifted, but it appeared to have carbon deposited on the surface. Because of this, the samples were reannealed in oxygen to remove the carbon surface and to try and get carbon to bond with TiO_2. Next, the nanotubes underwent photocurrent measurements to check for any increase in current. These measurements analyzed the water photolysis properties of the material, in regard to the amount of current they produced. IPCE measurements were conducted to measure the current at different wavelengths of light. No significant changes were present in IPCE measurements at visible wavelengths. The results remained constant after about 430 nm. Photocurrent measurements and IPCE were reduced compared to undoped samples indicating that carbon was not bonded to the nanotube structure. Based on this data, additional studies are needed to optimize the operating conditions. This technique of plasma treatment may prove useful if substitutional carbon can be obtained. The technique can be applied to other dopants, as well, which may bond more readily with TiO_2.

ACKNOWLEDGEMENTS

This material is based upon work supported by the National Science Foundation under Grant No. EEC-0244030.

REFERENCES

1. Varghese, C. K.; Paulose, M.; Shankar, K.; Mor, G. K.; Grimes, C. A., Water-photolysis properties of micron-length highly-ordered titania nanotube-arrays. *Journal of Nanoscience and Nanotechnology* **2005,** 5, (7), 1158-1165.
2. Asahi, R.; Morikawa, T.; Ohwaki, T.; Aoki, K.; Taga, Y., Visible-light photocatalysis in nitrogen-doped titanium oxides. *Science* **2001,** 293, (5528), 269-271.
3. Khan, S. U. M.; Al-Shahry, M.; Ingler, W. B., Efficient photochemical water splitting by a chemically modified n-TiO_2, *Science* **2002,** 297, (5590), 2243-2245.
4. Shankar, K.; Paulose, M.; Mor, G. K.; Varghese, O. K.; Grimes, C. A., A study on the spectral photoresponse and photoelectrochemical properties of flame-annealed titania nanotube-arrays. *Journal of Physics D-Applied Physics* **2005,** 38, (18), 3543-3549.
5. Park, J. H.; Kim, S.; Bard, A. J., Novel carbon-doped TiO_2 nanotube arrays with high aspect ratios for efficient solar water splitting. *Nano Letters* **2006,** 6, (1), 24-28.

Annual Research Journal, Vol. V
Electrical Engineering Research Experience for Undergraduates

ISBN 0-913260-07-X (http://www.ee.psu.edu/reu/)

6. Cai, Q. Y.; Paulose, M.; Varghese, O. K.; Grimes, C. A., The effect of electrolyte composition on the fabrication of self-organized titanium oxide nanotube arrays by anodic oxidation. *Journal of Materials Research* **2005,** 20, (1), 230-236.
7. Mor, G. K.; Varghese, O. K.; Paulose, M.; Shankar, K.; Grimes, C. A., A review on highly ordered, vertically oriented TiO_2 nanotube arrays: Fabrication, material properties, and solar energy applications. *Solar Energy Materials and Solar Cells* **2006,** 90, (14), 2011-2075.
8. Di Valentin, C.; Pacchioni, G.; Selloni, A.; Livraghi, S.; Giamello, E., Characterization of paramagnetic species in N-doped TiO_2 powders by EPR spectroscopy and DFT calculations. *Journal of Physical Chemistry B* **2005,** 109, (23), 11414-11419.

ISBN 0-913260-07-X (http://www.ee.psu.edu/reu/)

ANALYSIS OF ACE SATELLITE AND GROUND-BASED MAGNETOMETER DATA TO TEST CORRELATION OF SPACE WEATHER EVENTS OBSERVED IN SPACE AND ON EARTH

Andrew D. Hawk*, Dorey J. Livneh[+], and John D. Mathews[#]

Department of Electrical Engineering
The Pennsylvania State University, University Park, PA 16802

*Undergraduate student of
Department of Electrical and Computer Engineering
The Citadel, The Military College of South Carolina
Charleston, SC 29409

ABSTRACT

Space-platform and ground-based magnetometers are sensitive to space weather events. These events include large-scale plasma waves embedded in the solar wind and Coronal Mass Ejections (CMEs). We present analysis of magnetometer data from the ACE satellite, located at the L1 LaGrange point 1.5 million kilometers towards the sun from earth, and ground-based magnetometers, seeking examples of correlated events. Analyses of time periods when medium-scale events are occurring have also been tested for correlation to explain the ripples in ground-based magnetometer data. Correlation was accomplished using MatLab and visual identification techniques. Successfully correlated space weather events will serve to calibrate our view on how space weather events appear to magnetometers at varying latitudes.

[+] Graduate Mentor
[#] Faculty Mentor

Annual Research Journal, Vol. V
Electrical Engineering Research Experience for Undergraduates

ISBN 0-913260-07-X (http://www.ee.psu.edu/reu/)

INTRODUCTION

The Earth is constantly bombarded by charged particles from the Sun. These particles form the "solar wind" that is comprised of plasma embedded in a weak magnetic field. The solar wind speed is typically between 400 and 1000km/second with particle concentrations of between 1 and 10 protons per cubic centimeter. When the magnetic field of the plasma has a southward Bz component, coupling occurs between it and the Earth's magnetic field.

The Earth's magnetic field is generated by a dynamo process in the Earth's core that resembles at first order a simple dipole field. At the Earth's surface the field ranges from 30,000 to 60,000 nT and diminishes rapidly at distance. The Interplanetary Magnetic Field (IMF) is the Sun's magnetic field, carried by the solar wind to Solar System planets. The interactions of the Earth's magnetic field, the solar wind, and the IMF form the Earth's magnetosphere.

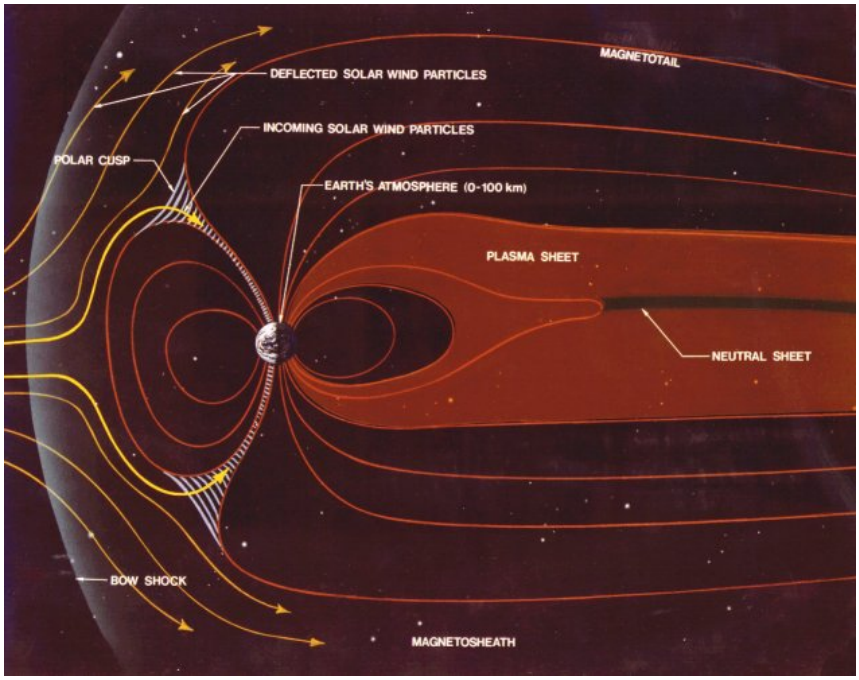

Figure 1. Side view of the Earth's magnetosphere. Picture taken from public domain.

The interactions between the charged particles in the solar wind and the magnetosphere are determined by magnetic reconnection rates at the magnetopause, the boundary of the magnetosphere, and in the magneto-tail, the portion of the magnetosphere that trails past the Earth, away from the sun. The proportion of terrestrial field lines, which the solar wind is interconnected with, is

Annual Research Journal, Vol. V
Electrical Engineering Research Experience for Undergraduates

ISBN 0-913260-07-X (http://www.ee.psu.edu/reu/)

controlled by these rates. The proportion of interconnected flux in any hemisphere increases when the interplanetary magnetic field is directed southwards (Milan, Wild et al. 2006)[3]. A complete discussion of this phenomenon is presented in the cited work.

The purpose of this study is to test for correlation between medium-scale solar wind events as seen by the Advanced Composition Explorer (ACE) with ground-based magnetometers. The time lag between ACE and ground-based instruments is also analyzed. Proven correlation between ACE and ground-based instruments would provide a springboard for future research and development into a mathematical model for mapping events as seen by ACE to events as seen by the ground-based magnetometers. The minute variations in Earth's magnetic field due to solar wind events could then be classified and understood as they pertain to other experiments involving fluctuations in the Earth's magnetic field.

This study was performed to analyze ACE and ground-based magnetometer data and identify correlations. Data used in this experiment are Bz from ACE; Bz in Geocentric Solar Ecliptic (GSE) coordinates from ground-based magnetometers, and the time in which changes in these occur. Analysis of the time delay between ACE and ground-based detection, and time delay between ground-based magnetometers at different high-to-low latitudes was also performed.

The ACE satellite makes observations of the solar wind from beyond the earth's magnetopause. It is an Explorer mission maintained by the National Aeronautics and Space Administration (NASA). ACE orbits the L1 libration point, approximately 1.5 million kilometers from Earth towards the Sun, providing a view of the solar wind well before it reaches the earth. ACE carries six high-resolution sensors and three monitoring instruments to sample these particles with a very high resolution. A semi-major axis of about 200,000 km allows ACE an excellent view of the Sun and beyond. ACE can provide advance warning of about an hour of geomagnetic storms via the real-time monitoring of the solar wind (Christian and Davis 2005) [1].

The International Real-time Magnetic Observatory Network (Intermagnet) is a global network of observatories set up to monitor the Earth's magnetic field. Intermagnet provides close to real-time monitoring of the Earth's magnetic field expressed in minute-long averages. Intermagnet allows specific location data to be used in correlation efforts (Kerridge 2001)[2]. Three ground-based magnetometers were chosen for correlation. The first is the Hornsnund Geomagnetic Observatory (HRN), maintained by the Institute of Geophysics, Polish Academy of Sciences. The station is located in Svalbard, Norway, at a co-latitude of 13.00° and a longitude of 15.55°. The second observatory is the Belsk Geomagnetic Observatory (BEL), maintained also by the Institute of Geophysics, Polish Academy of Sciences. This station is located in Belsk, Poland, at a co-latitude of 38.163° and a longitude of 20.792°. The third observatory is the Dourbes Geomagnetic Observatory (DOU), maintained by the Royal

Annual Research Journal, Vol. V
Electrical Engineering Research Experience for Undergraduates

ISBN 0-913260-07-X (http://www.ee.psu.edu/reu/)

Meteorological Institute of Belgium. This observatory is located in Dourbes, Belgium, at a co-latitude of 39.90° and a longitude of 4.60°. The co-latitude is the complementary angle, the difference between an angle and 90°, in spherical coordinates.

HRN was chosen because it is the first observatory that would be able to see fluctuations in Bz from the solar wind arriving through the magnetosphere. Importantly, the high geomagnetic latitude of the site allows the IMF to penetrate deep into the atmosphere. Visible correlation between ACE data and HRN data will demonstrate the initial time lag between ACE and Earth. BEL was chosen because it is a sizable distance southward of HRN, without being too far east or west. Correlation between HRN and BEL will assist in showing the time delay of the fluctuations moving from north to south. DOU was chosen because it is slightly south of BEL to aid in showing the lack of time-delay of fluctuations moving east or west. The availability and quality of data also played major roles in the selection of observatories.

EXPERIMENTAL DESCRIPTION

The ACE satellite Level 2 (Verified) data was used to analyze the solar wind in space. The ACE Magnetometer Instrument (MAG) consists of an electronics box mounted in the top deck of the craft, as well as twin triaxial fluxgate magnetometers mounted at the ends of two different booms. The sensors are 165 inches from the center of the craft on opposing solar panels (Smith, L'Heureux et al. 1998)[4]. The data from HRN was collected on site using Absolute –D/I Flux and PPM, and Variations- Torsion photoelectric magnetometer-PSM instruments. BEL data was collected on site using Absolute - DI-fluxgate ELSEC 810, Proton magnetometer PMP-7, Variations - Torsion photoelectric magnetometer, and TPM employing Bobrov-type quartz variometer instruments. The data from DOU was collected on site using vector magnetometer – LAMA, and GEM SM90R instruments. All data for this research was downloaded via the Internet from respective websites. ACE data was present in one-second intervals, so a MatLab script was used to generate one-minute averages. Interpolation was used to remove the bad data points from the ACE data. Ground based magnetometer data was already present in one-minute intervals, generated from one-second data. Ground based data is heavily influenced by the Earth's magnetic field; removing the mean and stepping down the magnitude of Bz removed this effect in MatLab. The goal was to make the graphs easier to read and correlations easier to identify.

Annual Research Journal, Vol. V
Electrical Engineering Research Experience for Undergraduates

ISBN 0-913260-07-X (http://www.ee.psu.edu/reu/)

RESULTS

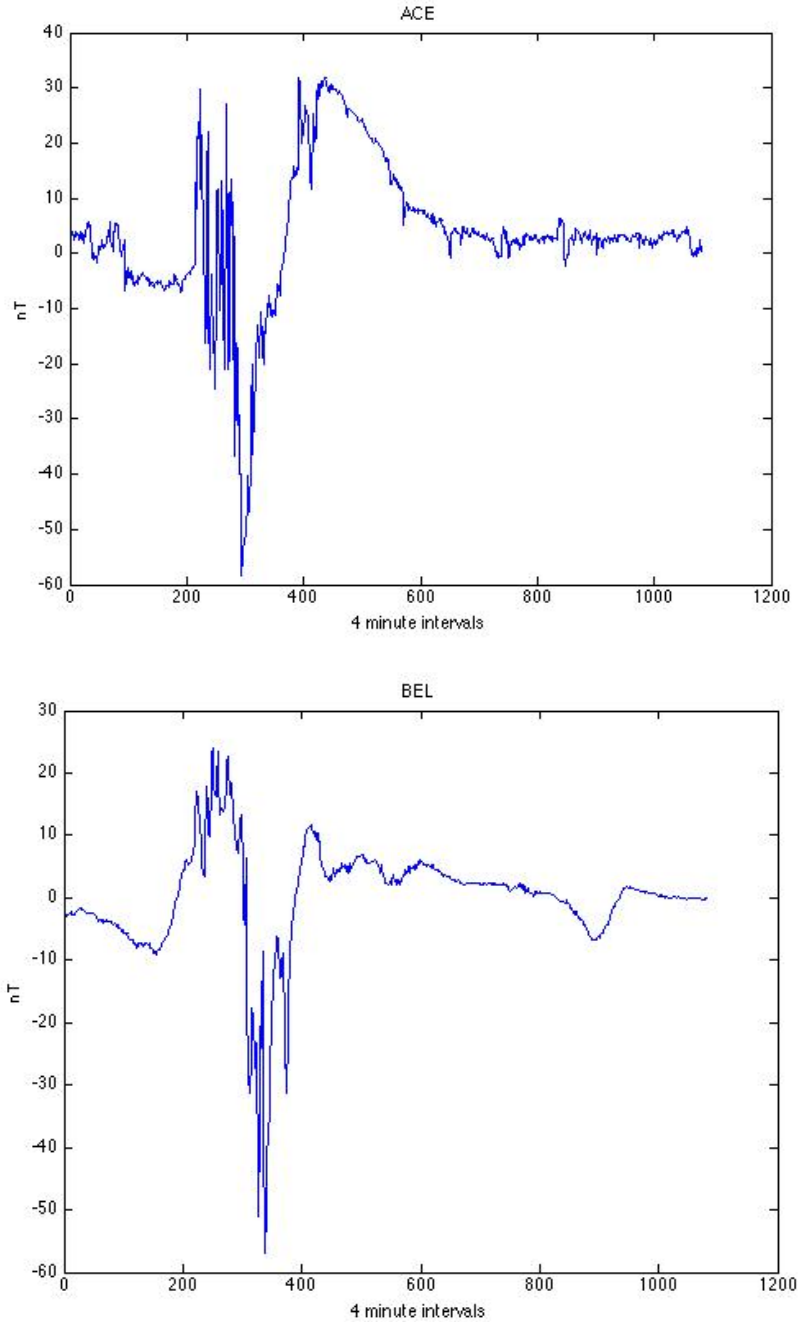

Figure 2. Initial correlation attempt between ACE and BEL, days 197 to 199, 2000

Annual Research Journal, Vol. V
Electrical Engineering Research Experience for Undergraduates

ISBN 0-913260-07-X (http://www.ee.psu.edu/reu/)

Figure 2 is the initial attempt at correlation done for this research. The days 197 to 199, 2000, were chosen due to prior knowledge that a massive CME occurred during this period. This CME caused a geomagnetic storm, and so was known to have interacted with the Earth's magnetosphere in some manner to have caused such a storm. Basic correlation of such a large event between ACE and BEL would give credence to moving onward to smaller, more common events to correlate.

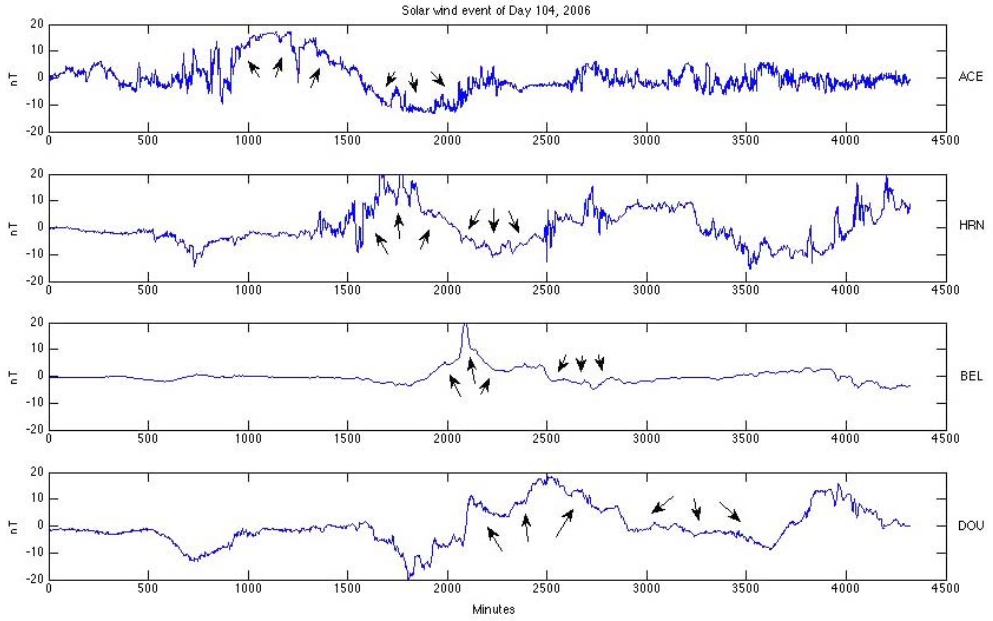

Figure 3. Solar wind event of Day 104, 2006. Data is plotted from ACE, HRN, BEL, and DOU

Figure 3 was generated using MatLab. The event of interest has been marked with arrows showing its characteristic portions. This eases the visual correlation between different plots. This event has a smooth concave-down portion followed by a smooth concave-up portion. The individual plots are ordered to assist in showing the event being analyzed being delayed in time as it passes ACE, and subsequently moves through the Earth's magnetosphere southward. The comparatively short distances between the three Earth-based magnetometers shows the time delay experienced by the fluctuations moving inside of the Earth's magnetosphere. Attenuation in the negative Bz direction becomes apparent in both the BEL and DOU observatories. Positive Bz portions of the event are seen to be carried forward; while the negative portions are more heavily attenuated the farther southward the event moves.

Annual Research Journal, Vol. V
Electrical Engineering Research Experience for Undergraduates

ISBN 0-913260-07-X (http://www.ee.psu.edu/reu/)

In Figure 4 arrows are added to the plots to show the characteristics of the event. This event has two sharp downward pulses framing a broken ridge. The arrows assist in identifying these features. The time dilation between ACE and HRN is again present, as it was in Figure 3, as well as the time lapse between HRN and BEL. The attenuation of the negative Bz component is not as prevalent in Figure 4 as in Figure 3. The stretching effect of the magnetosphere on solar wind events is evident here. The duration of the event as seen by ACE is shorter than that seen by HRN, which in turn is shorter than seen by BEL and DOU. BEL and DOU are very similar, with only a slight delay of DOU behind BEL, due to it being slightly more southern.

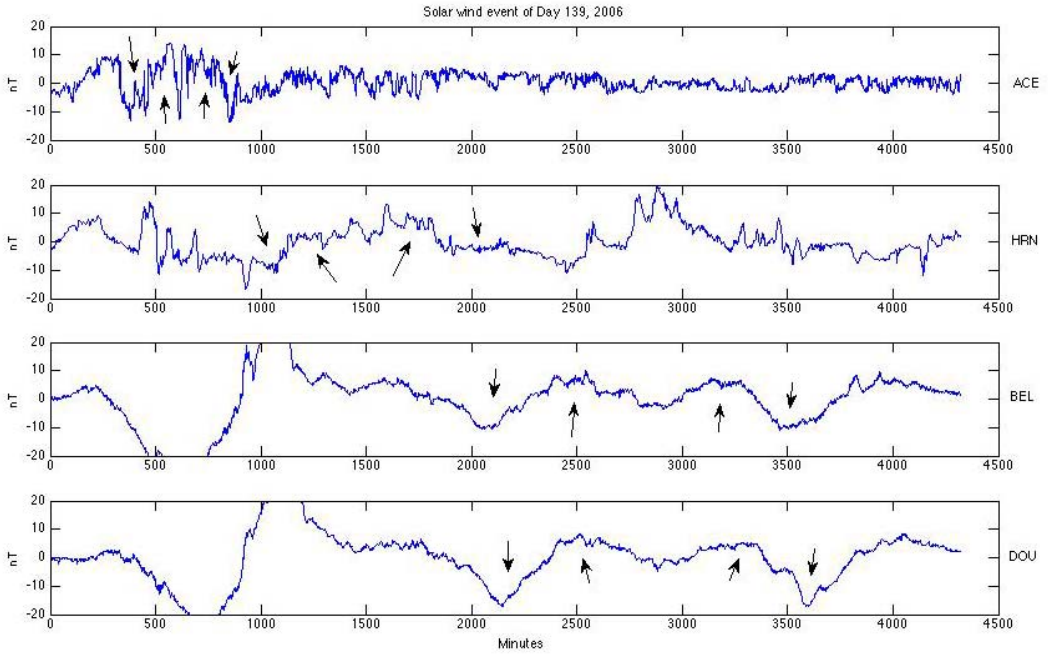

Figure 4. Solar wind event of Day 139, 2006. Data is plotted from ACE, HRN, BEL, and DOU

The Figure 5 event has a single smooth curve in the positive Bz direction, which is indicated by the arrows. The same time delay between ACE and HRN and between HRN and BEL and DOU is present. This matches with what Figures 3 and 4 have shown. There is no major negative Bz component to this event to show the aforementioned attenuation. The plot of BEL in Figure 5 shows a much shorter event than expected. Previous figures have shown that events seen by ACE tend to stretch as they move southward through the Earth's magnetosphere. The stretching is evident in both HRN and DOU of Figure 5, but not in BEL. Reasons for this are unknown.

Annual Research Journal, Vol. V
Electrical Engineering Research Experience for Undergraduates

ISBN 0-913260-07-X (http://www.ee.psu.edu/reu/)

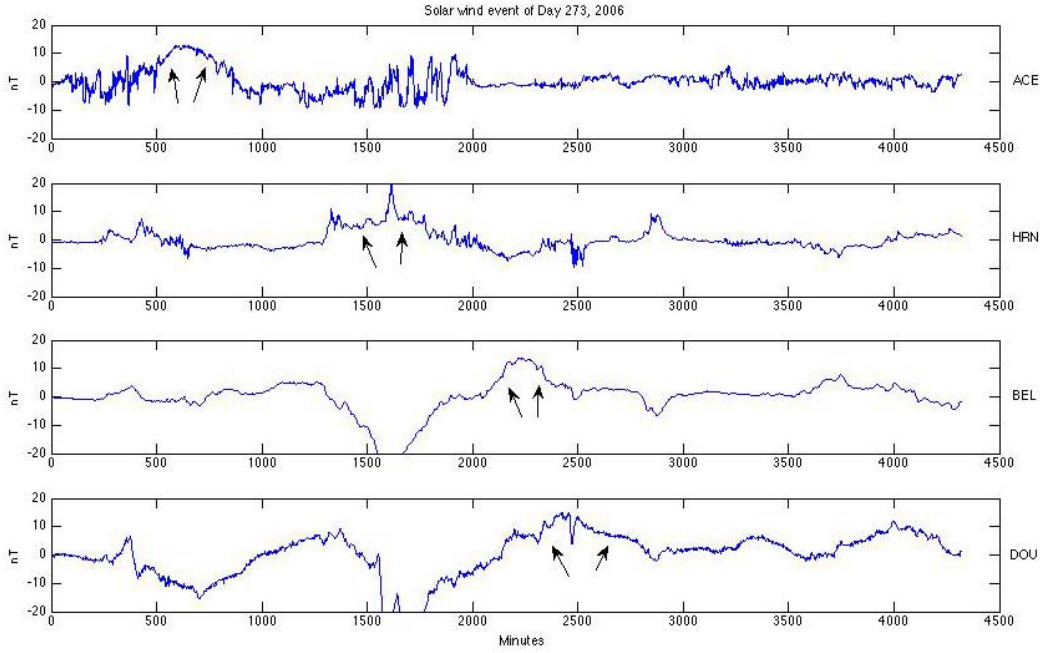

Figure 5. Solar wind event of Day 273, 2006. Data is plotted from ACE, HRN, BEL, and DOU

The Figure 6 event has a lengthy arc in the positive Bz direction, which is marked by arrows, as well as a sharp negative Bz component just before the arc. The same time lapse as was present in Figures 3, 4, and 5 is again present. The smooth arc correlates well between all of the observatories plotted. The sharp negative Bz component preceding the arc also correlates, and can be seen being stretched as expected. The arc itself is also being stretched as expected, but due to the low actual fluctuation tends to form a tail at the lower latitude observatories BEL and DOU. DOU and BEL have similar plots again for the area of interest, as they did for Figure 4. The strange behavior of BEL, the plot being drastically different from DOU, in Figures 3 and 4 is unexplained, but similar between the two figures. The resolution of BEL in Figures 3 and 5 appears to be less than the other observatories, and less than it is for BEL in Figures 4 and 6.

Annual Research Journal, Vol. V
Electrical Engineering Research Experience for Undergraduates

ISBN 0-913260-07-X (http://www.ee.psu.edu/reu/)

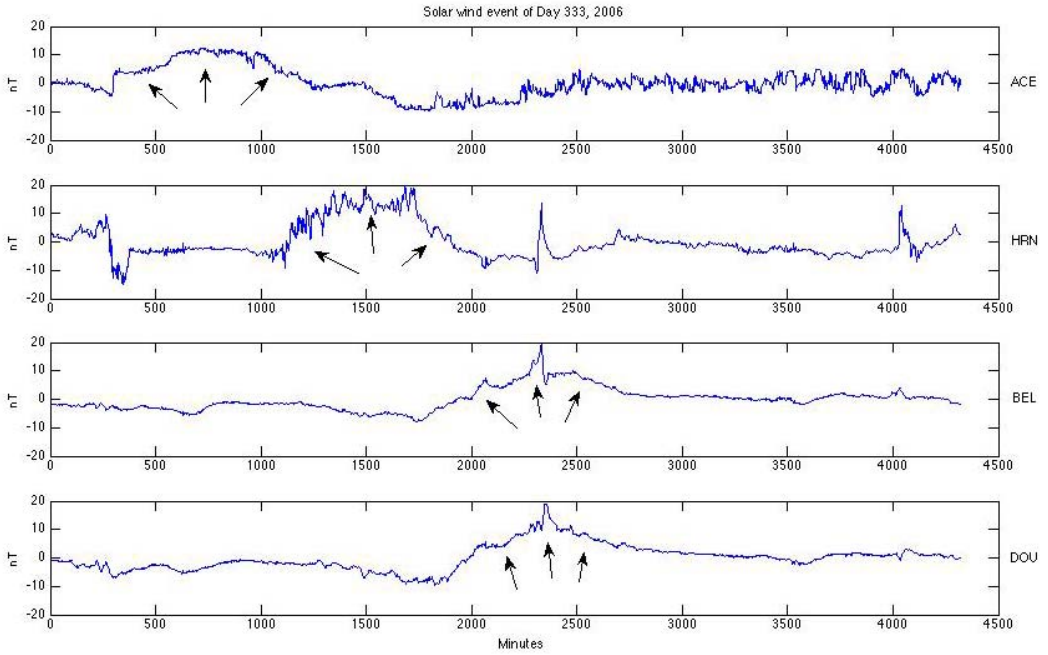

Figure 6. Solar wind event of Day 333, 2006. Data is plotted from ACE, HRN, BEL, and DOU

CONCLUSION

This research shows that medium scale solar wind events are able to be correlated between ACE and the ground-based magnetometers HRN, BEL, and DOU. The results show that visual correlation is possible of events of this scale. Time lag is longer than expected due to the amount of time taken for the propagation of the solar wind's magnetic field through the Earth's magnetosphere. Events as seen by ACE are stretched in time as they are seen at HRN as well as after they have propagated southward through BEL and DOU. The general shapes of the events remain intact, but the identifying features of the events are spaced farther apart at HRN, BEL, and DOU than they are at ACE. Evidence also suggests that the event's magnetic field in the negative Bz direction is heavily attenuated at lower latitudes, while the positive Bz direction is much less attenuated. With evidence that solar wind events are seen in the magnetosphere, more in-depth work can be done to generate a mathematical model for correlation.

Annual Research Journal, Vol. V
Electrical Engineering Research Experience for Undergraduates

ISBN 0-913260-07-X (http://www.ee.psu.edu/reu/)

ACKNOWLEDGEMENTS

I would like to thank everyone involved in the Penn State REU program for their support, and for providing this opportunity. Thanks go to NASA and CalTech for the ACE satellite and it's data, as well as the group responsible for Intermagnet, for collecting ground-based magnetometer data into one location. This material is based upon work supported by the National Science Foundation under Grant No. EEC-0244030.

REFERENCES

[1] Christian, E. R. and A. J. Davis. (2005, July 13, 2005). "Advanced Composition Explorer (ACE) Mission Overview." Retrieved July 9, 2007, 2007, from http://www.srl.caltech.edu/ACE/ace_mission.html.

[2] Kerridge, D. (2001) Intermagnet: Worldwide near-real-time geomagnetic observatory data. *Proceedings of the Workshop on Space Weather*, DOI:

[3] Milan, S. E., J. A. Wild, et al. (2006). "Space- and ground-based investigations of solar wind-magnetosphere-ionosphere coupling." *Advances in Space Research* (38): 1671-1677.

[4] Smith, C. W., J. L'Heureux, et al. (1998). "The ACE Magnetic Fields Experiment." *Space Science Reviews* **86**: 1-23.

Annual Research Journal, Vol. V
Electrical Engineering Research Experience for Undergraduates

ISBN 0-913260-07-X (http://www.ee.psu.edu/reu/)

GROWTH AND CHARACTERIZATION OF GALLIUM ANTIMONIDE NANOWIRES ON SILICON AND SAPPHIRE SUBSTRATES

Anne M. Itsuno*, Robert A. Burke[+,1], Joan M. Redwing[#,1,2], and Theresa S. Mayer[#,2]

[1]Department of Materials Science and Engineering
[2]Department of Electrical Engineering
The Pennsylvania State University, University Park, PA 16802

*Undergraduate student in
Electrical and Computer Engineering
Franklin W. Olin College of Engineering
Needham, MA 02492

ABSTRACT

There is interest in the integration of antimonide-based nanowires with silicon substrates for future applications in high speed nanoscale electronics. The growth of epitaxially-oriented gallium antimonide (GaSb) nanowires by the vapor-liquid-solid (VLS) technique on gold (Au) -coated silicon substrates is examined in this paper. Growth of the nanowires was attempted using both Au nanoparticles and thin films as metallic catalysts. A series of growth experiments were performed to determine the optimal growth conditions for nanowire growth. The conditions investigated included the concentration of Au nanoparticles, growth temperature, growth pressure, and V/III ratio. The growth of GaSb nanowires on Au-coated sapphire substrates has been shown previously; therefore, sapphire substrates with Au nanoparticles and thin films were utilized as controls for this series of experiments. Optimal growth conditions for nanowires on Si substrates were determined to be 300 Torr at 500˚C, with a V/III ratio of 1, using Au thin film as a catalyst, and conditions for nanowires on sapphire were 200 Torr at 500˚C, with a V/III ratio of 1, also using Au thin film. Following the completion of the growths, the structural properties of the nanowires grown on silicon and sapphire substrates were characterized and measured.

[+] Graduate Mentor
[#] Faculty Mentor

Annual Research Journal, Vol. V
Electrical Engineering Research Experience for Undergraduates

ISBN 0-913260-07-X (http://www.ee.psu.edu/reu/)

INTRODUCTION

The integration of semiconducting nanowires of different compositions on silicon (Si) substrates has large potential in current high-speed nanoscale applications. Nanowires provide smaller, high performance options for devices such as photodetectors, bipolar transistors, high performance field-effect transistors, light emitting and laser diodes.[1, 2, 3, 4] These potential applications motivate the research in this paper to determine the growth methodology of gallium-antimonide (GaSb) nanowires on Si and sapphire substrates.

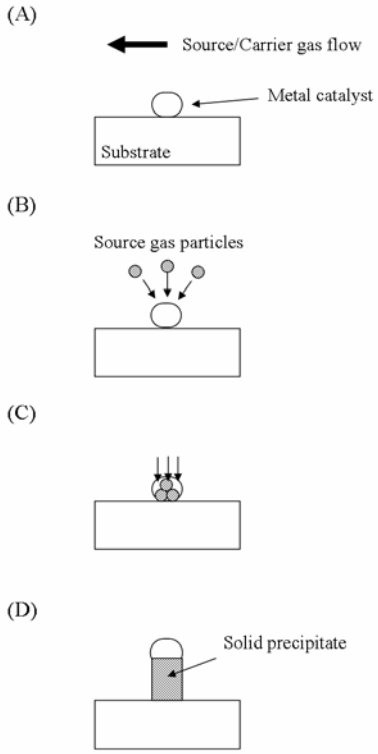

Figure 1. VLS growth mechanism. (A) Metallic catalyst nucleates, and source material gas is flowed into the system. (B) Source gas reacts with the catalyst to form liquid eutectic particles, and (C) diffuses through the catalyst. (D) When the catalyst supersaturates, the particles precipitate out at the liquid-solid interface as a crystal structure.

The development of the vapor-liquid-solid (VLS) growth method in 1964 by Wagner and Ellis has facilitated the growth of various one-dimensional nanostructures.[8] The VLS technique involves using metallic catalysts in the form of nanoparticles or thin films to facilitate nanowire growth. Gold (Au) is commonly used as a catalytic metal particle, but alternative metals, oxides, and silicides are also utilized.[9] The catalyst metal is selected based on its ability to

Annual Research Journal, Vol. V
Electrical Engineering Research Experience for Undergraduates

ISBN 0-913260-07-X (http://www.ee.psu.edu/reu/)

form a low temperature eutectic liquid phase with the elements that comprise the nanowire. In the case of a thin film catalyst, the high temperature in the hot wall reactor anneals the film, causing the catalyst to bead into particles due to stress and strain within the film. The precursors absorb onto the surface of the catalyst forming an alloy. It may be useful to point out that one shortcoming of this technique is the lack of control of the resulting particle diameter after annealing. Alternatively, the use of a pre-made colloidal solution allows there to be control over the catalyst diameter. In both cases, the source material used for nanowire growth is introduced into the system as a gas, as shown in Figure 1A. The source material decomposes in the isothermal reactor and reacts with the catalyst to form a liquid alloy at the eutectic point, as depicted in Figure 1B. The source atoms diffuse into the catalyst, as shown in Figure 1C, and when the liquid alloy supersaturates, a solid precipitates from the alloy and is deposited on the substrate beneath the catalyst, as illustrated in Figure 1D. As long as the source material gas flow is maintained, the precursor continues to diffuse through the catalyst to form a nanowire at the catalyst-substrate interface.

Antimonide (Sb) based nanowires are of special interest because of their excellent structural and electronic properties. GaSb has a narrow bandgap of 0.726 eV and a high carrier mobility within V-III compound semiconductors, making it a viable candidate for high performance nanotechnology applications. Si is investigated as a growth substrate because it is predominantly used in current mature semiconductor technologies, and there has been little research done in the area of GaSb nanowire growth on Si substrates to this author's knowledge. In this work, GaSb nanowires were grown on Si substrates using the VLS growth technique, and the optimal growth conditions were determined through a series of experiments. Previous results for GaSb nanowires on sapphire substrates using Au nanoparticles and thin films as catalysts were used as a control in these tests, and additional experiments were performed using sapphire as a substrate.

A number of different techniques have been developed to grow wires including metal organic chemical vapor deposition (MOCVD), molecular beam epitaxy (MBE), focused ion beam (FIE) approach, laser ablation, and thermal evaporation.[3, 5, 6, 7] In this paper, gallium-antimonide (GaSb) nanowires are grown on silicon (Si) and sapphire substrates using the MOCVD technique, which utilizes the concept of the vapor-liquid-solid (VLS) mechanism.

EXPERIMENTAL DESCRIPTION

GaSb nanowires were grown on (111) Si and c-plane sapphire substrates using Au nanoparticles and thin films as described in the previous section. The Si and sapphire substrates were prepared for Au nanoparticle application by coating the surfaces with a solution of 3-aminopropyltrimethoxysilane (APTMS, Gelest, Inc.) diluted to 0.001% with ethanol and shaking the mixture for 5 minutes at 600rpm. The substrates were then placed in 50nm Au colloidal (Ted Pella, Inc.) solution diluted to 7.5% for silicon and 5% for sapphire with DDI water and the samples were shaken for 15 minutes at 600rpm. The concentration of 7.5% Au for Si was

Annual Research Journal, Vol. V
Electrical Engineering Research Experience for Undergraduates

ISBN 0-913260-07-X (http://www.ee.psu.edu/reu/)

chosen after examining substrates coated with 2.5%, 5%, 7.5%, and 10% concentration of Au using SEM and comparing the distribution of the particles on the substrate surface. The samples were stored in DDI water at room temperature until later use. The thin film substrates were prepared by depositing a 2nm Au layer onto the Si and sapphire wafers by sputter deposition.

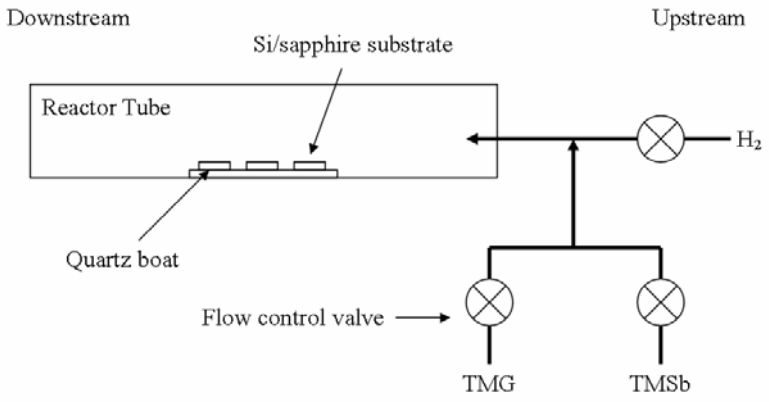

Figure 2. MOCVD system set up. TMG and TMSb are the precursors and H_2 is the carrier gas.

The growth experiments were performed using a chemical vapor deposition (CVD) system, and nanowires were grown in an isothermal quartz tube reactor with source gases feeding into the furnace from the upstream end as shown in Figure 2. Upstream is defined as the tube end through which the source gases are introduced. The substrates were loaded onto a 2 inch quartz boat and pushed into the tube reactor from the downstream opening. The boat was placed 2 inches past the center of the tube closer to the source gases. After evacuating the system to the proper pressure depending on the experiment, the furnace was heated to the appropriate growth temperature and stabilized for 20 minutes. Trimethylgallium ($Ga(CH_3)_3$, TMG) and trimethylantimony ($Sb(CH_3)_3$, TMSb) precursors were flowed through the quartz tube with hydrogen (H_2) as the carrier gas for 5 minutes. The bubblers for TMG and TMSb were held at constant temperatures of -10˚C and 4˚C, respectively.

Several growth conditions were studied to determine optimal growth conditions for GaSb nanowires on Si. Temperature, pressure, and V/III ratio were investigated for their effects on the structural, optical, and electrical properties of the wires. Because nanowires were successfully grown in previous experiments at conditions of 100 Torr, 500˚C, with V/III ratio of 1 and a 5 minute growth time for GaSb nanowires on sapphire substrates, these conditions were used as controls for the experiments in this paper. Consequently, nanowire growth was attempted at temperatures of 475˚C, 487˚C, 500˚C, 512˚C, 525˚C, 537˚C, and 550˚C at 100 Torr for 5 minutes. Pressure was varied and nanowire growth was attempted at

Annual Research Journal, Vol. V
Electrical Engineering Research Experience for Undergraduates

ISBN 0-913260-07-X (http://www.ee.psu.edu/reu/)

200, 300, and 400 Torr at 500˚C. In another experiment, the temperature was decreased from 525°C to 475°C after 30 seconds and the growth was continued at 475°C for another 4.5 minutes. This was also done for the pressure studies where the pressure was decreased from 300 Torr after 30 seconds to 100 Torr. Additionally, experiments were performed to grow wires at different combinations of pressures and temperatures with a 5 minute growth time: 13 Torr at 525˚C, 200 Torr at 500˚C, and 400 Torr at 500˚C. Growth was also attempted for different V/III ratios and experiments were run at 100 Torr, 500˚C for V/III ratios of 0.5, 1, 1.5, and 2. Some silicon wafers were cleaned using the buffered oxide etch (BOE) technique for growths with conditions of 300 to 100 Torr at 500˚C and V/III ratio of 1, 300 Torr at 500˚C and V/III ratio of 1, and 100 Torr at 500˚C and V/III ratio of 2. Both Si and sapphire samples were examined using an XL20 scanning electron microscope (SEM) for wire growth and structural characterization.

Between each growth run, a hydrogen bake was performed to ensure all residual deposits on the reactor tube were removed in order to prevent contamination of the samples and unwanted interaction with the source gases and the reactor tube wall. The gas lines to the system were filled with hydrogen, and the furnace was heated to 1000˚C for 15 minutes.

RESULTS

Nanowire growth on Si substrates with Au nanoparticle catalysts was observed at pressures ranging from 13 Torr to 400 Torr; at temperatures ranging from 487˚C to 500˚C; and at V/III ratios of 1, 1.5, and 2. Growth on Si with Au thin film catalysts was observed only at 500˚C, at pressures ranging from 100 Torr to 400 Torr, and at V/III ratios of 0.5, 1, and 2. While the growth window for GaSb nanowires on Si substrates is fairly narrow, wire growth on sapphire has been easier to achieve. On sapphire substrates coated with Au nanoparticles, growth was observed at pressures between 13 Torr and 400 Torr, at temperatures between 475˚C and 537˚C, and at V/III ratios of 0.5, 1, 1.5, and 2. Growth with Au thin film on sapphire substrates was successful between pressures of 13 Torr and 400 Torr, temperatures of 475˚C and 500˚C, and at V/III ratios of 0.5, 1, and 1.5. The growth conditions are summarized in Table 1.

Nanowire growth was most prevalent on sapphire substrates coated with the Au thin film catalyst. Although nanowires grew on more Si substrates treated with Au nanoparticle catalysts, Si substrates coated with the Au thin film exhibited higher quality nanowires, i.e. those with smaller diameter and minimal tapering. Of all the Si samples, the best wires were grown at 300 Torr and 500˚C with a V/III ratio of 1 and Au thin film as the catalyst. The wire density on the Au thin film coated substrates was consistently high across duplicate runs compared to the low density observed on Au nanoparticle treated substrates. The nanowires grown under these conditions with both catalysts, however, were all comparatively large, with diameters ranging from 270-480nm for Au thin film catalyst substrates, and 300-400nm for Au nanoparticle substrates. Although

Annual Research Journal, Vol. V
Electrical Engineering Research Experience for Undergraduates

ISBN 0-913260-07-X (http://www.ee.psu.edu/reu/)

samples grown with nanoparticle catalysts had a more controlled diameter, the length of the wires were considerably longer than those grown with thin film catalysts, 20μm and 7.5-8.5μm, respectively. These nanowires exhibited slight tapering, and some wires showed traces of the nanoparticles attached at their tips. The wires were oriented in random directions.

Table 1. Growth windows of nanowires on Si and sapphire with nanoparticle and thin film catalysts.

Growth Conditions for GaSb Nanowires on Si Substrate

Sample/Conditions	Pressure (Torr)	Temperature (˚C)	V/III ratio
Si with Au nanoparticles	13-400	487-500	1, 1.5, 2
Si with Au thin film	100-400	500	0.5, 1, 2
Sapphire with Au nanoparticles	13-400	475-537	0.5, 1, 1.5, 2
Sapphire with Au thin film	13-400	475-537	0.5, 1, 1.5

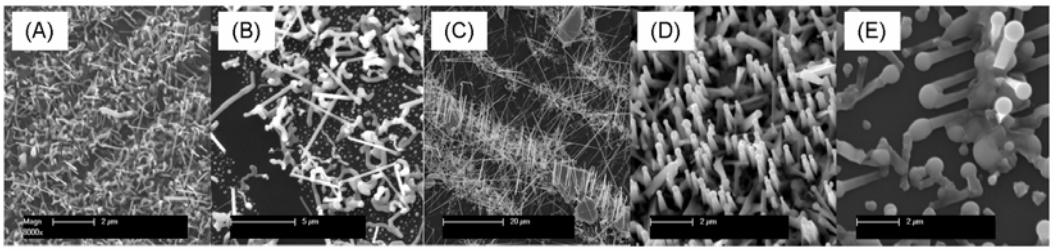

Figure 3. Samples on sapphire substrate grown at 500˚C, V/III ratio of 1, and at pressures of (A) 13 Torr, (B) 100 Torr, (C) 200 Torr, (D) 300 Torr, and (E) 400 Torr. Scale bar at 2μm, 5μm, 20μm, 2μm, and 2μm, respectively.

On the other hand, growth was achieved more frequently for both nanoparticle and thin film treated sapphire substrates. While no epitaxial growth was observed in wires grown on Si substrates, vertically oriented growths were present in several sapphire samples treated with Au thin film, as shown in Figures 3C and 3D. The conditions for these results were 200 Torr at 500˚C with a V/III ratio of 1, and 300 Torr at 500˚C with a V/III ratio of 1. The range of wire diameters of each sample is 55-200nm, and 120-220nm, respectively. Likewise, the range of

Annual Research Journal, Vol. V
Electrical Engineering Research Experience for Undergraduates

ISBN 0-913260-07-X (http://www.ee.psu.edu/reu/)

wire lengths of each sample is 7-30μm, and 3-4μm, respectively. The results for the nanowire growth on sapphire with Au thin film as a catalyst are summarized in Table 2.

Table 2. Diameters and lengths of nanowire samples grown with different conditions.

Dimensions of Highest Quality Nanowires
on Sapphire with Au Thin Film Catalyst

Conditions/Dimensions	Diameter	Length
200 Torr, 500˚C, V/III = 1	55-200nm	7-30μm
300 Torr, 500˚C, V/III = 1	120-220nm	3-4μm

These experiments were based off a successful control experiment previously done with growing GaSb nanowires on a sapphire substrate at 100 Torr and 500˚C with a V/III ratio of 1. The nanowires grown at these conditions exhibited a range of diameters of approximately 91±31nm, and lengths between 5-8μm for Au nanoparticles.

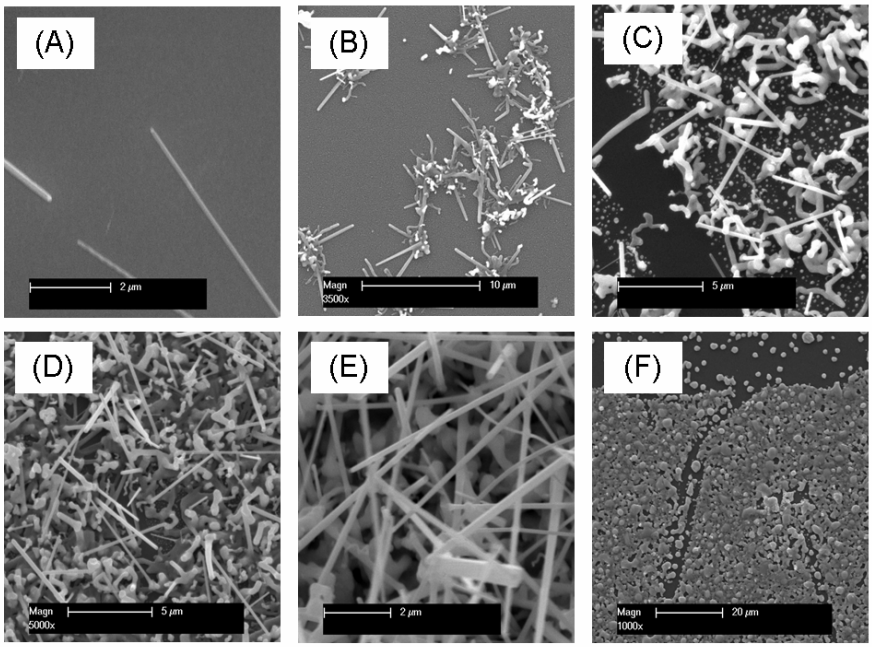

Figure 4. Samples on sapphire substrate grown at 100 Torr, V/III ratio of 1, and at temperatures of (A) 475˚C, (B) 487˚C, (C) 500˚C, (D) 512˚C, (E) 525˚C, and (F) 537°C. Scale bar at 2μm, 10μm, 5μm, 5μm, 2μm, and 20μm, respectively.

Annual Research Journal, Vol. V
Electrical Engineering Research Experience for Undergraduates

ISBN 0-913260-07-X (http://www.ee.psu.edu/reu/)

A number of growth experiments were run to examine the effect of slight adjustments in temperature, pressure, and V/III ratio conditions. As mentioned previously, a set of growths were run at 100 Torr with a V/III ratio of 1 for temperatures of 475˚C, 487˚C, 500˚C, 512˚C, 525˚C, 537˚C, and 550˚C. No wire growth was observed at any of these conditions for all Si samples with Au thin film, and for all Si and sapphire samples at 550˚C. Figure 4 shows that as the temperature condition increased, the wire density on the substrate also increased for sapphire samples with Au thin film catalysts. However, at temperatures above 525˚C, no nanowire growth was achieved. Very few or no wires grew on Si substrates with these conditions.

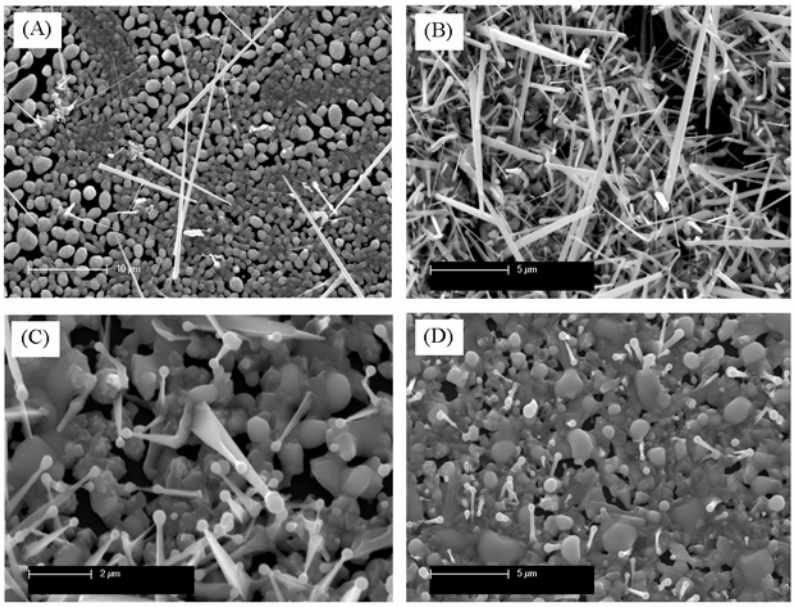

Figure 5. Samples on Si substrate grown at 500˚C and V/III ratio of 1 at pressures of 300 Torr with (A) nanoparticle and (B) thin film catalysts, and 400 Torr with (C) nanoparticle and (D) thin film catalysts. Scale bar at 10μm, 5μm, 2μm, and 5μm, respectively.

Another set of growths was run at 500˚C with a V/III ratio of 1 for pressures of 13 Torr, 100 Torr, 200 Torr, 300 Torr, and 400 Torr. Figure 3 illustrates the effects that varying pressure has on the direction of preferential growth for sapphire samples treated with Au thin film. Some preferential growth direction is evident in samples grown at 13 Torr and 100 Torr, but epitaxial growth is clearly observed at 200 Torr and 300 Torr. GaSb nanowires grown at 200 Torr exhibit little tapering, while those grown at 300 Torr are more tapered. At 400 Torr, the wires have all but disappeared, and the substrate is coated with some tapered, wire-like structures and crystal clusters. Large GaSb nanowires grew on Si with nanopartice and thin film catalysts at 300 Torr and 500˚C (Figures 5A and 5B),

Annual Research Journal, Vol. V
Electrical Engineering Research Experience for Undergraduates

ISBN 0-913260-07-X (http://www.ee.psu.edu/reu/)

and some less wire-like structures appeared at 400 Torr, 500˚C (Figures 5C and 5D). The best density was achieved at 300 Torr and 500˚C with Au thin film.

The V/III ratio was also varied in several growth sets, and ratios of 0.5, 1, 1.5, and 2 were tested at 100 Torr and 500˚C. Figure 6 shows that the density and structure quality of the nanowires decreases as the V/III ratio increases for sapphire samples treated with Au thin film. The sample with a V/III ratio of 0.5 exhibited the best wire structure and some preferential growth direction. Very few or no wires grew on Si substrates with these conditions.

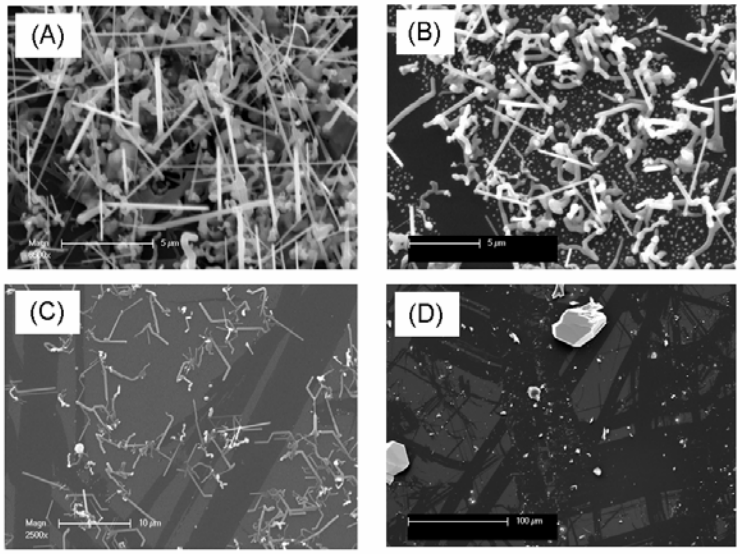

Figure 6. Nanowire samples grown on sapphire substrates at different V/III ratios. All samples grown at 100 Torr, 500˚C. Sample grown at (A) V/III ratio of 0.5, (B) 1, (C) 1.5, and (D) 2. Scale bar at 5μm, 5μm, 10μm, and 100μm, respectively.

Several Si sample growths were duplicated for both nanoparticle and thin film treated substrates under successful conditions. The samples in these growths were first treated with a buffered oxide etch (BOE) to remove any oxide forming on the sample surface from exposure to air. Figure 7 shows that dense nanowire growth was achieved when a BOE was done on samples before growth for conditions where pressure dropped from 300 Torr to 100 Torr at 500˚C with a V/III ratio of 1, and for 100 Torr at 500˚C with a V/III ratio of 2.

Annual Research Journal, Vol. V
Electrical Engineering Research Experience for Undergraduates

ISBN 0-913260-07-X (http://www.ee.psu.edu/reu/)

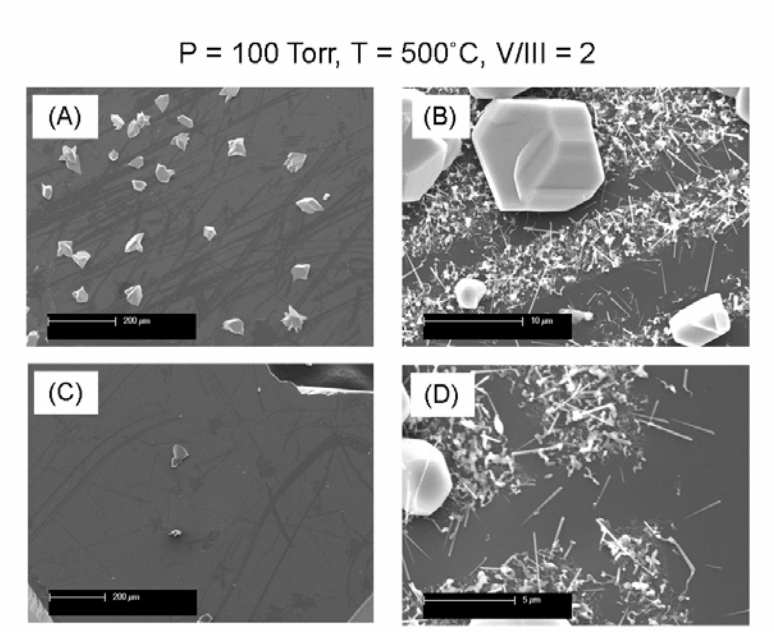

Figure 7**.** Nanowire samples with and without buffered oxide etch (BOE) before growth at 100 Torr, 500˚C, with V/III ratio of 2. Si substrate with Au nanoparticle catalysts without (A) and with (B) BOE. Si substrate with Au thin film catalyst without (C) and with (D) BOE. Scale bar at 200μm, 10μm, 200μm, 5μm, respectively.

DISCUSSION

As noted in the previous section, changes in temperature affected the density of the nanowire growth on the sapphire substrate. The increase in growth density was directly proportional to the increase in temperature up to a certain point after which wires ceased to grow, and thin film clusters dominated the substrate surface. It is possible that the increase in temperature led to a higher decomposition rate of the source gas particles, providing more reactants for growth. This would cause nucleation to occur more quickly, allowing faster and longer growth of the GaSb wires. However, above a certain temperature, 537˚C for the case of sapphire at 100 Torr, the nucleation rate may have surpassed the precipitation rate, and the rapid enlargement of the nanoparticles or nucleated thin films may have caused them to absorb into each other to produce alloy thin film clusters before any crystal structures manage to precipitate out.

Changes in pressure also affected wire growth in terms of nanowire quality. At pressures of 200 Torr and 300 Torr at 500˚C on sapphire with Au thin film, epitaxial nanowire growth was achieved. However, the nanowires grown at 300 Torr appeared significantly more tapered than those grown at 200 Torr. The increase in pressure plays a role in increasing the residence time of the gas within

Annual Research Journal, Vol. V
Electrical Engineering Research Experience for Undergraduates

ISBN 0-913260-07-X (http://www.ee.psu.edu/reu/)

the reactor and reducing the velocity of the gas particles, allowing for a higher interaction with the surface. The tapering of the GaSb nanowires can be explained by the fact that the axial and radial growth rates of wires remain constant during the growth period, but the longer exposure of the nanowire base causes more build up of GaSb thin film on the wire base than compared to the wire tip. Consequently, the probability that the wires will have more thin film build-up and tapering increases at higher than lower temperatures in part because the gas particles remain in the chamber for a longer residence time, and also because of the higher decomposition rate of the precursors.

Variations in V/III ratios produced most significant results for wires grown at 100 Torr, 500˚C, with a V/III ratio of 0.5. Wires grown at these conditions exhibited some preferential growth direction and very little tapering. GaSb has a native defect such that when grown at normal conditions, this compound semiconductor is unintentionally doped *p*-type. The defect arises from a Sb deficiency in the lattice structure of GaSb in addition to the Ga native acceptor being an anti-site defect.[10, 11] A lower V/III ratio implies that the wires formed will be highly *p*-type due to the larger amount of Ga as compared to Sb atoms. According to other authors, a high residual acceptor concentration in the wires will produce photoluminescence (PL) spectra with a strong peak as a result of the formation of more native acceptors.[11] It has also been found that when the V/III ratio shifts away from unity, the growth rate of GaSb decreases, which may account for the better quality wires found at 100 Torr, 500˚C with V/III ratio of 0.5. [12] In terms of high carrier mobility, different optimum V/III ratio exists for different pressures, and the electrical quality of wires grown at the aforementioned conditions cannot be stated without further research.

Densely distributed nanowire growth was observed for samples grown on Si that had been etched with the BOE technique before growth for conditions where pressure was decreased from 300 Torr to 100 Torr at 500˚C with V/III ratio of 1, and 100 Torr at 500˚C with V/III ratio of 2. It is possible that these results are due to the removal of the thin oxide film that forms on the sample surface due to air exposure, allowing more of the TMG and TMSb gas particles to interact with the sample and absorb to the catalysts.

FUTURE RESEARCH

Due to time constraints and equipment failure during the nine-week duration of this National Science Foundation (NSF) funded research program, the project was unable to be completed to its full extent. Additional work needed on this project includes the electrical and optical characterization of the GaSb nanowires. Transmission electron microscopy (TEM), photoluminescence (PL) spectroscopy, and 4-point backgate I-V measurements need to be performed on these samples to further characterize these structures and test their performance and functionality.

Annual Research Journal, Vol. V
Electrical Engineering Research Experience for Undergraduates

ISBN 0-913260-07-X (http://www.ee.psu.edu/reu/)

CONCLUSION

Due to the structural characteristics and electrical properties of the GaSb nanowires and their potential for integration into current semiconductor technologies, the growth of GaSb wires on Si and sapphire substrates was investigated to further the understanding of how controlled growth of these wires can be achieved. Optimal growth conditions of growing GaSb nanowires on both Si and sapphire substrates were discussed. Nanowires were grown under a number of conditions such as varying growth temperature, pressure, and V/III ratios, and the resulting wires were measured and characterized.

ACKNOWLEDGEMENTS

This material is based upon work supported by the National Science Foundation under Grant No. EEC-0244030. Special thanks to Dr. Joan Redwing, Dr. Theresa Mayer, and Robert Burke at the Pennsylvania State University at University Park for the selection of the project topic and their guidance.

REFERENCES

[1] C. Ruiz, J. Plaza, V. Bermudez, E. Dieguez. Study of induced structural defects on GaSb films grown on different substrates by the liquid phase epitaxy technique. *J. Phys.: Condens. Matter*, 14: 12755-12759, 2002.

[2] Y. Cui, L. Lauhon, M. Gudiksen, J. Wang, C. Lieber. Diameter-controlled synthesis of single-crystal silicon nanowires. *Applied Physics Letters*, 78(15):2214-2216, April 2001.

[3] Y. Guo, J. Zou, M. Paladugu, H. Wang, Q. Gao, H. Tan, C. Jagadish. Structural characteristics of GaSb /GaAs nanowire heterostructures grown by metal-organic chemical vapor deposition. *Applied Physics Letters*, 89(23): 231917-1-3, 2006.

[4] F. Qian, Y. Li, S. Gradecak, D. Wang, C. Barrelet, C. Lieber. Gallium Nitride-based nanowire radial heterostructures for nanophotonics. *Nano Letters*, 4(10): 1975-1979, September 2004.

[5] K. Yamamoto, H. Asahi, K. Inoue, K. Miki, X. Liu, D. Marx, A. Villaflor, K. Asami, S. Gonda. The n-type and p-type doping of GaSb and AlGaSb grown by metalorganic molecular beam epitaxy. *Journal of Crystal Growth*, 150: 853-857, 1995.

[6] A. Lugstein, J. Bernardi, C. Tomastik, E. Bertagnolli. Synthesis of nanowires in room temperature ambient: a focused ion beam approach. *Applied Physics Letters*, 88(16): 163114-1-3, 2006.

[7] N. Wang, Y. Tang, Y. Zhang, C. Lee, S. Lee. Nucleation and growth of Si nanowires from silicon oxide. *Rapid Communications*, 58(24): 16024-16026, December 1998.

Annual Research Journal, Vol. V
Electrical Engineering Research Experience for Undergraduates

ISBN 0-913260-07-X (http://www.ee.psu.edu/reu/)

[8] R. Wagner, W. Ellis. Vapor-Liquid-Solid mechanism of single crystal Growth. *Applied Physics Letters*, 4(5): 89-90, March 1964

[9] E. Bakkers, M. Borgstrom, M. Verheijen. Epitaxial growth of III-V nanowires on group IV substrates. *MRS Bulletin*, 32: 117-122, February 2007.

[10] W. Hu, Z. Wang, F. Su, Y. Dai, S. Wang, Y. Zhao. Gallium antisite defect and residual acceptors in undoped GaSb. *Physics Letters A*, 332: 286-290, September 2004.

[11] E. Chidley, S. Haywood, A. Henriques, N. Mason, R. Nicholas, P. Walker. Photoluminescence of GaSb grown by metal-organic vapour phase epitaxy. *Semiconductor Science Technology*, 6: 45-53, 1991.

[12] A. Subekti, E. Goldys, T. Tansley. Growth of gallium antimonide (GaSb) by metalorganic chemical vapour deposition. *IEEE*, 1997.

Annual Research Journal, Vol. V
Electrical Engineering Research Experience for Undergraduates

ISBN 0-913260-07-X (http://www.ee.psu.edu/reu/)

Annual Research Journal, Vol. V
Electrical Engineering Research Experience for Undergraduates

ISBN 0-913260-07-X (http://www.ee.psu.edu/reu/)

LONGITUDINAL PIEZOELECTRIC COEFFICIENT OF PMN-PT CRYSTAL AS FUNCTION OF TEMPERANCE AND FREQUENCY BY DYNAMIC INTERFEROMETRIC MEASUREMENT

Jarrett Blythe*, Hongbo Liu[+], and Ruyan Guo[#]

Department of Electrical Engineering and
Materials Research Institute
The Pennsylvania State University
University Park, PA 16802

* Undergraduate student of
Department of Optical Engineering
Norfolk State University
Norfolk, VA 23504

ABSTRACT

Piezoelectric devices have a vast amount of applications including their use in sensors, actuators, and various forms of electromechanical energy transforms. In order to design these devices, piezoelectric properties as functions of frequency and temperature are essential. A highly sensitive optical interferometer is adapted to evaluate the piezoelectric coefficient of the test samples. Linear scan, dynamic modulation, and phase sensitive lock amplification permit the measurement to be conducted in a wide range of frequencies from a few Hz to 100 kHz with sensitivities of better than ~10 pm. A modified optical stage is designed and constructed with both temperature control and electrical testing capabilities. The sample stage is used in this study to control the amount of heat that is absorbed by the sample from room temperature to about 200 degrees Celsius. Experimental results are obtained and reported for a high strain single crystal sample $0.68Pb(Mg_{1/3}Nb_{2/3})O_3$-$0.32PbTiO_3$ (PMN-32PT). The longitudinal piezoelectric d_{33} coefficient decreases with increasing frequencies but go through significant changes near a phase transition temperature. Poling effect and the resonant spectra of the sample were also studied to understand the long range order of polarization and its contribution to the piezoelectric properties.

[+] Graduate Mentor
[#] Faculty Mentor

Annual Research Journal, Vol. V
Electrical Engineering Research Experience for Undergraduates

ISBN 0-913260-07-X (http://www.ee.psu.edu/reu/)

INTRODUCTION

With the understanding of piezoelectric properties of crystal samples comes the ability to develop electromechanical energy transduction devices. Limitations on devices such as sensors and actuators may depend on the limit of the piezoelectric materials that are used within them. A piezoelectric effect occurs when a dimension change of a sample results in the development of an electric field (along with induced polarization), or conversely an applied electric field to a sample resulting in a change in the sample's dimension, known as a converse piezoelectric effect.[1] Longitudinal effects refer to the dimensional change $\Delta L/L_0$ in parallel with the application of an electric field, or vice versa, where L_0 is the initial dimension free from stress or electric field. Although there have been extensive experiments performed on the single crystals $(1-x)Pb(Mg_{1/3}Nb_{2/3})O_3$-$xPbTiO_3$ (PMN-PT) due to their excellent electromechanical application potentials, the measurements were typically conducted by d_{33} meters[2] under small signal condition according to IEEE test standards[3], or by hysteresis loop measurement under high electric field. There has been scarce report on frequency dependence of piezoelectric coefficients, even fewer the temperature dependence of such property. Although PMN-PT has large piezoelectric effect, a thin plate-shaped sample with sub-mm thickness produces sub-nm displacement which makes accurate measurement a very challenging task.

This research is designed to make high precision measurement using optical interferometric technique, in an attempt to obtain longitudinal d_{33} property of samples of thin disk-shape. In addition, the d_{33} will be measured as function of electric field frequency as well as temperature. The material parameter thus obtained will allow a better understanding of how piezoelectric devices react to changes in the environment and an insight to the limit or extent to which they may be able to function.

EXPERIMENTAL DESCRIPTION

Interferometry refers to the measurements that rely upon the interference of two (or more) light beams. There are various kinds of interferometers, some of which have very specific uses, others of which are more generally applicable to the study of optical phenomena. In this experiment, a setup known as the Michelson Interferometer was used.[4] Michelson Interferometer is the most widely known and is probably the most versatile interferometer.

Annual Research Journal, Vol. V
Electrical Engineering Research Experience for Undergraduates

ISBN 0-913260-07-X (http://www.ee.psu.edu/reu/)

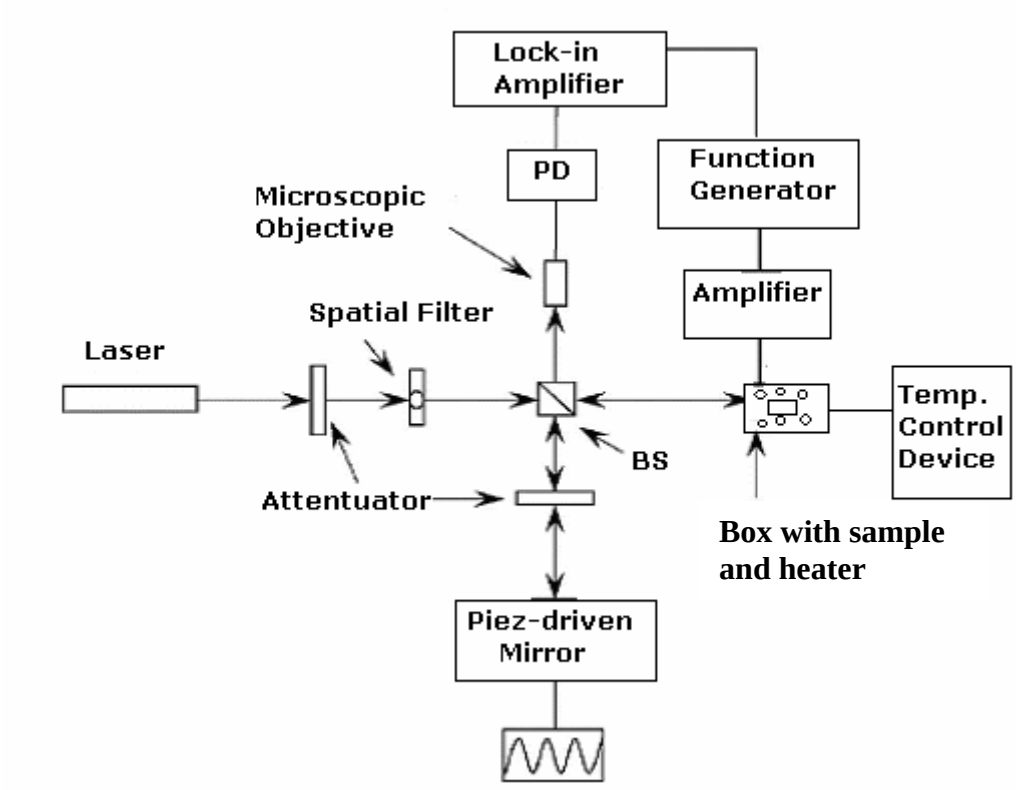

Fig. 1. Schematic Configuration of the Dynamic Interferometric Measurement

In this setup, a laser beam from a He-Ne laser is first sent through an attenuator to reduce the total intensity of the laser for safety purposes. The laser is then reflected off a mirror to ensure that when the beam is reflected directly back to the laser source and cause interference. The laser then continues through a pinhole spatial filter to trim off the duller outer edges of the laser making the intensity uniform throughout. After the beam is prepared, it is mounted to a holder within a temperature controlled device that will control the temperature of the sample throughout the experiment. This temperature controlled device will be a heater surrounded by pure, carbonized copper (Cu). This temperature controlled device will be hooked to a microprocessor-interfaced control unit that will sense the temperature and regulate the heating with ramping and soaking functions.

The differences between path lengths of reference wave and signal wave will remain constant and will be changed slightly when a voltage is applied to the sample and a small distortion occurs. The reference beam is reflected 90 degrees and then again reflected off a piezo-driven mirror. A piezo-driven mirror is a mirror which is mounted to a fixture that oscillates toward and away from the beam splitter. One reason that this mirror oscillates is to reduce noise. The other reason is to make sure that the system is working at $\pi/2$ points. This

Annual Research Journal, Vol. V
Electrical Engineering Research Experience for Undergraduates

ISBN 0-913260-07-X (http://www.ee.psu.edu/reu/)

interferometry system is very sensitive to mechanical oscillations and even just talking or slightly moving around it will disrupt the system due to turbulence of air. For this reason this experiment is generally performed at night when less people will be around the work station. Trying to adjust the two path lengths equal would be nearly impossible since this technique is trying to detect path differences from the displacement which can be in angstroms.

The data is taken at $\pi/2$ points because it is at these points where the system's intensity is most sensitive due to change in length. The $\pi/2$ point occurs when the rate of change of the sinusoid is the greatest. These points are optimal for the measurements to be taken at because for a small change in path length difference there will be a large intensity change. Since it is hard to locate the exact $\pi/2$ points, the length of the reference beam is oscillated around the $\pi/2$ points by the piezo-mirror. After these beams are combined at the beam splitter, they travel through a magnifier and then to a photo detector. The photo detector translates the intensity of the light at that point into voltage values that can be analyzed.

The waveform captured on the oscilloscope reveals the maximum signal from the lock-in amplifier (V_{out} ch.2) corresponds to the maximum point (ch.1) of the phase modulation slope at $\pi/2$. The output of the lock-in amplifier is then connected to a data acquisition device. The program currently used is developed within LabView. The LabView software gives a list of about 10,000 points taken during the 5 minutes the system is run. However, the only points needed to determine the piezoelectric coefficients are the maximum values.[5]

The phenomenon known as the piezoelectric effect can be expressed as:

$$(\Delta L/L_0)=d\,E$$

where E is electric field strength, d is known as the piezoelectric coefficient having unit of typically [m/V]. When the strain is developed along the same direction in which the electric field is applied, it is also more specifically refereed to as longitudinal piezoelectric effect:

$$(\Delta L_3/L_0)=d_{33}\,E_3$$

The piezoelectric property can also be caused by applying stress that generates polarization (known as direct polarization effect) with equivalent piezoelectric *d*; a pressure X applied on the surfaces along the thickness L_0 direction results in a polarization (surface change per area) P of the material.

Before any testing can take place, the sample PMN-PT crystal must be prepared by surface electrode (by gold sputtering). Also, the sample crystal must be poled (at room temperature, under 5kV/cm for 3 min.) so that the sample may posses a net acentric crystallographic symmetry that permits charge separation. The method used to verify the sample is properly poled is to observe its piezoelectric resonance spectrum. Also, there must electric (Ag) wiring applied to the sample to connect the electric modulation field. Besides wiring, attached to the sample will be mirrors so that the laser may bounce off the crystal sample and recombine with the reference beam so that interference may be measured.

Annual Research Journal, Vol. V
Electrical Engineering Research Experience for Undergraduates

ISBN 0-913260-07-X (http://www.ee.psu.edu/reu/)

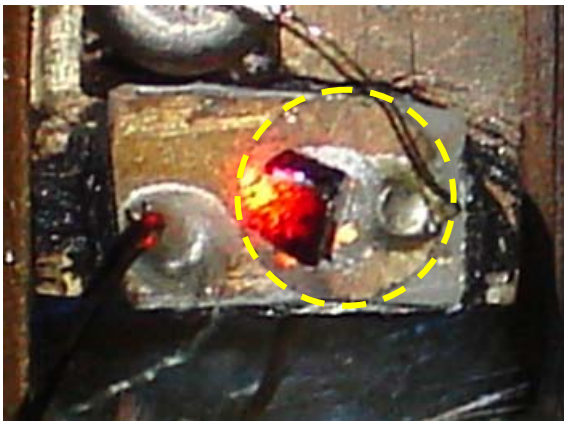

Fig. 2. Disc shaped PMN-PT crystal sample (encircled) is attached to sample holder by silver epoxy; with wiring attached to sample on top and bottom. The laser light is reflecting off the mirror affixed on surface of the sample.

General expression of EM wave function is used to describe the interference light intensity I:

$$I = \frac{1}{2}\left(I_{MAX} + I_{MIN}\right) + \frac{1}{2}\left(I_{MAX} - I_{MIN}\right)\cos\left\{\frac{2\pi}{\lambda}(2\Delta L)\right\}.$$

When the reference beam and the probing beam have a preset phase difference $\pi/2$, a small electric ac signal ($V_{app.}$ or $V_{lock\text{-}in}$) applied on the sample will induce linear displacement, due to piezoelectric effect. A very small displacement will cause intensity change proportional to the modulation field. The intensity change is measured by a lock-in amplifier as RMS value of V_{out}. The proportionality relation can be shown as:

$$\frac{2\pi(2\Delta l)}{\lambda} = \frac{V_{out}}{V_{lock-in}},$$

where Δl is the small displacement caused by the sinusoidal voltage ($V_{lock\text{-}in}$) applied on the sample.

$$2\Delta l = \frac{d_{33} \cdot V_{p-p}}{\sqrt{2}}$$

Substitute the above relation, we get:

$$d_{33} = \frac{\lambda}{\sqrt{2}\pi} \frac{V_{OUT}}{V_{lock-in} \cdot V_{p-p}} \quad \text{and}$$

Annual Research Journal, Vol. V
Electrical Engineering Research Experience for Undergraduates

ISBN 0-913260-07-X (http://www.ee.psu.edu/reu/)

$$\Delta l = d_{33} E \cdot L_0 = d_{33} \cdot V_{lock-in}$$

Note here this technique does not require accurate determination of the sample thickness to find piezoelectric coefficient (which is quite an advantage as the thickness of very thin sample may not be easy to know for certain.

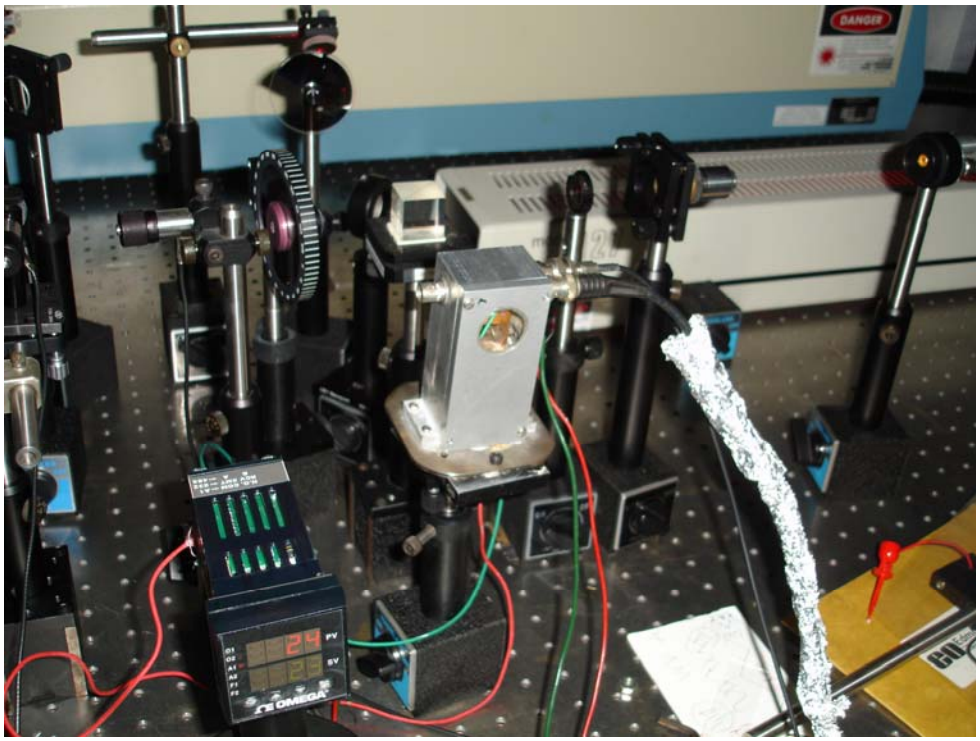

Fig. 3 Temperature Stage with Sensing and Controlling Unit

It has been noted that the sample will be held by a copper (Cu) sample holder, but the holder would also be attached to a heater surrounded by pure, carbonized Cu. This is done so that heat may easily be conducted to the sample, but to prevent the short-circuit of the sample, a alumina insulator was installed under the sample to protect it from outside noise and direct contact with the Cu base.

Two heater wires and a thermocouple are also connected to the temperature control device. By providing a set point, the temperature control device enables the heater to reach to a desired temperature. In order for this operation to work to full capability, a glass windowed metal box is built encasing the sample and the heating stage so no heat is allowed to escape. Metal pins are connected through the temperature stage for measurement and monitoring purposes. This way, everything can be measured without loss of heat from inside the box and the surface of the sample.

Annual Research Journal, Vol. V
Electrical Engineering Research Experience for Undergraduates

ISBN 0-913260-07-X (http://www.ee.psu.edu/reu/)

RESULTS & DISCUSSION

Before making further steps on the temperature dependence, the similarities and differences of the poled and partially depoled PMN-PT crystals must be taken into account. An ample amount of data, presented in Figs. 4-6, was collected at room temperature to exemplify the poled and partially depoled sample's response to the applied electric field at various frequencies, ranging from approximately 10 Hz to 102 kHz.

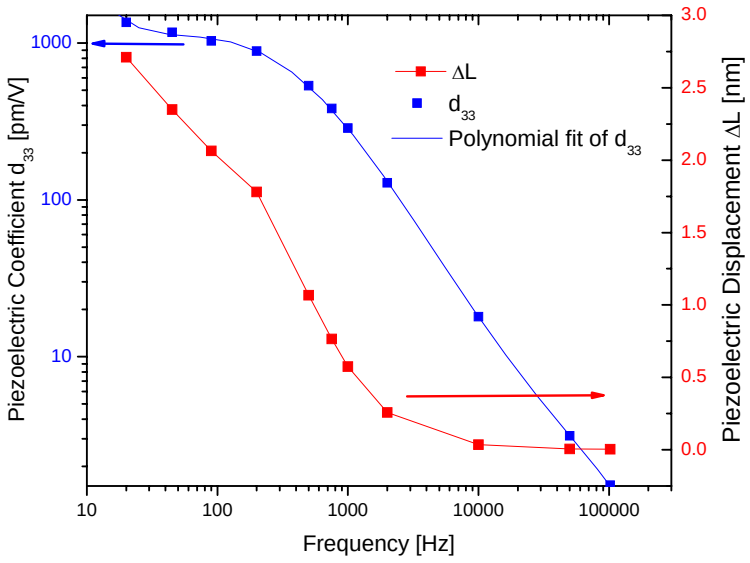

Fig. 4 Piezoelectric d_{33} coefficient (left scale) and displacement (right scale) of a partially de-poled PMN-PT crystal.

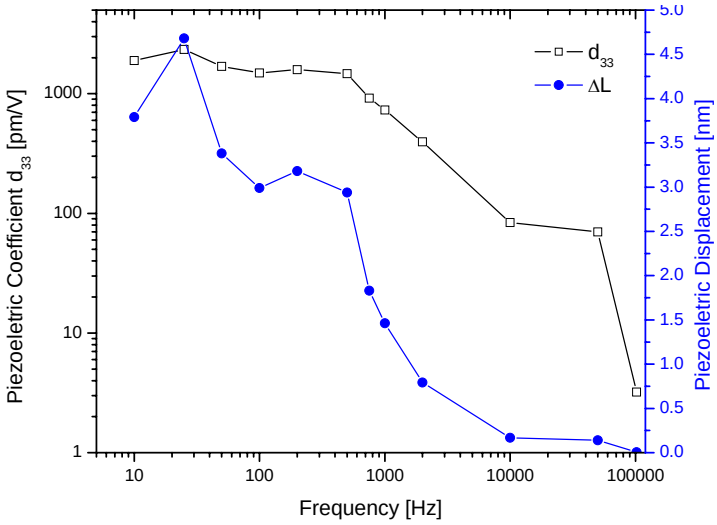

Fig. 5 Piezoelectric d_{33} coefficient (left scale) and displacement (right scale) of a poled PMN-PT crystal placed inside temperature chamber.

Annual Research Journal, Vol. V
Electrical Engineering Research Experience for Undergraduates

ISBN 0-913260-07-X (http://www.ee.psu.edu/reu/)

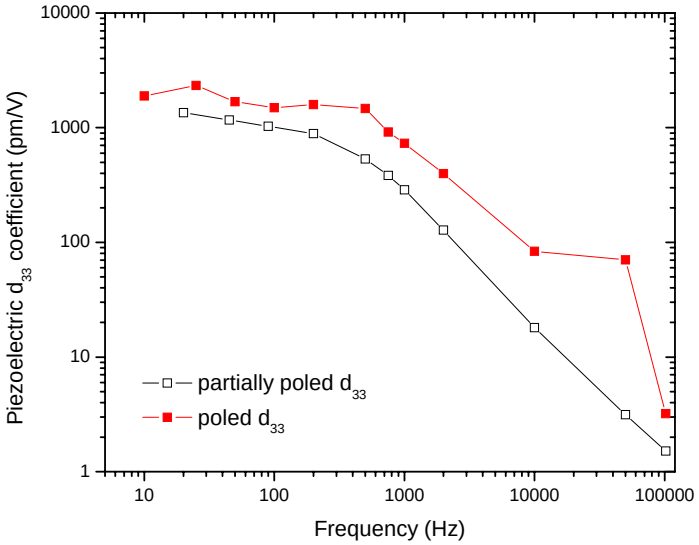

Fig. 6
Comparison of piezoelectric d_{33} coefficient in log. scale of poled (solid symbol) and partially depoled (hollow symbol) PMN-PT crystals.

It can be seen from Fig. 4 that the d_{33} of a partially depoled PMN-PT sample decreases monotonically with increase in frequency from 10Hz to 100kHz. This is in general expected as charge separation and mechanical displacement are time dependent processes. Similar to the partially depoled sample of PMN-PT, as seen in Fig. 5, the piezoelectric d_{33} coefficient of a poled sample decreases with increasing frequency, but non-monotonically showing complex behavior. Below 1kHz, the d_{33} values are uniformly high in poled sample varying between 1400 to 2500 pm/V (that is to compare with PZT ceramics that has d_{33} typically in the range of 300-500 pm/V).

It is very important to note that the optical interferometer technique allows one of the most precise evaluations compared to essentially any other conventional methods. The intricate quantities of displacement precisely measured can be orders smaller than an angstrom; although due to the extraordinarily large d_{33} coefficient, the measured displacements of PMN-PT as shown in Figs. 4-6 are in the order of nanometers.

As it is evident from Fig. 6, the poled sample has overall high piezoelectric coefficients compared with the partially depoled sample. Proper poling and handling therefore are important for device performance. To verify the effectiveness of the poling, the PMN-PT sample was measured using d_{33} meter at 100Hz. The d_{33} value obtained (1,470 pm/V) gives close agreement with the interferometric measured results. Additionally, piezoelectric resonance spectrum was also acquired, shown in Fig. 7 that confirmed the acentric crystallographic symmetry and the electromechanical resonances, the signature of a poled sample.

Annual Research Journal, Vol. V
Electrical Engineering Research Experience for Undergraduates

ISBN 0-913260-07-X (http://www.ee.psu.edu/reu/)

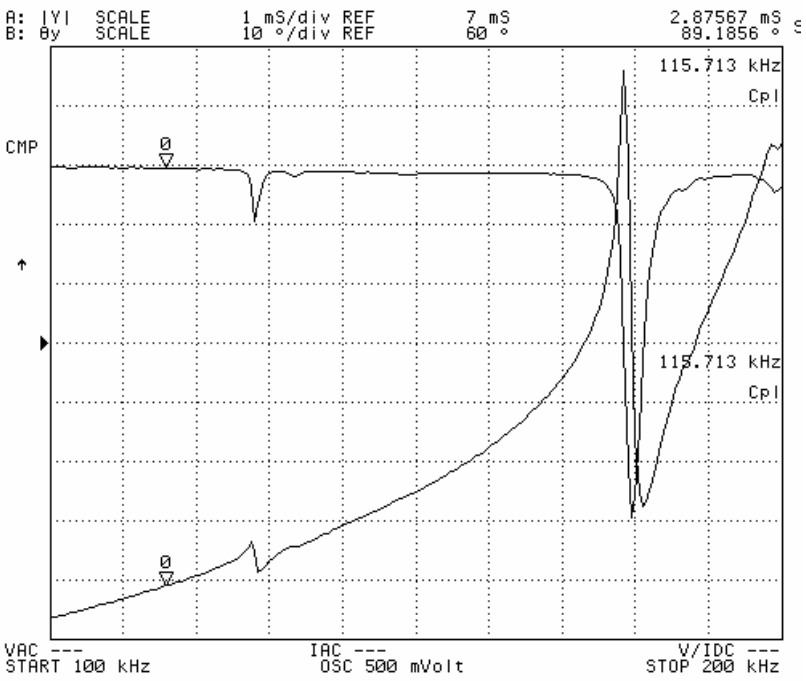

Fig. 7 Frequency spectra of admittance [Channel A] and phase angle [Channel B] of the poled PMN-PT between 100k Hz and 200k Hz

A temperature dependent piezoelectric measurement was conducted using the custom designed heater stage integrated with the interferometric system. PMN-PT sample was allowed to reach uniform temperature with the heater stage. At a selected frequency (100Hz) the measurement was conducted in various temperatures from 27 ^{o}C to 140^{o}C. The temperature variation, however, was relatively large (+/- 1^{o}C) in a single data scan/collection process due to the inadequately tuned controller parameters. As a result the temperature dependent piezoelectric measurement suffered higher noise than at constant temperatures, that could be overcome in future measurements. The results obtained, shown in Fig. 8, nonetheless are very revealing indicating two corresponding phase transitions in this sample. Accompanying the phase transitions, piezoelectric d_{33} coefficient goes through large change, reaching nearly 3,500 pm/V at ~85^{o}C. Another peak value (~750 pm/V) is obtained at near 120^{o}C. It is interesting to note that at temperatures well above the depolarization temperature, the crystal still maintains strong piezoelectricity (d_{33} ~300 pm/V at 140^{o}C). PMN-PT material's phase diagram is shown in Fig. 9 where two phase transitions in this composition, one at ~70^{o}C and one at >120^{o}C, were reported.[6]

Annual Research Journal, Vol. V
Electrical Engineering Research Experience for Undergraduates

ISBN 0-913260-07-X (http://www.ee.psu.edu/reu/)

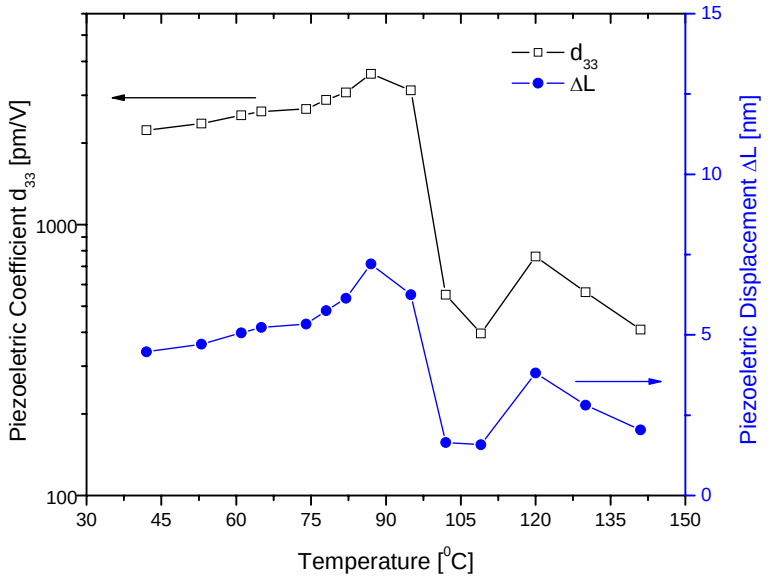

Fig. 8. Piezoelectric d_{33} coefficient (left scale) and piezoelectric displacement (right scale) as function of temperature (at 100 Hz).

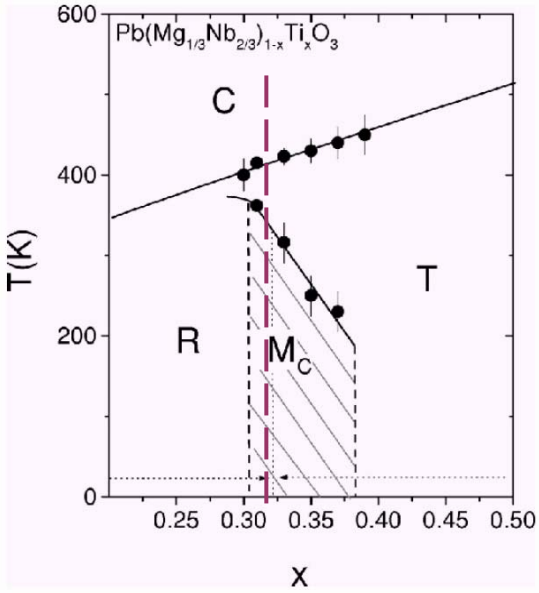

Fig. 9.
Phase diagram of PMN-PT showing (marked by the long dashed lines) two phase transitions for 32% PT.

SUMMARY

High precision optical interferometry system with temperature controlled sample configuration has been used to successfully determine the effect of temperature on the piezoelectric coefficient (d_{33}) and the piezoelectric displacement (ΔL) of a PMN-PT crystal. The piezoelectric coefficient in the poled PMN-PT crystal goes through two phase transitions below 140 degrees

Annual Research Journal, Vol. V
Electrical Engineering Research Experience for Undergraduates

ISBN 0-913260-07-X (http://www.ee.psu.edu/reu/)

Celsius. Near a phase transition temperature, peak values of d_{33} were found. At temperature higher than the ferroelectric-paraelectric phase transition, the sample is found not fully depoled with high/moderate piezoelectric coefficient remains. Overall properly poled samples have higher piezoelectric coefficients than partially depoled samples. In general the piezoelectric d_{33} coefficient decreases with increasing frequencies below a resonance frequency.

Careful tuning of the temperature controller parameters and the additional measurements with different poling conditions would be helpful in understanding of the temperature dependence as well as the resonance behavior on the piezoelectric effects.

ACKNOWLEDGEMENTS

Special thanks are given to the National Science Foundation and Penn State University for this research opportunity. JB would like to thank Kevin Deily for his interests and help. This material is based upon work supported by the National Science Foundation under Grant No. EEC-0244030.

REFERENCES

[1] Bernard Jaffe, William R. Cook, Hans Jaffe, *Piezoelectric Ceramics*, Techbooks (December 1989)

[2] e.g., Berlincourt Piezo d_{33} Test System

[3] ANSI/IEEE Standard 176-1987: IEEE Standard On Piezoelectricity.

[4] Ruyan Guo, EE422 Optical Engineering L abs Lecture Notes, #11, p. 2 (2007).

[5] Ruyan Guo, EE422 Optical Engineering Labs Lecture Notes, #11, p. 6-8 (2007).

[6] M. H. Lente, A. L. Zanin, S. B. Assis, I. A. Santos, J. A. Eiras, and D. Garcia, Ceramic Transactions, 136, 143 (2003).

Annual Research Journal, Vol. V
Electrical Engineering Research Experience for Undergraduates

ISBN 0-913260-07-X (http://www.ee.psu.edu/reu/)

Annual Research Journal, Vol. V
Electrical Engineering Research Experience for Undergraduates

ISBN 0-913260-07-X (http://www.ee.psu.edu/reu/)

FEMTOSECOND LASER BEAM SHAPING

Jason Okerman[*], Qian Xu[+], and Zhiwen Liu[#]

Department of Electrical Engineering
The Pennsylvania State University
University Park, PA 16802

*Undergraduate student of
Department of Electrical Engineering
Grove City College
Grove City, PA 16127

ABSTRACT

We studied one-dimensional femtosecond laser beam shaping. Lossless phase masks were designed to transform a one-dimensional Gaussian irradiance profile of an input femtosecond laser beam into a near-optimal flat-top profile which consolidates more than 90% of the total energy within the full-width half-maximum region. The resulting phase mask design will be used to fabricate ferroelectric diffractive optical elements (FDOE) to dynamically control the profile of the femtosecond laser beam.

[+] Graduate Mentor
[#] Faculty Mentor

Annual Research Journal, Vol. V
Electrical Engineering Research Experience for Undergraduates

ISBN 0-913260-07-X (http://www.ee.psu.edu/reu/)

INTRODUCTION

Laser beam shaping techniques have found many important applications, particularly in material processing and drilling [1,2]. Since the first paper by Roy Freiden [3] in 1965 introducing basic beam shaping ideas, interest and applications of laser beam shaping have increased steadily [4-7]. Many of the earlier work have been focused on continuous wave (CW) beam shaping. With the recent development of ultra-fast laser technology and the wide availability of these lasers, ultra-fast lasers have attracted a lot of interests for material processing applications and have been shown to have increased efficiency and accuracy for material ablation, etching, and precise laser cutting with less influence on the physical properties of the bulk material [8, 9]. The goal of this study is to design a one-dimensional phase mask to transform a femtosecond beam with a Gaussian intensity profile into a near-optimal flattop profile and to theoretically investigate the effect of beam shaping on the temporal properties of the pulses.

The three main methods currently used for beam shaping include magnification and aperture use, beam integration, and field mapping [1]. We chose the field-mapping technique here due to its relative ease to realize a dynamic beam shaper by using a ferroelectric diffractive optical element (FDOE) which can modulate the phase of an input Gaussian beam profile. In this paper we describe the design portion of the FDOE and results from computer simulations. Specifically, the modified Gerchberg-Saxton algorithm described in detail by Liu and Taghizadeh [10] was used in our work. This algorithm allows us to find a 'best case' phase distribution for the FDOE in order to achieve a flat-topped intensity profile with a theoretical convergence within the half-maximum region greater than 90%.

PHASE MASK DESIGN

As shown in Figure (1), the field-mapping techniques that we applied use a ferroelectric diffractive optical element (FDOE) to modulate the phase of the incoming laser beam. A thin lens, which computes the Fourier transform (FT) of the input field at the front focal plane [11] is used to produce the desired beam shape at the back focal plane of the lens. By controlling the phase distribution of the incoming light, we are able to manipulate output intensity profile after the Fourier transforming lens to a great degree. This paper describes the design of the FDOE and simulation portion of the research. The system was designed for a laser at center wavelength 800 nm, focused by of 50 mm focal length lens. The input beam size was chosen at 2 mm with a desired output spot of about 20 μm.
The design presented here relies on one-dimensional algorithms to design two phase masks (one horizontal, the other vertical) which could be overlaid to produce a flattop output profile with a square base. It should be noted that the

Annual Research Journal, Vol. V
Electrical Engineering Research Experience for Undergraduates

ISBN 0-913260-07-X (http://www.ee.psu.edu/reu/)

same methods can be applied in two dimensions to produce output profiles with circular or arbitrary shapes.

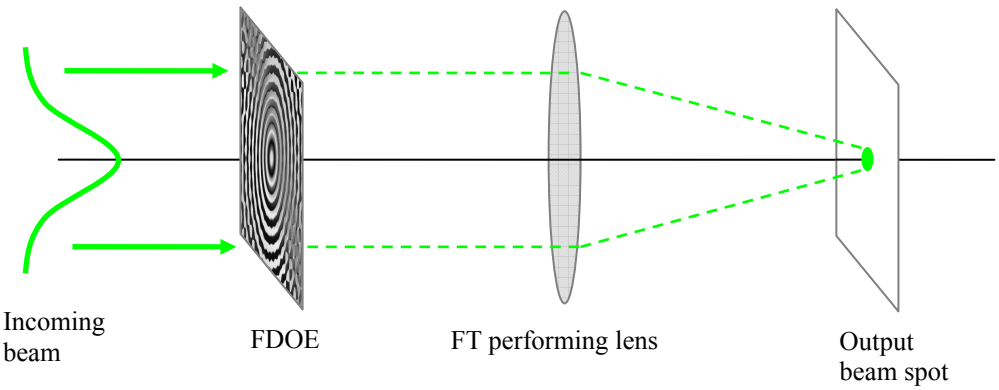

Figure (1): Set up of the beam shaping system

The one dimensional intensity profile of the unshaped laser is a Gaussian beam, given by the following equation,

$$I_{input} = e^{-x^2/r_0^2} \qquad (1)$$

where r_0 is the Gaussian radius at $1/e^2$ intensity, with a value of 2 mm. Without the FDOE, the intensity profile of the beam after passing through the lens would also have a Gaussian shape.

We used Gerchberg-Saxton (GS) equations [10] iteratively to mold the output towards the desired shape which is a square flat-topped profile of half width r_f = 17.6 μm. This process is described in detail in an article by Liu and Taghizadeh [10]. This method changes only the phase angle of the incoming beam profile, without modifying its amplitude. The method uses the ideal flat-top profile as a constraint, and by varying the incoming phase, allows the FT output to approach this model function. Pure GS iterations stabilize after about 50 repetitions, after which further iterations will yield little improvement. As shown in Fig. (2), this result is far from ideal.

Annual Research Journal, Vol. V
Electrical Engineering Research Experience for Undergraduates

ISBN 0-913260-07-X (http://www.ee.psu.edu/reu/)

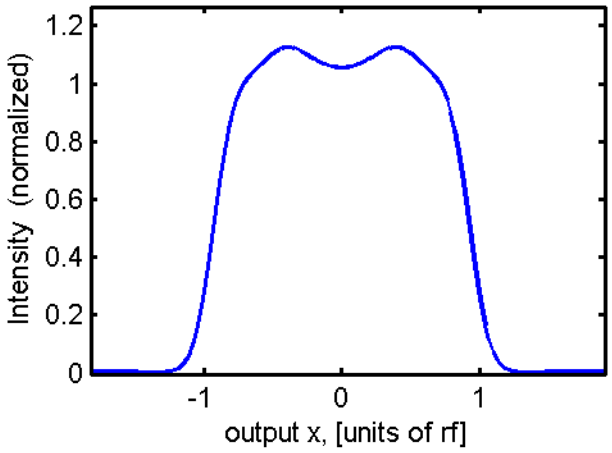

Figure (2): Output intensity distribution after 50 GS iteration.
Scale is in multiples of r_f, the output half-width

The results after 50 pure GS iterations can be improved by modifying the constraint function to something other than the ideal flat-top function and applying the GS method for a few more iterations. This modified constraint functions can be defined based on the difference between the desired and actual output profiles making it look like an 'overcorrected' version of the desired output. The following equation [5] was used to define this new constraint function,

$$E_{out}^{\mathrm{mod}\,ified} = \begin{cases} \left| \dfrac{E_{out}(u)}{FT\{E_{in}(x)\}} \right|^{c_1} & \text{for } |u| < r_f \\ 0 & \text{for } |u| \geq r_f \end{cases} \qquad (2)$$

where E_{out} is the output constraint function given in terms of energy (square root of Intensity), E_{in} is the input Gaussian shape receiving a phase shift, *FT{*}* represents a Fourier Transform, and r_f is the half-width of the output spot size.

By manipulating the constant c_1 in the above definition and the number of iterations, we found a best case output profile. We observed that after a finite number of iterations the output reaches its best shape, and further iterations causes the output to diverge and rapidly degenerate. This was different from the pure GS iterations which stabilized after 50 or more iterations. The near-optimal profile using this modified constraint function is shown in figure (3).

Annual Research Journal, Vol. V
Electrical Engineering Research Experience for Undergraduates

ISBN 0-913260-07-X (http://www.ee.psu.edu/reu/)

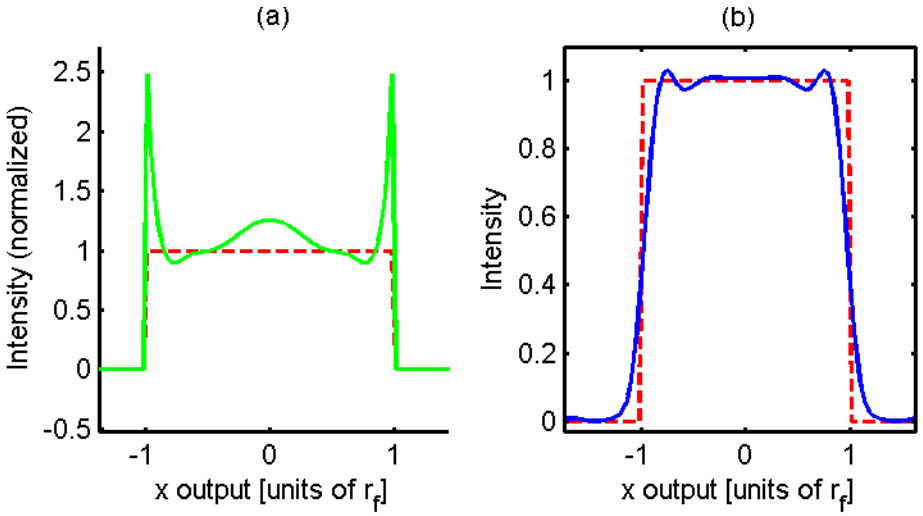

Figure (3): (a) Example modified constraint function with (b) improved output intensity profile using modified constraint. Dashed red line in both images represents an ideal flat-top shape.

The quality of output that can be reached by beam shaping is limited by the uncertainty principle. A dimensionless parameter referred to as β can be derived which indicates the maximum quality for a given set of values: [12]

$$\beta = \frac{2\sqrt{2\pi} \cdot r_0 r_f}{F\lambda} \qquad (3)$$

where r_0 is the Gaussian radius at $1/e^2$ intensity, r_f is the characteristic radius of the output profile, F is focal length of the focusing lens, and λ is the wavelength of the laser.

Larger values of β make it possible to get steeper skirts and shallower bumps on the output intensity profile. β can be improved by increasing the input beam radius, expanding output spot size, decreasing wavelength, or reducing focal length [12]. For a specified spot size, the easiest variable to change physically is the initial beam radius, r_0, using simple lens magnification. By changing β we were able to obtain a flatter output profile as shown in Fig. 4. A value of $\beta = 4.4$ was used to create the profile given in Fig. 3, above, whereas the improved profile given in Fig. 4 used a value of $\beta = 8.8$. We calculated that this shaped intensity profile converges more than 96% of the energy within the full-width half-maximum region.

Annual Research Journal, Vol. V
Electrical Engineering Research Experience for Undergraduates

ISBN 0-913260-07-X (http://www.ee.psu.edu/reu/)

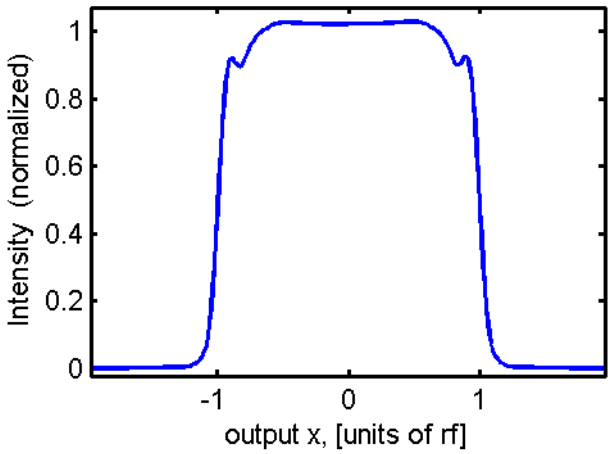

Figure (4): Output intensity profile achieved using increased β.

After the phase mask design process, we were able to model and simulate the shaping process taking into account various approximations and restrictions that would occur in manufacturing. The phase distribution, φ, of the final phase mask is given in Fig. 5.

The mask can be truncated so that its width is 3 or 4 times the input beam radius, r_0, with very little negative influence on the beam shape. Both the +φ and –φ solutions have the same effect. The graph shown in Fig. 5 uses an array of 70 grid points each applying a unique phase, with the half width of the mask set to 3 times r_0. We found that dividing the phase mask function into larger number of array points, beyond about a hundred, was mostly negligible in terms of its effect on the resulting beam profile. The 2π jumps in the phase mask shown below are very noticeable.

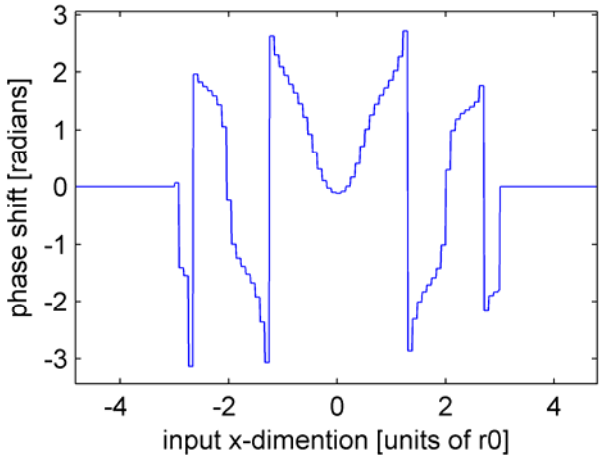

Figure (5): Phase distribution of optimized FDOE. Units along x-axis are given as multiples of r_0 since the same distribution can be scaled and applied to a different beam radius.

Annual Research Journal, Vol. V
Electrical Engineering Research Experience for Undergraduates

ISBN 0-913260-07-X (http://www.ee.psu.edu/reu/)

We also simulated the effects on beam shape from changes in orientation, size, and tilt of the incoming beam. Beam shaping using an FDOE is highly dependant on the beam being positioned through the center of the mask [12]. Also, if the beam width is a few percent greater than expected, the edges of the output profile will be raised, and if the beam is smaller the center will be raised up and the corners will be rounded off. Any of these misalignments, or having the FDOE tilted relative to the beam center, will cause the output intensity profile to degrade.

BEAM SHAPING WITH FEMTOSECOND LASER

Here we considered theoretical time-domain distortion effects on an ultra-fast pulsed laser passing through the shaping system. A femtosecond pulsed beam generated by a mode-locked laser has a wide frequency bandwidth. We modeled a 100 fs pulsed beam to calculate distortions. A 100 fs pulse has a spectrum with bandwidth of about 10 nm. Center wavelength used for simulations was 800 nm. Fig. 6 shows the unaltered pulse shape and its spectrum.

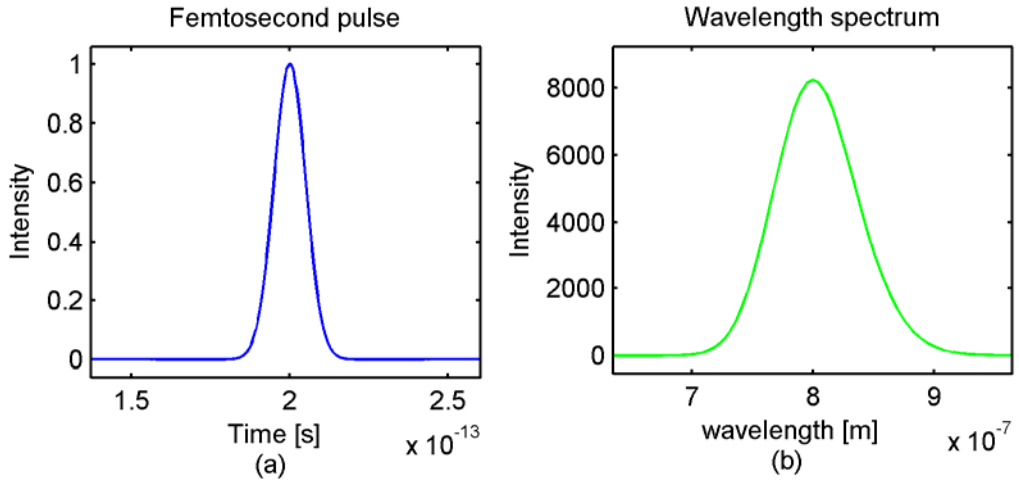

Figure (6): (a) 100 femtosecond pulse with (b) frequency spectrum (in terms of wavelength). Bandwidth is about 10 nm and is centered at $\lambda_0 = 800$ nm.

Using an FDOE, the amount of phase modulation that is applied to an incoming beam is inversely proportional to wavelength as given by the following equation:

$$\varphi = {2\pi \sum n_i l_i} \Big/ {\lambda} \qquad (4)$$

Annual Research Journal, Vol. V
Electrical Engineering Research Experience for Undergraduates

ISBN 0-913260-07-X (http://www.ee.psu.edu/reu/)

where λ is the wavelength in vacuum, n_i and l_i are the refractive index and thickness of each layer of material used to achieve the desired phase modulation at design wavelength. If φ_0 is the phase shift for the center wavelength of a femtosecond pulsed laser, then other wavelengths in its spectrum will be shifted by an amount according to the following relationship:

$$\varphi = \frac{\lambda_0}{\lambda}\varphi_0 \qquad (5)$$

We observed in our simulation that for longer wavelengths (where the phase shift will be less than ideal) the edges of the spatial profile were significantly lowered while the center was raised. For shorter wavelengths the reverse was true with a dip appearing in the center of the profile and the edges becoming over-emphasized. The amount of deformation increased with difference between the applied wavelength and the center wavelength. Examples of output intensity profiles for non-ideal wavelengths are shown in Figure 7.

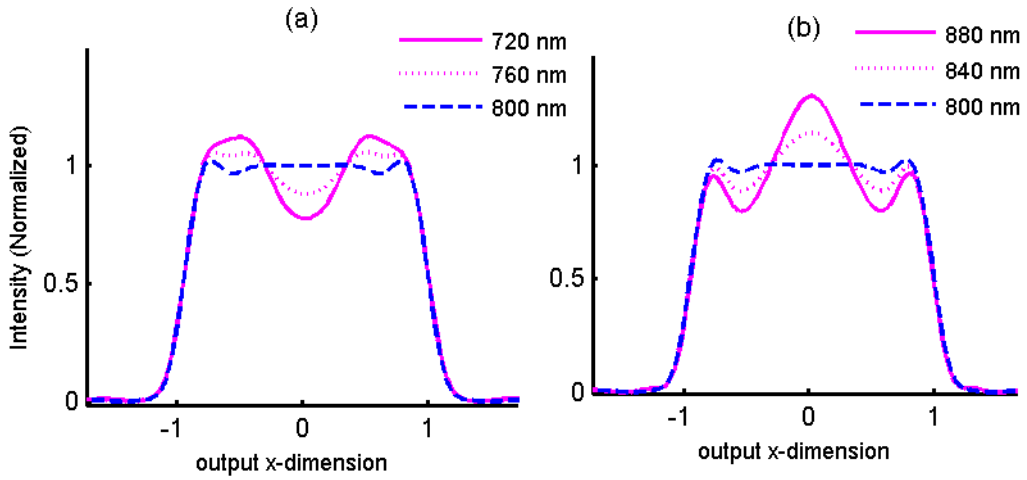

Figure (7): Deterioration in spatial intensity profile due to (a) wavelengths 5% and 10% shorter then λ_0 = 800 nm and (b) due to wavelengths 5% and 10% greater then λ_0.

By applying each of these wavelengths in the spectrum to the shaping system, we were able to obtain specific spectrum at each position on the output plane. Then using an inverse Fourier transform, we were able calculate the output pulse shape at each point. As shown in Figure (8), these pulses remained surprisingly stable, and appeared to retain very closely their original pulse shape and width.

Annual Research Journal, Vol. V
Electrical Engineering Research Experience for Undergraduates

ISBN 0-913260-07-X (http://www.ee.psu.edu/reu/)

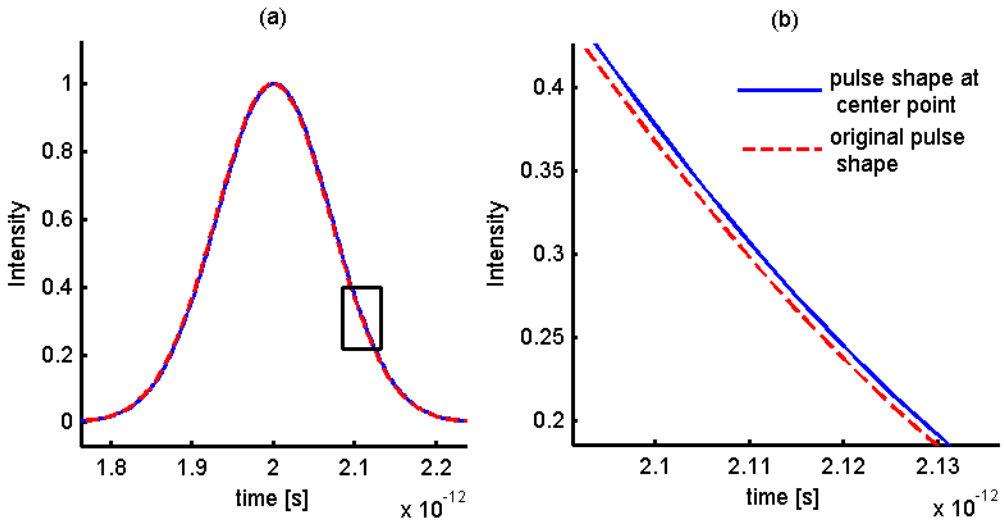

Figure (8): (a) 100 femtosecond pulse shape through center point of FDOE compared to original pulse shape. (b) Close up of edge of pulse shapes.

The only significant distortion we observed were at points which had extremely low intensity, much less then 0.1% compared to that of the center, and their effects on the overall pulse are negligible. For a 100 fs pulse with a 10 nm bandwidth, wavelengths with half-maximum intensity are about 800 ± 5 nm, and these wavelengths correspond to less than 1% change in the expected phase modulation by the FDOE. Since the intensity profile only degrades a small amount for this change in wavelength, and does so smoothly, we observed that the pulse shape suffered minimal distortion.

CONCLUSION

An algorithm using modified GS iterations were applied to design FDOE which achieved near-optimal flattop intensity profiles. We observed that a beam pulsed at 100 fs suffers very little distortion when passing through a shaping system. The pulse shape appears to remain very nearly Gaussian with no noticeable increase in pulse width, at least for all points of interests above 0.1% intensity.

This paper represents the design portion for shaping a femtosecond beam with some preliminary predictions. In future experimental work, the FDOE will be fabricated and the intensity and pulse profiles will be characterized and compared with the simulation results.

ACKNOWLEDGEMENT

This material is based upon work supported by the National Science Foundation under Grant No. EEC-0244030. J. O. thanks Peng Li for his help on time domain Fourier Transforms in Matlab.

Annual Research Journal, Vol. V
Electrical Engineering Research Experience for Undergraduates

ISBN 0-913260-07-X (http://www.ee.psu.edu/reu/)

REFERENCES

[1] F. M. Dickey, "Laser Beam Shaping" Optics & Photonics News, pp 31-35, April 2003

[2] C. Momma, S. Nolte, G. Kamlage, F. Alvensleben, A. von Tünnermann, "Beam delivery of femtosecond laser radiation by diffractive optical elements" Applied Physics A: Materials Science & Processing, Vol. 67, No. 5: pp 517-520, Nov 1998

[3] B. R. Freiden, Appl. Opt. 4 (11): pp 1400-1403 (1965).

[4] Y Kuroiwa, N Takeshimaa, Y Naritaa, S Tanakaa, K Hiraob, "Arbitrary micropatterning method in femtosecond laser microprocessing using diffractive optical elements", Optics Express Vol. 12 No. 9: pp 1908-15, May 2004

[5] Li Q, Gao HD, Dong YH, Shen ZC, Wang Q, "Investigation of diffractive optical element for shaping a Gaussian beam into a ring-shaped pattern" Optics and Laser Technology 30 (8): pp 511-514 Nov. 1998

[6] N Sanner, N Huot, E Audouard, "Programmable focal spot shaping of amplified femtosecond laser pulses" Optics Letters, Vol. 30, No. 12, pp 1479-81, June 2005

[7] O Ripoll, V Kettunen, and H Herzig, "Review of iterative Fourier-transform algorithms for beam shaping applications" Optical Engineering, Vol 43 (11): pp 2549-2556, Nov. 2004

[8] Barsch N, Korber K, Ostendorf A, Tonshoff KH, "Ablation and cutting of planar silicon devices using femtosecond laser pulses" Applied Physics: Materials Science & Processing, vol. 77, No. 2: pp 237-242 , July 2003

[9] S. Mailis, I. Zergioti, G. Koundourakis, A. Ikiades, A. Patentalaki, P. Papakonstantinou, N. Vainos, and C. Fotakis "Etching and printing of diffractive optical microstructures by a femtosecond excimer laser" Applied Optics, Vol. 38, No. 11, April 1999

[10] J. Liu, M. Taghizadeh, "Iterative algorithm for the design of diffractive phase elements for laser beam shaping", Optical Letters, Vol. 27 (16), August 2002

[11] J. W. Goodman, "Introduction to Fourier Optics" (3rd) Roberts & Company, Englewood, CO 2005

[12] F. M. Dickey, S. C. Holswade, "Laser Beam Shaping: theory and techniques," Marcel Dekker, NY, 2000

Annual Research Journal, Vol. V
Electrical Engineering Research Experience for Undergraduates

ISBN 0-913260-07-X (http://www.ee.psu.edu/reu/)

INVESTIGATION OF THE ZEEMAN EFFECT FOR QUADRUPOLE RESONANCE IMAGING

Jacqueline N. Queen*, Jeffrey L. Schiano[#], and Donald J. Natale[+]

Department of Electrical Engineering
The Pennsylvania State University, University Park, PA 16802

* Undergraduate Student of
Department of Physics and Engineering
West Virginia Wesleyan College
Buckhannon, WV 26201

ABSTRACT

Magnetic resonance imaging (MRI) systems employ costly superconducting magnets to generate static magnetic fields on the order of one Tesla. This paper investigates an alternative strategy that uses quadrupole resonance to avoid the requirement for large static magnetic fields. In both MRI and quadrupole resonance imaging (QRI) systems, a method is needed for spatially encoding the location of nuclei within the imaged material. In MRI, because the resonant frequency is directly proportional to the applied magnetic field, nuclei location is easily encoded using a static magnetic field gradient, and the image is recovered using Fourier transform analysis. On the contrary, in QR, the resonant frequency is less sensitive to static magnetic fields, and because the effect depends on the square of the field amplitude, Fourier imaging techniques are not easily applicable. In the last decade researchers have proposed two different techniques for encoding spatial information in QRI experiments. The first method uses static magnetic field gradients as in MRI, while the second method requires a spatial gradient in the radio frequency pulse used to excite a QR response. This paper investigates the potential for using magnetic field

[+] Graduate Mentor
[#] Faculty Mentor

Annual Research Journal, Vol. V
Electrical Engineering Research Experience for Undergraduates

ISBN 0-913260-07-X (http://www.ee.psu.edu/reu/)

gradients in QRI. As a starting point, the effect of uniform and gradient magnetic fields on the location and width of the QR line shape is studied by analyzing the Fourier transform of the free induction decay. From these results, a method for generating a one-dimensional quadrupole image using a static magnetic field gradient is demonstrated.

INTRODUCTION

Overview

Magnetic resonance imaging (MRI) scanners require a superconducting magnet that accounts for a significant fraction of the initial expense and operating costs of the scanner. In a contrast, a quadrupole resonance imaging (QRI) scanner does not require a superconducting magnet, and is correspondingly less expensive to purchase and operate.

Several significant challenges must be overcome to engineer a commercially viable QRI scanner. First, the signal-to-noise ratio (SNR) in measuring a magnetic resonance (MR) signal is significantly higher that of quadrupole resonance (QR) signal. In both MRI and QRI the resonance signal is observed using a Faraday law sensor, and so the amplitude of the induced voltage is proportional to the signal frequency. In MRI the signal frequency is proportional to the strength of the applied static magnetic field, which is about 64 MHz in clinical MRI scanners. In contrast, the QR signal frequencies are typically less than 5 MHz for nitrogen nuclei, which is the most abundant element admitting a QR signal in the human body. Unlike MR, where the signal frequency is set by the strength of the external magnetic, in QR the signal frequency is set is by the electrostatic interaction between the nucleus and the surrounding electron cloud[1].

Another challenge is finding a method for spatially encoding the location of nuclei. In MRI scanners the signal frequency is directly proportional to the strength of the applied magnetic field. This makes it possible to spatially encode nuclei location using static magnetic field gradients and to recover an image using Fourier transforms. This approach requires that the spectral width of the MR signal in the absence of a static gradient field is a factor of ten or smaller than the spectral width of the MR signal in the presence of a static gradient field. This technique is not directly applicable to QRI scanners for two reasons. Firstly, the QR signal frequency varies with the square of the applied magnetic field. Secondly, the spectral width of the QR signal in the presence of a static gradient field is on the same order of magnitude as the spectral width in the absence of the gradient.

During the past decade, several researchers have presented alternative techniques for spatially encoding the position of nuclei for QRI. These techniques include static magnetic field gradients[2] and spatial gradients in the radio frequency (RF) pulses used to excite a QR signal[3,4]. This paper describes the effect of uniform and gradient magnetic fields on the QR signal using

Annual Research Journal, Vol. V
Electrical Engineering Research Experience for Undergraduates

ISBN 0-913260-07-X (http://www.ee.psu.edu/reu/)

experimental data, and utilizes the observed effect to generate an image of a QR sample.

Quadrupole Resonance

QR is a radio frequency spectroscopy technique closely related to MR spectroscopy[1,5]. The QR signal originates from the interaction of the electric field of the nucleus with the gradient of the electric field generated by the surrounding electronic charges. The electric field gradient is characterized by an electric field gradient (EFG) tensor that contains nine elements. Because of symmetry and the requirement that Lapalce's equation holds at the center of the nucleus, the EFG tensor is described using two parameters. The parameter *eq* denotes the largest gradient, while the parameter $\eta \in [0,1]$ is a measure of the axial symmetry of the EFG tensor.

The spatial distribution of the nuclear charge density is described using the electric quadrupole moment tensor, which also contains nine elements. Because of symmetry of the nuclear charge distribution, the tensor can be described using a single parameter eQ. The axis of symmetry coincides with the axis of intrinsic angular momentum, or spin, of the nucleus. The sign of the parameter describes the symmetry of the nuclear charge distribution. When eQ is zero, the charge distribution is spherically symmetric. For nitrogen nuclei, eQ is positive, and the charge distribution is ellipsoidal with the major axis corresponding to the axis of symmetry.

The interaction of the EFG tensor and the electric quadrupole moment tensor produces a torque on the nucleus. The torque is directed so that the symmetry axis of the nucleus is driven towards the axis of the largest electric field gradient. When eQ is nonzero, the nucleus possesses intrinsic angular momentum, and as a result, there is a torque-induced precession of the symmetry axis of the nucleus about the axis of the largest electric field gradient. As the intrinsic angular momentum of the nucleus is quantized, so are the electrostatic interaction energy levels and the preferred orientations of the nucleus. For nitrogen nuclei where the spin quantum number is one, there are three energy levels and three corresponding orientations.

Figure 1 shows a sketch of the three energy levels for nuclei with a spin quantum number of one, as is the case for nitrogen. Applying an external RF magnetic field, whose frequency corresponds to the energy difference between any two energy levels, changes the orientation of the nucleus, and hence its energy. The three possible excitation frequencies are determined by the EFG tensor parameters *eq* and η, as well as the electric quadrupole parameter *eQ,* as

$$\nu_{\pm} = \frac{3}{4} e^2 qQ \left(1 \pm \frac{1}{3} \eta \right) \tag{1}$$

$$\nu_d = \frac{1}{2} e^2 qQ\eta. \tag{2}$$

Annual Research Journal, Vol. V
Electrical Engineering Research Experience for Undergraduates

ISBN 0-913260-07-X (http://www.ee.psu.edu/reu/)

When the EFG possesses axial symmetry, η vanishes leaving a single transition frequency.

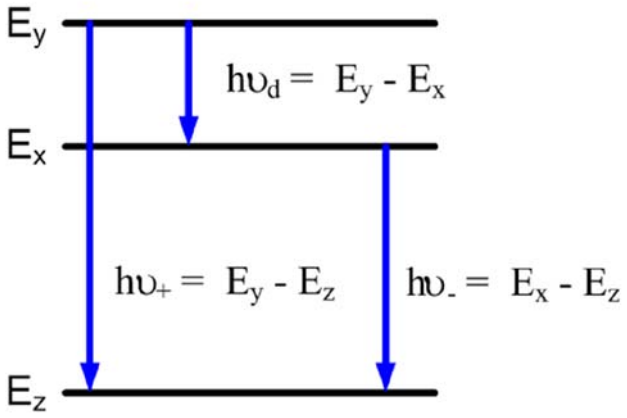

Figure 1: Energy levels and corresponding transition frequencies for nuclei with a spin quantum number of one.

The energy levels in Figure 1 are not sharp because of the spatial non-homogeneity of the EFG tensor. Impurities, mechanical strains, and temperature variations across the sample affect the parameters η and *eq*. In contrast, the electric quadrupole moment *eQ* is a property of the nuclei and is constant. One generally uses the normalized Lorentzian function

$$\Lambda(f) = \frac{1}{1+\left[T_2^*(f-\nu_*)\right]^2} \tag{3}$$

$$\text{FWHM} = \frac{1}{\pi T_2^*} \text{ [Hz]} \tag{4}$$

to approximate the distribution of resonant frequencies between two energy levels. The center frequency of the line shape is ν_*, and corresponds to a QR transition frequency. The full-width-half-maximum (FWHM) describes the width of the line shape, and is expressed in terms of the inverse line-width parameter, T_2^*. The latter parameter is useful for characterizing the temporal response of the QR signal, whose origin is now discussed.

The QR signal originates from the magnetic moment associated with the intrinsic angular momentum of the nucleus. The magnetic moment is proportional to the intrinsic angular momentum, and the proportionality constant is the gyromagnetic ratio γ. The application of a RF pulse at a transition frequency

Annual Research Journal, Vol. V
Electrical Engineering Research Experience for Undergraduates

ISBN 0-913260-07-X (http://www.ee.psu.edu/reu/)

causes the nuclei to rotate away from its thermal equilibrium orientation. The resulting precession of the nucleus causes the magnetic moment to induce a voltage across a probe coil located near the sample. Typically a single coil is used to apply the RF pulse that rotates the nuclei and to observe the induced voltage.

Figure 2(A) shows a sketch of the Lorentzian line shape centered at a QR transition frequency ν_*. Following the application of a RF pulse whose frequency is ν_*, the induced QR signal voltage across the probe coil exponentially decays with a time constant equal to the inverse line-width parameter T_2^*, and is called a free induction decay (FID). Figure 2(B) shows the time-domain FID signal and its squared magnitude spectra is equivalent to the Lorentzian line shape in Figure 2(A). Adopting terminology from MR spectroscopy experiments, when the duration and amplitude of the RF pulse are chosen to maximize the amplitude of the FID, the pulse is called a 90° pulse.

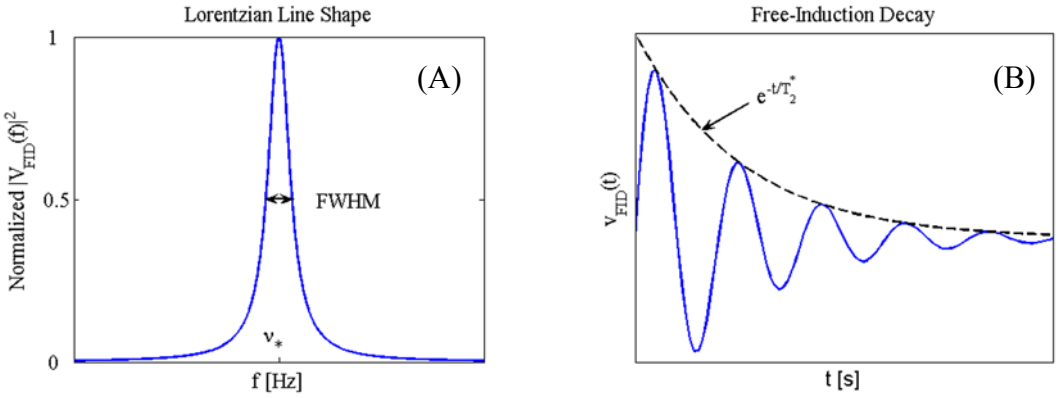

Figure 2: (A) Lorentzian line shape and (B) the FID following a RF pulse.

Zeeman Modulation

The application of a static magnetic field results in a torque that causes the nuclear magnet moments to align with the applied field. This effect, known as Zeeman modulation, alters the electrostatic interaction energy, and correspondingly, the QR transition line shape[6,7,8].

The static magnetic field shifts the QR transition frequencies and broadens the line shape. These effects are more pronounced for materials whose asymmetry parameter η is close to zero. For values of $\eta<0.14$, it has been shown that the ν_+ frequency increases while the ν_- frequency decreases. In this regime, the perturbed QR transition frequencies are [6]

$$\nu'_{\pm} = \frac{3}{4}e^2qQ\left(1 \pm \frac{1}{3}\eta\sqrt{1+\left(\frac{\gamma B_o}{\eta\frac{e^2qQ}{4}}\cos\theta\right)^2}\right), \qquad (5)$$

Annual Research Journal, Vol. V
Electrical Engineering Research Experience for Undergraduates

ISBN 0-913260-07-X (http://www.ee.psu.edu/reu/)

where B_o represents the amplitude of the static magnetic field and θ is the angle between the static magnetic field and the direction of the largest electric field gradient.

The experimental work in this study uses the QR signal from a material in which the asymmetry parameter η is zero. In the absence of a static magnetic field, there is a single transition frequency with a Lorentzian line shape at

$$\nu_+ = \nu_- = \frac{3}{4} e^2 qQ. \tag{6}$$

Two of the three states have the same energy and are said to be degenerate. The presence of a static magnetic lifts the degeneracy and results in the QR transition frequencies

$$\nu'_{\pm} = \frac{3}{4} e^2 qQ \pm \left| \gamma B_o \cos\theta \right|. \tag{7}$$

When η is zero, the change in resonant frequency is proportional to the magnitude of the applied static field, rather than the amplitude as in MR. As the static field B_o increases from zero, the line shape broadens symmetrically around the unperturbed transition frequency, with two peaks appearing at the perturbed transition frequencies $\nu'_{\pm}$. The amplitude of the peaks decreases as the perturbed line shape broadens because the area of the line shape is fixed by the number of the nuclei in the sample[7].

Imaging using Field Gradients

Matsui[2] noted that while the application of a static magnetic field does not significantly shift the QR transition frequencies, it does have a pronounced effect on the height of the line shape. The peak of the line shape decreases as the magnitude of the applied static magnetic field increases. This effect can be used to encode the location of the nuclei within the sample. Application of a static gradient field along a given direction in a sample labels the position of the nuclei by the peak value of their line shape.

The image reconstruction problem is to solve for the nuclei density $\rho(z_i)$ along a specified axis z at N points z_1 through z_N. Let $B_o(z_i)$ represent the static magnetic field experienced by the nuclei at z_i, and assume that in a small region around z_i that the magnetic field $B_o(z_i)$ is spatially uniform. If the line shape of the nuclei located at z_i is denoted as $L(f, B_o(z_i))$, then the line shape of the QR signal from the entire sample is approximated by the sum

$$L(f) = \sum_{i=1}^{N} L\left(f, B\left(z_i\right)\right)\rho\left(z_i\right). \tag{8}$$

Annual Research Journal, Vol. V
Electrical Engineering Research Experience for Undergraduates

ISBN 0-913260-07-X (http://www.ee.psu.edu/reu/)

By considering the value of the line shape $L(f_i)$ at M frequency points f_1 through f_M, equation (8) is expressed as the linear equation

$$\begin{pmatrix} L(f_1) \\ L(f_2) \\ \vdots \\ L(f_M) \end{pmatrix} = \begin{pmatrix} L(f_1, B(z_1)) & \cdots & L(f_1, B(z_N)) \\ \vdots & & \vdots \\ L(f_M, B(z_1)) & \cdots & L(f_M, B(z_N)) \end{pmatrix} \begin{pmatrix} \rho(z_1) \\ \rho(z_2) \\ \vdots \\ \rho(z_N) \end{pmatrix} \tag{9}$$

$$L_{M\mathrm{X}1} = \Phi_{M\mathrm{X}N}\ \rho_{N\mathrm{X}1} \tag{10}$$

that can be solved for the unknown $NX1$ density vector ρ.

The $NX1$ solution vector ρ represents a one-dimensional image of the sample along the z axis. The $MX1$ vector L is obtained by applying a magnetic field gradient along the z axis of the sample and calculating the Fourier transform of the resulting QR FID. Each column of the MXN matrix Φ is generated by applying a constant magnetic field $B(z_i)$ across the z axis and finding the line shape $L(f, B(z_i))$ of the resulting QR FID. In general, the matrix Φ is not square as there are more samples along the frequency axis f than the spatial axis z, and so equation (10) cannot be solving by inverting the non-square matrix Φ. Instead, a non-negative least-squares solution is obtained for $\rho(z_i)$ because the nuclei density is a positive semidefinite function of position[9,10]. The imaging experiments in this study contain a sample in which for each value of z_i the density is either zero or a positive constant ρ_o. The non-negative least-squares solution is forced to satisfy this constraint.

Specific Research Aims

There are two specific aims of this research project. The first objective is to study the effect of uniform and gradient static magnetic fields on the line shape of a QR sample. The second goal is to use the observed line shapes to reconstruct an image of the sample.

EXPERIMENTAL DESCRIPTION

Materials

In order to maximize the observed effect of a static magnetic field on the transition line shape, it is desirable to use a material with a small asymmetry parameter. For this reason the experiments use the nitrogen QR transition in hexamethylenetetramine (HMT) which has an asymmetry parameter η of zero. At room temperature the single QR transition is located near 3.3035 MHz, and the FWHM transition of the line shape in the absence of a static magnetic field is about 830 Hz.

Two sample vials of HMT are used. The first sample contains 30.8 gm of HMT in a glass vial that is 3.3 in long and 1 in diameter. The second vial contains

Annual Research Journal, Vol. V
Electrical Engineering Research Experience for Undergraduates

ISBN 0-913260-07-X (http://www.ee.psu.edu/reu/)

31.2 gm in a fiberglass tube that is 5 in long and 1 in diameter. The HMT is partitioned into two volumes of equal mass separated by 1 inch and centered along the length of the tube as shown in Figure 3. The first sample is used to generate the line shapes for constructing the matrix Φ in equation (10). This matrix is used to generate a one-dimensional image along the length of the second sample shown in Figure 3.

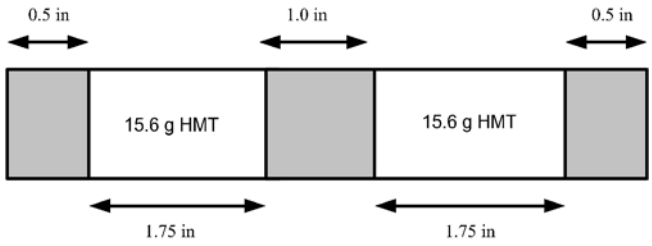

Figure 3: Sample vial containing two compartments of HMT separated by 1 in.

Methods

Uniform and gradient magnetic fields are generated using a pair of identical coils surrounding the sample vial as shown in Figure 4. The long axis of the sample defines the *z* axis, and the sample is centered at the origin of the *z* axis. The coils generate a magnetic field $B_z(z)$ along the long *z* axis. Each coil is wound with N=200 turns of 22 AWG copper wire in a loop that has an average radius of R = 10.5 cm. When the current direction in the coils is identical, the coils form a Helmholtz pair, or magnetometer, that provides a nearly uniform static magnetic field across the sample. Choosing the coil separation as R/2 minimizes the variation in $B_z(z)$ within the sample region. Reversing the current in the coil located at R/2 results in a gradiometer configuration that generates a linear magnetic field gradient across the sample. Figure 5 shows the physical set up along with a Hall affect sensor for measuring the field $B_z(z)$.

The magnetic field $B_z(z)$ is calculated as

$$B_z(z) = \frac{\mu_o N R^2 I}{2}\left[\frac{1}{\left(\left(z+\frac{R}{2}\right)^2+R^2\right)^{3/2}} + \alpha\frac{1}{\left(\left(z-\frac{R}{2}\right)^2+R^2\right)^{3/2}}\right] \qquad (11)$$

where μ_o is the permeability of free-space, *I* is the series coil current, and the parameter α is set to 1 for the magnetometer configuration and -1 for the gradiometer configuration[11]. Figure 6 and 7 show the predicted and measured magnetic field $B_z(z)$ for the magnetometer and gradiometer configurations when the series coil current is 1 A. For the magnetometer configuration, the predicted

Annual Research Journal, Vol. V
Electrical Engineering Research Experience for Undergraduates

ISBN 0-913260-07-X (http://www.ee.psu.edu/reu/)

and measured peak fields are 18.7 G and 17.6 G, respectively. For the gradiometer configuration, the predicted and measured gradient at the sample center is 0.89 G/in.

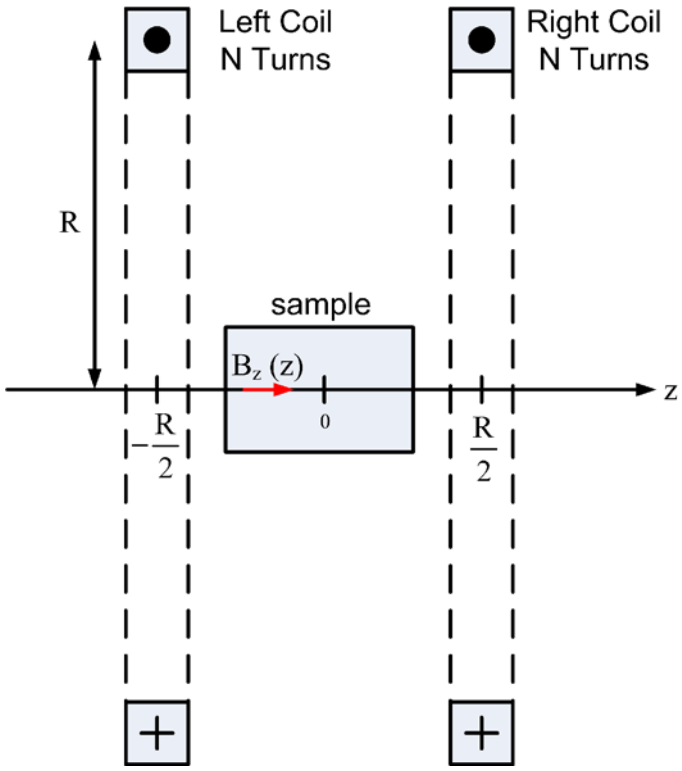

Figure 4: Schematic representation of the magnetic field system.

Figure 5: Photograph of the magnetic field system and Hall effect sensor.

Annual Research Journal, Vol. V
Electrical Engineering Research Experience for Undergraduates

ISBN 0-913260-07-X (http://www.ee.psu.edu/reu/)

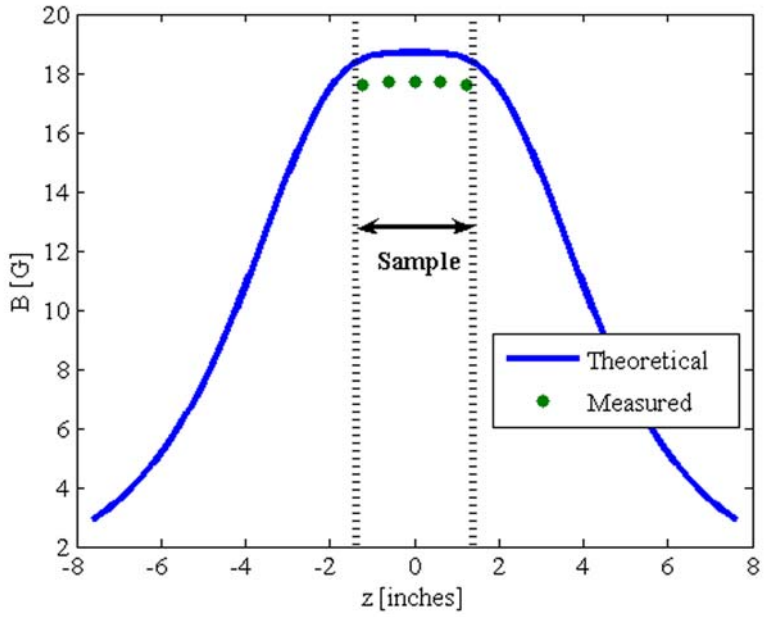

Figure 6: Predicted and measured magnetometer field.

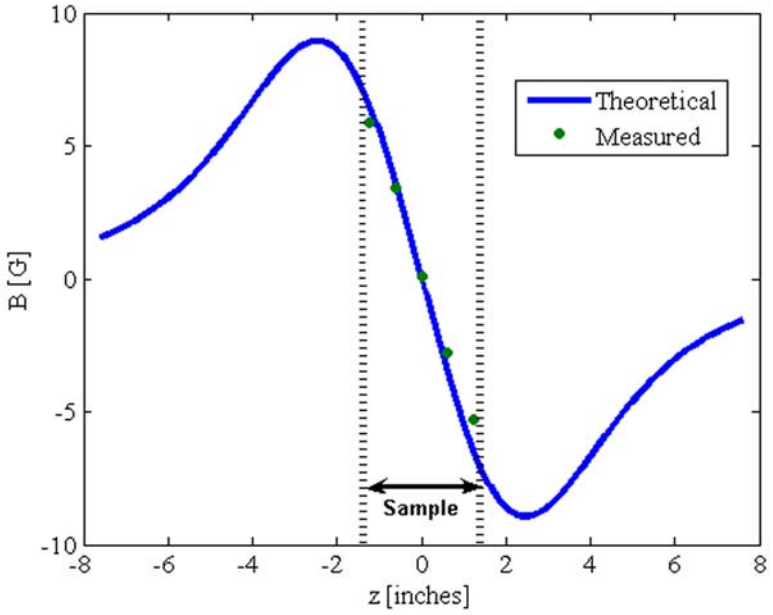

Figure 7: Predicted and measured gradiometer field.

Annual Research Journal, Vol. V
Electrical Engineering Research Experience for Undergraduates

ISBN 0-913260-07-X (http://www.ee.psu.edu/reu/)

RESULTS

Figures 8 and 9 show the effect of a uniform magnetic field on the QR line shape for twenty five magnetic field amplitudes ranging from 0 G to 37.4 G. For each magnetic field amplitude, one hundred QR FID signals are acquired and averaged to improve the measurement SNR. Each figure shows the magnitude spectra of the average QR FID as a function of the magnetic field amplitude. For data in Figure 8, the applied magnetic field is parallel to the axis of the RF magnetic field, while in Figure 9, the applied magnetic field is orthogonal to the axis of the RF magnetic field. Figure 8 shows that increasing the magnetic field decreases the peak amplitude of the line shape. Figure 9 shows a similar trend, and, unlike Figure 8, reveals the presence of well defined peaks at the perturbed transition frequencies $\nu'_{\pm}$.

Figure 10 shows a plot of the peak magnitude and FWHM of the QR line shape as a function of the uniform field amplitude. The solid and dashed curves show the results for the uniform static magnetic field parallel and orthogonal to the RF field, respectively. The trends for both orientations of the uniform magnetic field with respect the RF field are similar. As the magnetic field strength increases, the FWHM increases from about 800 Hz to 10 kHz, while the peak amplitude of the QR transition decreases by two orders of magnitude.

Figure 11 shows the effect of a gradient magnetic field on the QR line shape for twenty five field gradients ranging from 0 G/in to 6.15 G/in. The procedure for acquiring and constructing the plot is identical to that for the case of a uniform magnetic field. Results are shown for the case where the axis of the field gradient is parallel to the direction of the RF field. A similar plot results for the case where the gradient field is orthogonal to the RF field. As for the case of a uniform field, the static gradient magnetic field broadens the line shape and decreases its peak value. Figure 12 shows a plot of the corresponding peak magnitude and FWHM of the QR line shape as a function of the magnetic field gradient. The solid and dashed curves show the results for the static gradient magnetic field parallel and orthogonal to the RF field, respectively. As the magnetic field gradient increases, the FWHM increases from about 800 Hz to 6 kHz, while the peak amplitude decreases by an order of magnitude.

Figure 13 shows the set up for the QR imaging experiment. The sample in Figure 3 is mounted within the RF probe coil, and the axis of the gradient magnetic field is parallel to the RF field. The QR image is generated using a matrix Φ with M=400 rows and N=15 columns. The columns of Φ are taken from the data in Figure 8. The line shape contained in the vector L is obtained from the average of one hundred QR FID signals acquired in the presence of a gradient with amplitude of 1.34 G/in using the sample in Figure 3. The solid curve in Figure 14 indicates the true density of nuclei across the sample, while the open circles indicate the density obtained from the non-negative least-squares solution of equation (8). Three of the 15 points in the estimated vector $\rho(z_i)$ are incorrect, indicating the need for an improved imaging algorithm.

Annual Research Journal, Vol. V
Electrical Engineering Research Experience for Undergraduates

ISBN 0-913260-07-X (http://www.ee.psu.edu/reu/)

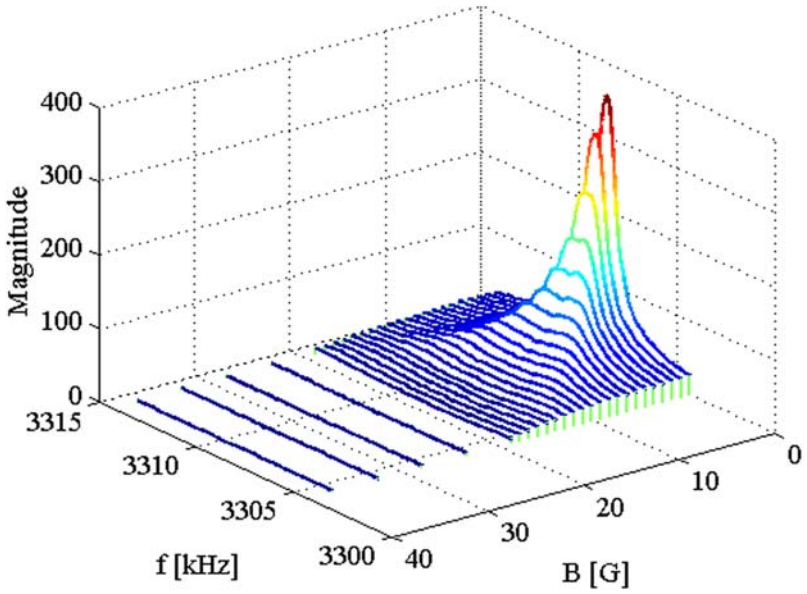

Figure 8: FID magnitude spectra using parallel magnetometer and RF fields.

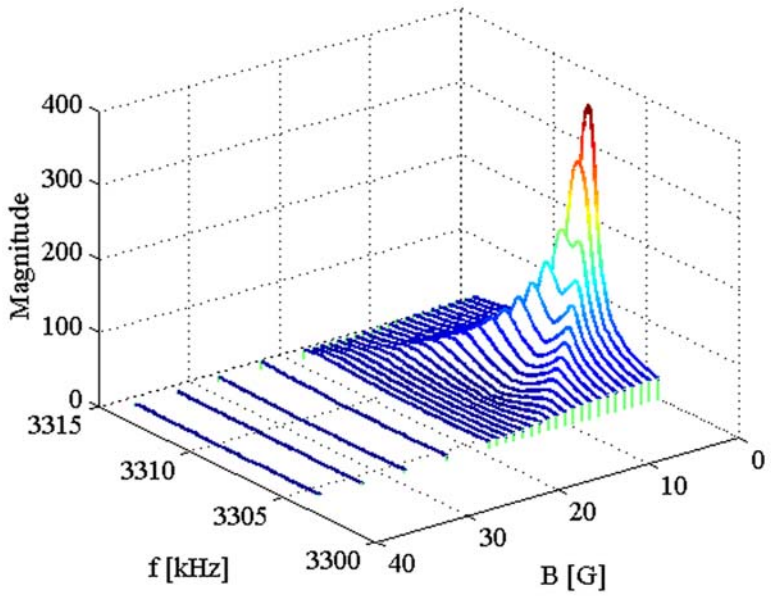

Figure 9: FID magnitude spectra using orthogonal magnetometer and RF fields.

Annual Research Journal, Vol. V
Electrical Engineering Research Experience for Undergraduates

ISBN 0-913260-07-X (http://www.ee.psu.edu/reu/)

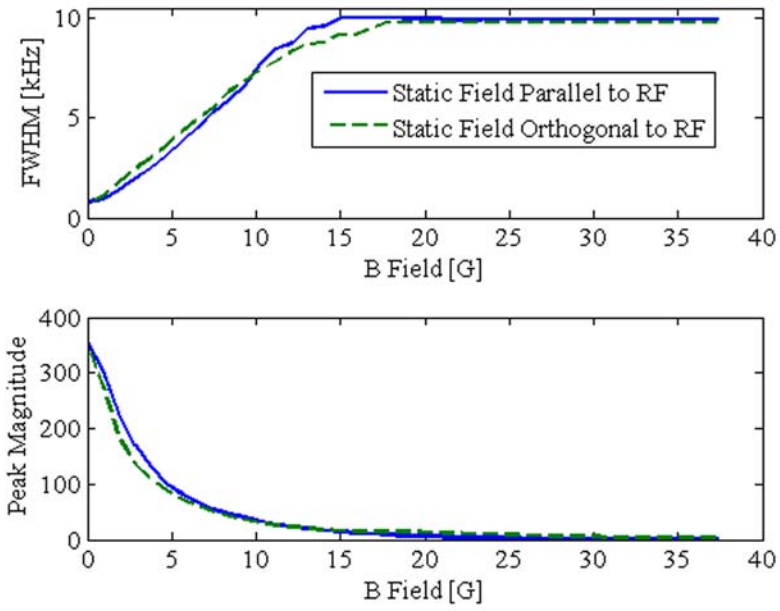

Figure 10: Peak and FWHM of the FID magnitude spectra for a uniform field.

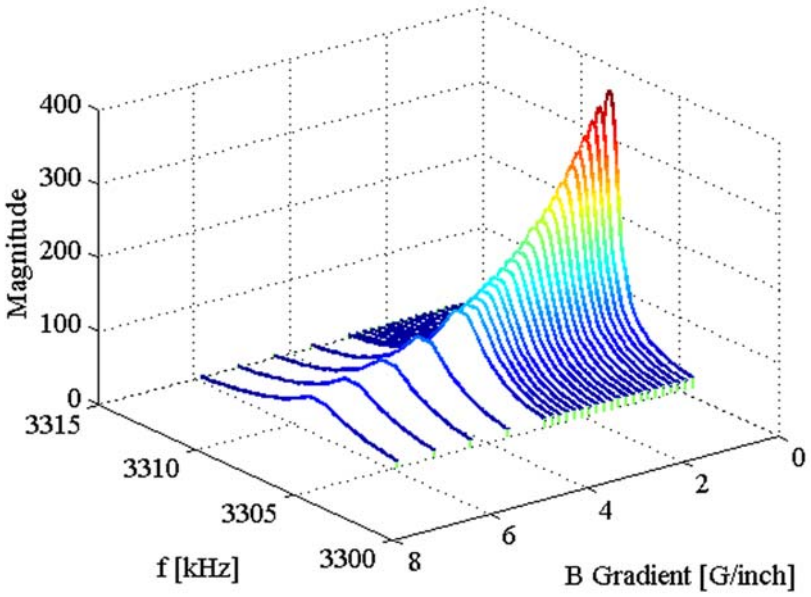

Figure 11: FID magnitude spectra using parallel gradiometer and RF fields.

Annual Research Journal, Vol. V
Electrical Engineering Research Experience for Undergraduates

ISBN 0-913260-07-X (http://www.ee.psu.edu/reu/)

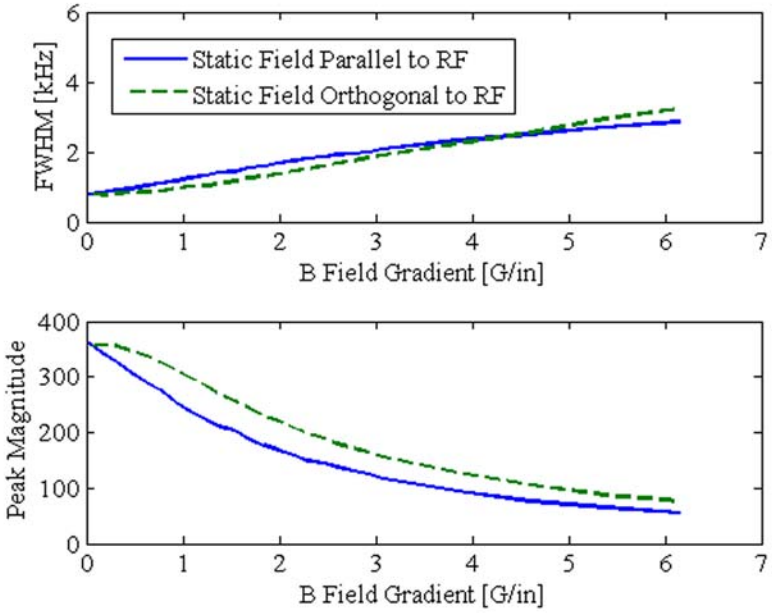

Figure 12: Peak and FWHM of the FID magnitude spectra for a gradient field.

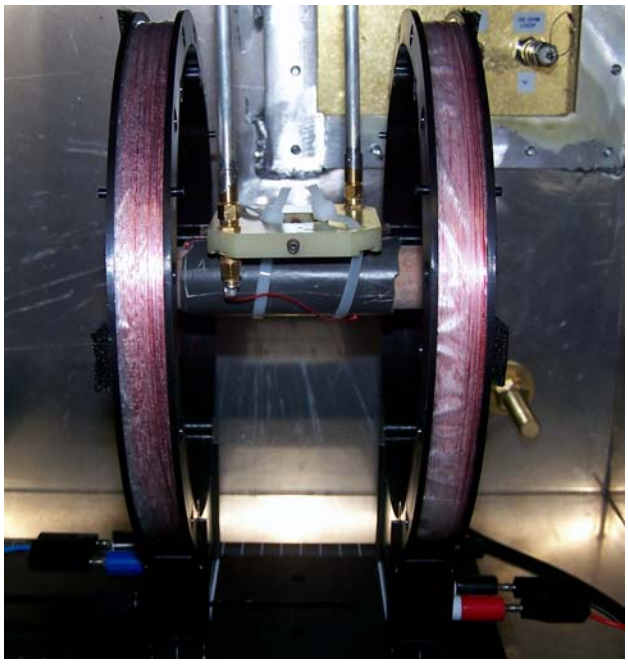

Figure 13: Set up for the QRI experiment.

Annual Research Journal, Vol. V
Electrical Engineering Research Experience for Undergraduates

ISBN 0-913260-07-X (http://www.ee.psu.edu/reu/)

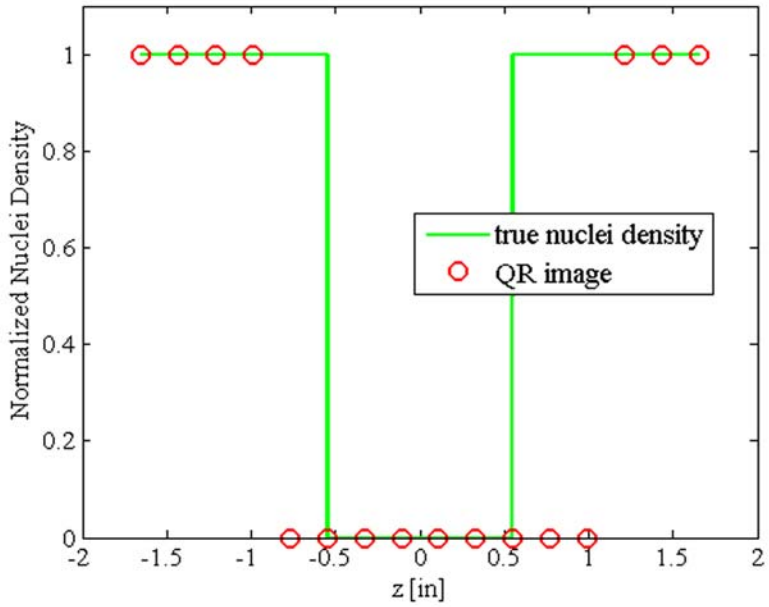

Figure 14: One-dimensional QR image of the HMT sample in Figure 3.

DISCUSSION

The principle effect of uniform and gradient magnetic fields on a QR transition is to broaden and decrease the peak magnitude of the line shape. The effect of the orientation of the applied magnetic field with respect to the axis of the RF field is expected from equation (7), which shows that the perturbed transition frequency for a single nucleus depends on the orientation of that nucleus with respect to the static magnetic field. The experimental results were obtained for a sample where the asymmetry parameter is zero. This is an exceptional case, as most materials admitting a QR response have a nonzero asymmetry parameter. For the latter case, the effect of the static magnetic field is considerably smaller.

The proposed method for recovering an image differs from the work of Matsui[2] in which the zero point of the magnetic field gradient is swept through the sample by mechanically moving the sample. In this study an image is recovered using a single magnetic field gradient, eliminating the need for mechanically moving the sample or electrically shifting the zero point location of the gradient field. As with the method of Matsui[2], the solution of the inverse problem yields only an approximation of the true nuclei density. In the experiments reported in this study, one source of error is that the RF magnetic field is not uniform across the length of the probe coil. For this reason, the QR line shape in the absence of an applied static magnetic field is different for the two HMT samples. It would be better to form the Φ matrix using line shape data acquired from the sample tube in Figure 3, rather than the solid HMT sample used to acquire the data in Figure 8. Another shortcoming of the analysis leading to an

Annual Research Journal, Vol. V
Electrical Engineering Research Experience for Undergraduates

ISBN 0-913260-07-X (http://www.ee.psu.edu/reu/)

estimation of the nuclei density using equation (10) is that the radial dependence of the static magnetic field is ignored.

CONCLUSION

The present study demonstrates the feasibility of generating a QR image by spatially encoding the location of nuclei using a static magnetic field gradient. In comparison to MR, there has been little effort in developing imaging techniques for QR. The economic incentive to eliminate the superconducting magnet in MRI scanners, as well as the utility of imaging contraband using QR, is likely to motivate further research in QRI.

ACKNOWLEDGEMENT

I would like to thank Dr. Jeffrey Schiano from whom I have learned so very much. Also, I owe a great deal of gratitude to my graduate student mentor, Don Natale. Finally I thank all those involved with the EEREU program, Penn State, and the NSF. This material is based upon work supported by the National Science Foundation under Grant No. EEC-0244030.

REFERENCES

1. Smith, J. A., Nuclear Quadrupole Resonance Spectroscopy: General Principles, *Journal of Chemical Education*, **48** (1), 39-48 (1971).
2. Matsui, S., Kose, K., and Inouye, T., "An NQR Imaging Experiment on a Disordered Solid", *Journal of Magnetic Resonance*, **88**, 186-191 (1990).
3. Rommel, E., Puslol, D., Nickel, P., Kimmich, R., "Spectroscopic rotating-frame NQR imaging (ρNQRI) using surface coils", *Measurement Science & Technology*, **2**, 866-871 (1991).
4. Kimmich, R., Rommel, E., Nickel, P., "Spatially Resolved NQR", *Journal of Magnetic Resonance Imaging*, **10**, 733-739 (1992).
5. Dehmelt, H. G., "Nuclear Quadrupole Resonance", *Discussions of the Faraday Society,* **19**, 263-274 (1955).
6. Casabella, P. A., Bray P. J., "Quadrupole Coupling of Solid Cyanogen Chloride," *The Journal of Chemical Physics*, **28** (6), 1182-1187 (1958).
7. Negita, H., "Line Shape of ^{14}N Pure Quadrupole Resonance by the Zeeman Modulation", *The Journal of Chemical Physics*, **44** (5), 1734-1740 (1966).
8. Pissanetzky, S., "Zeeman effect on ^{14}N nuclear quadrupole resonance with polycrystalline samples", *The Journal of Chemical Physics,* **59** (8), 4197-4207 (1973).
9. Lawson, C. W., Hanson, R. J., *Solving Least-Squares Problems*, Prentice-Hall, Englewood Cliffs, New Jersey, 1984.
10. Schiano, J., Lieblich, D., Ginsberg, M., "Imaging Explosive Depth and Volume using NQR", UXO/Countermine Forum (2001).
11. Smythe, W. R., *Static and Dynamic Electricity*, Hemisphere Publishing Corporation, New York, 1989.

Annual Research Journal, Vol. V
Electrical Engineering Research Experience for Undergraduates

ISBN 0-913260-07-X (http://www.ee.psu.edu/reu/)

COMPUTER SYSTEM CONTROL BUS: COMMUNICATING WITH NANOSATELLITE SUBSYTEMS

Christopher Rosser*, Adam Escobar[+], and Sven Bilén[#]

Department of Electrical Engineering
The Penn State University
State College, PA 16802

*Undergraduate Student of
College of Science, Engineering, and Technology
Jackson State University
Jackson, MS 39217

ABSTRACT

NittanySat, a nanosatellite being built by Penn State's Student Space Programs Lab, has many subsystems to ensure success of its mission, which include Power, Communications, Guidance, Navigation & Control, etc., each having one or more specific tasks. A computer onboard the nanosatellite is responsible for controlling each subsystem. A custom bus is implemented, based on experiments using a shift register, to allow the computer system to communicate with and control the nanosatellite's subsystems. This paper discusses the bus architecture and how it will be implemented on NittanySat.

INTRODUCTION

Penn State's students and faculty, through centers such as the Communications and Space Science laboratory (CSSL) and the Center for Space Research Programs (CSRP), have flown numerous instruments to measure the ionosphere. The current mission is to study the *D*-region of the ionosphere and its impact on communications, which will be carried out by the construction, design, and testing of a nanosatellite called NittanySat.

[+] *Graduate Mentor*
[#] *Faculty Mentor*

Annual Research Journal, Vol. V
Electrical Engineering Research Experience for Undergraduates

ISBN 0-913260-07-X (http://www.ee.psu.edu/reu/)

BACKGROUND

NittanySat's subsystems include Power, Command & Data Handling, Communications, Structure and Mechanisms, Thermal, Ground Data Systems, Guidance Navigation & Control, Ground-based instrumentation, Payload Integration, and Operations.

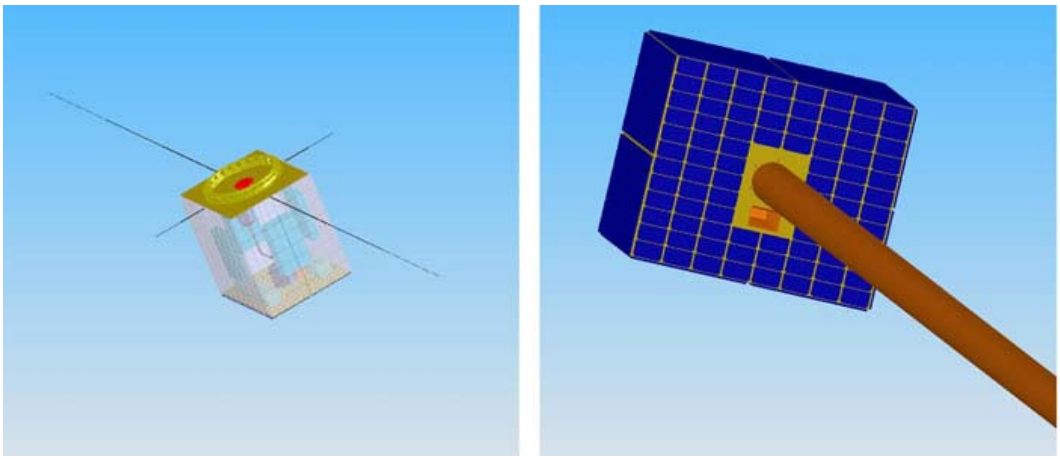

Figure 1. Images of NittanySat

Space Mission Analysis and Design Second Edition provides information on the requirements needed for a nanosatellite's operation. Each of NittanySat's subsystems will be designed to be able to perform their tasks while using the most resourceful methods and equipment.

Table I. Nanosatellite Subsystem Descriptions [1]

Subsystem Name	**Description**
Power	Provides, stores, distributes, and controls satellite's electrical power.
Command & Data Handling	Processes and distributes data and commands to other subsystems.
Communications	Transmits and receives signals from earth to the satellite.
Structures & Mechanisms	Supports all subsystems, attaches the satellite to launch vehicle, satisfies strength and stiffness requirements.
Thermal	Maintains elements within temperature limits for every mission phases.
Guidance and Navigation	Maintains the position and velocity of the satellite as it is in orbit.

Annual Research Journal, Vol. V
Electrical Engineering Research Experience for Undergraduates

ISBN 0-913260-07-X (http://www.ee.psu.edu/reu/)

The Command & Data Handling subsystem will include the use of computer buses, which are wires that transmit information to and/or between computer systems. Buses are important because they connect peripheral devices and computer systems to other computer systems, and they can be parallel, serial, internal, or external. Parallel buses transfer data at the same time across several wires, while serial buses transfer data across one wire, sequentially. Computer Bus features are listed in the following table.

Table II. Computer Bus Features

Bus Features	**Description**
Serial	Sends data, in sequences, across one wire
Parallel	Send data at once across several wires
Internal	Connects internal devices/components to computer motherboard
External	Connects external peripherals to the computer motherboard
Synchronous	Keeps systems in sync with an extra clock signal
Asynchronous	No clock signal, saves board space
Parity	An extra amount of memory to ensure correctness of data transmission

Several types of buses were reviewed, particularly SPI (Serial Peripheral Interface) and I^2C (Inter-Integrated Circuit), which are commonly used today. The biggest difference between the two is that SPI uses 4 wires to perform its tasks, while I^2C uses only two wires. Both are synchronous, but I^2C is more advanced because it can perform many functions with only two wires, as opposed to the SPI which requires four.

EXPERIMENTAL DESCRIPTION

Experiments were performed with Parallax Inc.'s Board of Education, which is a version of their BASIC Stamp Board series, single-board computers (microcontrollers) that use PBASIC, a programming language created specifically for BASIC Stamp Boards. Lighting LEDs (Light Emitting Diodes) demonstrates the microcontroller's ability communicate with other devices, and by extension, other subsystems on a nanosatellite. Using a 290 Ω resistor, a component that resists the flow of electricity, thus, reducing the amount of electricity used to power the LED, a Green LED, and Yellow LED, the BASIC Stamp Board is able to perform several experiments.

Annual Research Journal, Vol. V
Electrical Engineering Research Experience for Undergraduates

ISBN 0-913260-07-X (http://www.ee.psu.edu/reu/)

- Building and testing the LED circuit[2]
  - It is essential to test the components before using them in an experiment. To test the LED, the cathode is plugged into the black socket labeled Vss (Ground), and its anode (the longer of the LEDs two wires) is plugged into the breadboard socket. One of the resistor wires is plugged into the same row as the LEDs anode, connecting the resistor and the LED, while the other resistor wire is plugged into the black socket labeled Vdd (Power). Power, in the form of an AC adapter, is then connected to the Board of Education. The lit LED indicates that the LED functions properly.
- On/off control with the Basic Stamp[2]
  - The LED is connected to the BASIC Stamp Board so that it is programmed to turn on and off. This is done by modifying the previous circuit. Instead of connecting the resistor's second wire to Vdd, it is connected to any black socket labeled PX, X being a number from 0 to 15. These numbers represent the BASIC stamp I/O (Input / Output) pins. The Board of Education is then connected to a computer, and a program is written using PBASIC code. The program is run, and the LED turns on and off, successfully.
- Counting and Repeating[2]
  - The circuit design is the same for the previous experiment. The PBASIC keywords do…loop are introduced and used for counting and repeating. The code is modified so that the number of times the LED blinks is counted.
- Building and Testing a Second LED Circuit[2]
  - Like the first LED, a second, Yellow, LED is plugged into the breadboard area and is tested before the experiment is run. The previous programs are modified, this time they include an extra set of commands for the LED that is plugged into a different pin. The LEDs successfully blinked together, and, with a slightly edited version of the same program, alternated.

RESULTS AND DISCUSSIONS

The LEDs were successfully lit, displaying the Stamp Board's ability to execute tasks that are programmed by the user in the PBASIC language. Although unsuccessful in lighting the LEDs using a shift register, it is understood that a shift register can control more output while taking up fewer pins, thus, is able to command many of the nanosatellite's subsystems while taking up a minimum amount of space on the board.

CONCLUSIONS

When faced with budget, material, and time constraints, the cheaper and more effective methods are implemented in the design of a nanosatellite. Utilizing an I^2C Bus on NittanySat would be more ideal but due to costs and possible

Annual Research Journal, Vol. V
Electrical Engineering Research Experience for Undergraduates

ISBN 0-913260-07-X (http://www.ee.psu.edu/reu/)

incompatibility with the other systems onboard the satellite, an SPI bus would be more useful and would take up less space. 8-bit shift registers should also be used onboard so that the most outputs can be obtained with the limited amount of available board space.

ACKNOWLEDGMENTS

This material is based upon work supported by the National Science Foundation under Grant No. EEC-0244030. I'd like to thank Brendan Surrusco for always answering questions and sending information that I needed, and Dr. Sven Bilen for maintaining such a positive demeanor in the midst of what seemed to be, from time to time, chaos. I'd also like to thank Penn State's Electrical Engineering Department for allowing me to experience the ups & downs of research.

REFERENCES

1 James R. Wertz, *Space Mission Analysis and Design*, Second Edition, Microcosm, Inc., Torrance, CA, pp 339 – 468, (1992)

2 What's A Microcontroller? *Student Guide*, version 2.2, pp 46 – 69, Parallax, Inc., (2003-2004).

Annual Research Journal, Vol. V
Electrical Engineering Research Experience for Undergraduates

ISBN 0-913260-07-X (http://www.ee.psu.edu/reu/)

Annual Research Journal, Vol. V
Electrical Engineering Research Experience for Undergraduates

ISBN 0-913260-07-X (http://www.ee.psu.edu/reu/)

ELECTRIC FIELD EFFECT IN *n*-GRAPHENE LAYER (*n*-GL) FILMS IN DIFFERENT GAS ENVIRONMENTS

Karthik Sridhara*, Prasoon Joshi[+], and Srinivas Tadigadapa[#]

[#]Department of Electrical Engineering,
The Pennsylvania State University
University Park, PA, 16802

*Undergraduate student of
Department of Electrical Engineering
The Pennsylvania State University
University Park, PA, 16802

ABSTRACT

Graphene is the name given to a single 2-D sheet of carbon atoms that constitute graphite. The electronic transport properties of graphene are highly dependent on the surrounding environment. In this report we discuss electronic transport in graphene with air being the ambient test gas.

The experiment involves deposition of graphene flakes on a degenerately doped silicon substrate with silicon dioxide as the insulator. Metal contacts are made to a suitably chosen graphene flake. The metal contacts are analogous to source and drain and the silicon substrate to the Gate contact of a Metal Oxide Semiconductor Field Effect Transistor (MOSFET). A constant voltage bias is applied across source and drain and a voltage sweep is performed on the gate. The R_{DS} vs. V_G characteristics are plotted in real-time. A maxima in measured R_{DS} vs. V_G data, signifying ambipolar transport, is expected. When graphene flakes are exposed to the test gases the resistance maxima is expected to undergo a shift. The shift in the R_{DS} vs. V_G maxima may be used to sense the test gas.

[+] Graduate Mentor
[#] Faculty Mentor

Annual Research Journal, Vol. V
Electrical Engineering Research Experience for Undergraduates

ISBN 0-913260-07-X (http://www.ee.psu.edu/reu/)

INTRODUCTION

Graphene has been recently gaining prominence for its potential as a ballistic transistor. The history of graphene is long. However, it has been largely ignored due to the belief that two-dimensional carbon is highly unstable, thermodynamically [1]. Hence, it remained an academician's material[1]. In 2004, a team of researchers led by Andrew Geim reported their discovery of a supported single layer graphene film[2]. It is also reported that the carrier mobility in graphene can exceed 15,000 $cm^2V^{-1}S^{-1}$[1]. Only bulk, undoped InSb has carrier mobility that exceeds 77,000 $cm^2V^{-1}S^{-1}$ [1]. Since impurities are a limiting factor in a 2D crystal structure, it has been hypothesized that even in a high *n* - layer crystal of graphene, carrier mobility in excess of 10^{12} can be achieved [1].

The electric field effect in graphene is reported in detail in [2]. A single layer of graphene is a semimetal. Single layer graphene has linear energy band dispersion with a zero energy band gap. Upon application of an electric field, the Fermi energy level in graphene can be moved into the conduction band or the valence band. However, at the intersection of the conduction band and the valence band, called the "Dirac Point", there is a vanishing density of states. Vanishing density of states at the Dirac Point gives rise to resistance maxima when the resistance is plotted as a function of applied electric field. A resistance maxima signifies an inversion in the type of charge carriers upon application of an electric field.

Strictly speaking, for a single sheet of graphene terms like "surface" and "bulk", as used for bulk crystals, lose their meaning. Nonetheless, it is safe to say that graphene, being a quasi-two dimensional system, offers a very high surface to volume ratio.

It is well known that an un-isolated solid-state material is in a dynamic equilibrium with its ambience. Processes of adsorption and desorption establish a steady state concentration of adsorbed species on the materials' surface. In the case of bulk materials that have a relatively low surface-to-volume ratio, adsorbed species on the surface of the material do not perturb the material's properties by any significant amount. However, as the surface-to-volume ratio increases, contribution from the adsorbed species becomes increasingly important. In the limiting case, as in a single graphene layer, any adsorbed species contribute significantly to the properties of the system in question. Thus, the phenomenon of adsorption of ambient species on a graphene layer could be used towards gas (chemical) sensing applications.

EXPERIMENTAL SECTION

The experiment involves two stages: Fabrication of the graphene device and characterization of the fabricated graphene devices. A variety of graphene device fabrication schemes have been reported [2-4]. Here we present our fabrication scheme that has been arrived at to minimize the exposure of graphene to lithography and other chemicals.

We use oxidized (300 nm) and degenerately doped Si (100) wafers as substrates. These substrates are patterned with finding marks (Cr/Au). The substrates are then

Annual Research Journal, Vol. V
Electrical Engineering Research Experience for Undergraduates

ISBN 0-913260-07-X (http://www.ee.psu.edu/reu/)

cleaned in Oxygen plasma. Graphene is exfoliated onto the cleaned and patterned Si substrates from highly oriented pyrolitic graphite (HOPG). HOPG is cleaved using scotch tape. The piece of scotch tape used to cleave HOPG has, usually, a very fine layer of HOPG stuck on the scotch tape. This piece of scotch tape is then rubbed on the Si surface. During rubbing, micron sized flakes of *n*-graphene layers (n = 1, 2, 3…) get transferred onto the Si substrates due to van der Waals forces.

Si substrates with exfoliated graphene flakes are inspected under an optical microscope. Suitably thick flakes are chosen for device fabrication. Metal contacts consisting of Cr (5nm) and Au (100nm) are desired to make electrical contacts to graphene flakes. Electrical contacts are achieved by, first, masking the graphene flake using a Transmission Electron Microscopy (TEM) grid and, subsequently, doing an electron-beam evaporation of 5nm Cr and 100 nm Au. After the evaporation is done, the TEM grids are removed to realize an electrically contacted *n* - graphene layer (*n*-GL) flake device. A graphene flake after making electrical contacts and a schematic of the graphene device are shown in figures 1 and 2, respectively.

Electronic characterization of the fabricated *n*-GL device is done in a vacuum test setup. A schematic of the measurement process is shown in figure 3. The *n*-GL device does not show a resistance maxima when measured as fabricated in air [5]. With subsequent vacuum annealing that causes the adsorbed species to desorb, a maxima is expected. Once the position of the maxima is stable, we stop the annealing process and let the *n*-GL device cool down. After the device has cooled down we back-fill the vacuum chamber with test gases to about 500 Torr and measure the evolution of the resistance maxima with time. Then we pump out the test gas and try to recover the R_{DS} characteristics of our *n*-GL device by desorbing the adsorbed test gas with vacuum annealing.

The test setup is shown in figure 4. Measurement data is acquired using Keithley 4200 semiconductor characterization system. Temperature measurement is integrated with the Keithley 4200 using a GPIB interface. Vacuum annealing is carried out in-situ by using a Watlow Kapton™ heater. The best vacuum achieved in the vacuum test setup is ~ 8×10^{-7} Torr. To measure the pressure of the test gas a capacitance diaphragm gauge that can measure pressure in 10 - 1000 Torr range, is used. The whole setup can be programmed to make measurements over extended periods of time with little human intervention needed.

Annual Research Journal, Vol. V
Electrical Engineering Research Experience for Undergraduates

ISBN 0-913260-07-X (http://www.ee.psu.edu/reu/)

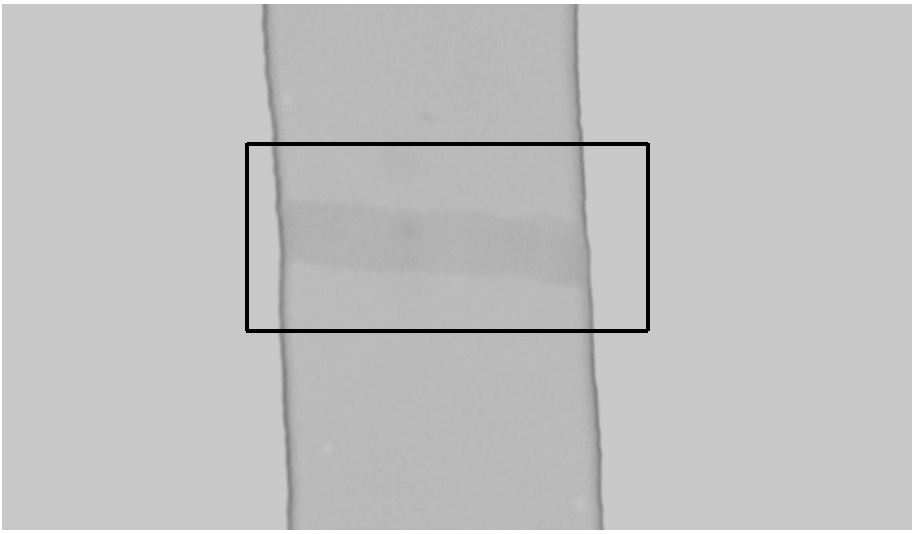

Figure 1: Device G029A5D01; The grayish strip enclosed in the rectangle is a graphene flake.

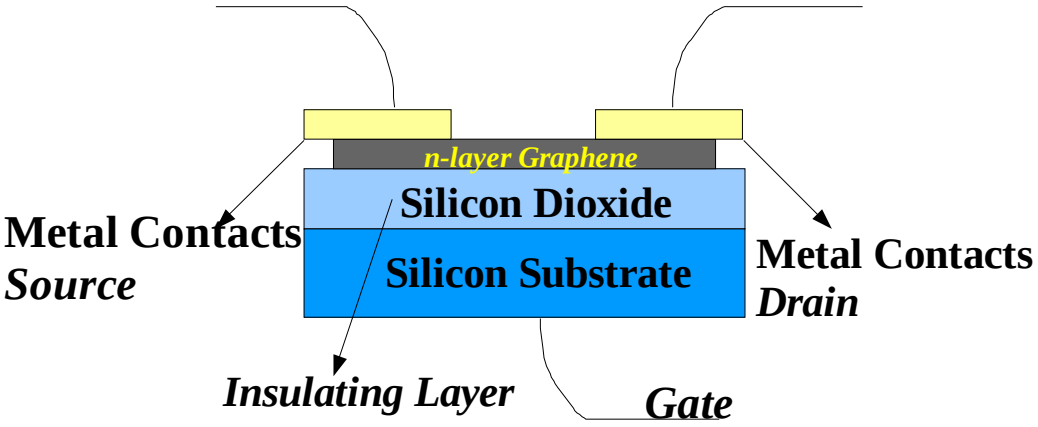

Figure 2: Schematic of a graphene device

The measurement data is analyzed using *Wolfram Mathematica 6*. Data from the Keithley 4200 is saved in the form of .txt files. Each file contains: Time, Gate Voltage (V_G), Gate Current (I_G), Voltage Drain-Source (V_{DS}), Drain-Source Current (I_D), Pressure (in Volts) and Temperature (°C). Using *Mathematica*, the Drain-Source Resistance (R_{DS}) vs. V_G is analyzed and plotted in different ways.

Annual Research Journal, Vol. V
Electrical Engineering Research Experience for Undergraduates

ISBN 0-913260-07-X (http://www.ee.psu.edu/reu/)

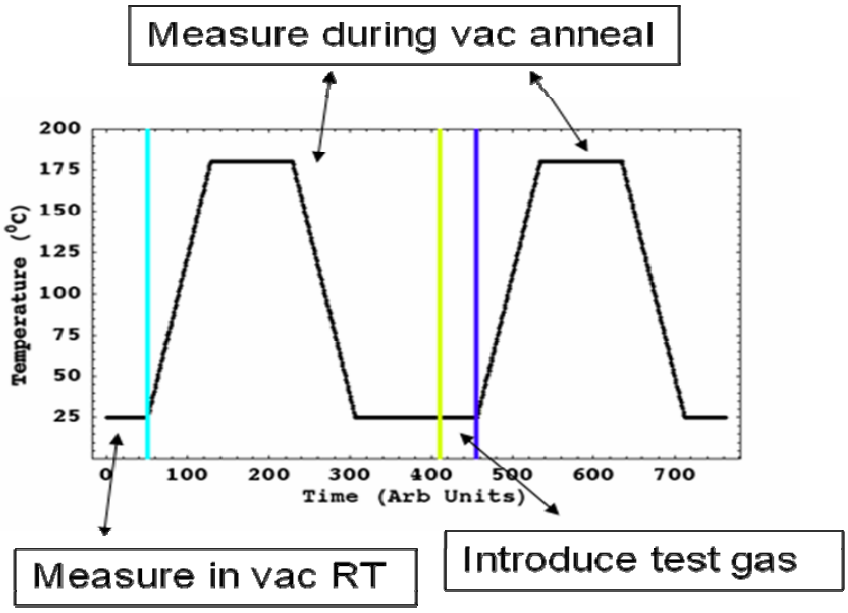

Figure 3: Schematic of the measurement process on a graphene device

RESULTS AND DISCUSSION

Two-Terminal (un-gated) Measurements

When the device is tested, a two probe resistance measurement is made by employing the source and drain contacts. The source is connected to the ground and a voltage sweep is performed on the drain. The voltage sweep is performed from -100 mV to 100 mV and the current compliance is started from 1 nA. The idea is to arrive at a minimum needed current compliance so that the device doesn't get destroyed when we make three-probe (gated) measurements. The current compliance is slowly increased by an order of magnitude. Satisfactory compliance values used are 100 µA to 1mA. The compliance values are device specific and are chosen keeping in mind the geometry of the device and the allowable current densities.

Source – drain resistance, R_{DS}, is defined as

$$R_{DS} = V_{DS} / I_D$$

where, V_{DS} is the source-drain voltage and I_D is the drain current.

Annual Research Journal, Vol. V
Electrical Engineering Research Experience for Undergraduates

ISBN 0-913260-07-X (http://www.ee.psu.edu/reu/)

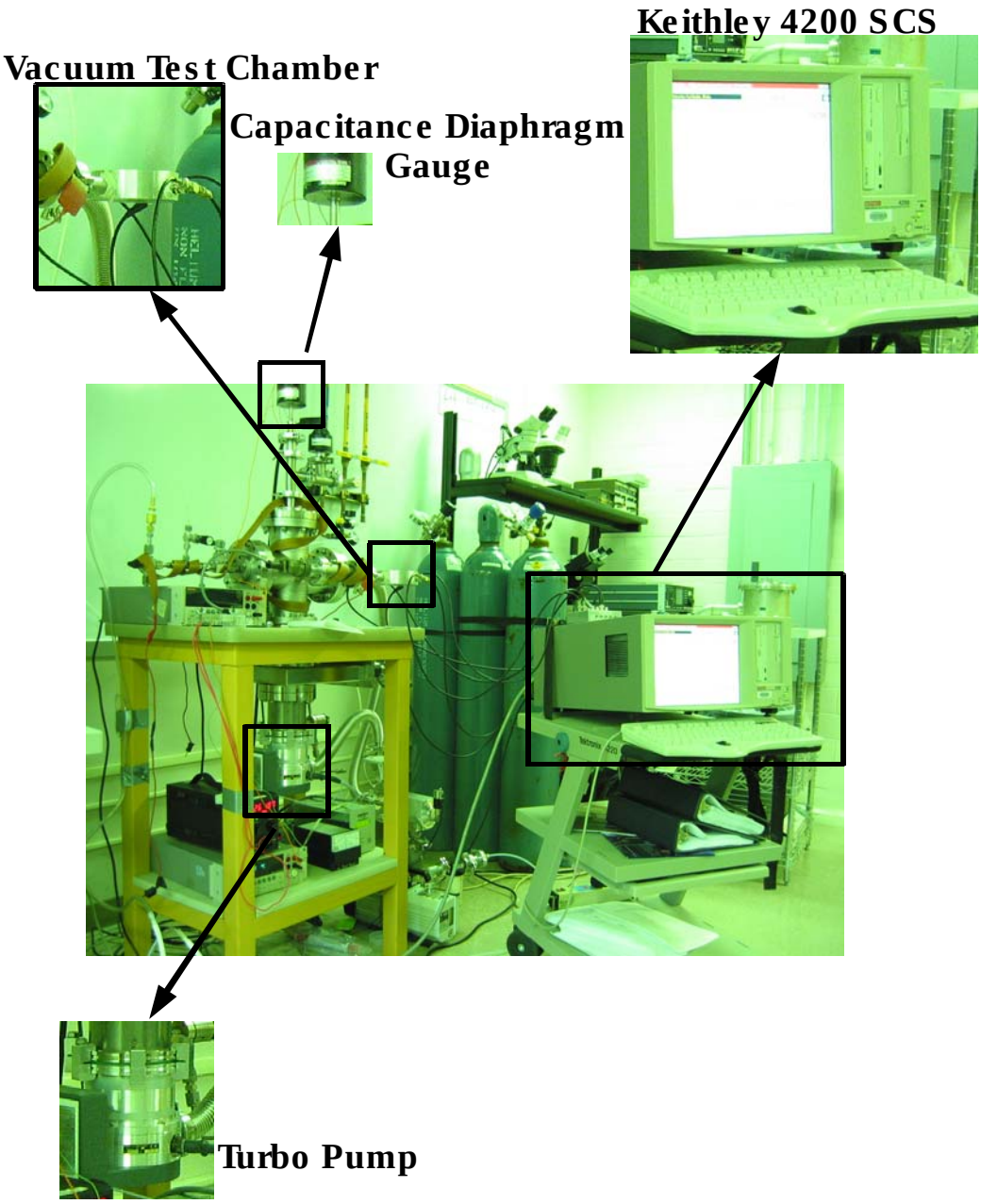

Figure 4: Experimental Setup

Three Terminal (gated) Measurements

R_{DS} vs. V_G data is shown in figure 5. No R_{DS} maxima is seen when the as fabricated device is measured in air. The R_{DS} vs V_G characteristics look quite linear. This can be attributed to species adsorbed from the atmosphere that have doped the graphene predominantly with holes. The p-type doping has shifted the

Annual Research Journal, Vol. V
Electrical Engineering Research Experience for Undergraduates

ISBN 0-913260-07-X (http://www.ee.psu.edu/reu/)

R_{DS} maxima far to the right. As the device is subjected to vacuum, we can see that the R_{DS} vs. V_G characteristics undergo a change. It is to be noted that resistance of the curve labeled "In vacuum" is lower than the resistance of the curve labeled "In air". We expect the resistance in vacuum to be higher than in air, because due to desorption higher slope of the R_{DS} maxima should be seen. With vacuum annealing at 200°C we start to see the left tail of the R_{DS} maxima.

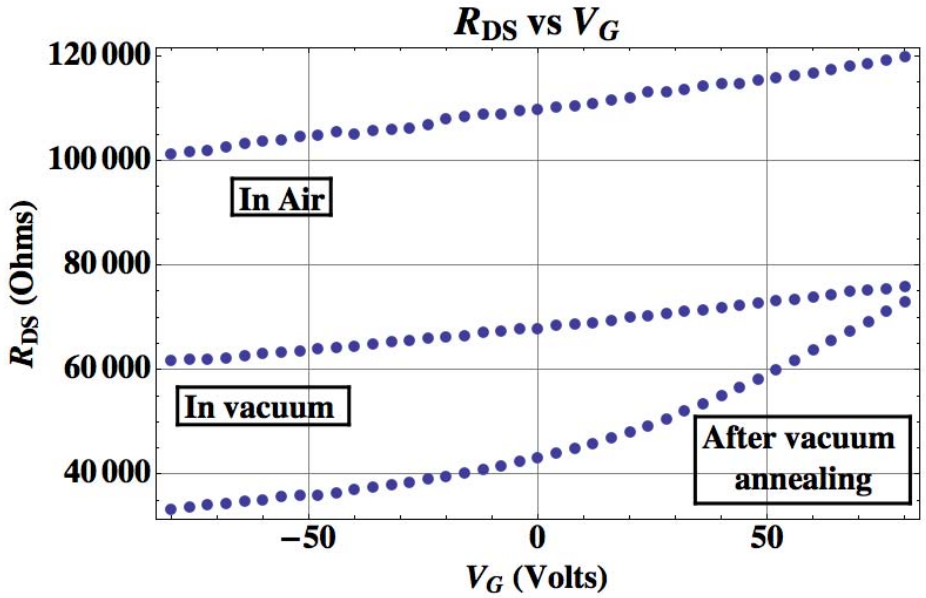

Figure 5: R_{DS} vs. V_G of a tested graphene device in air, in vacuum at room temperature and after annealing in vacuum to 200°C

We carried out two more 24-hour vacuum anneal cycles at 200°C on the device in figure 6. However, owing to time and apparatus limitations, we could not wait to see the complete R_{DS} vs. V_G maxima.

R_{DS} vs. V_G characteristics of the device in figure 5, upon exposure to air flown through a moisture trap that is expected to cut down moisture concentration to below 20 ppb, are shown in figure 6. As can be seen, in the initial few curves shown, it appears that the R_{DS} maxima may be shifting to the right, signifying that air is doping the graphene device to more positive values. However, the inset shows that with time, the R_{DS} at $V_G = 0$ first decreases but after about 100 mins starts to increase monotonically. This is unexpected. We expect that R_{DS} at any given V_G should decrease monotonically with time and then saturate, if the effect was a simple shift in the R_{DS} maxima. However, the monotonic increase in R_{DS} after 100 mins confirms with our R_{DS} measurement of the device in air (figure 5). Given enough time it may be expected that the R_{DS} characteristics of the device would revert back to those shown in figure 5 and labeled "In Air".

Annual Research Journal, Vol. V
Electrical Engineering Research Experience for Undergraduates

ISBN 0-913260-07-X (http://www.ee.psu.edu/reu/)

Having shown the results, it is interesting to ask the question, what component of air causes R_{DS} to change? Is it Nitrogen, Oxygen or moisture, as has been proposed in [2]? Nitrogen, being inert is an unlikely candidate. Moisture, we assume, is very low in concentration to cause any change. Oxygen could be believed to bring about this change. It is also known that Oxygen can induce p-type doping in carbon nanotubes [6]. However, to answer this question completely, it is necessary to do the converse experiment of exposing graphene to moisture which is Oxygen free.

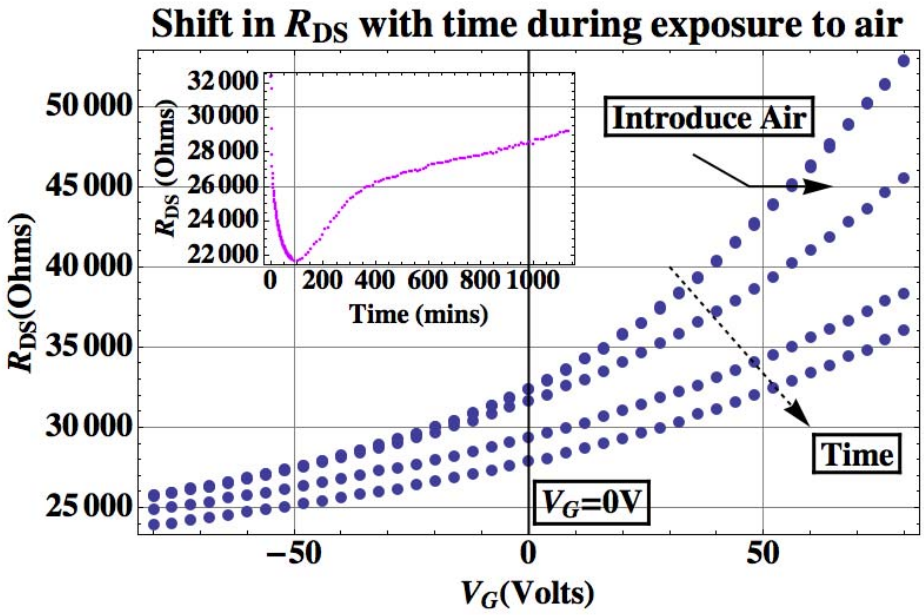

Figure 6: R_{DS} vs V_G of the device in figure 5, above, as it is exposed to air. Inset shows the evolution of R_{DS} with time at V_G = 0V during

SUMMARY

We have been able to show adsorption of species from atmosphere. Based on our study it seems that the doping in graphene from air may be due to Oxygen. However, our study is incomplete. The results need to be reproduced on more samples and the converse experiment with moisture needs to be done. We need to be able to show the R_{DS} maxima in our experiments. This may entail some modification of our test setup. All of the issues mentioned are being dealt with. However, at this time we do not have more results to include in this report.

Annual Research Journal, Vol. V
Electrical Engineering Research Experience for Undergraduates

ISBN 0-913260-07-X (http://www.ee.psu.edu/reu/)

ACKNOWLEDGEMENTS

This material is based upon work supported by the National Science Foundation under Grant No. EEC-0244030. I'd like to thank Dr. Guo and Dr. Jenkins for giving me the opportunity to work on this project. Thanks are due to Dr. Srinivas Tadigadapa who oversaw the project and arranged everything before my arrival. Special thanks to Prasoon Joshi, his hard work and dedication to the project has helped me achieve success even after repeated failures of the apparatus. He has been an excellent mentor. Thanks to Linda for making smooth arrangements during these rigorous nine weeks and Don for making this research experience more enjoyable.

REFERENCES

[1] A. K. Geim and K. S. Novoselov, "The rise of graphene," *Nat Mater, vol.* **6**, pp. 183-191 (2007).

[2] K. S. Novoselov, A. K. Geim, S. V. Morozov, D. Jiang, Y. Zhang, S. V. Dubonos, I. V. Grigorieva, and A. A. Firsov, "Electric field effect in atomically thin carbon films," *Science,* vol. **306**, pp. 666-9 (2004).

[3] K. S. Novoselov, D. Jiang, F. Schedin, T. J. Booth, V. V. Khotkevich, S. V. Morozov, and A. K. Geim, "Two-dimensional atomic crystals," *Proceedings of the National Academy of Sciences of the United States of America,* vol. **102**, pp. 10451-3 (2005).

[4] Y. Zhang, J. P. Small, W. V. Pontius, and P. Kim, "Fabrication and electric-field-dependent transport measurements of mesoscopic graphite devices," *Applied Physics Letters,* vol. **86**, pp. 073104-1 - 073104-3 (2005).

[5] P. Joshi, A. Gupta, P. C. Eklund, and S. A. Tadigadapa, "On the possibility of a graphene based chemical sensor," presented at *TRANSDUCERS & EUROSENSORS '07,* The 14th international conference on Solid State Sensors, Actuators and Microsystems, Lyon, France, 2007.

[6] D. Kang, N. Park, J.-h. Ko, E. Bae, and W. Park, "Oxygen-induced p-type doping of a long individual single-walled carbon nanotube," *Nanotechnology*, vol. **16**, pp. 1048-1052 (2005).

Annual Research Journal, Vol. V
Electrical Engineering Research Experience for Undergraduates

ISBN 0-913260-07-X (http://www.ee.psu.edu/reu/)

Annual Research Journal, Vol. V
Electrical Engineering Research Experience for Undergraduates

ISBN 0-913260-07-X (http://www.ee.psu.edu/reu/)

PITCH SHIFTING OF A SPEECH SIGNAL BY SOURCE-FILTER PROCESSING

Michael P. Steiner*, Robert Nickel[#], and W. Kenneth Jenkins[#]

Department of Electrical Engineering
The Pennsylvania State University
University Park, PA 16802

*Undergraduate of
Department of Electrical Engineering
Virginia Tech
Blacksburg, VA 24060

ABSTRACT

This project uses speech filtering techniques to modify the pitch of a speech segment while retaining the identity of the speaker. Source-filter processing is used to deconstruct a speech segment into an excitation signal and a linear predictive filter simulating the vocal tract. The excitation then goes through a pitch modification by time stretching and resampling. The excitation is then reconstructed using the inverse of the linear prediction filter used to deconstruct the signal. The output signal is a pitch modified version of the original with the formants of the original speaker intact. The resulting sound can be more easily identified with the speaker compared to methods that do not retain the formants. The methodology of finding the linear predictive filter and pitch modifying the excitation signal is shown in depth.

INTRODUCTION

The inspiration behind this algorithm is the natural processes involved in the creation of speech. In natural speech creation, an excitation (flow of air) passes through a cavity called a vocal tract. The shape of the vocal tract effectively filters the excitation into the speech that is heard. Directly modeling this method would be very difficult, however Moulines and Laroche propose a

[#]Faculty Mentor

Annual Research Journal, Vol. V
Electrical Engineering Research Experience for Undergraduates

ISBN 0-913260-07-X (http://www.ee.psu.edu/reu/)

source-filter method where speech can be modeled as the output of passing an excitation signal through a time-varying linear filter[1]. In this method, the excitation signal acts the same as in the natural model, and the time-varying filter acts as the vocal cavity. A simplified depiction of the speech creation model is shown in figure 1.

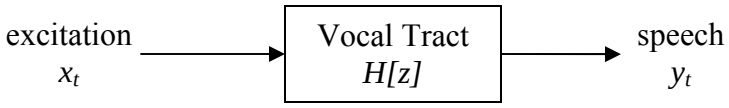

Figure 1. Simplified model of speech creation.

Several methods of pitch change involve stretching the spectral envelope. The benefit of using the source-filter method is that it retains the spectral envelope of the speech. Udo Zölzer et al. note that the spectral envelope is important in the recognition of a particular sound, especially those of speech[1]. The spectral envelope gains its significance from the formants it describes. Formants are the peaks in the spectral envelope that give sounds their individual characteristics, essential to the identification of a certain speaker. There are several ways to estimate the spectral envelope[2], the linear prediction method being chosen for this project because it is well established in the area of speech coding and speech recognition[3].

METHODS

The proposed method has many sub-algorithms used for specific tasks. Synchronous-overlap-and-add (SOLA) methods are useful in changing the duration of a signal by overlapping segments. Resampling combined with time stretching is a way to change the pitch of a signal. The linear prediction method is the basis of the procedure, allowing the signal to be reverse-filtered, and then filtered back again.

SOLA Method

The SOLA method uses windowed sections of a reasonable length to change the duration of a signal[2]. A reasonable length is the number of samples over which the signal may be considered stationary. In this time expansion process, the windows "slide" apart before they are faded and added together, resulting in a longer segment. During time expansion, some parts of the signal will be repeated. The compression method moves the windows closer together, and some windows may be lost in the process. When the signals are stitched back together, the overlapping segments are faded before summing up each sample. The fade occurs by creating a factor matrix which is the length of the overlap and has values from one to zero spaced in even increments. This matrix is then

Annual Research Journal, Vol. V
Electrical Engineering Research Experience for Undergraduates

ISBN 0-913260-07-X (http://www.ee.psu.edu/reu/)

multiplied to the last samples in the first overlapping segment, creating a linear fade-out of the magnitude of those samples from full value to zero. The second overlapping segment has a fade applied to the beginning samples, with the matrix values ranging from zero to one. This creates a fade-in effect where the segment starts at zero and then linearly goes to full value. Udo Zölzer et al. state that typical stretching factors for speech range from 0.25 to 2, while anything larger will cause audible buzziness[2].

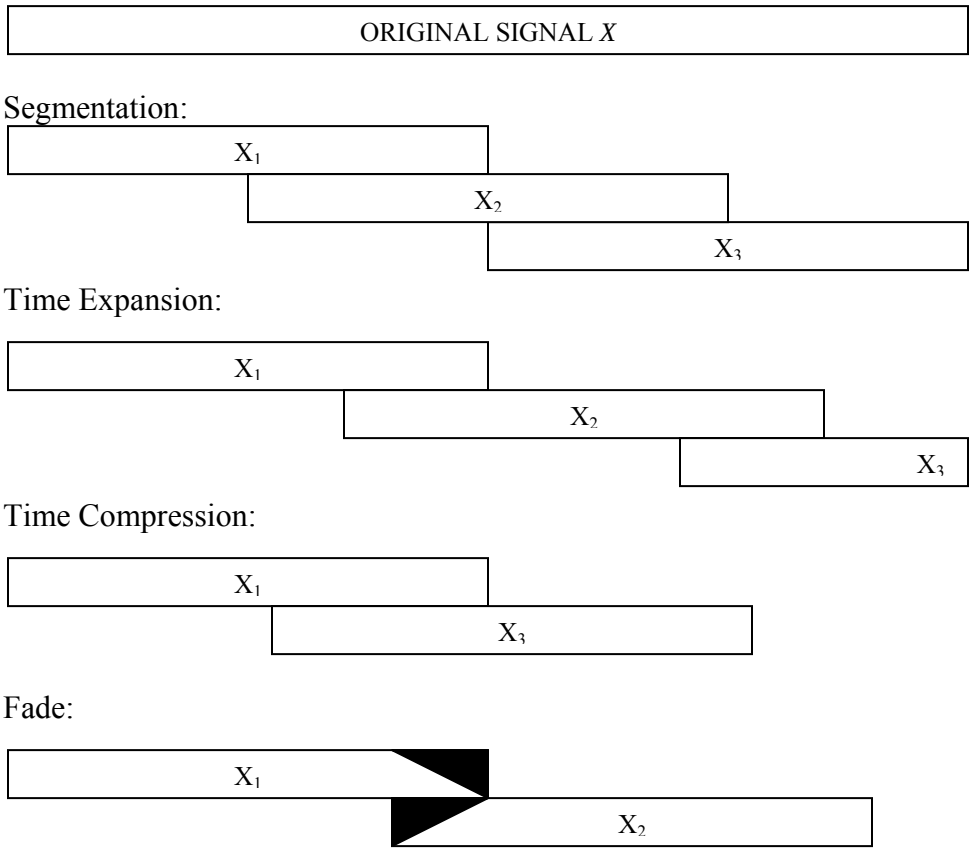

Figure 2. Diagram of SOLA operation.

PSOLA Method

Pitch-synchronous-overlap-and-add method is a variation of the SOLA method but uses pitch marks to identify the optimal length of windows. This method has the benefit of maintaining the pitch of a signal after it has been lengthened. One drawback of this algorithm is that the pitch marks may be

Annual Research Journal, Vol. V
Electrical Engineering Research Experience for Undergraduates

ISBN 0-913260-07-X (http://www.ee.psu.edu/reu/)

difficult to robustly locate, as no definitive method has been found for this purpose[2].

Resampling

The resampling theorem is important to signal processing because it allows for a discrete signal to be reconstructed into an analog version, assuming it was originally sampled correctly using the Nyquist theorem. The analog signal can then be sampled at different intervals than the original discrete signal, higher or lower resolutions of the data[4]. The resampling method used in this case combines several steps to create a discrete signal from the original discrete signal. Equation (1) shows the formula used for resampling, with T the original sampling period, τ the desired sampling period, and k and n the indexes for the discrete signals y and ŷ.

$$\hat{y}_k = \sum_{n=-\infty}^{n=\infty} y_n \text{sinc}(k\frac{\tau}{T} - n) \tag{1}$$

Linear Prediction

The linear prediction (LP) method uses a combination of past inputs and outputs as well as the current input to determine the output[5]. The LP method used for this project is the all-pole model. This procedure creates a set of coefficients, a_k, which describe a filter that can be applied to previous outputs, when combined with the input, to determine the current output.

$$y_n = x_n + \sum_{k=1}^{K} a_k y_{n-k} \tag{2}$$

Equation (2) shows the basic formula for a LP function with y, x, a, and K being the output, input, LP coefficients, and number of coefficients, respectively. Because the signal y is easily represented in matrix form, a least squares method using matrix multiplication was chosen to determine the LP coefficients. First, the input is padded with K zeros at the end to form a new matrix denoted $\boldsymbol{y}$. The matrix **Y** is populated in this way so that it creates a stable filter.

Annual Research Journal, Vol. V
Electrical Engineering Research Experience for Undergraduates

ISBN 0-913260-07-X (http://www.ee.psu.edu/reu/)

$$\mathbf{y} = \begin{bmatrix} y_1 \\ y_2 \\ \vdots \\ y_{N-1} \\ y_N \\ 0 \\ \vdots \\ 0 \end{bmatrix} \qquad \mathbf{Y} = \begin{bmatrix} 0 & 0 & \cdots & 0 \\ y_1 & 0 & \ddots & \vdots \\ y_2 & y_1 & \ddots & 0 \\ \vdots & y_2 & \ddots & 0 \\ y_N & \ddots & \ddots & y_1 \\ 0 & y_N & \ddots & y_2 \\ \vdots & \ddots & \ddots & \vdots \\ 0 & \cdots & 0 & y_N \end{bmatrix}$$

Once these new matrices are defined, they are substituted in for their corresponding part of the difference equation (2) as can be seen in equation (3). The goal of the least squares method is to minimize the error, and hence the input excitation, therefore the input is set to zero in the subsequent steps. Assuming that **Y** is a square matrix, this leads to the resulting equation (4).

$$\mathbf{x} = \begin{bmatrix} x_1 \\ x_2 \\ \vdots \\ x_N \end{bmatrix} \qquad \mathbf{a} = \begin{bmatrix} a_1 \\ a_2 \\ \vdots \\ a_K \end{bmatrix}$$

$$\mathbf{x} = \mathbf{y} - \mathbf{a}\mathbf{Y} \tag{3}$$

$$0 = \mathbf{y} - \mathbf{a}\mathbf{Y}$$

$$\mathbf{y} = \mathbf{a}\mathbf{Y}$$

$$\mathbf{a} = \mathbf{Y}^{-1}\mathbf{y} \tag{4}$$

This would be the solution if **Y** was a square matrix for which the inverse was defined. However, the matrix **Y** will not be square when performing this operation on a signal, so the pseudoinverse of **Y** is used instead. Therefore, the correct formula for determining the LP coefficients is shown in equation (5). These coefficients which are held in the matrix **a** describe the filter used to separate the spectral envelope from the source excitation.

$$\mathbf{a} = (\mathbf{Y}^T\mathbf{Y})^{-1}\mathbf{Y}^T\mathbf{y} \tag{5}$$

Annual Research Journal, Vol. V
Electrical Engineering Research Experience for Undergraduates

ISBN 0-913260-07-X (http://www.ee.psu.edu/reu/)

DESIGN

The implementation of this project is a multi-step process. The first process is to determine the LP coefficients to describe the linear filter. The LP process described above is used to this effect, however instead of doing the process once on the whole signal, the signal is broken down into small windows. Each window was chosen to have a length of about 20 milliseconds. Because the sampling frequency of the segments tested is 16000 samples per second, 320 samples were used in each window. The process uses 15 LP coefficients because there was no audible difference when more than 10 coefficients were used. The noticeable returns when using more than 15 coefficients diminish rapidly.

The next step in the filtering process is to remove the spectral envelope using the LP coefficients. This is done by finding the input excitation using equation (4) on each windowed segment (using the LP coefficients for only that window). In this process, the matrix **Y** is populated slightly differently than when finding the coefficients. This is because the excitation signal itself is not broken up into windows during the filtering process, so initial conditions are available for every window. The exception is the first window, for which the initial conditions are still assumed to be zero. This new matrix **Y**, which shall be called $\hat{\mathbf{Y}}$, is populated as in equation (6).

$$\hat{\mathbf{Y}} = \begin{bmatrix} y_0 & y_{-1} & \cdots & y_{1-K} \\ y_1 & y_0 & \ddots & \vdots \\ y_2 & y_1 & \ddots & y_{-1} \\ \vdots & y_2 & \ddots & y_0 \\ \vdots & \vdots & \ddots & y_1 \\ y_{N-3} & \vdots & \ddots & y_2 \\ y_{N-2} & y_{N-3} & \ddots & \vdots \\ y_{N-1} & y_{N-2} & \cdots & y_{N-K} \end{bmatrix} \tag{6}$$

The matrix $\hat{\mathbf{Y}}$ is then used in the place of **Y** in equation (3) and the unpadded signal is used in place of **y**. The result of the function is the excitation signal, **x** (equation (7)). The excitation is the signal that is modified for the pitch changing effect.

$$\mathbf{x} = \mathbf{y} - \mathbf{a}\hat{\mathbf{Y}} \tag{7}$$

After the excitation signal is found, it is time stretched using the PSOLA method. As described before, the PSOLA method uses pitch marks to identify windows which are used for changing the duration of a signal. When identifying pitch marks, there are two possible signals to use. One possibility is the original

Annual Research Journal, Vol. V
Electrical Engineering Research Experience for Undergraduates

ISBN 0-913260-07-X (http://www.ee.psu.edu/reu/)

signal, and the other is the recently created excitation signal. For this process, the original signal was chosen for deciding the pitch marks because the algorithm will use the same pitch marks as if using a normal time/pitch changing algorithm. After time stretching, the excitation is resampled at a factor that is the inverse of the time stretching factor. This creates an output that is the same length as the original.

Once the pitch modification of the excitation is complete, the excitation is passed back through the filter created using the coefficient matrix, **a**, determined before. Using equation (2), the new output *y* is found by adding the excitation to the sum of the previous outputs which are modified by the LP coefficient matrix. Figure 3 depicts the entire process in block form. The input x(t) is the original speech segment, while y(t) is the pitch-modified output. H(z) is the transfer function describing the LP filter used to strip away the spectral envelope. G(z) is the inverse of that filter which adds the spectral envelope back to the segment. The pitch change includes both the time stretching and resampling steps applied to the excitation. Notice that the pitch marks are found before the original signal is modified, even though they are not used until the pitch change portion of the algorithm. Finding the LP coefficients is the most important step in the algorithm as it sets this method apart from other pitch-changing algorithms. The coefficients found are used both to filter off the spectral envelope and to re-apply it after modification.

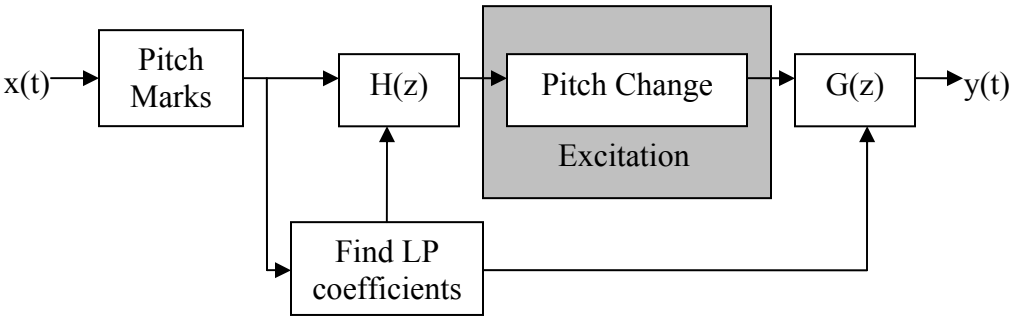

Figure 3. Diagram of program operations.

RESULTS

The pitch changing algorithm does retain the spectral information of the signal. This is especially apparent in the bandwidth of the spectral envelope. Figure 4 shows plots of the spectral data for an utterance. The top graph shows the original signal, while the second shows a pitch change without conserving the envelope, and the last shows the signal modified by the described method. The

Annual Research Journal, Vol. V
Electrical Engineering Research Experience for Undergraduates

ISBN 0-913260-07-X (http://www.ee.psu.edu/reu/)

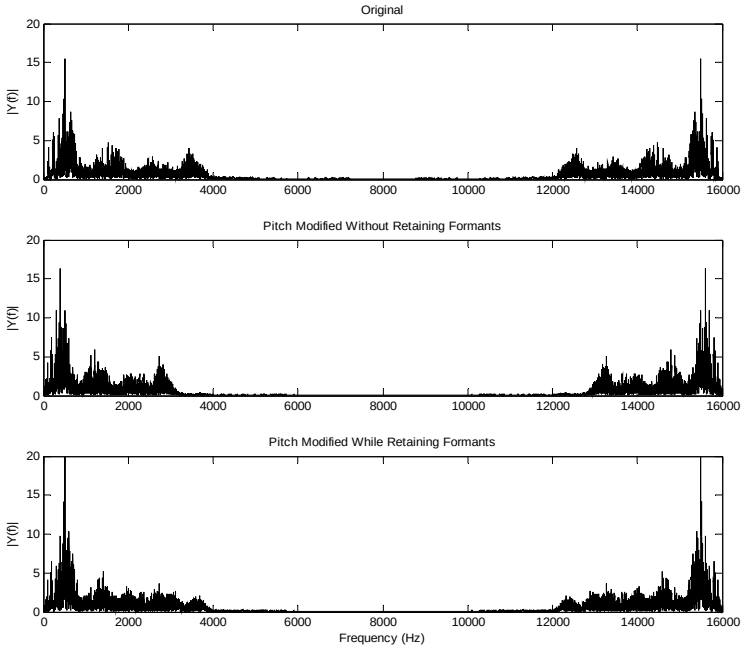

(a)

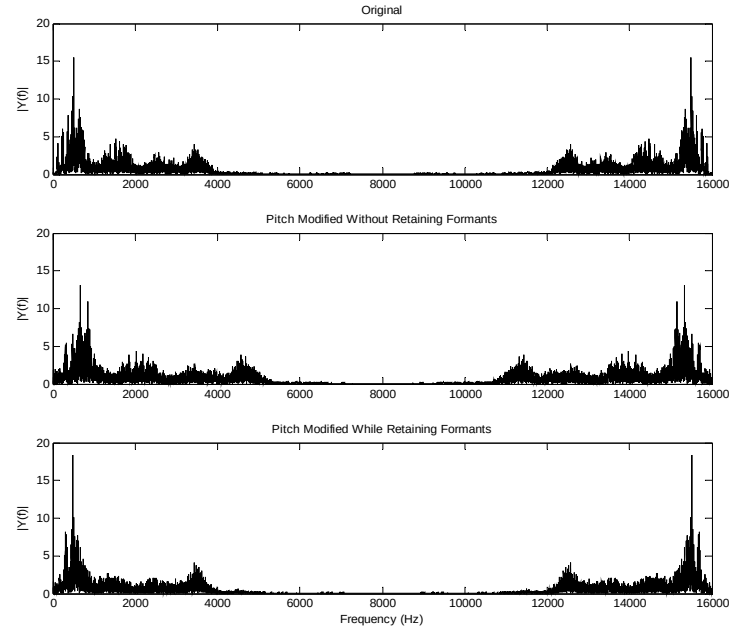

(b)

Figure 4. Plots of a 25% pitch decrease (a) and a 25% pitch increase (b) using various methods compared to the original signal.

Annual Research Journal, Vol. V
Electrical Engineering Research Experience for Undergraduates

ISBN 0-913260-07-X (http://www.ee.psu.edu/reu/)

center graph showing the normal pitch change has a different length of spectral envelope. This distortion demonstrates the common envelope stretching of normal pitch change methods. The top and bottom graphs depict spectral envelopes filling the same bandwidth, giving validity to the source-filter technique.

When the sound is played after pitch modification, the sample modified by the excitation method had no noticeable "Donald Duck" effect as usually seen with other methods that do not retain the spectral envelope[2]. The excitation method does have a noticeable hum when an "r" sound is made, such as in words containing "er" and "or." This distortion may be caused by repeated segments when using the PSOLA algorithm for time stretching. The use of another method for the time stretching or a more robust pitch marking algorithm may produce better results.

ACKNOWLEDGEMENT

I would like to thank Dr. Guo, Dr. Jenkins, and Mrs. Becker for providing this opportunity at the 2007 REU program at Pennsylvania State University. I would also like to thank Dr. Nickel and Dr. Jenkins for their guidance through this project. Also, I greatly appreciate the help of Xiaoqiang Xiao for answering numerous technical and mathematical questions throughout the course of the project.

This material is based upon work supported by the National Science Foundation under Grant No. EEC-0244030.

REFERENCES

[1] E. Moulines, J. Laroche, "Non-parametric techniques for pitch-scale and time-scale modification of speech," *Speech Communication*, **16**: 175-205 (1994).

[2] U. Zölzer, X. Amatriain, D. Arfib, J. Bonada, G. De Poli, P. Dutilleux, G. Evangelista, A. Loscos, D. Rocchesso, M. Sandler, X. Serra, T. Todoroff. DAFX: *Digital Audio Effects*. Edited by U. Zölzer. John Wiley & Sons, Ltd. West Sussex, England, 2002

[3] D. Satyanarayana, K. Satyaprasad, P. Reddy, "Efficient Methods in LPA Using Power Spectrum Estimation of Envelope of Speech Signal," *Information Technology Journal* **6**(2), 300-303 (2007).

[4] P. Tafti, S. Shirani, X. Wu, "On Interpolation and Resampling of Discrete Data" *IEEE Signal Processing Letters*, **13**(12), 733-736 (2006).

[5] J. Makhoul. Linear Prediction: A Tutorial Review. Proceedings of the IEEE, **63**(4), 561-580 (1975).

Annual Research Journal, Vol. V
Electrical Engineering Research Experience for Undergraduates

ISBN 0-913260-07-X (http://www.ee.psu.edu/reu/)

Annual Research Journal, Vol. V
Electrical Engineering Research Experience for Undergraduates

ISBN 0-913260-07-X (http://www.ee.psu.edu/reu/)

THE DEVELOPMENT OF A COGNITIVE DEVICE DRIVER (CDD)

Juan Tamez* and Julio Urbina[#]

Department of Electrical Engineering
The Pennsylvania State University
University Park, PA 16802

*Undergraduate student of
Department of Electrical Engineering
University of Texas at San Antonio
San Antonio TX, 78249

ABSTRACT

A device driver allows computer programs to interact with computer hardware devices. Therefore, the proposed Cognitive Device Driver (CDD) expands the conventional device driver capabilities to include: adaptive learning process, device discovery, translation, and the ability to modify itself to provide a standard interface for communication between an instrument/sensor and a data server. The CDD is built with a combined set of IEEE standards that include the 1451 and the 802.15.4. The IEEE 1451 is a set of standards to make it easier for transducer manufacturers to develop smart device whereas the IEEE 802.15 family of standards provides low complexity and low power consumption for wireless systems. This paper will discuss the first steps to implement the CDD which consists of the assembly of a mini-itx system and manual installation and configuration of the operating system Gentoo Linux. The mini-itx system contains special features which makes flexible and portable the overall design of the CDD. Additionally, Gentoo is a unique operating system that can be fully optimized to interface the CDD.

[#] Faculty Mentor

Annual Research Journal, Vol. V
Electrical Engineering Research Experience for Undergraduates

ISBN 0-913260-07-X (http://www.ee.psu.edu/reu/)

INTRODUCTION

The IEEE 802.15 family of standards specializes in the Wireless Personal Area Network (PAN) through Bluetooth or ZigBee[1]. The Smart Transducer Interface Standards of the IEEE 1451 family are standards that describe network-independent communication interfaces for connecting sensors to microprocessors, instrumentation systems, and control/field networks such as device drivers[2]. Device drivers[3] can be built as parts of the computer kernel or separately as loadable modules. Additionally, device drivers simplify programming by performing translations between devices such as compliant IEEE smart sensors[4] and operating systems. The Gentoo Linux is an open source operating system and its uniqueness is due to the simplicity to adapt to any working environment. In addition, all of the tools and utilities within Gentoo are built from source code such as C, C++, and assembly language. These tools are manually installed through the Portage in the system hard disk drive.

EXPERIMENTAL DESCRIPTION

The uniqueness of the mini-itx system is its architecture design for low power consumption and availability to use in any working environment. The mini-itx is a powerful system developed by VIA technologies. The VIA chipset motherboard (Figure 1) supports 400/355 MHz bus for data transfer, with a robust memory architecture and provides 133/166/200 MHz memory clock frequency. The Hard Disk Drive (HDD) of this system is part of the Samsung HM100JC series providing 100GB storage, 5400 RPM, 8MB Buffer Memory, an ATA 100 Interface and requires 5V to operate(Figure 2).

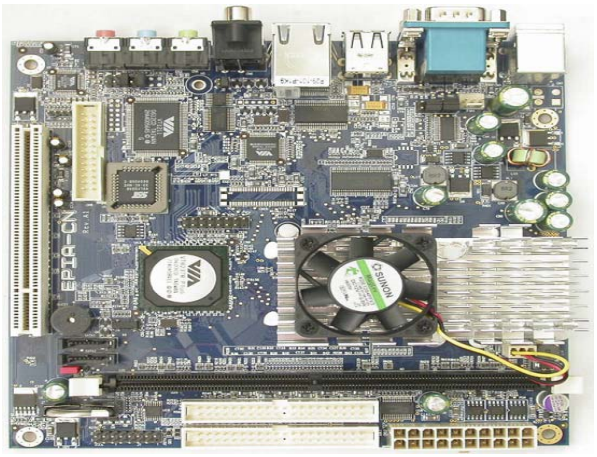

Figure 1. VIA Motherboard

Annual Research Journal, Vol. V
Electrical Engineering Research Experience for Undergraduates

ISBN 0-913260-07-X (http://www.ee.psu.edu/reu/)

Specification	*Description*
Design	Mini ITX form factor 6 layers PCB size: 17.0x17.0cm
Chipset	VIA CN700 Chipset
CPU	Embedded VIA CN700 NANO BGA processor
Memory Socket	240-pin DDR2 DIMM socket x1 Support DDR2 533/400 system RAM Modules DDR memory Expandable to 1GB
Expansion Slot	32-bit PCI slot x 1cs
Integrate VGA	Integrate 2D/3D graphic Engines 8/16/32/64MB frame buffer using system memory Internal AGP 8x performance Support 24-bit 250MHz RAMDAC
Integrate IDE and Serial ATA RAID	Two PCI IDE controllers support PCI Bus Mastering ATA PIO/DMA and the ULTRA DMA 33/66/100/133 functions that deliver the data transfer rate up to 133 MB/s
Dual Gigabit LAN	Integrated Dual Realtek RTL8110SC PCI LAN Chip Support 10 / 100 / 1000 BASE-T Transfer rate
BIOS	Award 4Mb Flash ROM
Dual 10 / 100 LAN	Integrated Dual Realtek RTL8100C PCI LAN Chip Support 10 / 100 BASE-T Transfer rate
Multi I/O	PS/2 keyboard and PS/2 mouse connectors Hard disk drive connector x1 VGA x1, Serial port x1 USB 2.0 connector x2 USB 2.0 Pin-header x2 (connecting cable is option) Parallel Port Pin-header x1(connecting cable is option) Serial COM Port COM2 Pin-header x1(connecting cable is option) Audio connector (Line-in, Line-out, MIC)

Figure 2. Motherboard Specifications

The open source operating system Gentoo Linux was obtained for the mini-itx system. A LiveCD of Gentoo can be obtained from http://www.gentoo.org and it can be automatically optimized for any desired application. Additionally, it has an unlimited adaptability to any source of working environment through its technological development called Portage. The Portage is the main source of Gentoo. It contains many key functions that are critical to the operating system performing to the best of its capabilities. One of

ISBN 0-913260-07-X (http://www.ee.psu.edu/reu/)

the key elements of Portage is the software distribution of Gentoo. It is powerful and unique in its ability to give the user the opportunity to update to new releases over the internet at any given time. For instance, the Gentoo user can easily update and install the latest Gentoo packages by just typing *emerge --sync* in the root command line. Therefore, due to the usefulness of Gentoo it was chosen to contribute as the main operating system for developing a CDD.

RESULTS

In general, the assembly of the mini-itx system was successful. After several trials the partition scheme, Portage installation files, profiles, global use flags and the kernel configuration with genkernel of Gentoo Linux operating system were successfully installed. Consequently, to implement the sensor network in the future, three TelosB mote TPR2420 sensors were ordered from Crossbow Technology Inc. The sensors are primarily designed for an advance research environment. These sensors have USB programming and data collection capabilities of an IEEE 802.15.4 radio with integrated antenna and RF transceiver. The sensors also provide the additional features such as a globally compatible 2.4 to 2.4835 GHz ISM band, 250 kbps data rate, 8MHz TI MSP430 microcontroller with 10 kB RAM, low power consumption, 1MB external flash for data logging, and light, temperature, and humidity sensors.

DISCUSSION

The assembly of the mini-itx system was not complicated, however, a couple of problems arose in the BIOS configuration. The system didn't recognize the HDD; the jumpers and connections were checked again, but the problem persisted. An older version of the HDD was connected for debugging simplicity, and everything worked. The problem was concluded to be due to a faulty HDD from the manufacturer. It was returned and the new one worked as expected.

Installing Gentoo was challenging at times. Once the LiveCD is booted, the user gets prompted to a command line where there are many commands that need to be entered in order to install all the Gentoo packages and kernel configurations. Although there is a Gentoo handbook available at http://www.gentoo.org/doc/en/handbook/index.xml to help with the installation of the operating system, the user must know the hardware devices in the system in as much detail as possible for ease of installation. The first step was to set up the internet connection using *ifconfig* to allow the user to view the available Ethernet networks to configure. Once a working network was obtained, the partition scheme was setup. Due to the flexibility of Gentoo, the partition setup was easily able to meet the needs of the user. For project simplicity only a boot, swap, and root partition were created. Additionally, file systems were created in the partitions to properly mount the partitions in the mini-itx system. Although the internet connection and partitions were created, the installation had just begun.

Annual Research Journal, Vol. V
Electrical Engineering Research Experience for Undergraduates

ISBN 0-913260-07-X (http://www.ee.psu.edu/reu/)

As previously discussed the Portage is the heart of Gentoo and must be installed before system setup. In the Portage the latest release of Gentoo 2007 was downloaded, including the stage3 installation files. The Portage resides in the Gentoo Linux mirrors found at http://www.gentoo.org/main/en/mirrors.xml. The installation of these files was not complicated, but the file name is critical for profile and kernel configuration. Nevertheless, before choosing the profile and configuring the kernel the global use flags were installed to fully optimize for the desired Gentoo working environment. Additional flag changes could be made later once the system was working, but it was preferable to installed them at that this point. Choosing the correct profile was not difficult; it was just a follow up of commands from the Gentoo installation handbook. The most critical step was configuring the kernel[5]. There were two options to choose, genkernel and manual kernel configuration. The genkernel configuration chooses to configure the kernel automatically and tries to select the best configuration for the system, but is not always able to make the best selection. Manual configuration allows the user to configure every part of the kernel. For this task both configurations were performed in one command, *genkernel -menuconfig all*, this allowed for the kernel to configure automatically and to manually choose a configuration for other devices that would not normally be chosen with genkernel.

About 75% of the installation process was completed once the kernel was configured properly. The rest of the installation process consisted of setting up the bootloader process using GRand Unified Bootloader (GRUB) instead of LILO, installing X, and installing Gnome. GRUB was set to run when the mini-itx system starts. It is responsible for loading and transferring control to the operating system kernel software of the Gentoo Linux. The installation process of X was long since 118 dependencies emerged. X provided the interface between the hardware and graphics software. Gnome is the desktop environment that was installed to provide the graphical user interface in the system which is also a long and tedious process.

CONCLUSION

Due to time limitations, only the assembly of the mini-itx system and the manual configuration and installation of the operating system were completed successfully. Gentoo Linux was fully optimized and configured to operate according to the development of a Cognitive Device Driver. It can be seen that the mini-itx system brings top edge technology for the device driver implementation and interface. Consequently, the project will continue in the future with the idea of the IEEE 1451 & 802.15.4 standards.

ACKNOWLEDGEMENTS

I would like to thank my faculty mentor Prof. Julio Urbina for his advice and knowledge in his field of expertise, Dr. Stan Briczinski for his help during the first weeks in the program and for patiently guiding every question I presented to

ISBN 0-913260-07-X (http://www.ee.psu.edu/reu/)

him, the REU directors Prof. Ruyan Guo, Prof. Kenneth Jenkins and co-directors for bringing us with the opportunity to further explore engineering research at Penn State University, and a special thanks to the National Science Foundation for founding the program under Grant No EEC-0244030.

REFERENCES

[1] IEEE Standards Association (July 2007). The IEEE 802 standards. At URL: http://standards.ieee.org/getieee802/.

[2] Wall, R.W. Ekpruke, A. Developing an IEEE 1451.2 compliant sensor for real-time distributed measurement and control in an autonomous log skidder.

[3] Corbet, A. R. J., and G. Kroah-Hartman (2005), *Linux Device Drivers*, 3rd ed., O'Reilly Media Inc. Eckmann, J.-P., S. O. Kamphorst, D. Ruelle, and S. Ciliberto (1986), Liapunov exponents from time series, *Phys. Rev. A*, 34, 4971-4979.

[4] Betts, B. (2006), Smart Sensors, *IEEE Spectrum*, *43 #4*, 50-53.

[5] Bovet, D. P., and M. Cesati (2005), *Understanding the Linux Kernel*, 3rd ed., O'Reilly Media Inc.

Annual Research Journal, Vol. V
Electrical Engineering Research Experience for Undergraduates

ISBN 0-913260-07-X (http://www.ee.psu.edu/reu/)

CHARACTERIZATION TECHNIQUE FOR THIN DIELECTRIC FILMS USING INTERDIGITAL CAPACITORS

Jeremiah P. Turpin[*], Oleg Maksomov[**], Volker Heydemann[**]
Joshua Robinson[**], and Michael Lanagan[#,***]

[***]Department of Engineering Science and Mechanics
[**]Electro-Optics Center
Materials Research Institute
The Pennsylvania State University
University Park, PA 16802

[*]Undergraduate Student of
Department of Electrical Engineering
Grove City College, Grove City, PA 16127

ABSTRACT

The use of interdigital capacitors deposited on a dielectric substrate was explored as a general-purpose characterization technique for the substrate material in the microwave spectrum. A mathematical model based on the physical geometry of the capacitor was implemented, and an experimental technique for measuring the actual capacitance was developed. Characterization with a vector network analyzer and simulations in CST Microwave Studio were compared with the theoretical results. A method of determining the permittivity of the substrate was derived from the expression for capacitance. Calculation of the properties of a thin film dielectric layer sputtered on the surface of the substrate was performed by a similar procedure. Interdigital capacitors lithographed on lanthanum oxide and magnesium oxide substrates coated with a barium strontium titanate thin film were tested under a DC voltage bias to measure the shift in capacitance due to the change in permittivity under the electric field. The capacitance change of the IDCs as a function of bias voltage was investigated and the results were assessed for a final goal of creating tunable filters for microwave applications.

[#]Faculty Mentor

Annual Research Journal, Vol. V
Electrical Engineering Research Experience for Undergraduates

ISBN 0-913260-07-X (http://www.ee.psu.edu/reu/)

INTRODUCTION

For decades, interdigital capacitors (IDCs) have been a standard circuit element in microwave integrated circuits [1]. Recently, interest has emerged in creating IDCs on substrates with an electrically tunable thin oxide film deposited on an insulating substrate to alter the electrical characteristics of the device. These structures are known as multilayered substrates. Some films' permittivity is related to the electric field present in the material. By changing the dielectric constant of the substrate via an electric field, the capacitance of the IDC also changes. Barium Strontium Titanate (BST) is one example of such a material, and has been used in many studies of tunable capacitors and filters [2]. However, there is little work published on an analytical method to accurately determine the capacitance of IDCs lithographed onto a multi-layer substrate. References [3,6] give equations for the capacitance of IDCs with a single layer substrate, but these equations do not apply for multilayered substrates. Gevorgian et al. [1] derived closed-form equations for the capacitance of multilayered IDCs using a conformal mapping technique to account for the different permittivity of the substrate layers. His model is the primary approach used by researchers investigating multilayered substrate IDCs. This analytical solution has been used by [7] in their studies of tunability. Wang et al. [8] evaluated the dependence of Gevorgian's model upon the physical parameters of the system in order to optimize IDC dimensions. Haney [9] used Gevorgian's model as an experimental technique to determine the permittivity of a thin film. In this study the analytical solutions from Gevorgian were compared with electromagnetic simulation and measurement for IDC structures. Measurements were taken of multilayer substrate IDCs with a constant electric field to test the tunability of the capacitors, and capacitance tunability of up to 20% was found. IDCs were found to be a useful method of evaluating the uniformity of a thin film deposition layer.

EXPERIMENT

IDC Model

Gevorgian's equations allowed for a broad range of capacitor designs. His approach includes the permittivity and height of three different dielectric layers – two below, and one above the electrodes. A limiting case of the IDC model in [1] was used in the analysis for this research, where the dielectric region above the electrodes was assumed to be air, or permittivity of 1. This removed consideration of any dielectric material deposited above the capacitor from Gevorgian's model. The geometry of the IDC structure used in this research is shown in Fig 1. The total capacitance was calculated as a sum of three partial capacitances due to first three digits, the periodical capacitance due to additional fingers, and the capacitance due to the ends of the digits, respectively.

Annual Research Journal, Vol. V
Electrical Engineering Research Experience for Undergraduates

ISBN 0-913260-07-X (http://www.ee.psu.edu/reu/)

$$C = C_3 + C_n + C_{end} \tag{1}$$

The parameter s_g specified in Fig. 1 is the geometric width of each digit, and is used with the thickness, t, to find the effective width s of the fingers using (2). The parameter s is used in Gevorgian's model.

$$2s = 2 \cdot s_g + \left(\frac{t}{\pi}\right) \cdot \left(1 + \ln\left(\frac{8\pi\, s_g}{t}\right)\right) \tag{2}$$

A limiting case of Gevorgian's model can be used for calculations of single-layer substrates as well, by setting $\varepsilon_{r2}=\varepsilon_{r1}$.

The model was implemented in a Mathcad 13.0 program. Problems existed calculating the filling factors k_{in} and k_{i3} when h_i was less than 1 micron, because it caused numerical overflow within Mathcad. h_2 can be in the 10nm range in some thin films, so for the program to be applicable, this issue should be corrected. A work around to this problem was created by noting that as h_2

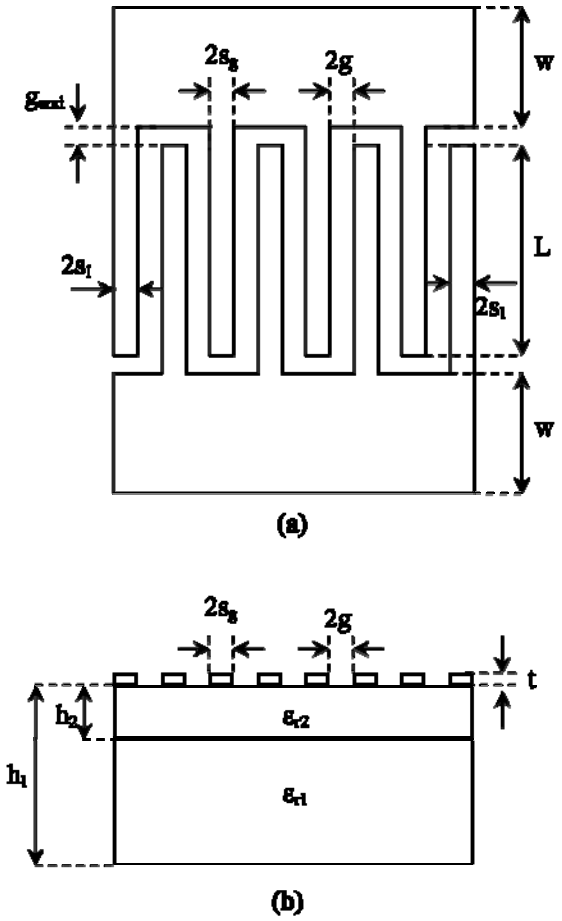

Fig. 1. Layout (a) and Cross Section (b) of an 8 digit (n=8) IDC

Annual Research Journal, Vol. V
Electrical Engineering Research Experience for Undergraduates

ISBN 0-913260-07-X (http://www.ee.psu.edu/reu/)

decreased, the ratio within the square root approached 1. When calculating the filling factors, if the parameters would cause an overflow in calculating the ratio, the square root term was omitted from the calculation. This is not an ideal solution. A more clever method of performing the calculation so as to maintain accuracy, while not creating overflow, is needed.

Haney had a set of capacitors fabricated during the course of his thesis work, and the same capacitor designs were used in this research. The mask contained nine capacitors of different dimensions, as shown in Table I.

Table I. Haney's IDC Dimensions

Label	n	$2s_g$ (μm)	2g (μm)	g_{end} (μm)	L (μm)
I	6	90	10	5	50
II	12	50	10	5	50
III	6	58	6	3	50
IV	12	30	6	3	50
V	6	72	6	3	50
VI	12	30	6	3	50
VII	6	75	6	3	50
VIII	12	40	6	3	50
IX	6	25	2	1	50

Dimensions in Common between Capacitors

w (μm)	h1 (μm)	t (μm)	ε_{r1}
75	650	1.5	9.6

The dimensions provided by Haney were confirmed by measurement with an optical comparator and a profilometer. Gold was used as the electrode material for these IDCs, and alumina as the substrate. Due to imperfections in the manufacturing process, many of the capacitors on each sample were inoperative. Out of three sample substrates, each with nine capacitors, only 10 IDCs were testable.

Measurements of the IDCs were performed using an HP 8510C Network Analyzer and a Cascade Microtech Probe station. The experimental setup is displayed in Fig 2.

Annual Research Journal, Vol. V
Electrical Engineering Research Experience for Undergraduates

ISBN 0-913260-07-X (http://www.ee.psu.edu/reu/)

Fig 2. HP 8510 Network Analyzer and Cascade Microtech 11000 Probe Station

The dimensions of the fabricated IDCs available for testing required the use of a 150 micron ground-signal probe to make contact with the capacitor terminals. The 8510 was calibrated with Cascade's 1-port SOL calibration standards. The data of interest for calculation of capacitance was the S11 reflection parameter, which was captured in tabular format by a LabView virtual instrument into a text file. According to the process outlined in [9], the complex S11 data was transformed to impedance by (3).

$$Z = Z_0 \frac{1 + S11}{1 - S11} \tag{3}$$

Z_0 is 50Ω, the characteristic impedance of the network analyzer. The imaginary component of impedance with respect to frequency was then used in (4) to calculate the capacitance with respect to frequency.

$$C = \frac{-1}{2\pi \cdot f \cdot \mathrm{Im}(Z)} \tag{4}$$

All capacitance values reported in this research, unless noted otherwise, are the capacitance at the frequency for which the imaginary impedance is closest to -50Ω, which is the impedance range that is most accurate for measurement by the vector network analyzer. The processing calculations to transform the S11 parameter into capacitance and choosing the nominal capacitance at -j50Ω were performed in a Mathcad program.

Permittivity Measurement

Gevorgian's equations can be solved algebraically for ε_{r2} or ε_{r1}, so if the measured capacitance is known for an IDC with specified dimensions, then the permittivity of the substrate or thin film can be calculated when the other is known. Haney [9]

Annual Research Journal, Vol. V
Electrical Engineering Research Experience for Undergraduates

ISBN 0-913260-07-X (http://www.ee.psu.edu/reu/)

used this strategy to use IDCs to determine the permittivity of thin oxide films by lithographing IDCs onto known substrates with unknown films. Combining Gevorgian's model and the experimental procedure above, this technique will only be accurate if both the measured capacitance and the analytical model are accurate.

Simulation

Electromagnetic simulation of IDCs, performed using CST Microwave Studio, proved to be extremely useful for understanding and comparing the behavior of the model. Fig. 3 shows the two-layer substrate model used for the simulations. The dimensions were set using parameters, so the same project was used to obtain simulation results for each set of IDC dimensions, which were loaded from a text file using a custom macro. Results matching the measured data were obtained after testing different values for settings in the simulation program. The input wave was launched directly into the terminals of the device, with no microstrip transmission lines to link the input to the capacitor. The initial simulation models had 200 microns of microstrip on each terminal, increasing the simulated capacitance significantly and introducing additional error due to the phase shift.

The time domain transient solver produced the most accurate results compared to the measured values, rather than the frequency domain solver of CST Microwave Studio. Boundary conditions on the model were set to Electric boundaries, where the E-field was equal to 0, and an air gap was added above the top of the contacts. The simulation was performed from 1 to 30 GHz, and the S11 parameter of the output was exported into the same format as the measurement S11 file. The same Mathcad program used to analyze the measurement data was also used to read the simulation results.

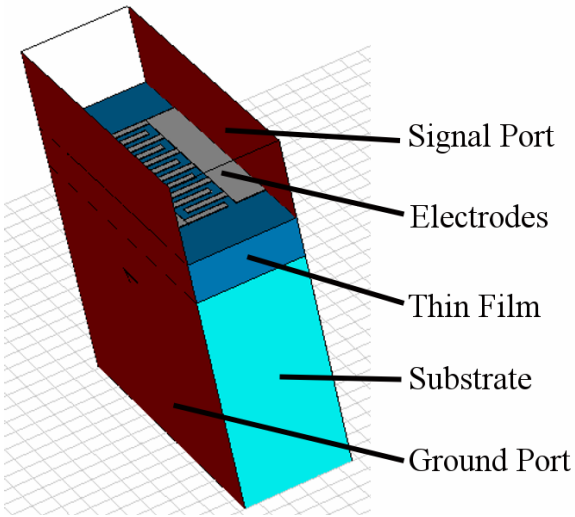

Fig. 3. CST Microwave Studio simulation model

Annual Research Journal, Vol. V
Electrical Engineering Research Experience for Undergraduates

ISBN 0-913260-07-X (http://www.ee.psu.edu/reu/)

RESULTS

Measurement and Calculations

Table II. Measurement Capacitance Results

#	Measured (pF)	Model (pF)	Model error	Simulated (pF)	Sim error
I	0.144	0.220	-41.63%	0.118	20.19%
II	0.188	0.234	-21.88%	0.150	22.29%
III	no data	0.149	no data	0.094	no data
IV	0.143	0.159	-10.87%	0.117	20.19%
V	0.133	0.196	-38.42%	0.108	20.91%
VI	0.145	0.159	-9.48%	0.117	21.57%
VII	0.141	0.205	-37.19%	0.111	23.92%
VIII	no data	0.211	no data	0.140	no data
IX	no data	0.179	no data	0.628	no data

Measurement, calculation, and simulation results are shown in Table II. The S-parameters of the IDCs were found to have a characteristic shape which gives some indication as to the magnitude of the capacitance. In Fig 4, the phase and log-magnitude of S11 are shown for a representative probe measurement, as well as the resulting capacitance. For low frequency, the magnitude is close to 1, and it decreases as the frequency increases. The location of the minima indicates the frequency for which the impedance is close to 50Ω. The capacitors measured were designed so the 50Ω impedance would occur near the 10 GHz frequency range. A precise and noise-free S11 measurement will result in a capacitance plot which does not vary greatly with frequency.

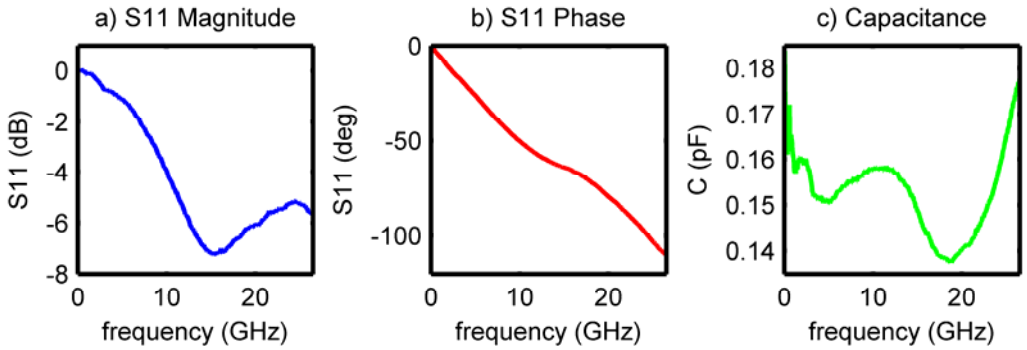

Fig 4. Representative trends of measured S11 and measured capacitance

Annual Research Journal, Vol. V
Electrical Engineering Research Experience for Undergraduates

ISBN 0-913260-07-X (http://www.ee.psu.edu/reu/)

The parameters of the simulation and calculation are the same as those specified in Table I. Due to the minute capacitance which IDCs of these dimensions possess, any experimental error creates very significant differences between the measurements and the model and simulation results.

The process of calibration tends to remove the electrical behavior of the probe tips from the following measurements, but with capacitances in the sub-picofarad range, even the tiny stray capacitance between the probe tips due to the higher dielectric constant could distort the measurement. The measured capacitance of the probe tips alone when touched to the surface of the alumina substrate was approximately 40fF at the same frequency that the measured capacitance of the IDC was 142fF. The probes will have a lower contribution to the IDC measurements, because when the probes are touched to a conductive surface the tips themselves will no longer be capacitively coupled as before. The capacitance would then be between the conductors. By testing substrates with different dielectric constants, it was found that the capacitance of the probe was related to the substrate permittivity, but not to the thickness of the substrate. For alumina samples 600 and 1200 microns thick, the probe capacitance was effectively the same. The exact contribution to the IDC measurement of the probe is unknown. The measured capacitance of the IDCs was small enough that significant variance due to uncontrollable factors was inevitable. Small experimental variation caused by lifting and re-settling the probe tip changed a capacitance measurement by several percent. In order to obtain accurate experimental measurements of capacitance, the measured capacitance of the IDC, including any contribution of the probe, should be much greater than a picofarad to limit the contribution of stray capacitances. The length of the fingers should be increased by a large factor, and/or the number of fingers n should be increased in relation to the capacitors in Table I. Haney's capacitors had length-to-width ratios that were close to 1:1, but better comparisons were obtained with an 8:1 ratio.

Gevorgian's model follows the general trends that were expected from the capacitance measurements, but there are significant differences between the calculated and the measured results. The fingers of the capacitors in Table I are very wide compared to their length. Capacitors I, II, III, V, and VII have fingers that are wider than they are long. In Gevorgian et al. [1], the model is derived under the assumption that the finger length L is much greater than the width 2s. Note the equal finger width and length in Fig 5. Since this is not the case for most of the capacitors measured, the accuracy of the model is very poor. But, for the two capacitors with 2s=30, the error of the calculation is small compared to the wider capacitors. This suggests that better accuracy using the model could be gained by making longer and narrower fingers.

Annual Research Journal, Vol. V
Electrical Engineering Research Experience for Undergraduates

ISBN 0-913260-07-X (http://www.ee.psu.edu/reu/)

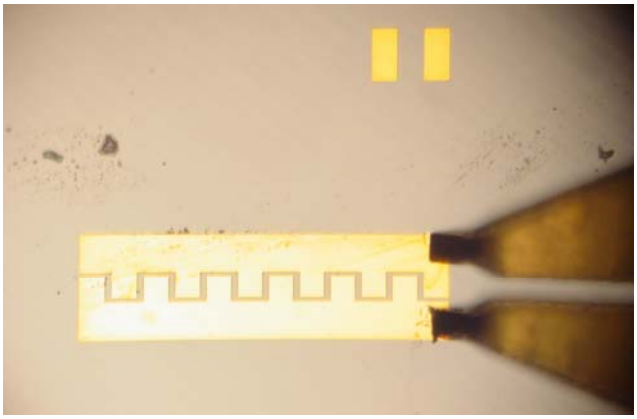

Fig 5. Making contact with Capacitor II using 150μm GS probe

Another error factor in the comparison of the measured and calculated results is that neither the model nor the measurement procedure includes the effects of resistive or inductive impedance. This is a shortfall of the model and the measurement method being used. A model which accounts for resistive and inductive effects with both measurement data and prediction would be more accurate.

Simulation Issues

The simulation results do not match the experimental results, but there is an almost constant error of 20% between the simulated and measured data. This suggests that an improved simulation model or more accurate dimensional measurements may result in more accurate simulations. Even allowing for the existence of experimental factors which are impossible to replicate, if the error factor of 20% proves to be relatively constant, then accurate predictive work could still be performed using the model.

Tunability Studies

Measurements were taken on IDC samples with a tunable film deposited by molecular beam epitaxy. The samples had Barium Strontium Titanate (BST) thin films, approximately 45 nm, on top of Lanthanum Oxide (LAO) and Magnesium Oxide (MgO) substrates. The BST film gave the devices tunable characteristics. Applying a DC bias created a DC electric field between the terminals of the IDC, which affected the permittivity of the BST thin film, thus varying the capacitance of the IDC.

The voltage was applied to the IDC through the signal probe from the HP8510. An HP E3631A digital DC power supply was connected to the bias port of the network analyzer to supply the bias. The power supply was capable of generating up to ±25v, so measurements of S11 were generally made at 5v increments, from -25v to 25v. The S-parameter data were captured using the

Annual Research Journal, Vol. V
Electrical Engineering Research Experience for Undergraduates

ISBN 0-913260-07-X (http://www.ee.psu.edu/reu/)

LabView program, and a Mathcad application was written to process the bias data in order to compare the results of several measurements in one plot. The capacitances were recorded at 10GHz. Multiple capacitors were measured under a voltage bias from each of the two samples. Fig 6 shows plots of capacitance versus bias voltage for representative tunability results. The dimensions for the capacitors in fig. 4 are listed in Table III. IDCs with the same dimensions were measured at different locations on the substrate for Capacitors 1 and 2, with the separate plots indicating different measurements.

The films deposited on LAO and MgO both demonstrated tunable characteristics, but the tunability of the LAO sample was much lower than that of the MgO. There were significant variations in tunability between capacitors on the MgO sample, as seen in Table III. Three different IDCs with the dimensions of Capacitor 1 were measured, and each yielded different results in terms of tunability and unbiased capacitance. Fig 4 shows this variation for Capacitors 1 and 2.

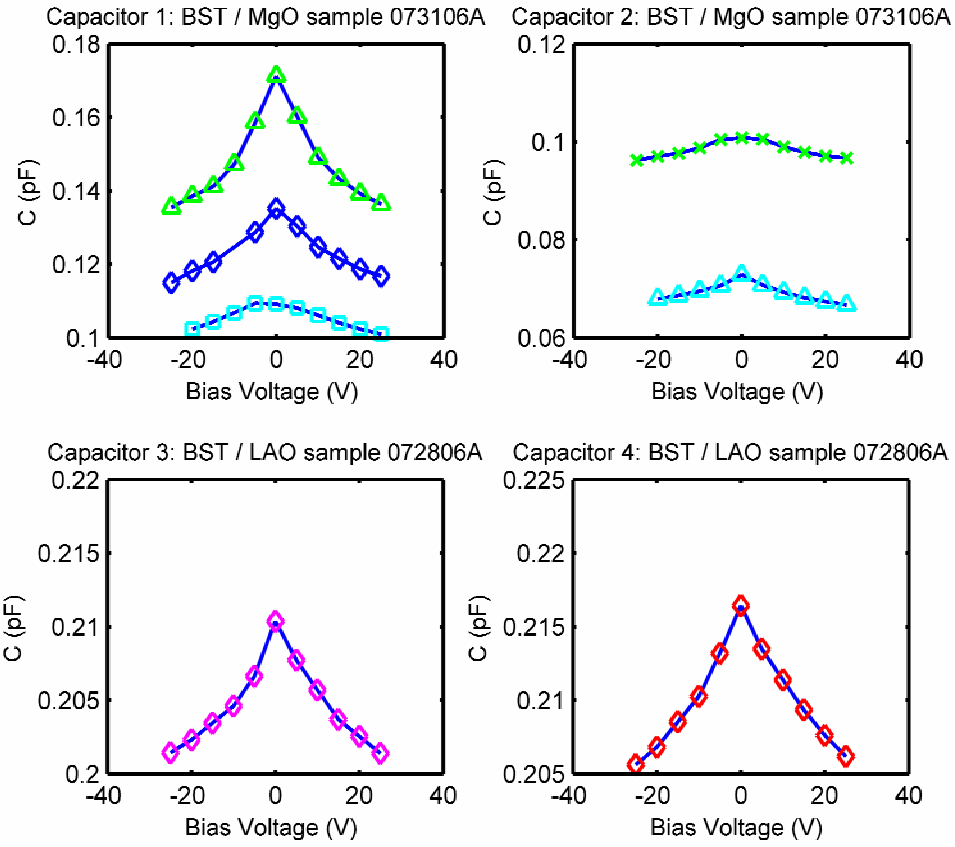

Fig 6. Capacitance of tunable IDC vs. bias voltage

Annual Research Journal, Vol. V
Electrical Engineering Research Experience for Undergraduates

ISBN 0-913260-07-X (http://www.ee.psu.edu/reu/)

Table III. IDC Dimensions for NRL samples used in Bias measurements.

a) BST on MgO sample 073106A

Label	$2s_g$ (μm)	2g (μm)	g_{end} (μm)	L (μm)	Tunability (fF)	%
Cap 1	10	6	6	74	36	20.9%
Cap 2	10	12	12	68	6.8	6.9%

Dimensions in Common

n	W (μm)	t (μm)	h_1 (μm)	h_2 (nm)	ε_{r1}	ε_{r2}
8	100	1.5	500	46.4	25	~1000

b) BST on LAO sample 072806A

Label	$2s_g$	2g (μm)	g_{end} (μm)	L (μm)	Tunability (fF)	%
Cap 3	10	12	12	68	8.9	4.3%
Cap 4	10	8	8	72	11	4.9%

Dimensions in Common

n	W (μm)	t (μm)	h_1 (μm)	h_2 (nm)	ε_{r1}	ε_{r2}
8	100	1.5	500	45.7	9.65	~1000

The higher tunability for IDCs on the MgO substrate can be explained by the difference in permittivity of the substrates. MgO has a relative permittivity of 9.6, while LAO's dielectric constant is 25. The electric field in the BST film was the same for both capacitors, and, if the film is uniform between the two substrates, the change in permittivity of the film under an applied bias would also be the same. The lower permittivity of the MgO substrate caused the same change in permittivity of the BST film to affect the 'average' permittivity of the film and substrate combined more for the MgO substrate than the LAO substrate. This leads to the conclusion for high-tunability structures that the substrates used should have as low a permittivity as possible, to maximize the effect of the permittivity change of the thin film. Minimizing the substrate permittivity is especially important when the films are very thin, as is the case for the samples in this research.

Gap size also was a factor in the tunability. The only difference between Capacitors 1 and 2 is the gap size 2g, which is smaller for Capacitor 1. The smaller gap, with the same voltage, will concentrate the electric field and cause more change in the permittivity of the oxide film.

The tunability and the unbiased capacitance for the same capacitor dimensions at different locations on the substrate varied greatly for measurements on the BST/MgO sample. The difference suggests that either the thin film lacked uniformity, or that the IDC electrodes were not uniformly formed and attached to the film. The capacitance and tunability decreased for the capacitors near the bottom of the substrate. Fig 7 shows the capacitance for IDCs in different locations, but with the same dimensions. The differences persist also in tunability. For Capacitor 1, the tunability was measured to be as low as 7.6% and as high as

Annual Research Journal, Vol. V
Electrical Engineering Research Experience for Undergraduates

ISBN 0-913260-07-X (http://www.ee.psu.edu/reu/)

20% with unbiased capacitances of 0.108pF and 0.171pF, respectively. These data would indicate the presence of higher film permittivity under the capacitor with 20% tunability, with decreasing permittivity as the location of the capacitor changes. The change in permittivity could have been caused by either a changing height of the film, or stoichiometric variations in the deposition process. These results suggest that IDCs could be used to determine the uniformity of a thin film deposition process.

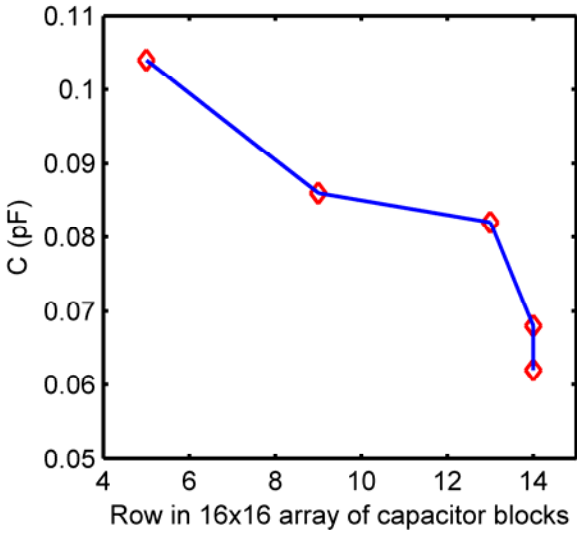

Fig 7. Lower capacitance as location of capacitor changes

As with the alumina substrate, the probe capacitance on the substrate was a significant fraction of the IDC capacitance. Testing in the same manner as before, the probe tip capacitance was approximately 40fF for both the MgO and LAO substrates. This capacitance demonstrated less than 1% tunability with the application of a voltage bias. The small capacitance change of the probe capacitance, on the order of 0.1fF, actually increased for greater bias voltages, which is opposite to the trend for the IDC structures.

The capacitor dimensions in Table 4 were used to calculate the predicted capacitance of the IDCs on the BST thin film with the Gevorgian model. The high film permittivity did not affect the calculation of the capacitance, however, because the thickness of the film was too small because of the program's precision. At h_2 = 45nm, the original calculations resulted in numerical overflow, and the use of an approximation to prevent the occurrence of overflow produced no effect on the calculated capacitance, even for extremely large values of film permittivity. According to a plot of capacitance versus film height in Gevorgian et al. [1], the contribution to the total capacitance by the thin film becomes very small as the film thickness decreases past 0.3 microns.

Were the BST film of the samples thicker, the IDC would be more tunable with a greater 'average' permittivity change, and predictive models would be more

Annual Research Journal, Vol. V
Electrical Engineering Research Experience for Undergraduates

ISBN 0-913260-07-X (http://www.ee.psu.edu/reu/)

accurate. An accurate model of a multilayer IDC could be used in this case as an analytical technique to determine the permittivity of the thin film from an experimental derivation of capacitance. Accurate measurements of the film permittivity with respect to bias voltage, instead of capacitance, could then be made and used to predict the tunability of a new IDC design or film thickness. This would be valuable when planning designs for tunable structures and filters, as it would allow analytical design with fewer validation measurements to determine the necessary IDC dimensions.

Another benefit of using thicker thin films is a byproduct of the higher tunability of the structure. If large tunabilities are achieved, then the precise unbiased capacitance of the IDC is not important for design of filters and components. A capacitor within a broad range near the required value can be more easily developed and tuned in the specific application much more accurately than could be done experimentally.

CONCLUSION

Tunable IDCs show potential to revolutionize the design of RF devices, but there are still areas of optimization to be examined. An accurate model for multi-layer devices is necessary before precise designs can be implemented in creating filters and phase shifters using IDCs. The comparison between the measured capacitance and Gevorgian's model showed the inadequacy of the model to obtain precise predictions of capacitance for the measurement technique used.

Haney [9] applied Gevorgian's equations to determine permittivity of a thin film layer. Haney's work on IDCs was incomplete, however, due to manufacturing defects in the IDCs, so the initial goal of this research was to complete his analysis of IDCs using Gevorgian's model as the basis for a method of determining the dielectric constant of the thin film layer. In implementing the equations in [1], significant differences were discovered between measured values of capacitance and the predictions of the model. With the shorter fingers used by Haney, there was excessive fringe capacitance that was not accounted for in the model. With longer fingers, the accuracy should improve. Gevorgian's model appears to have large error for capacitors with the dimensions that Haney was using for his work.

Without an accurate model which accounts for the thin film, using the measured capacitance to determine the permittivity of the film is not feasible. With improved accuracy, IDCs have the potential to be used as a general-purpose analytical technique for the thin film substance. For future work with Gevorgian's model and the measurement procedure outlined above, capacitor designs should be designed with the limitations of the model in mind. The length of the fingers should be much greater than the finger width, and any thin film layer should be thick enough for the model to calculate. For maximum tunability, gap sizes should be small to concentrate the electric field, and the substrate material should have a very low permittivity. As the substrate permittivity increases, the thin film must be made thicker or with higher permittivity to produce the same results.

Annual Research Journal, Vol. V
Electrical Engineering Research Experience for Undergraduates

ISBN 0-913260-07-X (http://www.ee.psu.edu/reu/)

ACKNOWLEDGEMENT
Thanks to Steven Perini for work in the lab. Thanks to Khalid Rajab for sharing his expertise with CST Microwave Studio and Mathcad.
This material is based upon work supported by the National Science Foundation under Grant No. EEC-0244030.

REFERENCES

[1] S. S. Gevorgian, T. Martinsson, P. L. J. Linner, E. L. Kollberg, "CAD Models for Multilayered Substrate Interdigital Capacitors," *IEEE Transactions on Microwave Theory and Techniques*, vol. 44, no. 6, pp. 896-904 (1996)

[2] W. Chang, J. M. Pond, S. W. Kirchoefer, J. A. Bellotti, "Strain-induced anisotropy in microwave dielectric properties of (Ba,Sr)TiO_3 thin films with directly applied uniaxial <100> stress," Applied Physics Letters, vol 87, 242904 (2005)

[3] G. D. Alley, "Interdigital capacitors and their application to lumped element microwave circuits," *IEEE Transactions on Microwave Theory and Techniques*, vol. MTT-18, pp. 1028-1033 (1970)

[4] R. Esfaniari, D. W. Maki, M. Siracusa, "Design of Interdigitated Capacitors and their application to Gallium Arsenide monolithic filters," *IEEE Transactions on Microwave Theory and Techniques*, vol. 31, no. 1, pp. 57-64 (1983)

[5] L. Zhu, K. Wu, "Accurate Circuit Model of Interdigital Capacitor and Its Application to Design of New Quasi-Lumped Miniaturized Filters with Suppression of Harmonic Resonance," *IEEE Transactions on Microwave Theory and Techniques*, vol. 48, no. 3, pp. 347-356 (2000)

[6] G. W. Farnell, I. A. Cermak, P. Silvester, S. K. Wong, "Capacitance and Field Distributions for Interdigital Surface-Wave Transducers," *IEEE Transactions on Sonics and Ultrasonics*, vol. SU-17, no. 3, pp. 188-195 (1970)

[7] J. Nath, D. Ghosh, J. P. Maria, M. B. Steer, A Kingon, G. T. Stauf, "Microwave Properties of BST Thin Film Interdigital Capacitors on Low Cost Alumina Substrates," *34th European Microwave Conference - Amsterdam, 2004*, pp. 1497-1500 (2004)

[8] Y. Wang, N. Chong, Y. L. Cheng, H. L. W. Chan, C. L. Choy, "Dependence of capacitance on electrode configuration for ferroelectric films with interdigital electrodes," *Microelectronic Engineering*, vol. 66, pp. 880-886 (2003)

[9] R. L. Haney, Chapter 6, pp. 63-79, *Microwave Characterization of Oxide Thin Films*, Master of Science Thesis, The Pennsylvania State University (2006)

Annual Research Journal, Vol. V
Electrical Engineering Research Experience for Undergraduates

ISBN 0-913260-07-X (http://www.ee.psu.edu/reu/)

IMPLEMENTATION OF A FPGA-BASED COGNITIVE RADAR CONTROLLER

Michael Wright* and Julio Urbina[#]

Department of Electrical Engineering
The Pennsylvania State University, University Park, PA 16802

*Undergraduate Student of:
Department of Electrical and Computer Engineering
Florida State University, Tallahassee, FL 32306

ABSTRACT

In this project, we describe the software implementation of a cognitive radar controller. This type of radar controller has the ability to learn from past experiences (events) in order to make automatic target detection without human intervention. The cognitive radar controller was investigated using field programmable gate array (FPGA). The project has two main sections that lead to the configuration of the controller: software and hardware prototyping. Due to time constraints, only the software portion of the radar controller was created and tested. For future work, the remaining section of the project can be prototyped to hardware components and then tested for use.

INTRODUCTION

A controller is a device that manages, directs, commands, or regulates the behavior of other devices. In this project, a radar controller was studied. A radar controller is a controller that has the ability to transmit wave pulses that will then be backscatter, and in conjunction with a radar receiver is able to detect or track an item [1]. The specific type of radar controller that was examined in this paper is referred to as an adaptive radar controller. An adaptive radar controller uses the basic principles of radar detection, but allows for the radar to gain knowledge through experience during operation. This knowledge refers to the controller's ability to use the experience that it has gained to produce its own decisions in tracking the scattering of objects. The core technology of the radar controller

[#] Faculty Mentor

Annual Research Journal, Vol. V
Electrical Engineering Research Experience for Undergraduates

ISBN 0-913260-07-X (http://www.ee.psu.edu/reu/)

will be done using the Spartan-3E field-programmable gate array (FPGA). The implementation was In this project, the implementation of creating an adaptive radar controller was investigated. The core technology of the radar controller will be done using the Spartan-3E field-programmable gate array (FPGA). The implementation was done by a process of code techniques using the VHDL and C++ languages to create a user interface and radar controller program.

EXPERIMENTAL DESCRIPTION

For this project, several software programs were used to implement the radar controller. Also, a FPGA was used due to its low-cost and wide range of possible applications. When performing the experiment, it was found that the implementation of an adaptive radar controller consists of various sections. These "sections" consist of an interface, a program that will save appropriate user input into memory, and a cognitive intelligence program (see Figure 1 for a flow chart of how the project is designed). Each of these processes is a project in itself and is discussed separately.

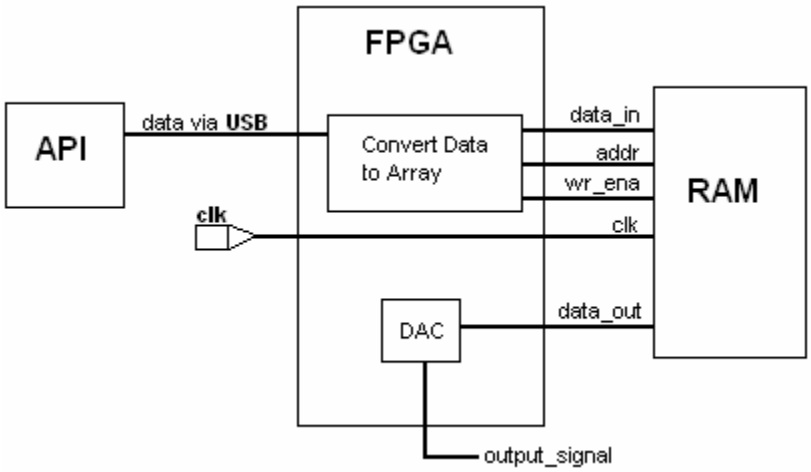

Figure 1: Project Data-Flow Chart

A graphical user interface (GUI) was created using the Visual Studio C++ application programming interface (API). A GUI is a type of interface that is user-friendly and utilizes graphical elements to show information and allow actions from the user. With making use of the C++ software, an easy to use interface was created. This interface program allows the user to be able to save, open, or load a file containing data, input data waveform data in the specified textbox locations, and output data based on the input specified by the user.

Annual Research Journal, Vol. V
Electrical Engineering Research Experience for Undergraduates

ISBN 0-913260-07-X (http://www.ee.psu.edu/reu/)

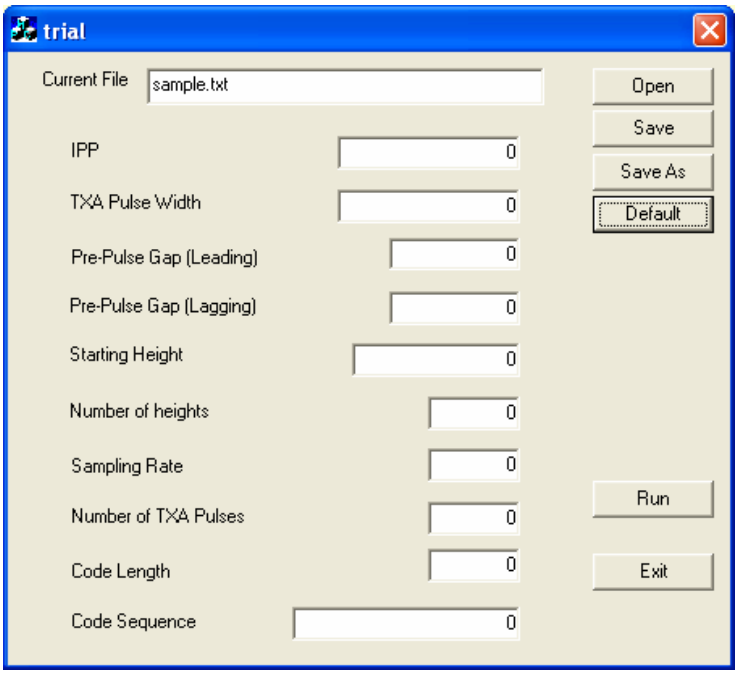

Figure 2: User Interface

More specifically, the user interface will do the following. It will automatically open a specific data file called data.txt that will contain the previous data values saved in the file. A separate data file called sample.txt is provided to give a same set of valid values for the user. The current file that was opened will be continued to be used unless the user specifies a new filename to be saved under or opened. Following the automatic opening of the file, the interface will allow for 10 inputs that correspond to the waveform data. Such things as the period length, the length of time when the pulse is set as high, the number of samples, and the length of waveform using Barker code are available to be set as input.

The interface program also checks to ensure that the data input of the waveform is valid when the "Run" command is pressed. A separate "Default" option is available to set all the default values of input to 0, if necessary. A "Save" option allows the user to save the input data at any time. A "Load" option is accessible to allow the user to be able to input a data file. If an appropriate filename is entered under the load option, then the program shows an error to the user. Also, an "Exit" option is available. This option will close the program after sending a prompt to the user inquiring if the current data is wanted to be saved.

Once that data is set as input into the user interface and the "Run" button is pressed, the data will be sent using via USB cable to the *field programmable gate array* (FPGA). When the data arrives to the FPGA, a program that was made using the VHDL software language will begin its implementation stage. This program accepts the input data and saves it into specified locations in RAM using

Annual Research Journal, Vol. V
Electrical Engineering Research Experience for Undergraduates

ISBN 0-913260-07-X (http://www.ee.psu.edu/reu/)

gate logic. The data is kept in SRAM. SRAM, otherwise known as *static random access memory*, is a type of semiconductor memory device that retains its memory contents for as long as there is power applied [2]. With this, data will be preserved and used when the adaptive intelligence program is executing.

The SRAM was programmed to be 16 bits long and 8 bits wide. This 16x8 RAM allows for the clock and write/read enable bit inputs. Also, it accepts 8 bit data input along with 4 bit addressing. The 8 bit data input is in the binary convention, in that it only accepts the values of 0 or 1, with a maximum of 8 of these bits being present. This means that in base 10, the maximum value that can be obtained is 255. This is similar to the 4 bit addressing. There are four bits; each with the value of either 0 or 1, but the maximum values of these bits combined in base ten is 15.

The write/read enable bit that is accepted as input into the programmed RAM is used to control when the RAM will read from or write to RAM. If a value of 1 is input into this control bit, then the RAM will be able to be written to. If the value of 0 is set as input, then RAM will be read from.

While RAM is being written to or read from, there will be data output from RAM. This data is read from the position in which the input address is designated to. There is a very slight delay time from inputting setting input and receiving output. The delay is on the scale of approximately 1ns should always be noted. Although this delay is apparent, it can be considered to be deemed as something non-pertinent. This is because the 1ns delay is of such a small value, that it can be ignored.

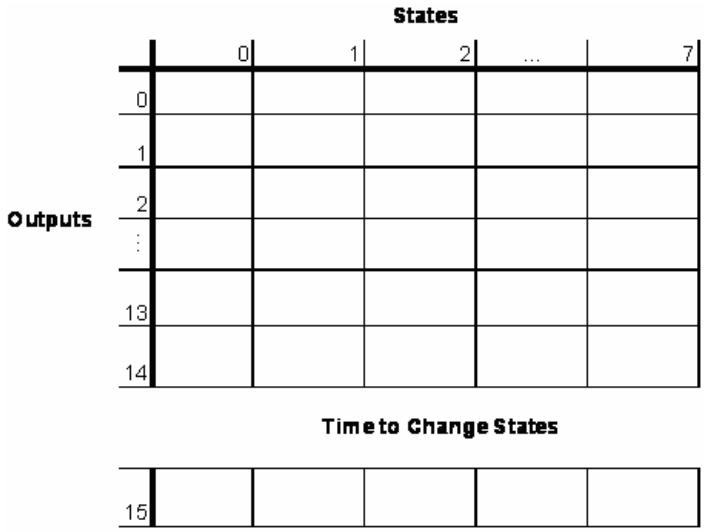

Figure 3: Graphical Representation of RAM distribution

Annual Research Journal, Vol. V
Electrical Engineering Research Experience for Undergraduates

ISBN 0-913260-07-X (http://www.ee.psu.edu/reu/)

The way the 16x8 RAM was programmed can be seen in **Figure 3** above. It shows that the rows for the data are configured as the different waveforms that can be saved into memory. Also, it can be seen that each column of RAM corresponds to the different periods in time, called states, that the waveform are currently at. The last row in memory is dedicated towards keeping track of the time between each state. This is added into the program to add functionality, due to the initial condition that the state count is determined by the output time for the adjacent state.

The waveforms that are saved into memory follow the *pulse-amplitude convention*. This convention assumes that a bit value of 1 in memory, allocates a certain amplitude growth increase [3]. That is the same for when a bit value of 0 is in memory, except it assumes the wave decreases amplitude by a certain amount. When the bits in memory are displayed, that will either be low or high (0 or 1), but following the pulse-amplitude convention, a waveform can be created that represents that sinusoidal output signal.

Following the programming of RAM, the process of linking the interface and the RAM was conquered by using the Front Panel software. Using ModelSim III, the RAM was first programmed into the chip design. Afterward, using preconfigured functions, found from internal libraries found by using the Front Panel software, was used. These functions allow the interface to send information to the simulated design.

DATA AND RESULTS

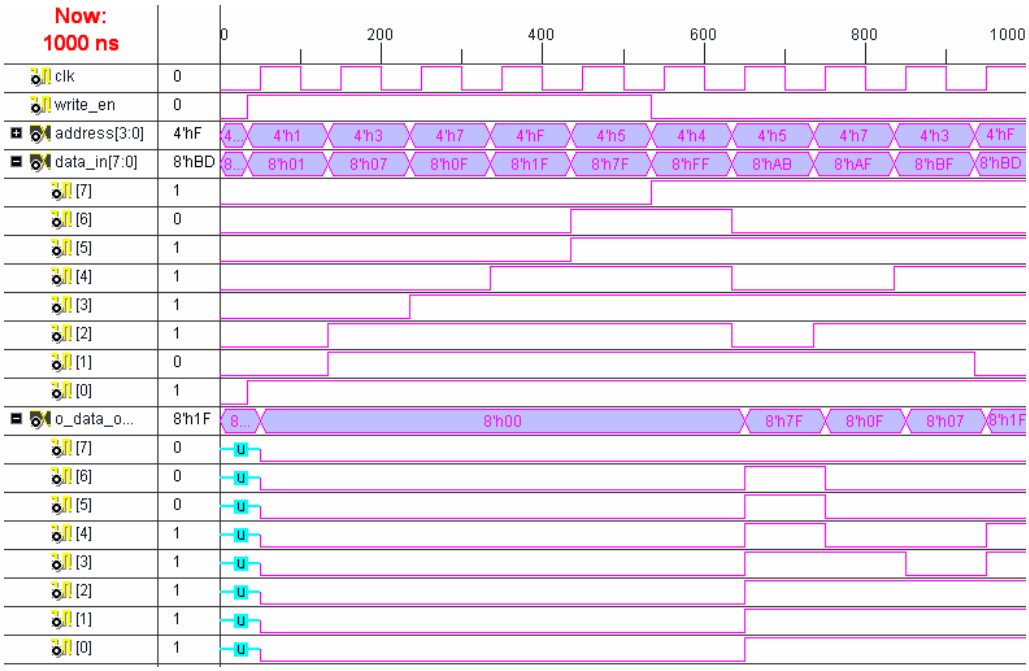

Figure 4: RAM Simulation Testing

Annual Research Journal, Vol. V
Electrical Engineering Research Experience for Undergraduates

ISBN 0-913260-07-X (http://www.ee.psu.edu/reu/)

DISCUSSION

A generic radar works by sending a signal to a designated object a certain distance, d. This signal is assumed to move at the speed of light, c = 3E8 meters per second (or 0.3 kilometers per microsecond) [5]. The transmitted signal will then reflect off of the object and will be read by the receiver. This "returned" signal will have some sort of distortion by way of absorption, transmission, and/or reflection of the waveform.

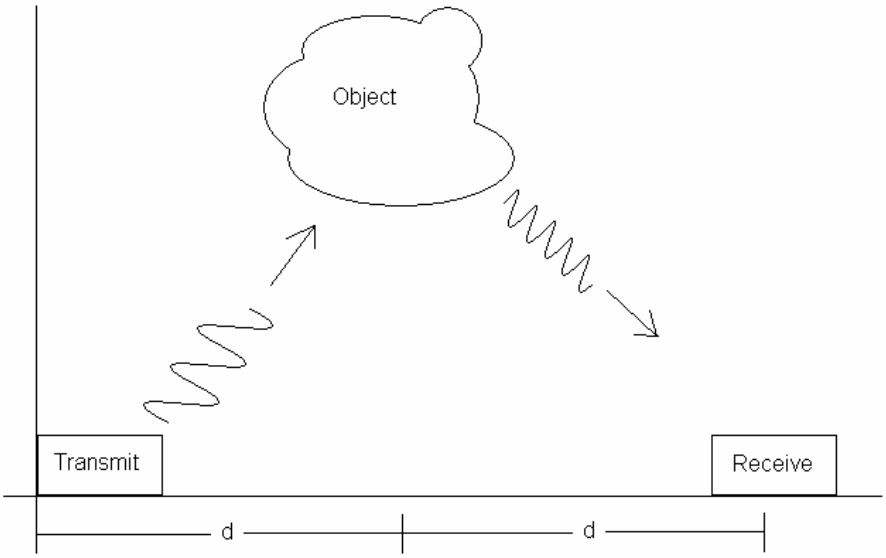

Figure 5: Generic Radar

Since the signal travels one way to the object a distance d and back to the receiver positioned in the original location, then the total distance the signal travels is 2d (See **Figure 5**). From the behavior of electromagnetic waves, time and distance can be related using the equation:

$$2d = ct$$

$$d = \frac{ct}{2} \text{ and } t = \frac{2d}{c}$$

Using this equation, the parameters for the radar can be described from time to distance (vice versa). For example, the period of the wave T, is converted to the period's distance IPP. It should be noted that the parameters will vary depending upon each other and also the various inputs allowed. With the

Annual Research Journal, Vol. V
Electrical Engineering Research Experience for Undergraduates

ISBN 0-913260-07-X (http://www.ee.psu.edu/reu/)

availability of the parameters, a basic knowledge of how adaptive radars work was to be understood using the knowledge gained from **Figure 6**.

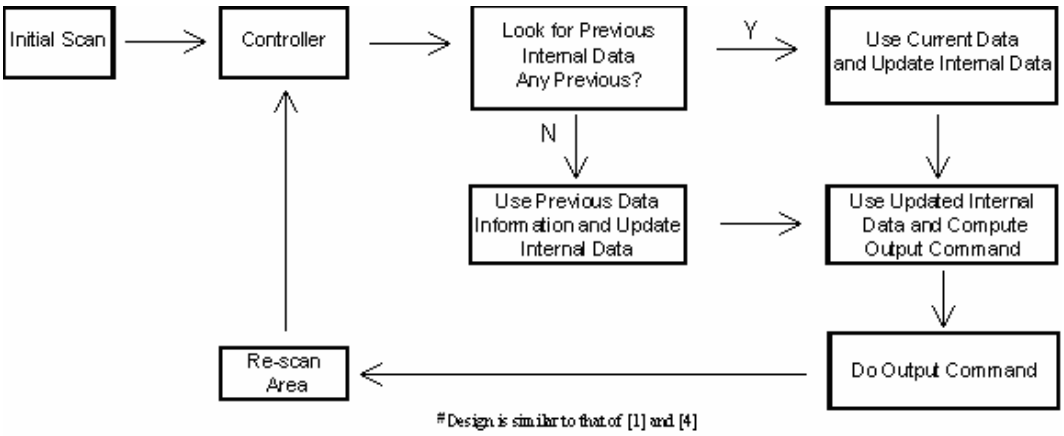

Figure 6: Flow-chart of Generic Adaptive Radar

Using the above figure, it is understood that adaptive radars work in the following fashion. They work in the following manner:

1) Read input from Sensors (Scan)
2) Learn and Update Internal data to allow for adaptivity
3) Use updated data to describe new controller parameters
4) Compute next output commands
5) Send output commands to actuators
6) Repeat Process

#Taken from [1]

Figure 7: Generic Adaptive Radar Actions

With the knowledge gained thus far, the implementation of the project was begun. Using a prior knowledge of Visual C++, it was deemed as not troublesome to create a user interface that can be used. Windows, buttons, and editable textboxes can be added easily using a wizard [6] or can be created from scratch with a little more effort. Either way, the end result will create a user-interface that is similar to **Figure 2**.

Following the interface, programming the RAM caused much strife. Using VHDL without prior experience can be overwhelming and should be taken slowly. Different styles of VHDL programming could have been used to set up the RAM accordingly. Those styles are the Behavioral, Structural, and Data-flow descriptions [7]. Each of these modeling styles has its own pros and cons that should be considered before implementing. The Behavioral modeling style is done similar to programs done in C++ or Java. It only takes in the characteristics

Annual Research Journal, Vol. V
Electrical Engineering Research Experience for Undergraduates

ISBN 0-913260-07-X (http://www.ee.psu.edu/reu/)

of the project and a program is based from it. It works similar to "cause and effect" actions. The Structural description style works by creating gates (ie: NOT, AND, XOR) and using them to control the bits in a signal. This style is similar to those ones done in basic Digital Logic classes that one might take in college. Lastly, the Data-flow modeling description works by using the flow of data to perform various functions.

Using a combination of the Behavioral and Data-flow modeling description styles, the RAM was programmed to accomplish all of its goals. These goals include updating the waveform in memory and having a specific section in memory that corresponds to the state times for each portion of the signal. Also, it was made so the FPGA can just call the address to read data (or write data if the write enable bit is active and valid input data is given).

After the application interface and RAM were configured correctly, the project was tested using the ModelSim III software. From **Figure 5**, it can be seen that the data is written and saved into memory in the proper locations. Also, the data output was correct when the program was set to read the data. With this, a prototype board can be tested using the XEM3005 evaluation board.

Due to time constraints, the hardware prototype testing using the XEM3005 evaluation board containing the Spartan-3E FPGA could not be examined. Due to this, the output data signal was not able to be tested using a digital-to-analog converter and an oscilloscope to see if a valid signal was produced. But due to the appropriate data being output in the simulation, it is assumed that when prototype testing, the program would work accordingly.

It should be noted that additional features could be added to this project to increase functionality. Advanced intelligence software could be implemented to solve the issue of saving unimportant data into memory. This issue that was raised of saving unimportant data was found by noticing that there is a specific size in memory that allows for data. Since there is a limitation in memory, the future intelligence to be implemented should take that issue in account and find a process to either update the data in RAM by overwriting similar occurrences with the new data, deleting data that is not primarily use, or by some other unknown process.

CONCLUSION

Even though there were time constraints for the project and the prototype testing was not completed, this project shows promise for future usage. With the opportunity of completion, this radar controller will be highly valuable and useful in various applications. The adaptive controller can be used for tracking systems in autonomous robots to help avoid objects or recall where different objects are, or in sonar tracking, or in various other relevant processes. Using the FPGA for its low-cost and high manufacturability, it is possible that this process can be implemented and used for various adaptive components.

Annual Research Journal, Vol. V
Electrical Engineering Research Experience for Undergraduates

ISBN 0-913260-07-X (http://www.ee.psu.edu/reu/)

ACKNOWLEDGEMENTS

Foremost, I would like to thank the NSF (under Grant No. EEC-0244030) and SROP programs for funding my research. Without either of these programs, it would have never been possible for me to conduct this research. Also, I would like to thank Dr. Stan Briczinski and my mentor Prof. Julio Urbina for helping me along every step of the way toward completing this project. I would also like to acknowledge Dr. Ruyan Guo, Dr. Evelyn Ellis, Mrs. Jenneth Layaou, and Dr. Anita Persaud for giving me the opportunity to participate in the summer research program at Penn State.

REFERENCES

[1] J. C. Santamarta and A. Ram, "*Multistrategy Learning of Adaptive Reactive Controllers*", Technical Report, pp.1-8, 1997. <http://www.cc.gatech.edu/faculty/ashwin/papers/git-cc-97-05.pdf>

[2] "Static Random Access Memory". Wikipedia Online Encyclopedia. 5 July 2007. <http://en.wikipedia.org/wiki/Static_random_access_memory>

[3] "*Analog and Digital: Sound Representation*", 06 Jun 2007. <http://puma.wellesley.edu/~cs110/lectures/M07-analog-and-digital>

[4] M. Beetz, "*Structure Reactive Controllers – Controlling Robots that Perform Everyday Activity*", The ACM Digital Library. 2007. <http://portal.acm.org/citation.cfm?id=301201&coll=portal&dl=ACM&CFID=2123128&CFTOKEN=32227866&ret=1#Fulltext>

[5] M. N. O. Sadiku, "*Elements of Electromagnetics*", Oxford University Press, USA, 2006

[6] S. Holzner, "*Fast Track Visual C++ 6.0 Programming*", pp. 3-94, 149-187, John Wiley & Sons, New York, 1998.

[7] Nazeih M. M. Botros, "*HDL Programming Fundamentals: VHDL and Verilog*", Da Vinci Engineering Press, 2005.

ISBN 0-913260-07-X (http://www.ee.psu.edu/reu/)

Annual Research Journal, Vol. V
Electrical Engineering Research Experience for Undergraduates

ISBN 0-913260-07-X (http://www.ee.psu.edu/reu/)

AUTHOR INDEX

(* indicates REU Student Author)

Annual Research Journal, Vol. V
Electrical Engineering Research Experience for Undergraduates

ISBN 0-913260-07-X (http://www.ee.psu.edu/reu/)